Title

Microstructural Control and Elevated Temperature Mechanical Properties of Inconel 718 Manufactured by Selective Laser Melting

Author

McLouth, Tait

Publication Date

2020

UNIVERSITY OF CALIFORNIA

Los Angeles

Microstructural Control and Elevated Temperature Mechanical Properties of Inconel 718 Manufactured by Selective Laser Melting

A dissertation submitted in partial satisfaction

of the requirements for the degree

Doctor of Philosophy in Materials Science and Engineering

by

Tait DeWitt McLouth

2020

ABSTRACT OF THE DISSERTATION

Microstructural Control and Elevated Temperature Mechanical Properties of Inconel 718 Manufactured by Selective Laser Melting

by

Tait DeWitt McLouth

Doctor of Philosophy in Materials Science and Engineering

University of California, Los Angeles, 2020

Professor Jenn-Ming Yang, Chair

There is increasing interest in using selective laser melting (SLM) to produce flight hardware in the aerospace industry. Lower costs, faster lead times, and increased design freedom are among the driving forces for the use of SLM, but its relative novelty and a lack of research into the process-structure-property relationships are inhibiting progress. Inconel 718, one of the most prominent high-temperature alloys used in the industry, is quite popular for use in SLM but the mechanisms by which the microstructure and mechanical properties are affected by the AM process have not been thoroughly discussed in the fully heat-treated state.

Experiments were conducted to analyze how certain process parameters—laser focal shift and the scanning strategy—may affect the microstructure formation and resulting mechanical properties. Heat flow and solidification directionality were found to play dominant roles in microstructural formation, and careful manipulation of these parameters can allow users to create highly anisotropic microstructures. It was also found that the as-built microstructure will heavily influence the fully heat-treated structure in terms of grain size, crystallographic texture, and precipitate distribution.

The mechanical behavior was studied as a function of these process parameters and revealed significant differences among the conditions when tested at an elevated temperature. Room temperature tensile testing did not provide a substantial separation of properties between microstructures. However, characteristics like grain shape and the distribution of precipitates that are determined by the as-built structure were found to play significant roles in the elevated temperature performance. Furthermore, anisotropic structures led to variations in mechanical properties based upon sample orientation. Although differences due to the process parameter variations were found to be substantial, they were insignificant compared to the differences found between SLM and wrought material. A major finding of this work is the sensitivity of SLM IN718 to the environment when testing at elevated temperatures. Elongation increases on the order of 600% were found between wrought and SLM as well as a stark difference in notch ductility; SLM samples consistently fail in the vicinity of a stress concentration where wrought samples remain strong.

Modified heat treatments were performed to address differences between the SLM and wrought microstructures to improve the elevated temperature ductility. Thermal treatments designed to increase the precipitation of the δ phase, minimize the formation of NbC, and increase the overall microstructural homogeneity were performed on SLM material. The changes were evaluated based on the same mechanical tests that revealed environmental sensitivity and were found to improve elevated temperature ductility. However, the failure mechanisms remained the same and substantial oxidation and premature failure were observed in all elevated temperature tests. Although the modified heat treatments were effective in precipitating the δ phase and reducing NbC, further optimization is necessary.

The findings of this dissertation conclude that SLM IN718 given typical thermal treatments as outlined by existing AMS standards do not meet current elevated temperature testing requirements. A susceptibility to gas phase embrittlement mechanisms renders the alloy vulnerable to premature failure in these environments. The information presented here will assist users of SLM IN718 in their understanding of the alloy in the AM state and in the development of appropriate thermal post-processing techniques to achieve the correct level of elevated temperature ductility.

The dissertation of Tait DeWitt McLouth is approved.

Jiann-Wen Ju

Xiaochun Li

Jaime Marian

Jenn-Ming Yang, Committee Chair

University of California, Los Angeles

2020

Table of Contents

List of Figures

List of Tables

Acknowledgements

Many people have helped me reach this point, and I would like to express my immense gratitude for their guidance and help throughout this entire process.

Thank you, Dr. Rafael Zaldivar, for always believing in me and pushing me to become a better scientist. You have consistently gone out of your way to help me and to provide new opportunities for my personal and career growth, and for that I am forever thankful. Thank you for showing me the bigger picture when I could not see it, and for teaching me the importance of knowing what matters.

And to Professor Jenn-Ming Yang, thank you for sticking with me all these years. This would not have been possible without your continuous support, and the opportunities you have given me.

A huge thank you to Dr. David Witkin. Thank you for helping me grow as a metallurgist and move forward with research. Your thorough reviews, sense of humor, and sound metallurgical advice were always well-received and much appreciated.

Thank you to the Metals group at Aerospace. Dr. Glenn Bean, thank you for all the lessons you’ve taught me. Julian Lohser, thank you for all the help with this work and for bringing more entertainment to the lab. Dr. Woonsup Park, thank you for your contributions to my research and presentations. Dr. CC Wan, thank you for your calm advice, and helping me build my career.

To Scott Sitzman, thank you for your contagious enthusiasm and unparalleled knowledge of EBSD. It is a pleasure to work with you, and I look forward to our future projects together!

To Paul Adams, thank you for your time and effort helping me with my research. Thank you for your patience, and for some of the best SEM images around.

Thank you to all my Aerospace colleagues who have helped shape me and my work. Dhruv Patel, you have taught me so much in the lab and been a steady mentor throughout this program. Thank you for your patience when I broke things, and for showing me how to put them back together. Dr. Joe Severino, thank you for working with me on so many projects, and always being a reliable source of guidance and lab-hacks. Thank you to Daniel Rivera-Bermeo for all your help and support in the lab, and for understanding what a reasonable time to eat lunch is. Thank you to Dr. Kelsey Folgner and Geena Ferrelli, my fellow Fellows, for being on this wild journey with me. I would not have made it into the program or through it without friends like you.

Thank you to the Aerospace leaders who helped make this program possible. Dr. Sherrie Zacharius, thank you for believing in us and championing for support of the fellowship program. Thank you also to Dr. Jim Nokes, Dr. Tim Graves, and Dr. Chuck Gustafson for your constant endorsement of the fellowship.

I would like to acknowledge the support and funding from the Aerospace Corporate Fellowship, which enabled this work and put me through school. And thank you to the Aerospace Technical Investment program (ATIP) for funding this research.

Thank you to the members of my doctoral committee, Professor Jamie Marian, Professor Xiaochun Li, and Professor Jiann-Wen Ju, for guiding me in my research. You have helped shape this work into its best possible form.

I owe a special thank you to Nicole Carpentier for being my most constant source of support and encouragement. Thank you for picking me up when I’m down, and for always making me smile. You've postponed trips, put up with my loud keyboard, and listened to every one of my presentations at least twice. Thank you for all your positivity and for always being there for me. I am so excited for this new chapter in our life to begin.

To my parents, Larry and Premwadee McLouth, thank you for your advice and encouragement. Thank you for pushing me in school and always supporting my educational pursuits. You have helped me grow from breaking lamps at home for free to being paid to break superalloys at work. Whatever the next step is, I know you'll be there to support me.

Thank you to my brother, Dr. Joel McLouth, for always setting the bar too high and giving me something to strive for. You have always been, and continue to be, a role model of mine.

Thank you to all my friends who have supported me. Without your constant sources of laughter and entertainment I would not have made it this far. Thank you Dr. Dean Cheikh, for showing me that Ph.D.s can have fun too, and always being "up for whatever". Thank you Dr. Ryan DeBlock, for being an incredible roommate and friend for this whole adventure. Your constant encouragement and advice helped me get through the harder parts of the program. Thank you also to Grace Whang, Dr. Jon Lau, Dr. Terri Lin, Dr. David Ashby, Andrew Nuss, Alexander Cheikh, Mark Seal, Brett Beekley, and Douglas Chen for your friendship and all the good times in grad school.

Thank you to Element Materials Technology for assistance with creep rupture testing and chemical analysis. Thank you to Westmoreland Mechanical Testing & Research Inc. for help with combination stress rupture testing.

Portions of Chapter 3 and 4 are derived from two separate publications: T. D. McLouth, G. E. Bean, D. B. Witkin, S. D. Sitzman, P. M. Adams, D. N. Patel, W. Park, J. Yang, R. J. Zaldivar, "The effect of laser focus shift on microstructural variation of Inconel 718 produced by selective laser melting" *Materials & Design* 149, 2018, p205-213, and T. D. McLouth, D. B. Witkin, G. E. Bean, S. D. Sitzman, P. M. Adams, J. R. Lohser, J. Yang, R. J. Zaldivar, "Variations in ambient and elevated temperature mechanical behavior of IN718 manufactured by selective laser melting via process parameter control" *Materials Science and Engineering A* 780, 2020.

Vita

2014	*Bachelor of Science in Materials Science and Engineering, Cum Laude* University of California, Los Angeles
2014-2017	*Graduate Student Researcher & Teaching Assistant* University of California, Los Angeles
2015-2017	*Graduate Intern/Materials Science Staff* The Aerospace Corporation, El Segundo, California
2017 – Present	The Aerospace Corporation Ph. D. Corporate Fellowship
2017	*Master of Science in Materials Science and Engineering* University of California, Los Angeles
2017 – Present	*Advanced Degree Fellow* The Aerospace Corporation, El Segundo, California

Publications

1. **T. D. McLouth**, S. M. Gustafson, H. I. Kim, R. J. Zaldivar, “Enhancement of FDM ULTEM® Bond Strength via Atmospheric Plasma Treatment”, *Journal of Manufacturing Processes*, Submitted Manuscript

2. G. E. Bean, D. B. Witkin, **T. D. McLouth**, R. J. Zaldivar, “Process gas influence on microstructure and mechanical behavior of Inconel 718 fabricated via selective laser melting”, *Progress in Additive Manufacturing (2020) 1-13*

3. **T. D. McLouth**, D. B. Witkin, G. E. Bean, S. D. Sitzman, P. M. Adams, J. R. Lohser, J-M Yang, R. J. Zaldivar, “Variations in ambient and elevated temperature mechanical behavior of IN718 manufactured by selective laser melting via process parameter control” *Materials Science & Engineering A* 780 (2020) 139184

4. D. B. Witkin, D. N. Patel, T. V. Albright, G. E. Bean, **T. D. McLouth, “**Influence of surface conditions and specimen orientation on high cycle fatigue properties of Inconel 718 prepared by laser powder bed fusion”, *International Journal of Fatigue* 132 (2020), 105392

5. D. B. Witkin, R. W. Hayes, **T. D. McLouth**, G. E. Bean, “Anomalous Notch Rupture Behavior of Nickel-Based Superalloy Inconel 718 Due to Fabrication by Additive Manufacturing”, *Metallurgical and Materials Transactions A* 50, 8, (2019) 3458-3465

6. G. E. Bean, **T. D. McLouth**, D. B. Witkin, S. D. Sitzman, P. M. Adams, R. J. Zaldivar, "Build Orientation Effects on Texture and Mechanical Properties of Selective Laser Melting Inconel 718", *Journal of Materials Engineering and Performance* 28, 4, (2019) 1942-1949

7. R. J. Zaldivar, **T. D. McLouth**, G. L. Ferrelli, D. N. Patel, A. R. Hopkins, D. B. Witkin, "Effect of initial filament moisture content on the microstructure and mechanical performance of ULTEM® 9085 3D printed parts", *Additive Manufacturing* 24, (2018), 457-466

8. G. E. Bean, D. B. Witkin, **T. D. McLouth**, D. N. Patel, R. J. Zaldivar, "Effect of laser focus shift on surface quality and density of Inconel 718 parts produced via selective laser melting", *Additive Manufacturing* 22, (2018) 207-215

9. **T. D. McLouth**, G. E. Bean, D. B. Witkin, S. D. Sitzman, P. M. Adams, D. N. Patel, W. Park, J-M. Yang, R. J Zaldivar, "The effect of laser focus shift on microstructural variation of Inconel 718 produced by selective laser melting", *Materials & Design* 149, (2018) 205-213

10. R. J. Zaldivar, **T. D. McLouth**, D. N. Patel, J. V. Severino, H. I. Kim, "Strengthening of plasma treated 3D printed ABS through epoxy infiltration", *Progress in Additive Manufacturing* 2, 4, (2017) 193-200

11. **T. D. McLouth**, J. V. Severino, P. M. Adams, D. N. Patel, R. J. Zaldivar, "The impact of print orientation and raster pattern on fracture toughness in additively manufactured ABS", *Additive Manufacturing* 18 (2017) 103-109

Select Presentations

1. **T. D. McLouth**, D. B. Witkin, J. R. Lohser, G. E. Bean, S. D. Sitzman, P. M. Adams, , R. J. Zaldivar, "Modified Post-Processing Thermal Treatments Addressing Notch Sensitivity in SLM Inconel 718", *TMS 2020*

2. **T. D. McLouth**, G. E. Bean, D. B. Witkin, J. R. Lohser, S. D. Sitzman, P. M. Adams, Z. R. Lingley, R. J. Zaldivar, "Build Orientations and Focal Shift Dependence of Microstructural Evolution, Precipitation, and Mechanical Properties in SLM Inconel 718", *NSMMS 2019*

3. **T. D. McLouth**, G. E. Bean, D. B. Witkin, S. D. Sitzman, P. M. Adams, R. J. Zaldivar, "Microstructural Variation in Additively Manufactured Inconel 718 and Corresponding Mechanical Properties", *Manufacturing Problem Prevention Program (MP3) 2018*

Chapter 1: Introduction

1.1 Additive Manufacturing

Additive manufacturing (AM) is the production of a predefined geometry through the deliberate addition of material. Material is added layer-by-layer only in the areas that correspond to the part, effectively producing a net-shape with little to no waste. In this way, both the material and the part are produced simultaneously, with material melting and solidifying in its near-final form. This is in stark contrast to more traditional manufacturing techniques where cast ingots undergo extensive thermomechanical processing and machining before reaching a final geometry. Because of the reduction in processing steps, additive manufacturing can result in massive cost and time savings when compared to other manufacturing methods. AM has seen rapid incorporation into many different modern industries: automotive, biomedical, nuclear, and aerospace, to name a few. However, AM is still relatively new when compared to more traditional manufacturing processes, and its products have not been as thoroughly studied. An understanding of the entire process, and its relationship with the structure and properties of the resulting material, is necessary for proper implementation.

1.2. Selective Laser Melting (SLM)

Selective laser melting is one of the most popular metallic additive manufacturing techniques available due to the wide range of alloys it can produce and the high geometrical resolution it provides. Popular among the SLM alloys are Ti-6Al-4V [1, 2], AlSi10Mg [3], Inconel 625 [4, 5], and Inconel 718 [6-9], but as research progresses more alloys are being added to this list [10-12]. Process parameter variables can be optimized and tailored for each alloys' specific requirements, but regardless of the material being printed the overall SLM process remains the same.

The first step in SLM is generating the part in a computer aided design (CAD) program. This 3D rendering is “sliced” into the individual layers that are read and produced by the SLM machine one at a time. Every Z-height increment of a layer contains information about the laser scan vectors and boundaries that correspond to the specific geometry at that layer’s height.

The SLM module allows for careful control over powder spreading, the current build height, and powder supply. This is shown schematically in Figure 1, where the major areas and moving parts are labeled: laser, recoater blade, build platform/plate, part, powder overflow, and powder supply chamber. The laser is the primary source of energy for the process, and it is responsible for melting material in specified areas. The XY positioning of the laser is controlled by a mirror galvanometer and f-θ lens system located above the build platform. The recoater blade spreads powder from the powder supply chamber to the build platform and rests at a constant Z-height, moving only in the X-direction. The powder supply chamber is filled with the raw metal powder, incrementally moving upward to supply more powder for every layer. During building, the parts must be secured in place to ensure geometric integrity and reduce warping. To achieve this, parts are built directly onto a substrate of a similar composition or other weld-compatible material known as the build plate. This is attached to the build platform which moves up and down in the Z-direction. The coordinated movement of these components allows the build to proceed.

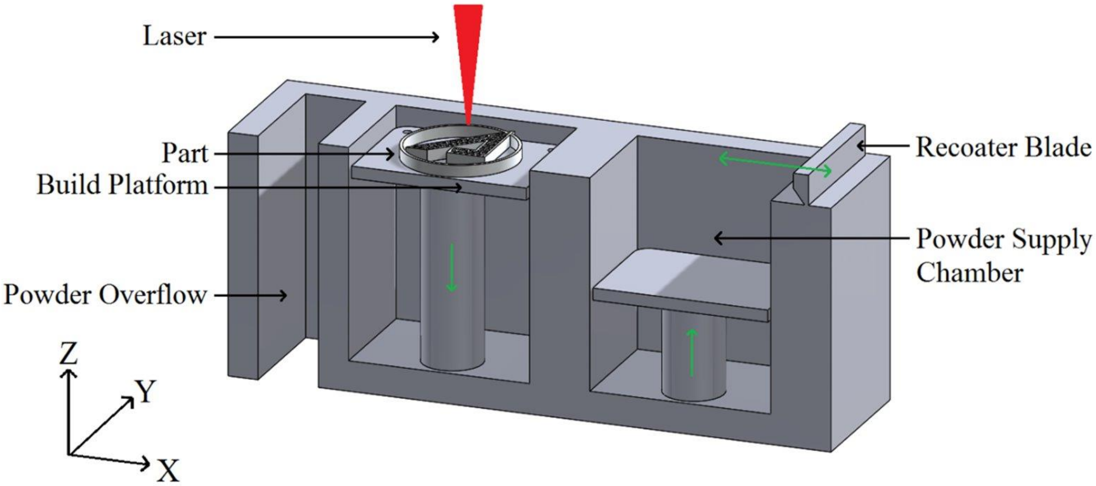

Figure 1: SLM Schematic with major parts listed: laser beam, part, build platform/plate, powder overflow, powder supply chamber, and recoater blade. Green arrows indicate movement directions.

During processing, the build platform will move in the -Z direction a distance equivalent to one layer thickness, and the powder supply chamber will move in the +Z direction an amount greater than one layer thickness. This difference is based upon the dose factor, which can be adjusted based on the volume of powder needed to fully cover the previous layer. When a high amount of surface area is being melted per layer, a larger dose is needed to resupply the area with powder. A typical dose factor used in day-to-day operation is 250%. Once the powder supply chamber has risen, the recoater blade will move across the top surface, skimming the raised powder bed and bringing powder over the top of the build plate. After returning to its original position, the next layer can be melted. The laser fires and the f-θ lens system directs it down onto the plate, selectively melting powder in predefined areas. This process repeats itself until the entire part has been built.

1.2.1 Raw Material for SLM

Prior to the production of parts an appropriate feedstock, or powdered metal alloy, must be chosen. There are many different powder characteristics to consider when selecting the feedstock for SLM: powder size distribution, flowability, particle shape and morphology, porosity, and oxidation [13]. Each of these factors may influence the building process.

The raw material used in SLM is a pre-alloyed powder, most commonly made via gas atomization [13]. This process takes the alloy in its liquid form and creates a melt stream. Then, a high-pressure inert gas is passed through this stream causing the liquid to disperse and form into spherical particles. These particles cool down rapidly as they encounter a cooling plate, leaving a fine powder of the desired alloy [14]. Particles are then sorted by size and distributed accordingly. An example of the morphology of typical virgin powder particles prior to use in an SLM machine can be seen in Figure 2. Not all particles appear as perfect spheres; some particles are elongated in one direction, while others may have irregular surfaces. Some particles have smaller particles attached to them, called satellites, giving them an irregular geometry. All these factors must be taken into account for powder quality.

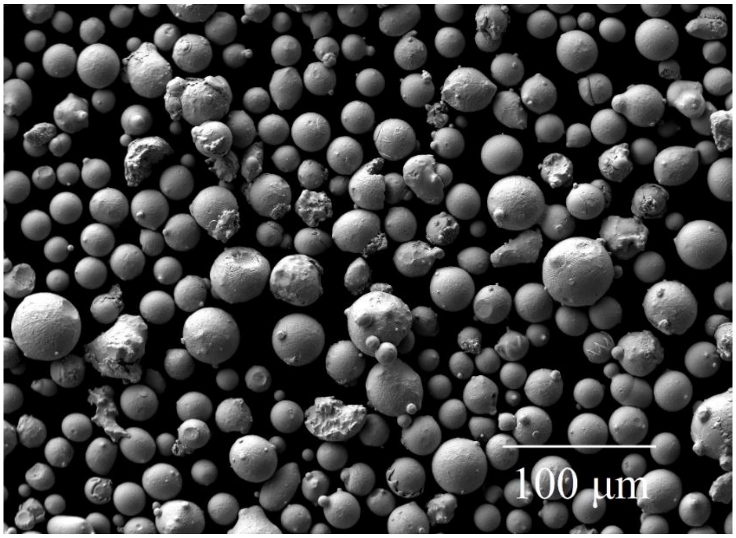

Figure 2: Image of raw powder after gas-atomization and prior to being used in the SLM process. Satellites and irregularly shaped particles are observed in the as-received condition. The D90 particle size distribution metric for the displayed powder is ~45 µm.

The particle size distribution will determine the minimum layer thickness that can be used for production because particles that are too large will prevent thinner layers from being produced. The recoater blade will be unable to evenly spread them on the surface. Particles in SLM nominally range in size from 10 – 65 μm [8, 15] when layers of approximately 30 μm are used. Variations in layer thickness may call for particles of a different size. The size of particles can affect the surface roughness of components; smaller particles will result in smoother surfaces but are more expensive to manufacture [15]. It is also important to have a well-balanced powder size distribution, where smaller particles exist between larger particles. This will improve the packing density of the spread powder compared to a distribution of only a single size [16, 17]. Gürtler et al. [18] demonstrated that with a powder size distribution that contained smaller particles to fill in voids within the powder bed, higher densities could be achieved in SLM parts.

The flowability of a powder is a measure of its ability to spread evenly in a layer. If powder does not spread well it is likely that streaks or defects will appear and destroy the dimensional integrity of the part. Spierings et al. [19] observed that powders with too low of a flowability cannot be used for SLM as the formation of agglomerates may result in defects that are printed into the surface of the part.

The powder that is used in the SLM process passes from the powder supply chamber to the powder overflow and is spread across the build plate, but not all of it is melted during the process. This unmelted and unused powder can be recycled for use in future builds, minimizing the waste generated by the SLM process; only the material necessary to form the net-shape is melted. Recycled powder passes through a sieving machine with a predefined mesh size which separates powder particles that have become too large through partial sintering or satellite attachments from those that are still useful. The effectiveness of powder recycling has been studied in the literature for various alloys [20, 21]. Cordova et al. [20] found that the chemical composition of IN718, Ti-64, and Scalmaloy were insensitive to powder reuse, but that AlSi10Mg was particularly sensitive due to its affinity for oxygen. Powder size distributions were shown to increase in size with increased number of recycles, but only approaches a threshold limit with an appropriate sieving operation. Particles also tend to elongate and change in shape, picking up satellites on the surface with time. However, the results of both studies indicate that for certain alloys like IN718, the reusability of the alloy is nearly unlimited, as detrimental properties, such as reduced toughness, porosity, unfavorable powder size distributions, or increases in oxygen content did not accumulate over time but instead either tapered off or remained unchanged [20, 21].

1.2.2 Solidification Behavior in SLM

Before investigating specific process parameters, it is important to first describe the solidification behavior during SLM. Material undergoes rapid melting and solidification similar to a welding process; however, while the scale of a welding operation may span several centimeters, the SLM process spot size is on the order of 50-100 μm. The difference in scale impacts the cooling rates, which occur much more rapidly in SLM ($10^5 – 10^8$ °C/s) when compared to traditional welding operations ($10 – 10^3$ °C/s) [22, 23].

Common metrics for describing the solidification characteristics of metals are the thermal gradient, G, solidification velocity at the solid-liquid interface, V, and the cooling rate, $\dot{T}$ [23]. The thermal gradient is defined as the difference in temperature between two points, the solidification velocity, also called the growth rate, is the speed at which the solidification front is moving, and the cooling rate is the product of G and V. The ratio of G/V can be used to determine the solidification mode, where high values promote planar growth, and low values form a more dendritic structure. In the case of SLM, the values are low due to the fast solidification rates [3, 24]. These metrics can help to understand the relationship between solidification behavior and the resulting microstructural morphology.

Much of the solidification behavior depends on the melt pool, or the molten bead that is formed in the wake of the moving energy source, the laser. The melt pool takes on a semi-circular appearance and can vary in size and shape based upon the process parameters that will be described in the following section. Typically in laser welding processes there are two heating "modes" that are used to describe the melting behavior and resulting melt pool shape. These are known as keyhole and conduction. Conduction occurs at nominal power densities where the laser melts the powder and the melt pool reaches the underlying layers. The size of the melt pool is governed by thermal conduction into the already solidified layers [25]. In keyhole mode, the power density is high enough that vaporization of material in the melt pool occurs, and the beam penetrates much further into the material from a lack of conduction outward and multiple reflections of the laser within the cavity [26]. Keyholing can result in large amounts of porosity, and extremely deep melt pools.

A diagram of a common conduction-type melt pool is shown in Figure 3. The orientation of the interface between solid and liquid depends on the shape of the melt pool. Due to the Gaussian nature of the laser beam, the melt pool takes on a semi-circular/elliptical shape as shown in Figure 3a [27, 28]. The highest energy density at the center of the beam produces the deepest penetration in the center of the melt pool, tapering off on either side. A cross-sectional view of the melt pool is seen in Figure 3b, where the melt pool normal, solidification velocity, and orientation of the melt pool normal are identified. The melt pool geometry will change the variation of α along the walls of the melt pool. A deeper melt pool would form a shallower angle, α, with respect to the movement of the laser beam and would have a corresponding increase in the solidification front velocity.

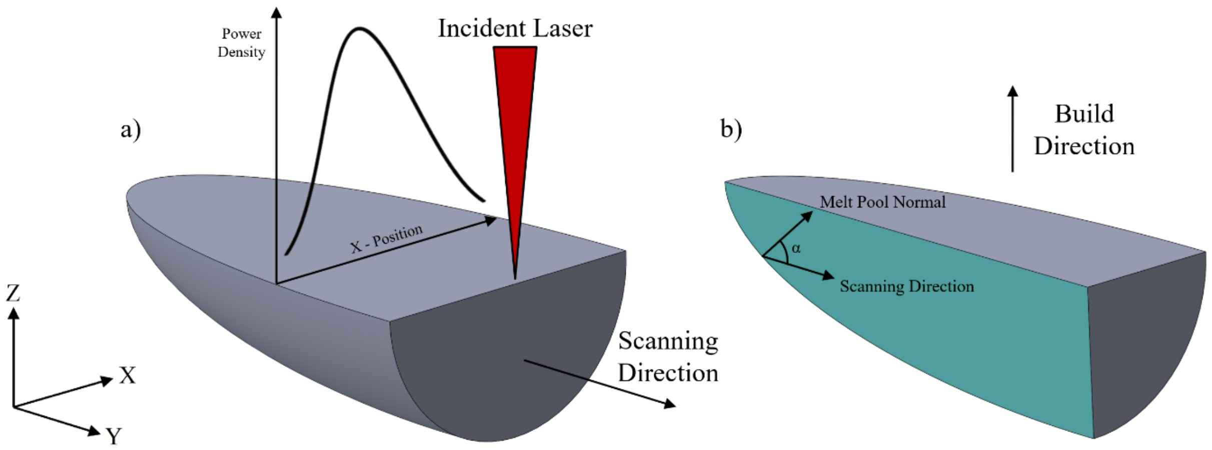

Figure 3: Schematic of a melt pool (a) and its cross section (b), highlighting its geometry and how various solidification metrics relate to it. The power density vs. x-axis position curve is shown in (a) to demonstrate the Gaussian distribution of energy in the laser beam.

Solidification of the melt pool begins at the solid-liquid interface and progresses towards the center of the melt pool [3, 29]. This is because most of the heat is conducted through the bottom and sides of the melt pool that are in direct contact with the previous layer which has already solidified [30]. This creates a degree of directional solidification that occurs at the bottom of the melt pool, facilitating dendritic growth and anisotropic grain formation. It has been observed that the dendrites form perpendicular to the solid-liquid interface, which is the direction with the largest temperature gradient [29]. Rather than forming a perfect radial pattern around the melt pool, there is a variation of the solidification front velocity along the edge of the melt pool. The solidification front velocity varies as follows [23]:

$$\mathrm{V} = \mathrm{V}_b \cos{(\alpha)} \tag{1}$$

Where V_b is the laser beam speed, and α is the angle between the melt pool normal and the direction of the laser beam movement. Thus, the bottom of the melt pool will solidify more slowly than the side walls. With a faster solidification front velocity grain formation will be finer, which can lead to fine-grained areas near the sides of the melt pool [3]. Deviation from solidification along the build direction (BD) will also promote the formation of new grains; a larger volume of constitutionally undercooled liquid will form that promotes grain nucleation [31].

The variation of solidification along the melt pool border contributes to the unique solidification structures observed in SLM material where grains comprised of a dendritic microstructure are observed to grow in different directions depending on where in the melt pool they solidify. At the edges, perpendicular growth occurs nearly horizontally, and so there cannot be continuity across melt pool boundaries of different layers. This is shown in Figure 4, where near the edges the growth is more randomly oriented. Furthermore, edges of the melt pool experience an elevated energy input; subsequent laser scans will remelt these areas due to the overlap of adjacent melt pools. The remelting will result in higher temperatures and larger thermal gradients in combination with more extreme solidification front velocities, which contribute to the finer grain sizes. Near the melt pool centers continuity is possible because the growth/solidification direction is aligned between subsequent layers. This is also observed in Figure 4, where dendrites from one melt pool extend into the adjacent pool. Although the continuity does not span multiple melt pools in this example, the manipulation of process parameters can result in highly continuous grains that can result in a single-crystal-like structure [22, 31-34].

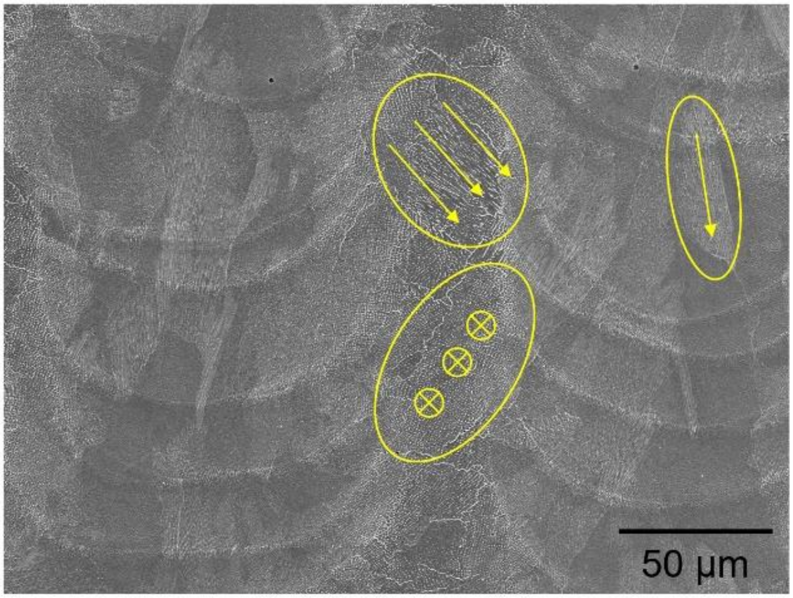

Figure 4: SEM image of melt pool boundaries where dendritic structures are observed. Random growth directions occur near the edge of the melt pool, while aligned growth parallel to the build direction occurs through the melt pool center.

Microstructures that develop in the as-built (AB) condition in SLM depend strongly upon the direction of solidification and the corresponding thermal gradients. Grains are typically columnar, as there is a strong tendency in SLM to form grains oriented parallel to the build direction (BD). Dendritic cells have been observed in the literature to grow parallel to the build direction, as the maximum thermal gradient is aligned downward due to the substrate heat sink effect [7, 8, 27, 35]. These dendritic cells have a width of λ that has been shown to vary as a function of $\dot{T}$, where higher values of $\dot{T}$ correspond to finer cells [36-38]. Grains within the as-built structure are comprised of parallel dendrites. It has been observed that the MPBs that form because of laser passes do not always coincide with the grain boundaries. Grains tend to span multiple layers, providing some degree of continuity between subsequent layers. Furthermore, these grains tend to have a favored crystallographic orientation based on the crystal structure of the parent material and direction of dendrite growth. In the case of Inconel 718 with an FCC matrix, there is a tendency of dendrites to form along the (100) direction [36]. The observation of solidification dendrites dictates that the solidification front cannot be planar, and thus a region of constitutional supercooling must exist in front of the planar interface [36].

Constitutional supercooling arises during alloy solidification when the buildup of solute elements in front of the solidification front alters the local equilibrium solidification temperature. If the liquid front exists below its equilibrium solidus temperature, then it is said to be supercooled. This supercooling results in the formation of stable protrusions at the solidification interface which turn into dendrite arms [36]. As the dendrites grow solutes are rejected laterally, building up in the interdendritic regions and forming local areas of high solute concentration. This phenomenon has been observed in IN718 for alloying elements such as Nb, Mo, and Ti [35, 38, 39]. These elements are more likely to segregate as they exist in the matrix phase in low relative concentrations. Within these regions, there is a higher tendency to form detrimental phases, such as the Laves phase or MC-type carbides. Segregation effects can be reduced when the cooling rate is increased, as there is less time for the lateral diffusion of these elements [38].

The aligned growth of dendrites in SLM creates a crystallographic texture in addition to a morphological one. For example, dendrites of a cubic material will tend to grow cells along the <100> direction [36, 37]. The preferred growth direction is chosen as the growing crystal seeks to minimize total surface energy and also surface stiffness; for cubic crystals this is achieved in the <100> direction [40]. This phenomenon occurs most readily along the centerline of the melt pools where dendrites form continuously due to aligned thermal gradients and growth directions. The previous layer acts as the substrate, and when the uppermost portion of the melt pool is remelted, the newly solidifying material can take on a <100> texture in areas where this crystallographic orientation aligns with the heat flow [3, 24]. This epitaxial growth gives rise to elongated grains of the same crystallographic texture throughout a SLM part. Near melt pool edges there is the nucleation of new grains and the same continuous growth does not occur; grains of this area tend to be more equiaxed in morphology [6].

The AB structures in SLM can be complex and will vary depending on the process parameters chosen. The morphology, size, and distribution of these structures changes based on energy input. The energy directly impacts the cooling rate, solidification speed, and even the directionality of heat flow. So far, ideal energy inputs have been assumed; however, with unoptimized parameters, defects and imperfections can form within a part and degrade material properties.

1.2.3 Defects in SLM

Prior to a discussion of the variability that process parameters can introduce, it is important to define the potential defects that may form because of an unoptimized process. The complex nature of the SLM process creates opportunities for imperfections to form. Starting with the initial laser-powder interactions all the way through cooling of the final part, each step of the process presents its own unique challenges.

When the laser initially melts the powder to form a solid shape, it is important that there is sufficient energy to fully melt the powder in the region of interest. If the energy input is too low, there may be porosity that forms as a result of unconsolidated and unmelted powder. An example of this can be seen in Figure 5a, where distinct spherical particles can be seen within the pores of the material. Another type of porosity is trapped gas porosity, which is a natural result of the trapped shielding gas that is used during the process. Gaps that exist between powder particles or pores that are entrapped during the gas atomization process that do not escape from the melt pool will remain as trapped gas porosity. Average pore diameters for trapped gas pores are small relative to unmelted powder particle diameters, and is spherical in nature as shown in Figure 5b. This type of porosity is easily closed by post-processing techniques, such as hot isostatic pressing (HIP). Lastly, with too high of an energy density keyhole porosity may form; the narrow and deep penetration of the laser forms the namesake "keyhole" geometry in the substrate material [2]. Keyhole instability occurs as local vaporization of the metal creates a vigorous oscillation of the weld pool and a pocket of trapped shielding gas may form as a result if the material solidifies around it [41-43]. The typical keyhole pore is elongated in nature and occurs in the center of the weld bead or melt pool. This type of porosity can be seen in Figure 5c.

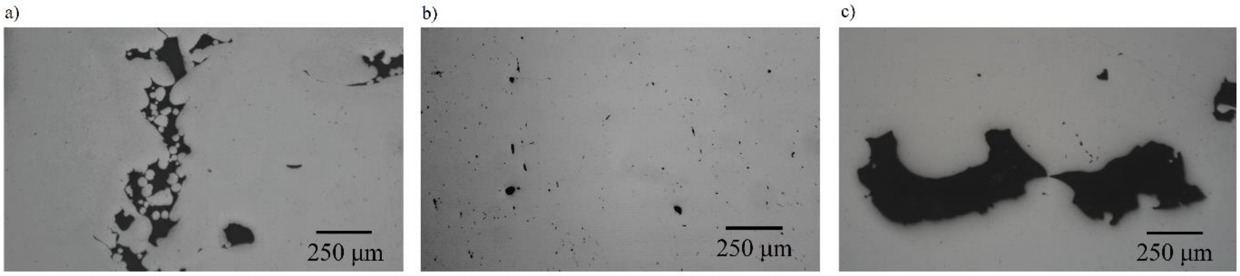

Figure 5: Types of porosity commonly found in SLM: lack of fusion porosity (a), trapped gas porosity (b), and keyhole porosity (c).

Once the material has been properly melted, it must wet the substrate surface to form a smooth surface prior to solidification. Balling occurs when the material does not wet properly, but instead forms into a sphere on the surface. The balling phenomenon is a result of the minimization of free energy through a reduction in surface area, and the surface tension can result in the balling up of molten material. Balling has been correlated to insufficient energy input and melt pool splashing [44, 45]. Balling on the surface has the deleterious effect of creating highly irregular surface roughness features and decreasing the overall quality of the build. These surface imperfections may require additional post-processing to eliminate.

Cracking of the material can occur during production with unoptimized parameters. Solidification cracking and liquation cracking are common forms of cracking during AM operations [46-48]. Solidification cracking occurs during solidification, when the last bit of liquid remains between two solidification fronts. As it cools further, forces due to thermal contraction and solidification shrinkage create a tensile load on the material. The interface between the two advancing fronts creates an easy path for a crack to propagate between the tensile forces [49, 50]. Solidification cracking can be overcome by grain boundary engineering techniques that induce the formation of equiaxed grains that can rotate and deform more easily to accommodate stresses that may build up [11]. Furthermore, the equiaxed grains do not provide an easy crack propagation pathway like a single elongated grain does. Liquation cracking occurs in the heat affected zone (HAZ) around the melted metal where the local temperature has risen above the eutectic point [49, 50]. This weakens the surrounding grain boundary structure, and results in local intergranular cracking. Low heat inputs and energy densities can help to reduce liquation cracking.

A second solidification related defect is the buildup of residual stress within the part. This type of stress resides within the material after the process is completed and can result in warpage and macro-scale deformation of the part [51]. The formation of residual stress is a thermal effect, which results from the temperature gradients that occur during production. Rapid remelting and solidification cycles create very high local temperatures near the top surface, and as heat is conducted away from the top surface there is a significant tensile force that develops during the corresponding contraction. Underlying layers will resist the contraction force, and a residual tensile stress exists across the top surface and a compressive layer beneath it [51].

If the stresses that build up during production are too high, it can lead to delamination of the part from the build plate substrate or cracking of the support material due to tensile forces in the build direction. This typically occurs with larger parts where enough residual stress builds up to overcome the interface between the part and the substrate. An example of a part warping to crack the build supports can be seen in Figure 6. This type of defect can have catastrophic results, ruining a part's geometric integrity and sometimes being so severe as to halt the building process; warped parts can interfere with the movement of the coater blade.

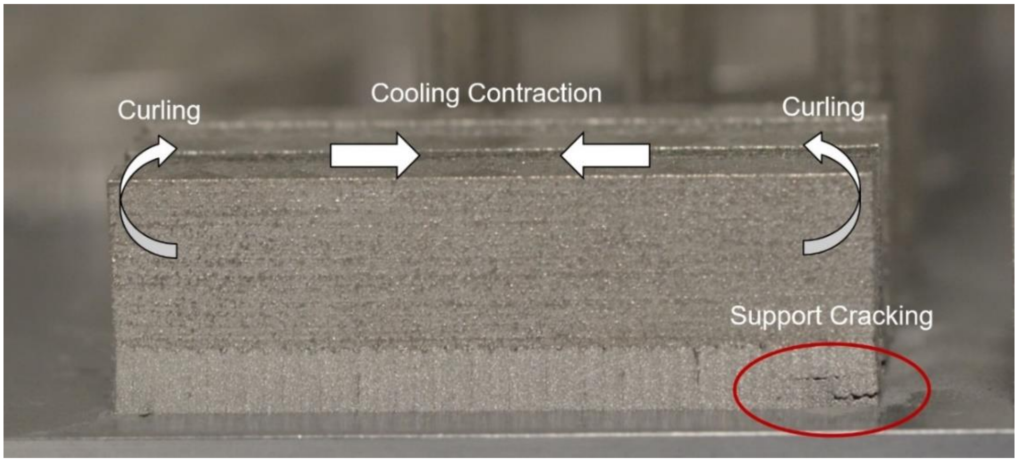

Figure 6: Macro image of a part that has begun to detach from its build supports. The cracked supports can be seen outlined in red. White arrows indicate the direction of force that results from the rapid cooling of parts during the process.

1.3 Process Parameters

The process parameters in additive manufacturing dictate the material properties; understanding which parameters are important and their effects on material properties is an ongoing study that must be understood if high-quality parts are to be made. Process parameters are split up into two major groups: universal parameters and local parameters. The universal parameters affect every part in a single build in the same way; the inert environment and layer thickness are good examples of universal parameters. Local parameters can be assigned individually to specific parts within a build, and even specific layers within a part. These typically affect laser-powder interactions: laser power, scanning speed, scanning strategy, and hatch spacing, to name a few. Many of these parameters will alter the rate of energy input into the raw material, while others will change the pathways of this energy transfer. It is important to consider that there are many different combinations of processing parameters that can result in similar microstructures, densities, and surface finishes. Some of these variations will be relatively minor, while others can be the difference between a part failing to build and one that builds well. The following section will outline what has been done in the current literature and provide a foundational understanding of the work to be discussed in this dissertation.

1.3.1 Laser Power & Scanning Speed

The two parameters that are the subject of most studies are the laser power, P, and scanning speed, ν. The laser power is a measure of the energy output of the laser beam, measured in watts. The scanning speed refers to the velocity of the laser beam as it is scanned across the powder bed and is measured in mm/s. Their popularity stems from their simplicity, availability in a wide variety of laser melting setups, and direct effects on the laser-powder interactions. This section includes a discussion of both of these parameters, as they are frequently altered together in the literature [52, 53]; an optimized balance between them is essential for any laser melting operation. Many common SLM machines utilize a range of laser powers from as low as 40 W [53] to as high as 900 W [22, 54], while the scanning speeds range from 200 mm/s to 2500 mm/s [53].

A common relationship between laser power and scanning speed is the linear energy density (LED), which is given by Equation 1.

$$\text{LED} = \frac{P}{\nu} \tag{2}$$

The balance between these parameters can be seen in this equation. Higher laser power increases the energy output of the laser, and the corresponding local energy density increases. Conversely, a higher scanning speed will decrease the local energy density by decreasing the dwell time of the laser at any given point. With a shorter dwell time, less energy is transferred to the material. The effects of varying both laser power and scanning speed have been observed through the characterization of melt pools in SLM.

Sadowski et al. [53] measured the melt pool width and depth of SLM IN718 as a function of both laser power and scanning speed. It was observed that the melt pools grew consistently in both directions as the laser power was increased and the scanning speed was decreased. Interestingly, they found a higher dependence of the melt pool geometry at low scanning speeds, with 200 mm/s yielding much higher sensitivity to increased beam power than > 700 mm/s speeds. This is most likely due to the large increase in dwell time of the laser at the slow speed. Dilip et al. [2] also observed the increase in melt pool width with increasing laser power and constant scanning speed. The increase in laser power results in a more intense beam and a larger volume of melted material. As the scan speed was increased, the melt pool dimensions shrunk. Shi et al. [52] observed density dependence of Ti-47Al-2Cr-2Nb on laser power and scanning speed. Density measurements yielded an optimal range of scanning speeds when a constant laser power was used. If too high of a speed was chosen, then there would not be enough energy input and the material would not melt fully. This resulted in a phenomenon known as balling, where the material fails to wet to previous layers and spherical particles are found on the surface from the surface tension [55]. On the other end, at too high of an energy input keyhole porosity would form. These observations are explained by the dwell time of the laser, and the corresponding energy input.

1.3.2 Scanning strategy

The scanning strategy determines the physical layout of the laser scan vectors in SLM. Although it does not affect the laser's parameters, it plays an important role in the determination of energy input into the material. Some of the common scanning strategies used in SLM are the island scanning strategy [56-60] and continuous scanning strategy [29, 61, 62]. Other common strategies used across the PBF techniques include point scanning [32, 33, 63] and stripe scanning [64], but the most studied strategies in SLM are island and continuous scans.

A schematic of each of these layouts can be seen in Figure 7. In island scanning (Figure 7a), the control software divides the two-dimensional area into 5-mm squares and randomly scans one square at a time. The squares overlap one another by a user-specified parameter similar to the hatch spacing. After each layer, the checkerboard pattern is shifted 1 mm in both the X and Y directions, offsetting the squares to avoid seam formation along the overlapping lines. The second common scanning strategy used is called the continuous strategy (Figure 7b). Laser scans will raster across the entire length of a layer, and continuously move from one side to the other.

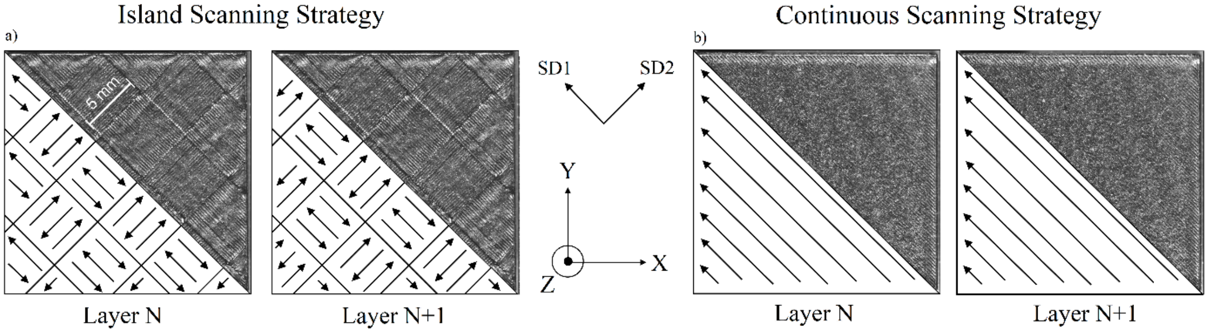

Figure 7: a) The alternating and bidirectional island scanning strategy is shown with both scan directions (SD1 and SD2) shown. b) The continuous scan strategy using a non-alternating and non-bidirectional patter is shown, with scan vectors only parallel to SD1.

While island and continuous notations determine the overall layout of the laser tracks, two further classifications—alternating and bidirectional—are used to determine how the scans change within a single layer and in subsequent layers. If a pattern is said to be alternating, each layer rotates the scan vectors by a specified angle. Some common angles are 90° [57, 60] and 67° [29]. The alternating pattern prevents seam formation along parallel scan lines that are directly on top of one another. Bidirectionality refers to a back-and-forth, or snakelike, pattern. In this way, no two adjacent laser scan vectors travel in the same direction. The island scanning strategy in Figure 7a is an example of an alternating and bidirectional island scanning strategy, while Figure 7b presents a non-bidirectional and non-alternating continuous scanning strategy. All of these parameters will determine the orientation of local thermal gradients and can change the resulting microstructures.

Wan et al. [61] investigated the effects of the alternating parameter on the microstructural formation and mechanical properties of SLM IN718 processed with the continuous scanning strategy. It was found that with the non-alternating strategy, samples would form strong <100> crystallographic textures parallel to the scanning direction (SD) and the build direction (BD), while a 90° rotation produced a strong cube texture. This texture produces strong {001} peaks that are 90° apart, producing a symmetry like that of a cubic single crystal. Peaks in their pole figures are observed parallel to the scan direction, but also offset 45° from the Z-axis as a result of the solidification along the edges of melt pool boundaries. Differences between alternating and non-alternating scans arise due to the complex nature of local heat flows, which vary widely with and without alternation. Sun et al. [29] also investigated the effects of alternating layers in Ni-25 at.% Mo with the continuous scanning strategy, choosing to observe rotations of 0°, 67°, and 90°. For an alternating continuous strategy, a strong {100} texture developed along the two scan directions as well as the build direction. This single-crystal like texture strongly follows the scan vectors. For a non-alternating continuous strategy, the strength of texture is increased along the scanning direction, and decreases in a direction perpendicular to it, once again confirming that texture develops parallel to the scan vectors. Interestingly, with a 67° rotation, no single direction in the scanning plane (XY-plane) dominated the texture, but a strong {100} texture developed along the build direction. The formation of this fiber-like texture is due to the distribution of scan vectors that constantly rotate around the Z-axis. The net heat flow is therefore downward, rather than following any one scan vector. These studies on alternating vs. non-alternating scans highlight the importance of knowing the directionality of local scan vectors, as they can play a large role in determining crystallographic texture.

Comparisons between island scan strategies and continuous scan strategies were made by Carter et al. [57] and Robinson et al. [56] on CM247LC and commercially pure Ti, respectively. Carter found a bimodal distribution of grain morphologies in the island scan strategy where fine grains coincided with the island overlapping regions, and coarse grains were found between them within the islands. The fine-grained regions formed due to the high energy input in the overlap regions, which undergo twice as many melt and cool cycles as the inner regions. A high energy input results in steep thermal gradients and rapid cooling; the result of this was extensive cracking found in these regions. The continuous scans resulted in a more even distribution of grain sizes and an overall homogeneous structure because of the more even distribution of energy input and cooling rates. Robinson et al. [56] focused on how scanning strategy affected the formation of residual stress. They found that a non-bidirectional continuous scanning strategy produced stress parallel to the scan direction, an unsurprising result considering the high directionality in these components. Cooling consistently in a single direction can produce high stresses parallel to the scan vectors. Island scans, although designed to distribute heat more evenly, did not show an improvement in stress levels; short scans within an island may create higher local heat input than the longer scans of the continuous scans. Alternating continuous scans demonstrated the best levels of residual stress among all the samples. As the size of the islands was increased, the residual stress levels trended towards that of the alternating continuous samples.

The scanning strategy has shown that local heat input can be greatly affected by the length of the scans, their orientation, and relative layout to one another. The directionality and variation of thermal gradients significantly affects the microstructural formation, a phenomenon that will be further examined in future chapters of this dissertation.

1.3.3 Hatch Spacing

The hatch spacing is defined as the spacing between the centers of adjacent scan tracks. For full or near net consolidation of a part, there should be some overlap of adjacent scans to avoid any regions of unmelted powder. Too little overlap and porosity can form with unmelted powder particles due to insufficient thermal energy at the edges of the melt pool, and too much overlap can result in keyhole porosity that forms from too high of an energy density. Ideally, the hatch spacing provides a more uniform distribution of energy density across the width of the scan tracks.

Cao et al. [30] investigated the relationship between residual stress, recrystallization, and the hatch spacing in laser solid formed Inconel 718, a similar process to SLM. They specify two regions of importance, the overlap area and inner pass area. The overlap area, which is in closer proximity to the substrate layers generates a higher degree of residual stress upon solidification. The inner pass area cools more slowly, and therefore contains a lower residual stress. This leads to microstructural inhomogeneity during recrystallization, as the overlap regions will preferentially form new grains due to high stress levels. A more uniform distribution in heat input that stems from the hatch spacing is critical to producing more homogeneous materials.

Nadammal et al. [65] explored the hatch length for SLM IN718, a similar process parameter to the hatch spacing. The hatch length is defined as the length of a single track; longer hatch length samples will have more time in between adjacent remelted areas, whereas shorter hatch length samples will have rapid remelting of overlapped regions. They found that the longer hatch length samples allow more time for cooling, and therefore temperature gradients are not as severe. This is similar to the inner melt pool areas investigated by Cao et al. in the previous paragraph in that residual stresses are lower in these areas. Additionally, they explore texture development, and found the crystallographic texture to be reduced alongside residual stress in these areas.

These studies highlight the importance of thermal gradients and solidification rates, and how the hatching parameters can affect these. Rapid remelting and high local heat inputs result in high residual stresses, rapid solidification due to steep thermal gradients, and an overall finer microstructure.

1.3.4 Layer Thickness

The layer thickness is the step height in the Z-direction of each new layer and will affect the overall build time, print resolution, and necessary energy input. It determines the amount of raw powder spread over the previous layer prior to the next melting cycle. Thicker layers will require a higher energy input as there is more material that needs to be melted and deeper penetration to reach the previous layer is required. On the other hand, thinner layers must have a reduced energy input so as not to form keyhole porosity and solidify as a dense form. Typical values of the layer thickness in SLM vary from 30 μm [58-60] to 50 μm [66], but values as high as 100 μm [22, 54] have been reported.

Sufiarrov et al. [66] found that the impact strength of SLM 280HL was affected when the layer thickness was increased from 30 μm to 50 μm without a corresponding change in other laser parameters. With thicker layers, there were areas that did not fuse properly, leaving cracks within the bulk structure that acted as stress concentrators. Ma et al. [67] observed uniformity in the density of 1Cr18Ni9Ti samples as the layer thickness was increased but noted a change in the microstructural scale. Thinner layers were shown to form finer microstructures than thicker layers due to the increased cooling rate that could be achieved. Not only can the layer thickness affect part quality, but it can also affect resulting microstructures.

1.3.5 Process Gas

A universal parameter that is held constant for each build is the process gas, which creates an inert environment for the duration of the printing process and carries away by-products of the melting process. A typical SLM machine will have both an inert environment and an active flow of shielding gas over the surface of the powder bed. The inert environment prevents oxidation of the freshly melted surface and underlying powder; the oxygen content is kept as low as 0.1%. The constant flow of shielding gas is designed to remove by-products of the melting process which include ejected particles, metal vapor, spatter, condensate, and material redeposits [68]. Each of these may have a detrimental effect on build quality if they settle back on the powder or part surface. Redeposition on the powder surface will locally increase the effective layer thickness and may result in incomplete melting and balling on the surface. Furthermore, by-products that are not quickly removed from the path of the laser beam will absorb some of the incident laser energy, attenuating the laser. This can result in a change in the local energy density leading to insufficient melting, a lack of fusion, and decreased part quality. The constant flow of a shielding gas carries these by-products away from the laser and the part being printed. Typical process gases used in SLM are nitrogen and argon [59, 60, 69-71], although helium has also been investigated for its effects on build quality [69].

The selection of a process gas is an important parameter to consider; cost, heat conduction, and material characteristics must all be considered. Bean et. al [69] studied the effects of using three different shielding gases: nitrogen, argon, and helium. They found no observable differences in the chemistry of samples printed under the three different gases; exposure to nitrogen did not increase the susceptibility to nitride formation. However, differences were observed when printing under the nitrogen environment based on measured grain sizes. Nitrogen, with a higher heat transfer coefficient [72, 73], will remove heat more quickly from the surface of the melt pool, resulting in a faster cooling rate and finer microstructures.

A second variable for the process gas is the flow rate, or how fast the shielding gas travels over the powder bed. Ladewig et al. [68] varied the gas flow rate from approximately 48.8 m^3/hr to 65 m^3/hr, and characterized single scan vectors of SLM iN718 at various locations on the build plate. It was first found that the flow of gas is not equal across the entire build plate; at locations near the gas inlet there is a higher flow rate when compared to farther locations despite a constant input flow rate. In areas of high flow, the beam scan width was smaller than areas of low flow, due to better removal of by-products and less beam attenuation. When the flow rate itself was changed, they found that beam attenuation could be altered, and a resulting “splashy process” [74] would occur that increased the surface roughness. This occurs with beam attenuation, which occurs more often at low flow rates when by-products interact with the laser beam.

Nonuniformity of the gas flow as pointed out by Ladewig et. al [68] and Bean et al. [69] produced a significant variation in the build quality across the plate for SLM IN718. Figure 8 is a schematic of gas flow in a Concept laser M2 machine, highlighting how shielding gas enters the building chamber and how the flow can easily become turbulent [69]. With improper flow, process byproducts may redeposit on surfaces or negatively interact with the laser beam and result in increased surface roughness [68, 69, 75]. Ferrar et al. [75] investigated the effects of gas flow uniformity and designed a custom fixture to improve the uniformity across the plate. Their improved gas rail design involved an adjustable nozzle and a diffuser to ensure an even distribution of gas flow across the plate. Design improvements were modeled with computer simulation and validated through a reduction in porosity and standard deviations via physical measurements.

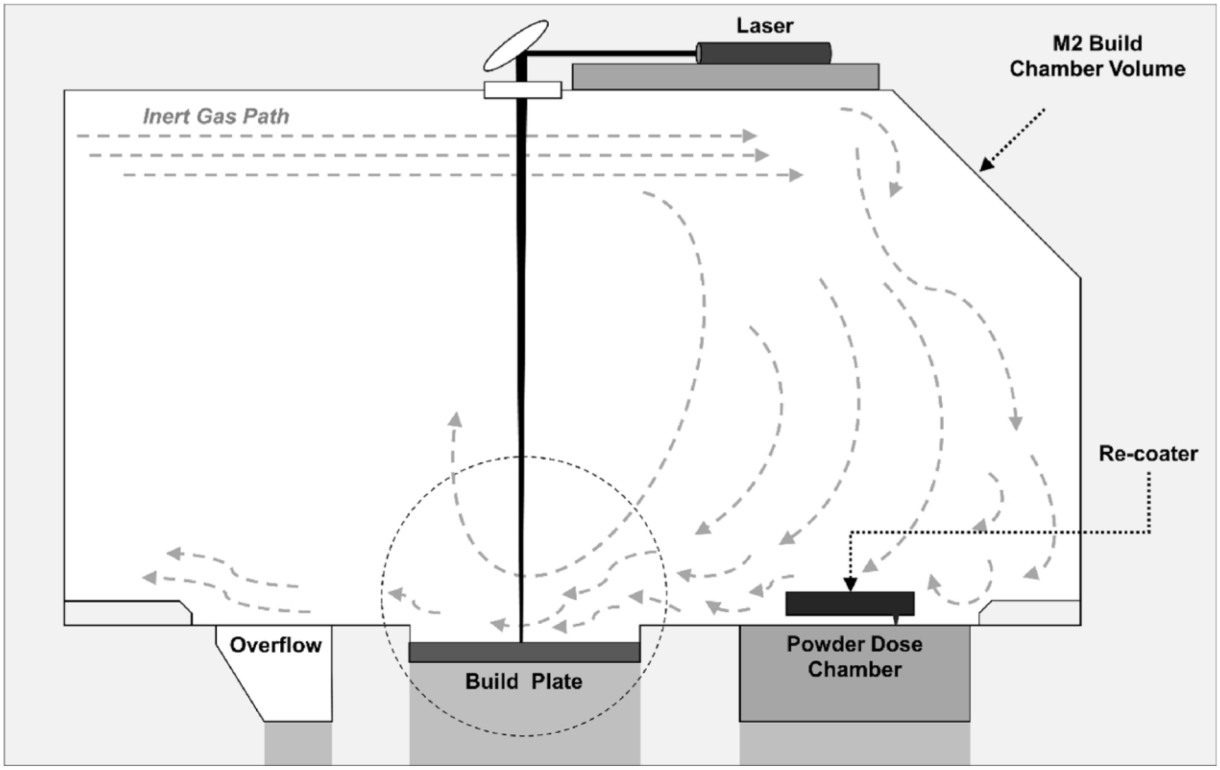

Figure 8: Schematic of the gas flow path in a Concept Laser M2 system [69].

1.3.6 Spot Size

The laser spot size affects the overall area of energy input into the material, which can have important implications for the melt pool shape and solidification kinetics [58-60, 62, 76]. Some machines can manipulate the spot size directly through the use of various lenses in the optical train [77], while others must rely on the physical location of the build plane with respect to the fixed position of the laser. Both techniques achieve similar results.

Shi et al. [77] performed an experiment on Ti-6Al-4V where the beam size as varied by the former method, and they utilized single scan laser tracks to determine build quality. With a smaller diameter laser but constant laser power, they found the geometry of the melt pool was extremely deep, with a large aspect ratio of height to width. This resulted in keyhole porosity and material evaporation during production. The larger diameter beam better distributed the incoming laser energy over the powder surface and resulted in more stable and uniform melt pools and lower porosity.

Although it is one of the less common process parameters, the laser focal shift has proven to be no less powerful than the others in terms of its effects on resulting microstructures and mechanical properties. The parameter itself is a physical change in the height of the build plate during the scanning of the laser. A shift of +X mm would move the build plate X mm down, and a shift of -X mm would raise the build plate up closer to the f-θ lens. Because of the fixed position of the laser beam, and the nature of the laser's convergence, this has the effect of changing the incident spot size on the metallic powder symmetrically for + or - shifts. A schematic of this parameter is shown in Figure 9.

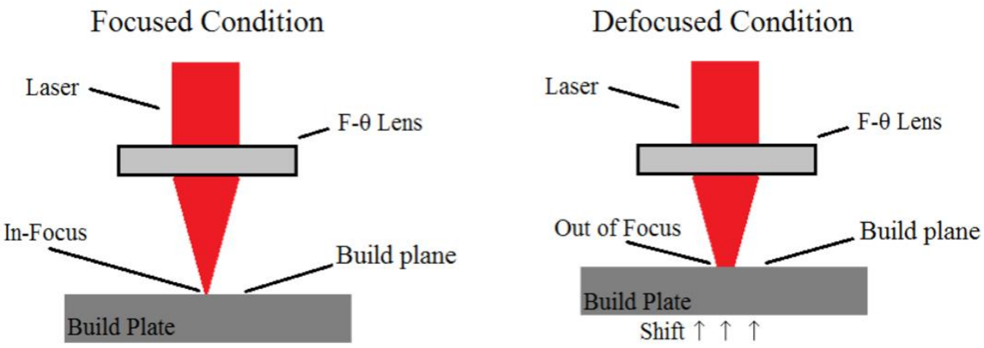

Figure 9: Schematic of the focal shift mechanism through the Z-movement of the build plate.

Through a shift in the spot size, the local power density is altered, as given by the following equations:

$$\text{Power Density} = \frac{\mathrm{P}}{\pi\omega^2} \tag{3}$$

$$\text{Spot Size} = \omega(\mathrm{z}) = \omega_0\sqrt{1 + \left(\frac{z}{Z_r}\right)^2} \tag{4}$$

Where P is the laser power, ω is the local spot size radius, ω_0 is the spot size at the focal point, z is the distance from the focal plane, and Z_r is the Rayleigh distance. The Rayleigh distance is defined as the axial distance from a radiating aperture to a point where the difference between an axial ray and an edge ray is λ/4, where λ is the wavelength of light [78]. These equations show that as the spot size decreases, the power density rapidly increases; the same amount of energy is concentrated into a smaller overall area.

The effects on build quality metrics in SLM IN718 as a function of the laser focal shift (LFS) were studied by Bean et al. [59]. In their experiment, the focal shift was varied in 1 mm increments 5 mm above and below the 0-height of the machine. The variation of the laser spot size and relative power density over this range is shown in Figure 10. Porosity values are shown to vary with the laser focus shift as a function of the beam spot size. At the -2 mm focal shift the porosity is a maximum and pores are shown to be characteristic of too low of an energy density, as there are traces of unmelted power. With higher values of the focal shift, the porosity begins to decrease, reaching a minimum at the +1 mm focus shift. The porosity in this sample appears to be trapped gas porosity, indicating a stable melt pool of sufficient energy density. Further increases of the focal shift lead to another maximum of porosity at the +3 mm shift. The porosity at this location is of a keyhole-type geometry, which is a result of too high of an energy density. An interesting result of this research was that the focal plane of the laser coincided with the +3 mm shift; the maximum energy density corresponds to the smallest spot size, which is at the +3 mm position in this study. The laser focal shift is found to be a significant process parameter due to the changing spot size of the laser. The effects that this can produce in the microstructure will be a main topic in this dissertation, to be covered in a later chapter.

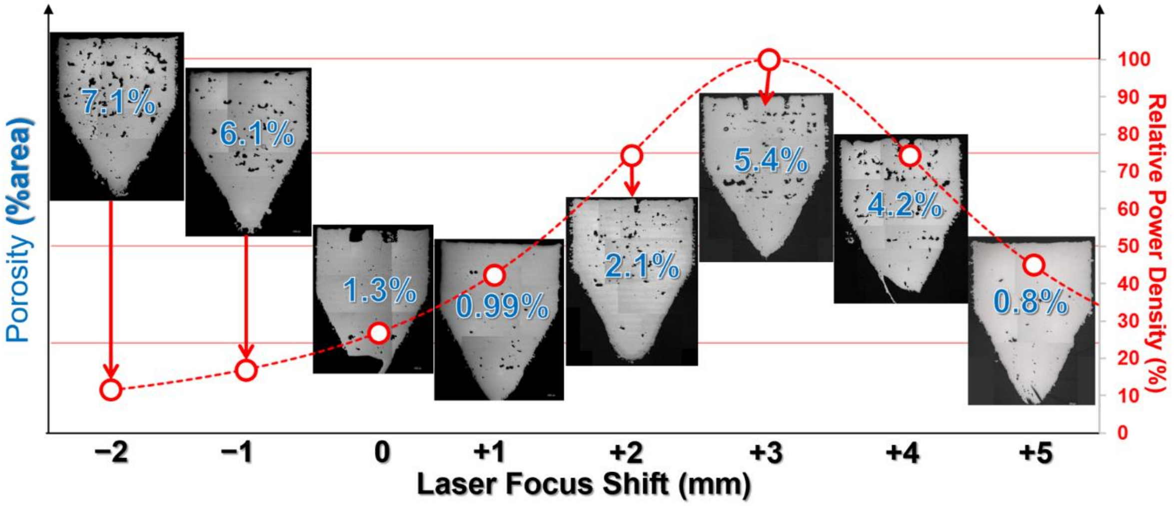

Figure 10: Porosity and relative power density plotted as functions of the laser focus shift in a study by Bean et al. [59]. The study revealed that the focal point was centered on the +3 mm focal shift position, as evidenced by the most intense keyholing in this location.

1.3.7 Energy Density

The energy density is a measurement used to describe a combination of process parameters, and it is not directly altered within the machine's software. The four common parameters that are used in this calculation are laser power, scanning speed, hatch spacing, or layer thickness. Typically, the energy density is measured in one of three forms: linear energy density (L.E.D.), area energy density (A.E.D.), and volumetric energy density (V.E.D.). Each form adds in one of the previously mentioned parameters that adds a new dimension to the measurement. The L.E.D. was previously given in Eqn. 1.

$$\mathrm{A.E.D.} = \frac{P}{V * h} \tag{5}$$

$$\mathrm{V.E.D.} = \frac{P}{V * h * t} \tag{6}$$

In these equations, P is the laser power, V is the scanning speed, h is the hatch spacing, and t is the layer thickness. It is interesting to note that equivalent levels of energy density can be achieved through different means, e.g. an L.E.D. of 2 J/mm can be achieved with a laser power of 200W and 100 mm/s, or 100 W and 50 mm/s. Each of these parameters can produce a component with different properties. An interesting example of this phenomenon is in the work of Popovich et al. [22, 54], where functionally graded alloys are produced with two distinct regions. A fine-grained structure in the 5-125 μm grain size range and coarse-grained structure with grains on the order of 1000 μm are both produced with the same volumetric energy density and in the same sample. They achieve this through variations to the laser power, scanning speed, hatch spacing, and layer thickness. Although the energy density is useful in describing the energy input into a sample, it has limitations in describing the actual microstructural characteristics.

Bertoli et al. [79] elaborate on this idea further, demonstrating that the energy density metric does not address the complex physics of the melt pool. Since the melt pool shape and size can vary drastically without a corresponding change in the energy density, this metric alone does not fully capture what may be happening on a smaller scale. For that reason, it is best to describe an additive process by the parameters themselves, rather than a metric that combines them together.

1.3.8 Post-Processing

Although much of the existing literature on SLM focused on the effects of the process parameters on the as-built condition, some studies investigated samples that have undergone thermal post-processing. For IN718, a heat-treated alloy, this is a critical step in achieving IN718's full strength; analysis of only the as-produced structure does not provide an adequate scope of material properties that can be used in the industry. Of these studies, many omit important steps to deal with 3D-printed microstructures such as HIP or homogenization treatments that can eliminate by-products of the printing process. These studies treat the as-built material like a mill product that is ready for solution and aging treatment, but the remnant structures can be harmful if left unaddressed. In a recently released technical standard entitled *Specification for Control and Qualification of laser Powder Bed Fusion Metallurgical Processes,* NASA emphasize the need for post-processing of laser fused parts [80]:

> The metallurgical process shall demonstrate controlled evolution of the microstructure from the as-built state to the final state, with the final state consisting of predominantly uniform and non-directional recrystallized grain structure, free of remnants of the as-built structure, and reflecting proper homogenization, grain boundary quality, and strengthening mechanisms appropriate to the alloy.

This excerpt from NASA highlights the shared view of the aerospace industry that there is a need for post-processing and elimination of potentially deleterious structures within the microstructure. For 3D-printed parts, HIP processes have commonly been used for this purpose.

The HIP step is important for 3D-printed material as a means of pore closure, elemental homogenization, relief of residual stress, and recrystallization of the microstructure. Zhang et al. [35] observed Laves phase in their fully heat-treated samples, due to a lack of a high temperature HIP treatment. The homogenization treatment they employ at 1080° C is not adequate for Laves phase dissolution. Furthermore, precipitation of δ phase in their samples occurs along the interdendritic boundaries established by the printing process [35]. This distribution of the δ phase along interdendritic boundaries can create favorable paths of crack propagation and result in degraded mechanical properties. A similar effect is seen in a study by Chlebus et al. [39], where no HIP/homogenization treatment was employed and instead AB samples were directly given solution treatments at various temperatures. In their as-built microstructures, characteristic dendrites spanning melt pool boundaries are formed through epitaxial growth. Samples that were directly aged contained highly irregular precipitation of the γ’ and γ’’ as well as the columnar microstructure observed in the AB condition. Small δ phase precipitates were also observed in formerly interdendritic regions. Solution steps were not effective at 980° C or 1040° C for 1 hour, as grains maintained their original shapes and Laves phase was observed throughout the structure. Only at a solution temperature of 1100° C was there a significant change in the microstructure, where recrystallization and partial elimination of the AB structure was observed. These studies highlight the importance of a HIP or similar high-temperature treatment in order to eliminate traces of the AB structure.

When used properly, the HIP treatment can effectively homogenize the material. Tillmann et al. [81] demonstrated this with SLM IN718, where HIP temperatures were varied from 500 °C – 1300 °C and pressures from 500 MPa to 1500 MPa. They found that at temperatures above 1150 ° C and pressures over 100 MPa nearly full densification (99.985% – 99.989%) could be achieved. They note that full densification is nearly impossible for samples with entrapped Argon gas, as it is not soluble in the microstructure. In addition to decreased porosity, the characteristic SLM microstructures were eliminated during heat treatment, resulting in a homogeneous grain structure. However, homogenization is not always observed post-HIP, even at elevated temperatures. When a highly anisotropic AB structure exists, the recrystallized post-HIP structure takes on an anisotropic form as well. Despite a HIP treatment at 1180° C and 150 MPa for 3 hours, Popovich et al. [54] observed a highly anisotropic post-HIP microstructure. Purposeful manipulation of the process parameters resulted in highly elongated columnar grains in the AB condition, which promoted the formation of extremely coarse grains after HIP. Others have observed a similar phenomenon for AM material [82].

In addition to the HIP/homogenization treatment, typical solution and aging steps are necessary prior to mechanical testing. The former steps create a uniform microstructure, while the latter provide the correct phase distribution in the microstructure for strengthening. In a study by Amato et al. [83], they perform a HIP treatment at 1163° C, but omit further solution and aging treatment prior to mechanical testing. This leads to a weakened microstructure despite the lack of Laves phase and the typical solidification structures. The corresponding properties are much lower than their wrought counterparts that received full heat treatment. However, it has been shown that mechanical properties of fully heat-treated SLM material can be equivalent to those of wrought material [54, 84].

Because typical post-processing procedures observed in the current literature do not fully eliminate the directionality that stems from the AB condition, the build direction of parts becomes a critical parameter. The direction of loading is a significant consideration in the presence of anisotropic microstructures. Elongation of grains along one axis may create favorable properties parallel to the elongation but can have deleterious effects in the transverse direction.

1.3.9 Build Direction

The build direction is not necessarily a process parameter in the traditional sense of a machine setting but can have serious implications for material properties. The SLM process inherently produces anisotropic textures due to varying solidification directions, and this is something that must be considered alongside traditional parameters when producing an additively manufactured part.

Typically, directional properties in SLM are aligned parallel to the building direction, which coincides with the maximum thermal gradient; heat enters the material from above and is conducted downward through the substrate. The raw powder adjacent to the component being built is a poor thermal conductor due to the minimal contact between particles and empty pockets of inert gas that separate them, and cooling via convection is relatively small in comparison to conduction. Therefore, thermal gradients, and subsequent dendritic growth and grain formation follow this path. Because of this, many studies have found that the best mechanical behavior is found when testing parallel to the building direction, while the transverse directions produce poor mechanical results [82, 85-87].

Anisotropic microstructures comprised of highly elongated grains can be a detriment to mechanical properties. Many studies have shown the deleterious effects of these anisotropic structures. Shassere et al. [82] performed creep tests on IN718 produced by EBM that had either highly anisotropic or equiaxed microstructures. They found that when the elongated grains were aligned parallel to the load, a large increase in the creep life and ductility was achieved; however, when loading transverse to the grains there was a significant reduction in ductility. The source of this embrittlement was the high number of grain boundaries oriented transverse to the loading direction. These grain boundaries can preferentially nucleate voids that can coalesce into cracks. Crack propagation along grain boundaries oriented transverse to the load provides an easy path for fracture to occur. A similar result was found by Kuo et al. [86] in creep, but their failures occurred due to the accumulation of δ phase along the original solidification dendrites. They did not perform a homogenization treatment, and so remnant elemental segregation from the original dendritic growth during processing remained within the microstructure. These pockets of enriched Nb precipitated δ phase parallel to the building direction, an unfavorable orientation for horizontally printed samples. Because of this, vertically printed samples displayed excellent ductility and time to rupture, while horizontal samples failed prematurely.

The build orientation is important to consider for material properties because anisotropic solidification features are carried through thermal post-processing. These can result in unfavorably oriented grain boundaries, precipitates, and inclusions within the matrix. Each of these provides a favorable pathway for crack propagation and is deleterious to the overall mechanical performance of the material.

1.4 Inconel 718 Metallurgy

Nickel-based superalloys are used in a wide variety of applications within the aerospace industry due to their outstanding mechanical properties at elevated temperatures [88, 89]. Inconel 718 (IN718), a precipitation-hardened alloy, is considered the workhorse of these superalloys because of its superior mechanical properties and corrosion resistance at elevated temperatures [90-94]. Initially designed and patented (US3046108) in 1959 by Herbert Eiselstein, IN718 was originally designed to trade off higher temperature capabilities for a high weldability[95, 96]. To fully understand why this alloy has such unique properties when compared to other superalloys, the microstructure must be explored.

1.4.1 Microstructure

The nominal composition of IN718 used in this study can be found in Table 1, where each element plays a specific role in the development of a strong microstructure. Ni, Fe, and Cr account for the bulk of the alloy, and make up the γ phase. The Cr content helps to improve the oxidation resistance [97]. The γ phase is the matrix material, which also contains small amounts of Ti, Nb, Mo, and Al in solid solution. On its own, the γ phase is weak, and must rely on alloying and heat treatment to provide adequate strength for IN718's intense applications. Solid solution strengthening contributes slightly to the overall strength of the material as the primary strengthening mechanism is precipitation strengthening. Notable phases found within the IN718 microstructure are the γ'', γ', δ, MC-type carbides, and Laves phase.

Table 1: Nominal chemical composition of IN718 with maximum and minimum wt. % from AMS 5662 [98, 99].

Element	**Ni**	**Cr**	**Fe**	**Nb**	**Mo**	**Ti**	**Al**	**Co**	**Mn**	**Si**	**C**
Max Content wt.%	55.00	21.00	Bal.	5.50	3.30	1.15	0.80	1.00	0.35	0.35	0.08
Min Content wt.%	50.00	17.00	Bal.	4.75	2.80	0.65	0.20	-	-	-	-

γ' is an ordered $L1_2$ face-centered cubic (FCC) crystal structure ($a_0 = 0.3561 – 0.3568$ nm) in IN718 consisting mostly of Ni, Al, and Ti in the stoichiometric ratio $Ni_3(Al,Ti)$ [94]. This phase takes on a spherical shape in the γ matrix and is precipitated through a long aging process in the 650° C – 850° C range. Typically, the γ’ phase constitutes about 4% of the volume fraction [100]. This intermetallic compound is the dominant strengthening precipitate is many other superalloys such as Incoloy 901, A-286, Waspaloy, IN100, MAR-M-247, but for IN718 it is secondary to the γ’’ phase, contributing to roughly 10-20% of the overall strength [97].

Because IN718 contains significant quantities of Nb, it readily forms γ’’, the primary strengthening phase in IN718. It has a body-centered tetragonal (BCT) $D0_{22}$ crystal structure (a_0 = 0.3624 nm, c_0 = 0.7406 nm) and a composition of Ni_3Nb [94, 97]. γ’’ precipitates coherently as discs on the {100} planes of the FCC matrix, allowing for three variants to exist [94, 101, 102]. The average diameter of these discs (along the major axis) is 60 nm, and the thickness is on the order of 5-10 nm, and accounts for ~15% of the volume fraction [100]. Typical precipitation of this phase occurs between 650° C – 760° C, above which coarsening is accelerated [97]. Aging treatments to precipitate γ’’ typically last for 18-20 hours, as the sluggish diffusion of Nb through the matrix and coherency strains with the matrix prolong the nucleation and growth of this phase [103]. The slow formation of the strengthening phase promotes weldability in IN718 [104-106]; superalloys that readily form the γ’ phase—those that are rich in Al and Ti—may form hot cracks during the welding process [94]. The solvus temperature for γ’’ is approximately 899° C. Strengthening from the γ’’ phase stems from the high coherency strains that exist with the γ matrix and also the limited number of slip systems available [103]. This strengthening mechanism will be elaborated on in a later section. The phase is a metastable form of Ni_3Nb, and when exposed to temperatures above 816° C, it will transform into the δ phase.

The δ phase is the equilibrium form of the primary strengthening phase γ’’ in IN718, having an orthorhombic DO_a structure (a_0 = 0.5106 – 0.511 nm, b_0 = 0.421 – 0.4251 nm, c_0 = 0.452 –

0.4556 nm) and a stoichiometry identical to that of γ'', Ni_3Nb [94] . For comparison between the two phases, the unit cells and atomic arrangements of both phases can be seen in Figure 11. The periodicity of the Nb atoms in the δ phase is like that of the (112) plane in γ'' [92]. The difference in the atomic arrangements of these close packed planes causes these phases to have dissimilar behavior despite identical stoichiometries. In the $D0_{22}$ structure of the γ'' phase, the stacking sequence is *abcabc*, whereas in the $D0_a$ structure it is *ababab*. In a study of the precipitation of the δ phase, Sundararaman et al. [92] found that because the δ phase has a stacking sequence different than that of the parent γ lattice, coherency strains are not generated like they are for either the γ' or γ'' phases. Instead, a high energy incoherent interface is formed as δ precipitates.

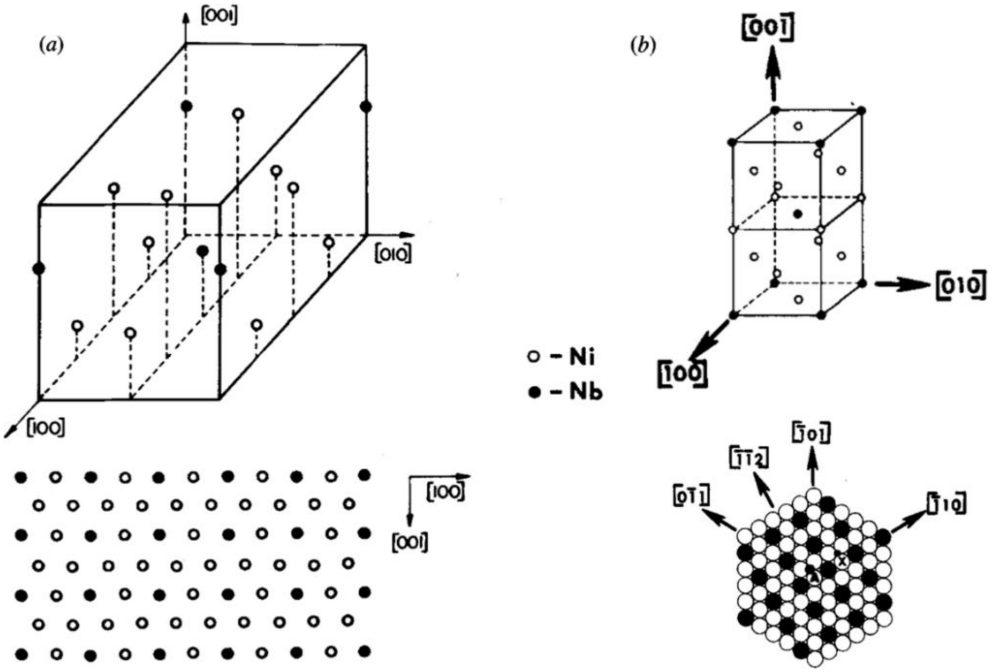

Figure 11: Comparison of the crystallography and atomic arrangements of the (a) δ phase [92] and (b) γ'' phase [102].

This is a non-coherent phase with the FCC matrix, and typically forms as needles or spheroids on the grain boundaries [107]. The δ phase will form with its (010) plane along the

{111} lanes of the γ matrix. Because of its lack of coherency, the δ phase does not directly confer strength to IN718, but does provide some benefit in local ductility near grain boundaries and grain boundary pinning [94, 108]. Since the δ phase and the γ'' phase compete for Nb, it is possible to form a precipitate free zone (PFZ) in the vicinity of the δ phase; the immediate area will be denuded of Nb, and no γ'' will form in these areas. This creates a region of the γ matrix that is relatively more ductile, allowing for local plastic deformation around the GBs. During heat treatment, the δ phase can pin grain boundaries in place, maintaining a constant grain size during manufacturing. However, because the solvus temperature for the δ phase is 1020° C, at higher temperatures different precipitates must be used to help control the grain size.

Carbides are common in the superalloys and take on many different forms: MC, $M_{23}C_6$, M_6C, and M_7C_3 [94, 109]. The most common carbide that forms in IN718 is of the MC-type, NbC, due to its high Nb content. This cubic phase ($a_0 = 0.43 – 0.47$ nm) has a globular appearance and tends to form near grain boundaries. Titanium is also commonly found as one of the constituent elements in the MC-type carbides. At elevated temperatures, NbC can be used to pin the grain boundaries, but is known to be deleterious to the mechanical properties in excessive amounts.

Detrimental phases also exist in IN718, the most common of which is referred to as the Laves phase. This topologically close-packed phase contains a significant amount of niobium and has a hexagonal crystal structure. The stoichiometric ratio of the Laves phase is typically reported as $(Ni, Fe, Cr)_2(Nb, Mo, Ti)$ [97]. It forms upon excessive high temperature exposure in areas where extreme segregation of alloying elements has occurred, and its morphology depends on solidification conditions and subsequent thermal exposure. The Laves phase is highly detrimental to the mechanical properties of IN718 as it reduces the availability of other alloying elements to produce strengthening phases. The dissolution temperature has been reported as ~1162° C in IN718. Table 2 summarizes the main phases found in IN718 presented below:

Table 2: Common phases found in Inconel 718 with details on crystal structure, lattice parameter, stoichiometry, and dissolution temperatures.

Phase	**Crystal Structure**	**Lattice Parameter, nm**	**Dissolution Temperature, ° C**
γ [110]	FCC	0.3594 – 0.3604 [111, 112]	1351 - 1362 °C [113, 114]
γ’, $Ni_3(Al,Ti)$ [94]	FCC, $L1_2$	0.3599 – 0.3603 [111]	788 – 816 °C [97]
γ’’, Ni_3Nb [94]	BCT, $D0_{22}$	$a_0 = 0.3624$ $c_0 = 0.7406$	885 °C [103]
δ , Ni_3Nb [94]	Orthorhombic	$a_0 = 0.5106\text{-}0.511$ $b_0 = 0.421\text{-}0.4251$ $c_0 = 0.452\text{-}0.4556$	982 °C – 1038 °C [103]
MC, NbC [94]	Cubic	$a_0 = 0.43\text{-}0.47$	1230 - 1252 °C [113, 114]
Laves Phase, $(Ni, Fe, Cr)_2(Nb, Mo, Ti)$ [39, 94]	Hexagonal	$a_0 = 0.475\text{-}0.495$ $c_0 = 0.770\text{-}0.815$	1162 °C– 1177 °C [115]

1.4.2 Strengthening Mechanism

IN718 is a precipitation strengthened material, deriving most of its strength from the γ’ and γ’’ precipitates. Because deformation occurs via massive planar slip, dislocation-particle interactions will be of paramount importance in understanding the mechanical behavior of this material [100]. These small particles within the γ matrix present obstacles to dislocation motion via coherency and order strengthening mechanisms [116]. Coherency strengthening is based on the lattice parameters between host lattice and the precipitate. When the lattice parameters do not align perfectly, but the precipitate remains coherent with the matrix, it induces misfit strains and corresponding misfit hardening [117]:

$$\epsilon = \frac{\mathrm{a}_{\mathrm{precipitate}} - a_{lattice}}{a_{lattice}} \tag{7}$$

$$\tau \propto G\epsilon^{\frac{3}{2}}(rf)^{\frac{1}{2}} \tag{8}$$

Where ϵ is the strain induced by the differences in lattice parameters of the precipitate, $a_{precipitate}$, and the lattice, $a_{lattice}$. The strengthening contribution, τ, is proportional to the shear modulus G, the precipitate radius r, the misfit strain, and the volume fraction of precipitates. Misfit strain impairs dislocation movement through the lattice and strengthening phases. The γ'' phase is coherent with the matrix and has a high tetragonal distortion (c/a = 2.04), which contributes to its high misfit strain of 2.86% [102, 116].

Order strengthening arises in the presence of precipitates with an ordered lattice, such as the $L1_2$ or $D0_{22}$ structure of γ' and γ'', respectively. These phases are comprised of atoms in specific lattice sites where each type of atom exists in an ordered array among the ordered array of the other element [118]. The atoms are in a specific order, and this structure is called a superlattice. If a dislocation were to upset this order, an antiphase boundary (APB) is formed because the lowest energy nearest-neighbor condition is no longer met and order is destroyed [117]. Thus, as one dislocation passes through a precipitate, an APB trails in its wake. The equilibrium structure can be restored by the passage of a second dislocation behind the APB, with the entirety of the now planar defect being referred to as a superdislocation. The need for dislocations to travel in pairs in an ordered structure provides a strengthening effect in certain alloys, e.g. γ' and γ'' containing superalloys.

Chaturvedi and Han investigated the contributions of both order and coherency strengthening mechanisms in IN718 due to both the γ' and γ'' phases and their relationship with the γ matrix [116]. With contributions from both the γ' and γ'' phases, the equation for the critical resolved shear stress (CRSS), or the stress necessary to initiate slip, is as follows:

$$\Delta\tau_{total} = \left(\Delta\tau_{\gamma'}^{2} + \Delta\tau_{\gamma''}^{2}\right)^{\frac{1}{2}} \quad (9)$$

Where each Δτ term corresponds to its respective strengthening phase. The equations for the contributions of γ’ and γ’’ due to order hardening is given below [102, 116]:

$$\Delta\tau_{0\gamma''} = \frac{\gamma_{APB''}}{2b}\left\{\left[\frac{4\gamma_{APB''}f_{v''}}{\pi T}\left(\frac{\sqrt{6}*Rh}{3}\right)\right]^{\frac{1}{2}} - \beta \mathrm{f}_{\mathrm{v}''}\right\} \quad (10)$$

$$\Delta\tau_{0\gamma'} = \frac{\gamma_{APB'}}{2b}\left\{\left[\frac{4\gamma_{APB'}f_{v'}R_S}{\pi T}\right]^{\frac{1}{2}} - \mathrm{f}_{\mathrm{v}'}\right\} \quad (11)$$

In Eqn. 9, $\Delta\tau_{0\gamma''}$ is the CRSS when a disc shaped γ’’ particle is sheared by a glide dislocation, $\gamma_{APB''}$ is the antiphase boundary energy, *R* is the particle radius, *h* is half of the thickness of a particle, $f_{v''}$ is the volume fraction of the γ’’ phase, *T* is the line tension of the glide dislocation, *b* is the Burger’s vector, and *β* is equal to 1/3 when all three variants of the γ’’ phase are present. In Eqn. 11 $\Delta\tau_{0\gamma'}$ is the CRSS for a spherical shaped γ’ particle, $\gamma_{APB'}$ is the antiphase boundary energy, R_s is the effective radius, and $f_{v'}$ is the volume fraction. These contributions of order strengthening can be compared to the equations for coherency strengthening for each type of particle given below [100, 102, 116].

$$\Delta\tau_{c\gamma''} = 1.7\mu\left(\epsilon_{\gamma''}\right)^{\frac{3}{2}}\left(h^2 * \left(\frac{f_{v''}(1-\beta)}{2bR}\right)\right)^{\frac{1}{2}} \quad (12)$$

$$\Delta\tau_{c\gamma'} = \alpha\mu\left(\epsilon_{\gamma'}\right)^{\frac{3}{2}}\left(\frac{R_S}{b}\right)^{\frac{1}{2}}(f_{v'})^{\frac{1}{2}} \quad (13)$$

In Eqn. 12 $\Delta\tau_{c\gamma''}$ is the contribution to CRSS for disc shaped γ’’ particles via coherency strengthening, $\epsilon_{\gamma''}$ is the mismatch with the matrix, and the other parameters remain the same as in Eqns. 10 and 11. Similarly in Eqn. 13, $\Delta\tau_{c\gamma'}$ is the contribution for spherical γ’ particles via coherency strengthening. Chaturvedi and Han [116] found that for the γ' particles it could not be distinguished whether or not order or coherency strengthening dominated. However, they found that the majority of IN718's strength comes from the coherency strengthening of γ''. Their study, in addition to one by Oblak et al. [102] found that experimental quantification of the CRSS more closely matched that of the calculated CRSS from the coherency strengthening equations when compared to the order strengthening equations. Chaturvedi and Han utilized tensile testing of specimens aged at different temperatures for various lengths of time, and Oblak et al. [102] performed tensile tests on specimens aged under stress to influence the directionality of the microstructure. Both were in good agreement with the coherency strengthening equations.

1.4.3 Wrought Material

For comparative purposes, wrought IN718 will be discussed throughout this dissertation. This is the traditional manufacturing technique for IN718 used in the aerospace industry and has been employed for many decades. Wrought processing involves extensive thermomechanical processing, a technique that is not found in SLM. Understanding how this affects the material will be critical in differentiating microstructural characteristics and mechanical behavior from that of SLM-processed IN718.

Wrought processing first involves melting of raw material, and the formation of an ingot. Typical melting procedures for IN718 include vacuum induction melting (VIM) + electroslag remelting (ESR), VIM + vacuum arc remelting (VAR), or VIM + ESR + VAR [94]. These techniques meet the criteria of economics, melt segregation, and chemistry control required for IN718. Care must be exercised during the solidification and cooling of an ingot to avoid gross segregation of alloying elements. Too slow of a cooling rate can result in the formation of freckles, or channels of high solute content which cannot be dissolved by further heat treatment [94].

Niobium is the most susceptible element to segregation in IN718 and plays a role in the formation of many detrimental phases [110]. Laves phase and carbide formation occurs in these areas and are detrimental to overall material performance; extremely slow cooling rates should be avoided.

Once an ingot has been made, forging and forming occur. These operations impart heat and deformation into the part, often referred to as thermomechanical processing (TMP). Typical deformation processes include rolling, drawing, die forging, swaging, and ring rolling [94, 119]. TMP works the part into useful shapes for various applications and further machining, while also imparting desirable microstructural characteristics: uniform grain refinement, recrystallization, and stress relief.

Severe plastic deformation imparted to the material from the forging operations combined with the elevated temperature of the forging process drive the microstructure to recrystallize. This results in an equiaxed microstructure throughout the component with stress-free grains and a more homogeneous distribution of alloying elements. Forging temperatures can change the microstructural scale; forging performed above the δ solvus may have a grain size of ASTM 4-6, while those below the δ solvus can be in the range of ASTM 8-10 [94]. Forging below the δ solvus temperature enables users to move directly into the aging process, as enough δ phase can be precipitated during forging steps. This direct age capability is not possible in SLM material, which does not have the thermal processing steps to precipitate δ phase in the correct amount or morphology during the SLM process. More commonly, wrought material is delivered in the mill-annealed state and must be aged to achieve full strength.

1.4.4 Post-Processing and Mechanical Behavior

IN718 is an alloy that must be heat treated to reach its full-strength. Precipitation hardening only occurs in the presence of γ' and γ'', which form over the duration of specific aging treatments. Post-processing of IN718 in its wrought form, and many AM applications in recent years, has followed AMS 2774, 5662, 5663, and 5664 [98, 99, 120, 121]. These specifications outline the processes that must be followed for proper heat treatment of IN718, as well as required minimum mechanical properties to be met.

AMS 2774 provides general guidance for heat treating specifications of wrought nickel alloys. All of the post-processing techniques used in this dissertation will follow guidelines set forth by AMS 2774, such as methods of temperature control, soaking times, cooling techniques, and inert environments used.

AMS 5662, 5663, and 5664 provide specific time and temperature requirements for the heat treatment of IN718 [98, 99, 121]. AMS 5662 and 5663 occur below the δ phase solvus temperature (sub-solvus), and 5664 above the solvus temperature (super-solvus). The primary difference between AMS 5662 and 5663 is the inclusion of the precipitation—or aging—treatment step. Both specifications call out the same sub-solvus treatment; 941° C – 1010° C for an appropriate time based on the thickness of the part being heat treated followed by an air cool or faster technique. AMS 5663 goes on to detail the aging treatment in two steps. First, a hold of 8 hours between 718° C – 760° C, followed by a furnace cool of 56° C per hour to a temperature in the 621° C – 649° C range. The second step is a dwell for a total aging time of 18 hours.

AMS 5664 outlines the super-solvus treatment and aging steps. Initial treatment includes a hold between 1038° C and 1066° C for an appropriate time depending on part thickness, which serves to dissolve any δ phase in the microstructure. The aging process is also detailed in two steps. The first step is a hold for 10 hours at 760° C, followed by a furnace cool to 649° C at 56° C per hour. Next, a hold for a total aging time of 20 hours is used, followed by cooling. The longer aging cycle promotes the formation of γ’’ and γ’. The heat treatment path for AMS 5663 and AMS 5664 can be traced on the TTT diagram for IN718 in Figure 12.

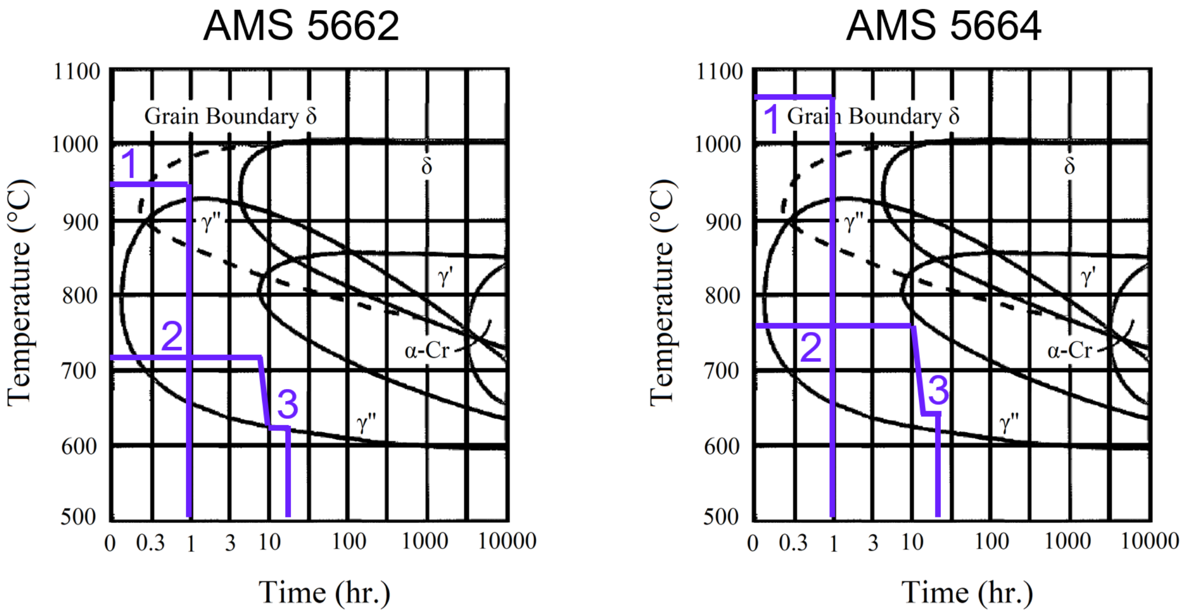
AMS 5662

AMS 5664

Figure 12: TTT diagrams showing the heat treatment path outlined by AMS 5663 and AMS 5664 [98, 121, 122].

Mechanical tests called out by the AMS specifications include room temperature tensile, elevated temperature tensile at 650° C, and combination stress rupture. Table 3 outlines the required properties for each heat treatment and tes

t.

Table 3: Tabulated properties called out by AMS specifications 5663 and 5664 [98, 121].

Room (RTT) and Elevated (ETT) Temperature Tensile Testing				
AMS Specification	**Yield Strength**	**Ultimate Tensile Strength**	**Reduction of Area**	**Elongation**
	MPa	**MPa**	**%**	**%**
AMS 5662/5663 RTT	1034	1276	15	12
AMS 5662/5663 ETT	862	1000	15	12
AMS 5664 RTT	1034	1241	12	10
Combination Stress Rupture (CSR) Testing				
AMS Specification	**Time to Rupture**	**Elongation**	**Failure Location**	
	hours	**%**		
AMS 5662/5663 [98, 99]	23	4	Smooth Section	
AMS 5664 [121]	N/A	N/A	N/A	

A comparison of the mechanical properties of IN718 to other common metallic alloys is shown in Figure 13. While other alloys have a more severe temperature dependence and lower overall strength, IN718 retains its high mechanical strength up until approximately 650° C. At this point, the strengthening phases begin to coarsen and the yield strength is degraded.

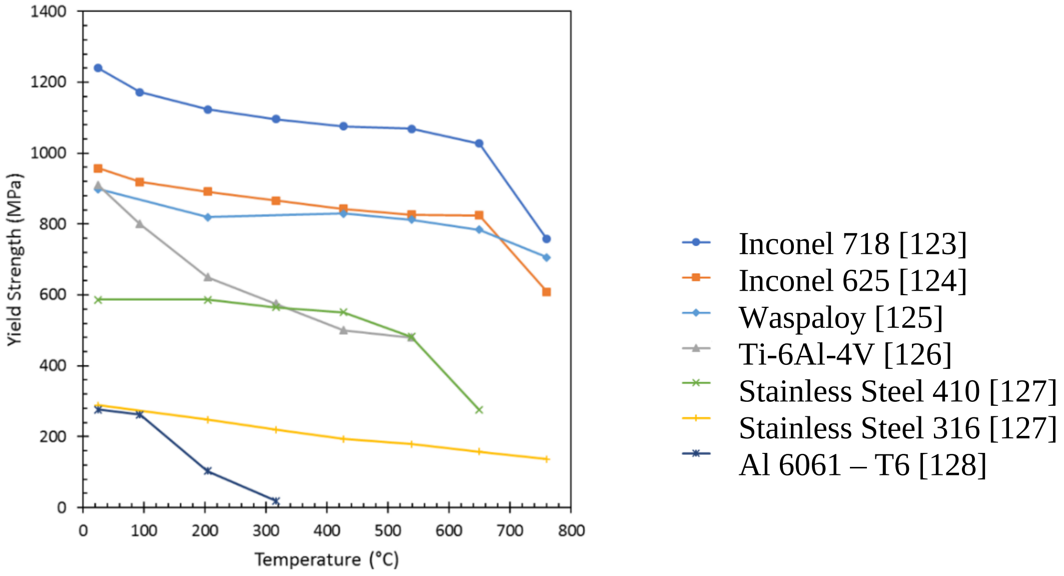

Figure 13: Yield strength of common metal alloys used in the aerospace industry as a function of temperature [118-123].

1.4.5 Applications

IN718, due to its use in a wide range of temperatures and excellent weldability, has found many uses across the aerospace industry. It can be used on both sides of the temperature extremes in cryogenic or elevated temperature environments. Jet engine components, liquid rocket engines, thrust chamber jackets, bellows, and nuclear fission applications are all examples that show off both the versatility of this alloy and the extreme environments in which it is used [95, 129, 130]. Excellent weldability comes from the lack of a readily precipitating strengthening phase as mentioned previously. However, the alloy itself is quite heavy and difficult to machine. The combination of high hardness and strain hardening promote tool wear and greatly increase machining costs and times [131, 132].

The unique combination of excellent weldability and poor machinability has driven IN718 to be an immensely popular alloy for use in additive manufacturing. AM is essentially a continuous welding process; the melting and rapid solidification mimics typical welding operations. Without rapid precipitation of its strengthening phases, IN718 does not readily crack like many other alloys do in AM. Typical applications of IN718 require complex geometries but machining these forms can be difficult. AM, which produces near net-shaped parts, does not produce much waste material and has no tool wear, making it a vastly superior option when compared to typical subtractive manufacturing.

Chapter 2: Motivation and Objectives

Compared to traditional manufacturing of metals, additive manufacturing is still in its infancy. Despite this, there is an increasing push in the aerospace industry to produce flight hardware through AM processes like EBM and SLM. Increased agility in the space domain, lower lead times, reduced costs, and novel geometries are all factors that make AM components so desirable, but there is still a lack of foundational research and understanding regarding how AM material may behave differently than what is currently available. Inconel 718 is one of the materials being pushed for use in 3D-printed liquid rocket engine components, as it is a highly weldable and robust alloy; however, there are still lingering questions about how appropriate SLM IN718 is as a drop-in replacement for wrought material. There is a need to understand the process-structure-property relationships that exist for this material.

The purpose of this dissertation is to investigate how the SLM process affects the microstructure and ultimately the mechanical behavior of IN718. The microstructure will be initially studied through variations of select process parameters that significantly affect solidification behavior. The mechanical properties will be characterized through a variety of tests that span multiple temperatures, strain rates, and loading conditions. A comparison to traditional wrought microstructures and mechanical properties is offered as well. Specific objectives of the dissertation are as follows:

1. Gain a deeper understanding of the underlying mechanisms behind microstructure formation in IN718 produced by selective laser melting and analyze how they will affect the fully heat-treated microstructures.

2. Relate observed structures to the mechanical properties, focusing on unique aspects of the microstructure that result from the SLM process: grain anisotropy, crystallographic texture, and precipitate distributions.
3. Characterize the room and elevated temperature mechanical properties of SLM IN718 and compare to their wrought counterparts. Testing will include room temperature tension, elevated temperature tension, combination stress rupture, and creep rupture, as outlined by current standards in the aerospace industry.
4. Utilize the knowledge we gain from these studies to develop modified post-processing thermal treatments designed to further improve the mechanical behavior of SLM IN718.

Chapter 3: Microstructural Variation in SLM

3.1 Introduction

Process parameter variation has been studied extensively in SLM materials as previously addressed in Chapter 1. Many of these studies analyze the direct impact of process parameters on the as-built microstructures, but do not perform typical post-processing steps. To fully capture the process-structure relationships that exist for SLM IN718, this chapter will focus on microstructural variation in as-built, as-HIP'ed, and fully heat-treated samples. The laser focal shift and the scanning strategy were chosen as they have not received as much attention in the literature as some of the other available parameters. Furthermore, both parameters affect the directionality of solidification. As previously mentioned, the laser focal shift can significantly alter the melt pool shape, and in doing so the directionality of solidification, crystallographic texture, and overall morphology. The scanning strategy determines the direction and rate at which energy is input into the material and the local concentrations of heat input. These parameters can be used in conjunction with one another to create a range of microstructural textures, which will further our understanding of the complex solidification mechanisms in SLM.

The experiments detailed in the following sections will analyze how these microstructures form, characterize them both morphologically and crystallographically, and investigate how they influence the post-processed microstructure. Finally, a comparison to typical wrought microstructures is offered to put the SLM samples into perspective. A later chapter will investigate the mechanical properties of all the microstructures studied here.

3.2 Experimental

3.2.1 Materials

The samples used in this study are built in the X and Z-orientations within the print bed from a pre-alloyed powder in a Concept Laser M2 SLM machine. Cylinders measured 12.7 mm in diameter and 90 mm in length regardless of print orientation. An example layout of the two build plates can be seen in Figure 14. Table 4 gives the chemical composition of the raw powder, bulk SLM structure, wrought material, and the maximum and minimum values outlined by AMS 5663 [98]. All parts were made in an Ar protective environment using a laser power of 180 W, scanning speed of 600 mm/s, hatch spacing of 0.115 mm, and layer thickness of 30 µm. Initially, the position of the laser focus was adjusted to change the spot size and area power density by operating in either focused (spot size 50 µm, area power density = 91.7 kW/mm^2) or defocused (spot size 95.8 µm, area power density = 25.0 kW/mm^2) for each sample. The focused condition corresponds to a focal shift of 0 mm, while the two defocused positions used are 3 mm shifts up (-3 mm) or down (+3 mm) in the Z-direction.

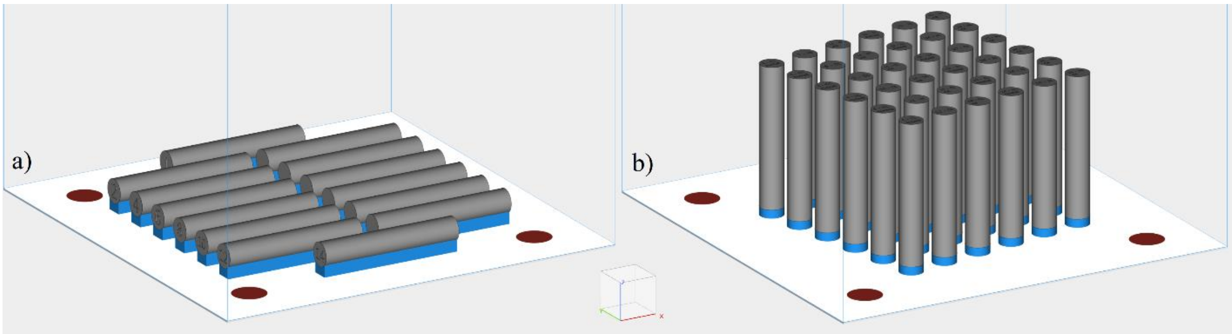

Figure 14: X-orientation (a) and Z-orientation (b) build plate layouts generated in the Magics Materialise software.

Table 4: Chemical compositions (wt. %) of IN718 used in the current study [98].

Sample	**Ni**	**Cr**	**Fe**	**Nb**	**Mo**	**Ti**	**Al**	**Co**	**Mn**	**Si**	**C**
IN718 Powder	53.0	19.0	18.0	5.1	3.0	0.9	0.4	0.2	0.1	0.04	0.03
IN718 Bulk SLM	53.7	18.5	17.9	5.3	3.0	0.9	0.5	0.1	0.1	0.06	0.02
Wrought Material	52.8	18.3	18.5	5.2	2.9	0.9	0.5	0.3	0.07	0.07	0.03
AMS 5663 Max wt. %	55.0	21.0	Bal.	5.5	3.3	1.2	0.8	1.0	0.4	0.4	0.1
AMS 5663 Min wt. %	50.0	17.0	Bal.	4.8	2.8	0.7	0.2	-	-	-	-

Specimens were prepared using one of the scanning strategies shown in Figure 7. In island scanning (Figure 7a), the control software divides the two-dimensional slice into 5-mm squares and completes the part by tiling. Each island is scanned using a back-and-forth raster pattern, and islands near the edge of a boundary will fill to match the slice geometry. After each layer, the next layer rotates the scan vectors by 90° and offsets each island by 1 mm in both the X and Y directions. This is an alternating and bidirectional pattern. In the continuous scan strategy (Figure 7b), individual scans extend over the entire length of the part at a given location and the part is completed at each layer by successive adjacent scans. These scans only travel in a single direction and subsequent layers were not rotated 90° to exacerbate microstructural texture development in these samples. This specific scan strategy is called non-alternating and non-bidirectional.

3.2.2 Post-Processing

In the current chapter, samples were post processed with only a single HIP and HT combination treatment. SLM samples were HIP'ed prior to solution treatment and aging to relieve printed-in residual stress, close porosity, dissolve the Laves phase, and redistribute alloying elements. The HIP cycle was performed at 1163 ± 12 °C and 103 ± 2 MPa in an argon environment for 3 hrs., which has been shown to be effective for pore closure [58, 59, 69, 81]. The heat treatment was carried out in accordance with AMS 5663 and 2774 [98, 120] as follows: a 954 ± 14 °C anneal for 1 hr. followed by a water quench, an aging treatment at 718 ± 8 °C for 8 hr. before a furnace cool to 621 ± 8 °C, and a hold at the final aging temperature for a total cycle time of 18 hrs. This heat treatment was selected because it is commonly used in the aerospace industry and was used on all samples.

3.2.3 Microstructural Characterization

Microstructural observations were made using scanning electron microscopy (SEM) and electron backscatter diffraction (EBSD). Specimens were sectioned at a 45° angle to the scan vectors, along the XZ plane as oriented in Figure 1. This was followed by polishing to a 0.3 μm finish and etching with Kalling's Reagent #2 as recommended by ASTM E407-07 [133]. A JEOL JSM 7600F field emission SEM operated at 20kV, an Oxford Instruments Aztec EBSD using a Nordlys Max2 EBSD detector, and an X-Max 50 EDS detector were used to gather grain boundary information, high resolution images, crystallographic texture information, and conduct elemental analysis. Transmission Kikuchi Diffraction (TKD), a variant of the EBSD technique, was used for crystallographic and elemental phase identification. A FEI Helios DualBeam 600 operated at 30kV and an Oxford Instruments Aztec EDS/EBSD system equipped with a Nordlys II EBSD detector and X-Max^n 150 EDS detector were used for the TKD work. Scanning transmission electron microscopy (STEM) was done on an aberration-corrected FEI Titan TEM at 300kV. High angle annular dark field (HAADF) and bright field detection (BFD) were both used to create Z-contrast images. EDS within the TEM was done with an FEI Super-X detector with beam currents between 100-150 pA. Collection times were approximately 20 minutes. Samples for TKD and TEM were prepared by the focused ion beam (FIB) lift-out method using an FEI Strata 400 dual-beam FIB. Final thinning of samples was done at 2 kV to reduce surface damage.

3.3 Results and Discussion

3.3.1 As-Built Microstructures

3.3.1.1 Build Quality

The three laser focus shift conditions all produced crack-free samples using the current set of parameters, regardless of focal position. The biggest difference in build quality arose from the porosity. The (0), (-3), and (+3) samples had porosities of 1.67%, 0.25%, and 0.26%, respectively. The dramatic increase in porosity in the (0) focal shift sample is attributed to keyhole porosity due to excessive energy at the focused position where laser energy density is the highest due to the small spot size and high power density based on Eqn. 3 and 4. Calculated values for the spot size and power densities of each sample are given in Table 5.

Table 5: Tabulated spot sizes and power densities for each focal shift condition.

Focal Shift	**Spot Size (µm)**	**Power Density (kW/mm^2)**
(+3)	95.8	25.0
(0)	50	91.7
(-3)	95.8	25.0

3.3.1.2 Laser Focal Shift

The initial investigation of the laser focal shift only considers samples made with the island scanning strategy. In the AB condition, (0) focal shift samples exhibit narrow and deep melt pools compared with the wide and shallow melt pool morphologies of (+3) and (-3) samples as shown in Figure 15. All samples have the characteristic half-circle shape, but the size and shape vary based on focal shift condition. Table 6 provides the average measured width, depth, overlap, and aspect ratio of each samples' melt pools. Measurements were taken across the visible melt pools from metallographic images and are approximations of the true melt pool size. Additionally, the calculated spot sizes and power densities from Eqns. 3 and 4 are provided. Approximate melt pool overlap values are given based on calculated widths and the hatch spacing used during production. The defocused conditions exhibit a roughly 75% lower energy density than the focused condition, and a spot size that is nearly twice as large. It should be noted that slight differences between the (+3) and (-3) conditions may exist due to variability in the shielding gas flow over the powder bed or an imperfect centering of the (0) focal shift on the laser focal point. The interaction of the shielding gas with the powder bed directly over the laser melt pool will influence the removal of process byproducts and may also affect the cooling rate. The defocused building conditions require a movement of the build plate up or down relative to the base level of the building chamber which may alter the flow of the shielding gas and give rise to small differences between (+3) and (-3) focal shifts [69].

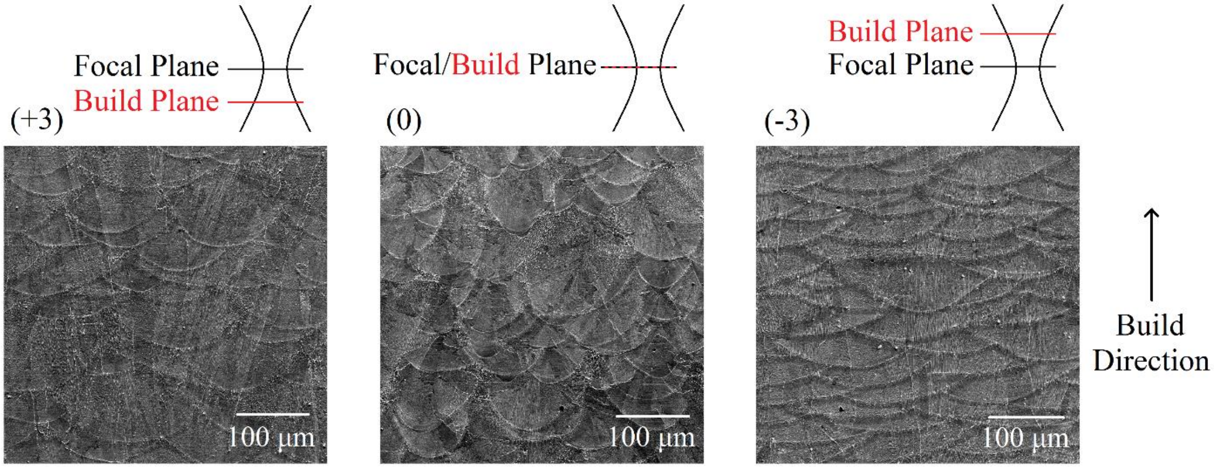

Figure 15: SEM melt pool morphology images and representative schematics of building positions for all three focal shifts. Trough-like melt pools shown for (-3) and (+3), and well-like melt pools for (0) demonstrate the differences a focal shift can cause in the as-built condition.

Table 6: Tabulated values for the measured width, depth, and aspect ratio of the melt pools for each of the focal shift conditions.

Focal Shift	**Average Width (μm)**	**Average Depth (μm)**	**Approx. Overlap (μm)**	**Aspect Ratio**
(+3)	182	48	77	3.9
(0)	122	77	17	1.6
(-3)	203	46	98	4.7

If the (0) focal condition is not centered on the laser focal point, then symmetric shifts above or below this plane will not be perfectly equal. The results shown here indicate that the focal plane is located slightly below the build plane; however, for this study the differences between the two defocused positions are insignificant when compared to those that arise in the much larger shift to the focused position. For this reason, the (-3) and (+3) conditions are assumed to be symmetric around the (0) location, and only the (-3) and (0) conditions will be presented from this point forward. They will be referred to as defocused and focused, respectively.

The melt pool geometries studied by Helmer et al. [31] in EBM are similar to those observed in the current study but on a larger scale due to an increased spot size in each condition (~500 μm for the defocused beam and ~400 μm for the focused beam) and an over 50% higher area energy density. For defocused samples the increased spot size created a wider melt pool, but the decreased power density resulted in a reduced depth of penetration into previous layers [2, 31]. In the present study, while the width of the melt pools changed the hatch spacing remained unchanged so the overlapping area of adjacent melt tracks increased with melt pool width. The schematic shown in Figure 16 demonstrates this relationship. An increase in the melt pool overlap and amount of material remelting will slow down the cooling rate of the material, similar to what was observed by Sateesh et al. [4], to produce a coarser final microstructure.

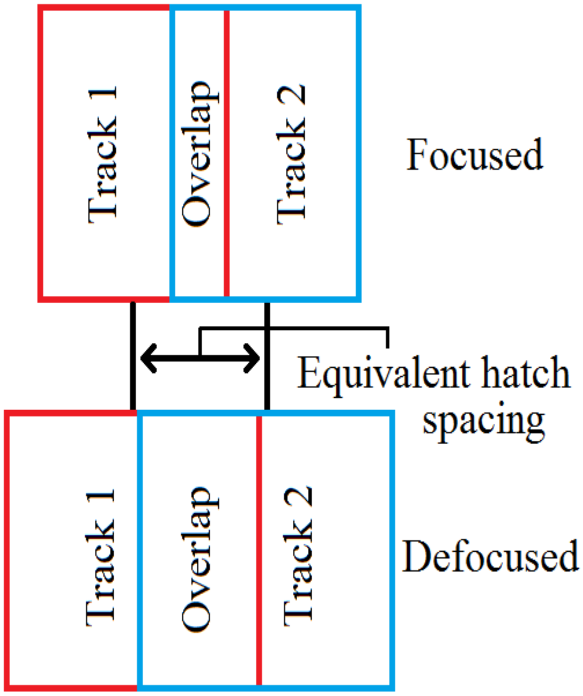

Figure 16: Schematic showing the difference in material overlap behavior due to variable focal shift and spot size. The hatch spacing remains the same, but the overlapping area increases.

EBSD was used to evaluate the microstructures in the as-built condition and how they compare by focal shift. Figure 17 shows EBSD-determined high angle grain boundary positions overlaid on the melt pool boundaries apparent in SEM images for all three samples. The melt pool boundaries in the defocused samples do not correspond to grain boundaries; single grains span multiple melt pools and have a distinct elongation parallel to the build direction. Samples built at the focal plane have grains that coincide with melt pool boundaries and do not show significant elongation in any direction. New grains are consistently nucleated at the melt pool boundary rather than continuing the growth of a previously formed grain. This contributes to the lack of continuity in the focused condition. Helmer et al. [31] attributes this behavior to a strong deviation from the primary solidification direction at the melt pool edges. From the EBSD map overlay, the defocused sample shows large elongated grains parallel to the build direction with small areas of equiaxed grains. On the other hand, the focused sample shows a much finer microstructure and a higher number of equiaxed grains. These microstructures are a result of the different solidification behaviors for defocused and focused samples.

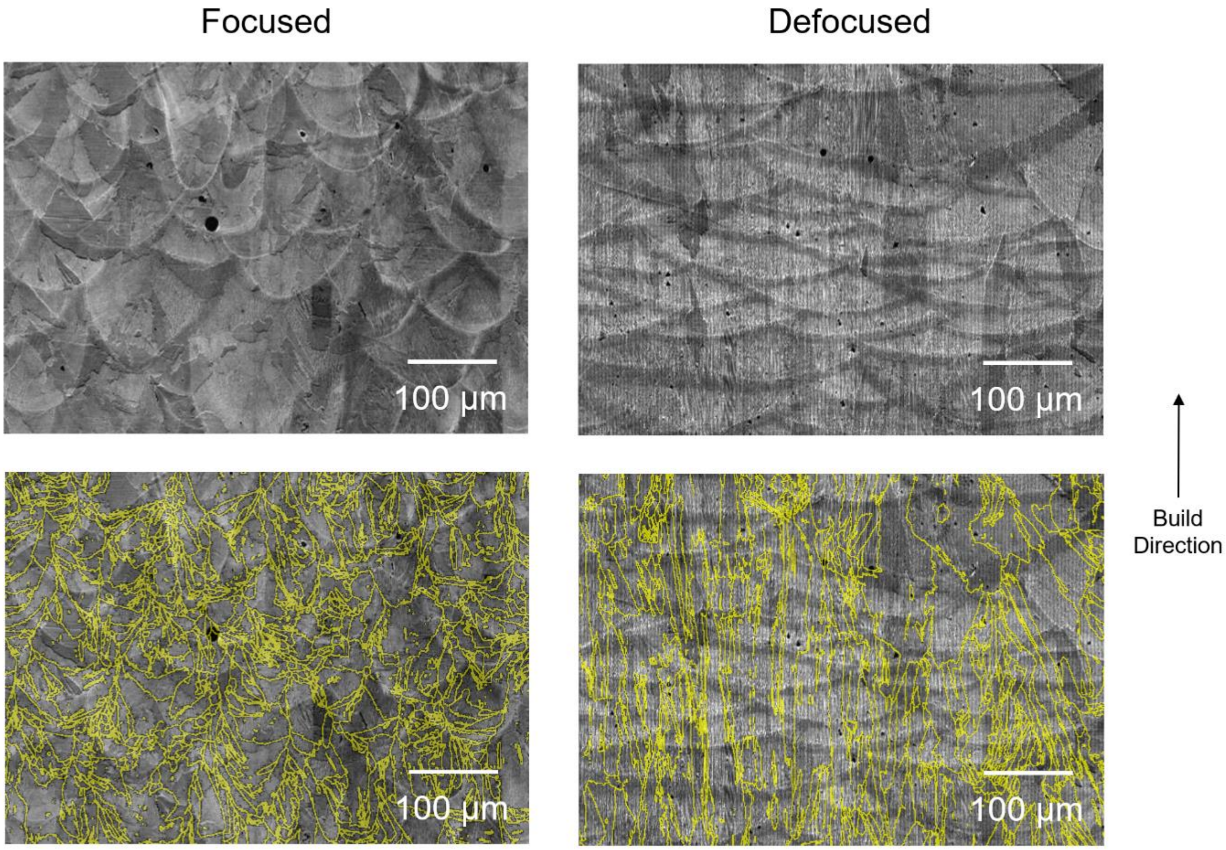

Figure 17: EBSD maps of high angle grain boundaries (yellow) overlaid on top of SEM images of the melt pool morphologies. Columnar grains that span multiple melt pools are observed for the defocused samples, while a higher number of equiaxed grains are present in the focused sample.

The change in solidification behavior is related to the melt pool shape and the local solidification metrics of cooling rate, temperature gradient, and solidification front velocity. Variable cooling rates between focal shifts are a result of different thermal gradients, which in turn produce microstructural morphologies of varying fineness [37, 134]. With a higher energy density the maximum temperature, T_{max}, of the focused condition is higher than the defocused condition which induces larger thermal gradients and faster cooling rates. Higher temperatures and larger thermal gradients can also result in more energetic motion within the melt pool, facilitating dendrite fragmentation and promoting the nucleation of new grains [31]. On the other hand, the lower energy density of the defocused beam produces a lower maximum temperature, driving the temperature gradient down between the melt pool and surrounding material and producing a slower cooling rate and more undercooling [3, 36]. As mentioned previously, undercooling occurs during alloy solidification when a compositional gradient exists, and it creates a region in front of the solidification plane where the liquid melt is below the equilibrium freezing temperature. Protrusions can form at this front, which solidify and grow into dendrites [36]. A slower cooling rate facilitates large columnar grain growth that is aligned to the BD, which is opposite but parallel to the direction of maximum heat flow [135]. The defocused samples exhibit larger and more elongated grains than the focused sample, and a high degree of continuity across layers. Grain formation in the focused samples is short, unaligned, and discontinuous. These features are highlighted in Figure 18, an EBSD-generated aspect ratio map. This figure provides a better visual of the difference between the two laser focus conditions, highlighting the grain morphologies in each microstructure. Similar grain structures have been found in other published literature in SLM [22, 54, 65, 136].

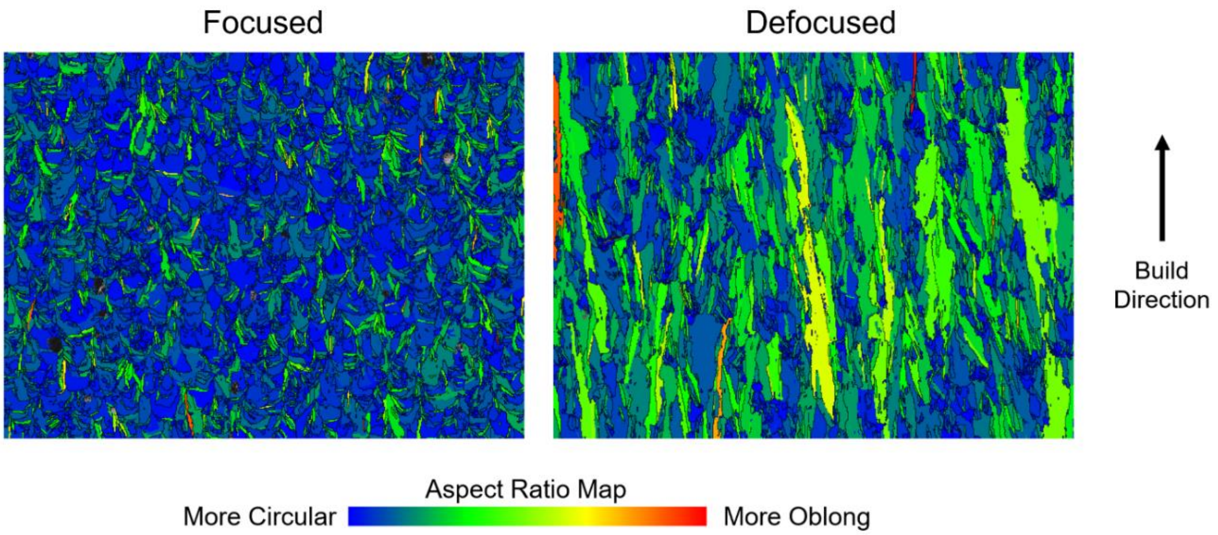

Figure 18: Aspect ratio showing the difference in grain morphology between the two conditions. There is a strong elongation parallel to the build direction in the defocused condition.

Further inspection via EBSD revealed that a crystallographic texture exists in addition to the morphological texture in as-built samples. Figure 19 shows orientation maps and pole figures (PF) for a focused sample and a defocused; the orientation maps are inverse pole figure (IPF) type and use the build-direction as an orientation reference. The elongated columnar grains that exist in the defocused sample are shown to have a strong {001} texture in grains parallel to the BD. Similar texture in AM materials has been observed previously and has been attributed to the occurrence of epitaxial growth [32, 33, 57, 83, 122, 135]. Epitaxial growth may occur when grains in the solidifying material are aligned with the heat flow and the substrate, which in the case of SLM are the previously solidified layers. Cubic metals preferentially solidify along the <001> direction [36, 37], and as heat flows out of the melt pool nuclei that are aligned preferentially will dominate growth. This gives rise to the crystallographic texture observed in the defocused samples. Additionally, columnar growth that occurs during solidification due to the slower cooling rate produces a stronger crystallographic texture. Epitaxial growth provides a mechanism for the formation of long grains that span multiple melt pool boundaries and build layers.

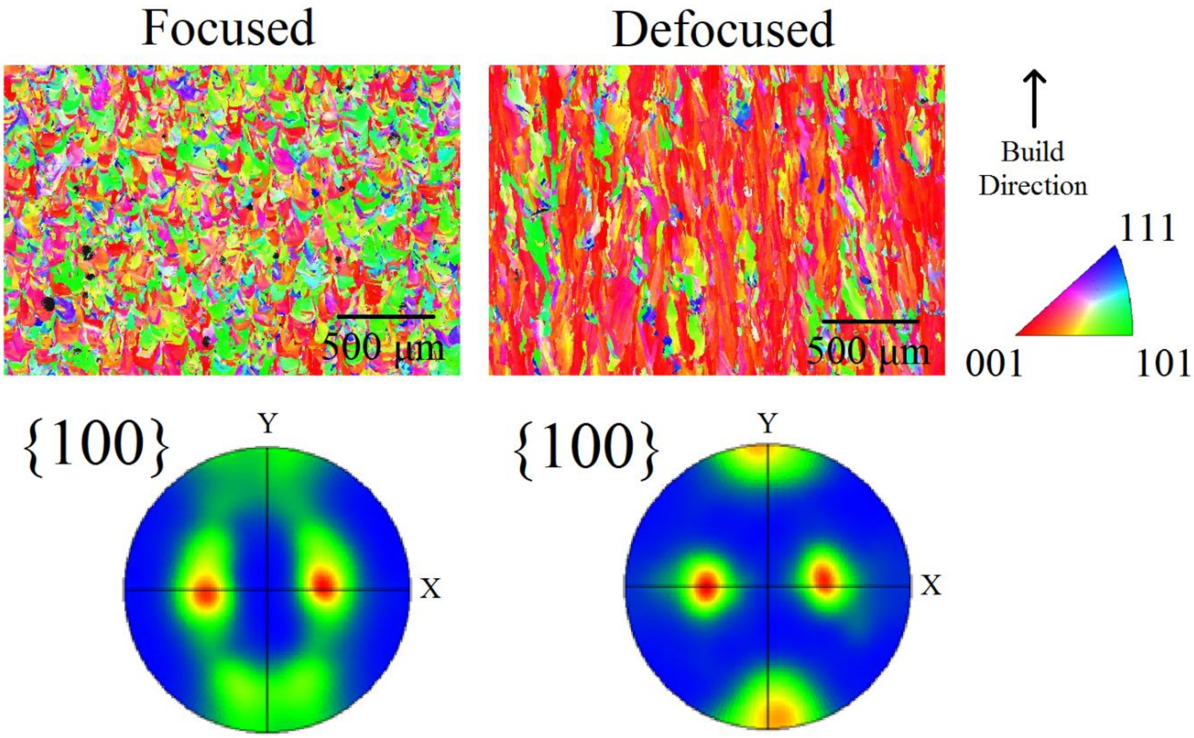

Figure 19: EBSD crystallographic orientation map of the XZ-plane, using a Y-based (build direction) projected IPF. Corresponding pole figures show a stronger build direction parallel texture in the defocused sample and a weaker texture in the focused sample. The crystallographic texture alignment to the building direction for defocused samples is due to the smaller thermal gradient.

The pole figure for the defocused condition has three relatively strong {100} peaks when compared to that of the focused condition due to the slower cooling rate which facilitates aligned growth. The defocused sample more closely resembles a single crystal. On the other hand, the focused condition has a much weaker preferred orientation parallel to the build direction, consistent with an absence of epitaxial growth. Helmer et al. [31] demonstrated that the direction of maximum heat flow in trough-like melt pools is more parallel to the BD than in narrow and deep melt pools where the solidification front normal along the melt pool sides is more perpendicular to the BD. This creates a multi-directional heat flow pattern in the deeper melt pools, as there are more available heat dissipation pathways. As heat flows away in many directions, the resulting grains will be less aligned along a single pathway; furthermore, when the heat flow is not aligned with the BD, formation of stray grains ahead of the solidification front can cause dendrite fragmentation and a weaker overall crystallographic and morphological texture [31]. A more uniform heat flow is present for defocused samples based on the solidification front normal in a shallow melt pool, facilitating the growth of crystallographically aligned grains. This effect is more pronounced in the SLM samples presented here due to the larger relative difference in spot sizes between focused and defocused samples. Helmer et al. [31] demonstrate stray grain formation, but retain highly textured samples in both conditions, which had a difference in spot size of only 25%. In the SLM process, the difference in our calculated spot size is nearly 100%, resulting in much steeper melt pool boundary walls in the focused sample and an increased number of equiaxed grains when compared to the defocused condition. This steepness of the melt pool boundaries decreases the angle θ between the moving laser and the solidification direction, which will increase the growth rate, R. A result of the increased growth rate is a finer microstructure, which is supported by microstructural analysis.

Sectioning in the XY-plane yields similar results in EBSD. The IPF-Z maps (based on the build direction, here normal to the plane of the map) with corresponding pole figures are shown in Figure 20. Like Figure 19, the focused sample shows less build-direction parallel crystallographic texture when compared to the defocused sample. There is a broader distribution of grain orientations in focused samples, but in the defocused ones the {001} grains are more aligned parallel to the build direction, shown in red, and dominate the IPF-Z map. These grains correspond to the same {100} grains observed in the defocused condition in Figure 19. Three strong peaks are present in the defocused sample PF but are now rotated 90° with respect to the corresponding pole figure in Figure 19 due to the change from an XZ to an XY cross-section. For the focused sample, there are two strong peaks and one weak peak shown in the PF, an indication of a weaker overall crystallographic texture parallel to the BD and a confirmation of results obtained from the Z-cross section.

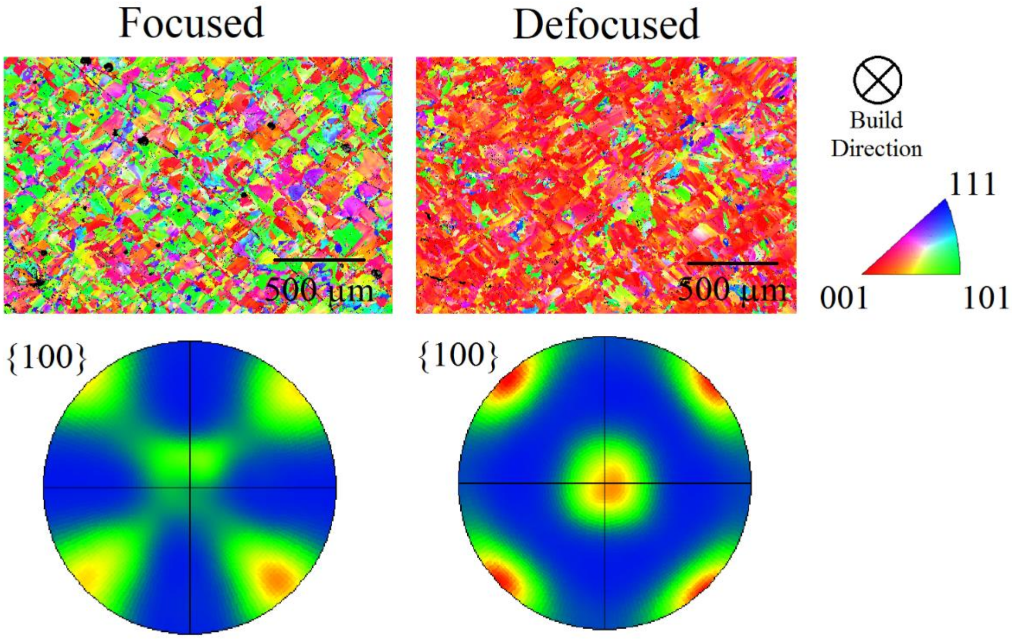

Figure 20: EBSD crystallographic orientation map of the XY-plane, using a Z-based (build direction) projected IPF with corresponding pole figures. Strong crystallographic texture is present for grains with the <001> direction aligned parallel to the building direction.

3.3.1.3 Scanning Strategy

The solidification behavior from the melt determines the morphology of the microstructure and the crystallographic texture as seen in from the change in laser spot size via the focal shift. Combining those results with the scanning strategy allowed for a higher degree of crystallographic alignment; the non-alternating and non-bidirectional scan vectors enhance directional solidification behavior in the samples.

The AB structures of the continuous scanning strategy are presented in Figure 21, with an EBSD overlay of high angle grain boundaries shown in yellow. The appearance of the melt pools is similar to that observed in the island scanning strategy, where the focused condition takes on narrow and deep melt pools relative to the wide and shallow ones of the defocused condition. The primary difference is in the layout of the melt pools with respect to one another. There are distinct columns of melt pools, as the laser scans are located on top of one another and scan in the same direction.

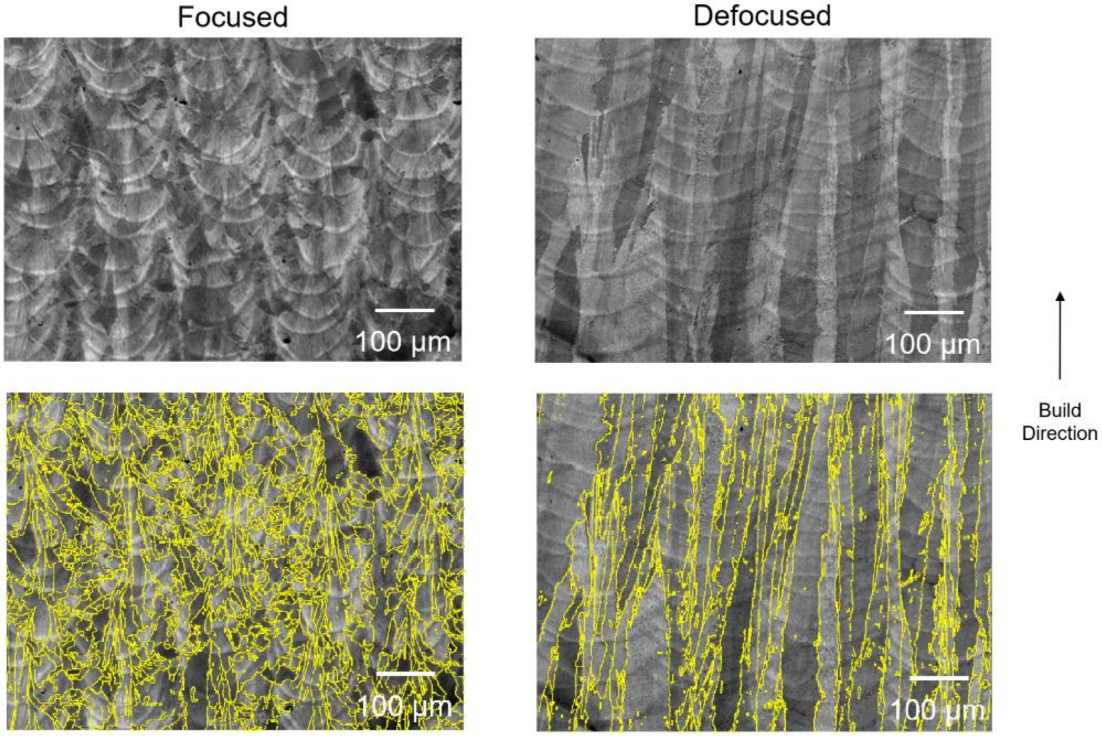

Figure 21: Continuous melt pools of the focused and defocused condition with an EBSD-generated HAGB overlay to demonstrate the contrast in grain morphology generated by the two conditions.

The crystallographic texture of the samples shows variation as well, both with respect to one another and when compared to the island scans. Figure 22 shows inverse pole figure based crystallographic orientation maps and corresponding contoured pole figures for the focused and defocused conditions for the continuous scanning strategy; grains in the map are colored by the crystallographic directions that are aligned parallel to the build direction (BD) per the key given in the top-center. In addition, a higher magnification view of a portion of the EBSD maps is shown centered on a column of melt pools for each condition. It is important to note that samples were sectioned at a 45° angle with respect to the scanning directions, causing the dominant poles to be oriented away from the center of the pole figure. The focused condition solidifies with a similar crystallographic texture to that of the island strategy, where the rapidly solidifying grains form a weak {100} crystallographic texture parallel to the BD. On the other hand, the defocused condition forms an even stronger {100} texture parallel to the SD, and a strong {110} texture parallel to the BD. In both IPF-maps, the red pixels correspond to a {100} pole aligned with the BD and green pixels a {110} pole aligned with the BD. Based on the multiples of uniform distributions (MUD) within pole figures described in Table 7, the {100} texture for continuous scans is stronger than that of the island scans. The MUD number is one measure of the strength of texture in an EBSD pole figure, with higher values indicating more pole “clustering” or alignment. A M.U.D. value of 1.0 would theoretically represent a perfectly uniform distribution of poles in a polycrystal. These maps demonstrate that the laser focus shift can alter both crystallographic texture and microstructural morphology in the continuous scanning strategy.

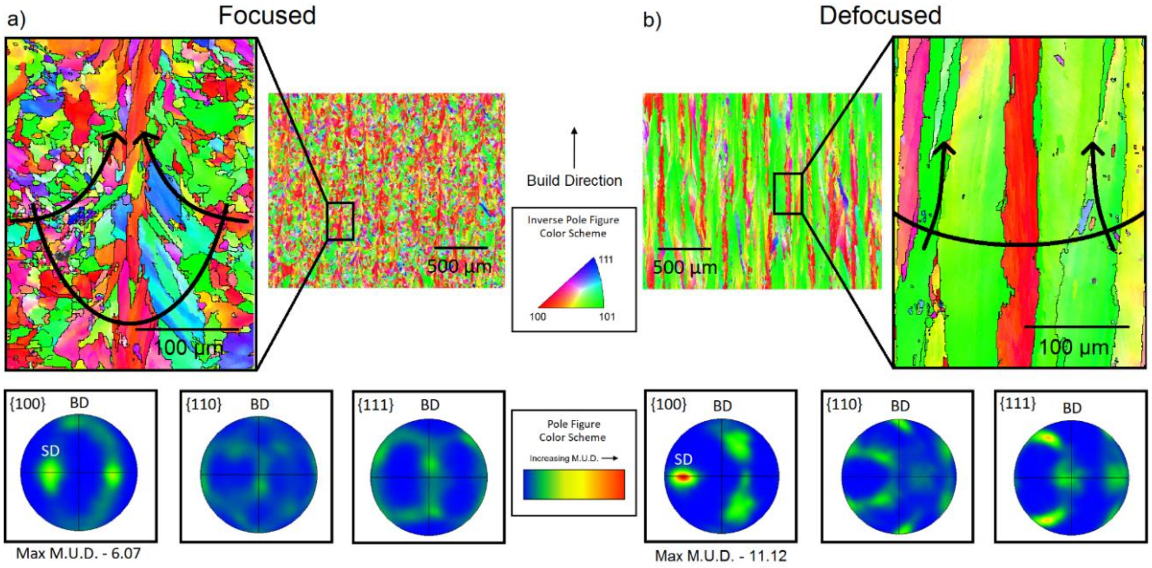

Figure 22: Build direction projected inverse pole figure maps with corresponding {100}, {110}, and {111} pole figures to compare the crystallographic texture from the focused (a) and defocused (b) conditions in continuous scan strategy material. The position and size of a melt pool is approximated with the black curve in the higher resolution EBSD maps.

Table 7: Tabulated M.U.D. values comparing the strength of texture in each as-built condition.

Sample	Max M.U.D. in {100} Pole Figure
Island – Focused	5.4
Island – Defocused	7.1
Continuous – Focused	6.1
Continuous – Defocused	11.1

The texture from the defocused continuous scan strategy is starkly different than that shown in previously for the island scans, where the defocused condition produced a {100} texture parallel to the BD. A direct comparison between both laser focus conditions in the island scan strategy and the continuous scan strategy is shown in Figure 23. Samples were sectioned at a 45° angle with respect to the scanning directions, causing the dominant poles to be oriented away from the center of the pole figure. The inset of the inverse pole figure map shows a contoured {100} pole figure for each condition, providing further insight on how scan direction influences texture formation.

The island scans produce two dominant contouring peaks that are oriented at a 90° angle to one another in the XY-plane, and a third aligned parallel to the Z-axis. These poles correspond to scan direction 1 (SD1), scan direction 2 (SD2), and the BD, respectively. When looking at the pole figure for the defocused continuous scans, there is one dominant peak along the SD, and weaker ones that are approximately 90° away because of the cubic crystal system. Tabulated MUD values are given in Table 7 for each condition. The continuous scan strategy has a stronger crystallographic texture when compared to the island scanning strategy in both focal shift conditions. However, there is a larger separation of properties between the two defocused conditions when compared to the focused conditions. The slower, more uniform cooling of the defocused condition exaggerates the alignment that occurs with the continuous strategy used in the present study.

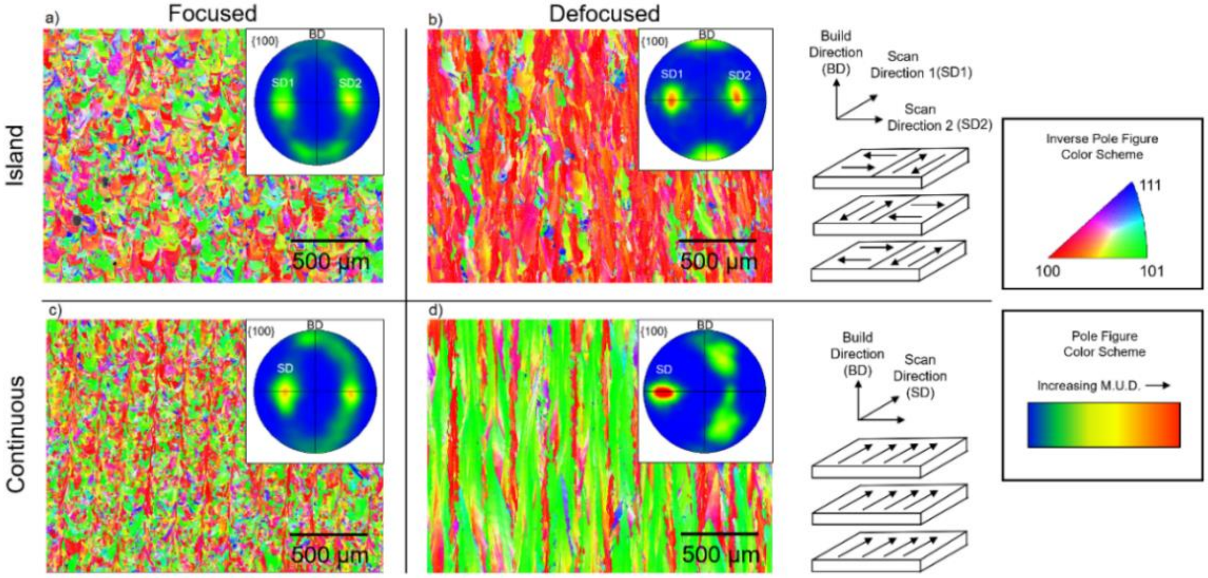

Figure 23: BD-referenced inverse pole figure maps for the island (a, b) and continuous (c, d) scan strategies in the defocused conditions show the difference in texture formation due to the scanning strategy.

For the focused condition, the initial solidification of grains occurs at the edge of the melt pool in a nearly horizontal direction perpendicular to the BD where θ, the angle between the solid-liquid interface and the scanning direction, is the smallest. Melt pools simulated with finite element analysis (FEA) by Ghosh et al. [38] had a variation of θ ranging from 89° at the bottom of the melt pool to 68° at the top, with corresponding solidification front velocities, V, of 0.01 m/s and 0.3 m/s, respectively. An approximation of a melt pool is shown with a black arc in Figure 22. The first grains to solidify will have a strong preference to form parallel to the scan direction (SD), with a preferred {110} texture parallel to the BD. As these grains grow inward, new grains form that are more morphologically aligned to the BD based on the change in the direction of the thermal gradient, indicated by the black arrows in the image. Rapid solidification near the edge of the melt pool due to the orientation of the thermal gradient and increased solidification front velocity facilitates the nucleation of fine grains; as grains grow inward and the thermal gradient changes, the frequency of fine grain nucleation decreases. Eventually, extremely thin and elongated grains are formed that run through the center of the melt pool, representing the last remaining liquid to solidify. These grains have a strong {100} texture parallel to the build direction, shown in Figures 2 and 23 by the red colored vertical grains that correspond to the centers of the melt pools, and are notably coarser. Similar to the finite element modeling work of Ghosh et al. [38], the grains near the melt pool center in the current study have a slower solidification front velocity and are more prone to solidify as coarser, more elongated grains compared to the rapidly solidifying grains near the side walls of the melt pool. It is likely that solidifying grains form in a dendritic manner, but their orientation and size depend on the direction of maximum temperature gradient and solidification front velocity, which changes based on location within the melt pool. Although solidification occurs along the trailing edge of the melt pool along the SD, the focused condition effectively has a second solidification direction perpendicular to the SD due to steep side walls of the melt pool. The resulting crystallographic texture is like that of the island scans, where two distinct peaks for SD1 and SD2 are observed.

In contrast to the focused condition, contoured pole figures for the defocused condition in Figure 23 reveal a single strong {100} peak and two weaker {100} peaks 90° away. The defocused condition also shows a {110} peak aligned with the BD, which itself lies perpendicular to the strong {100} peak and between the weaker {100} peaks. Given the positions of the {100} texture peaks, the alignment of a {110} peak with the BD may be in part imposed by cubic crystallography. A strong {100} parallel to the SD texture was observed in an aluminum alloy by Thijs et al. [3] when using a Concept Laser M1 machine and the same continuous scanning strategy. This indicates that the dominant thermal gradient during solidification is parallel to the SD and the grains are solidifying along the trailing edge of the melt pool. Liu et al. [137] found that by using a single raster direction in laser solid formed (LSF) IN718 better continuity of texture between layers was achieved when compared to a sample with 90° rotations between layers. They claim that rotation between layers creates a new path of heat dissipation, eliminating the single dominant texture in favor of two competing textures. The melt pools of the defocused condition facilitate long range continuity because there is less nucleation of new grains at the melt pool edges. This behavior, when combined with the continuous scanning strategy, promotes the formation of a strong {100} texture parallel to the SD.

In Figure 23, the two scan directions are a result of the inherent nature of the island scan strategy, which is similar to the texture found in samples that utilize the alternating continuous scan strategy; the introduction of a second scanning direction produces a second dominant pole. Sun et al. [29] showed with EBSD that for a continuous scan strategy with alternating layers applied to a different nickel alloy, three peaks were observed corresponding to each of the two scan directions and the build direction, similar to the island strategy shown here. The bidirectional scanning of the islands offsets previous scans, generating a net thermal gradient parallel to the build direction rather than allowing a single scan direction to dominate. Alternating between layers further contributes to the offsetting effect by decreasing the number of adjacent scans that are parallel to one another, creating multiple directions of grain growth, and weakening the overall crystallographic texture. When only a single scan direction is utilized, there is no offsetting effect, resulting in the single strong peak observed in Figure 23.

3.3.1.4 Elemental Segregation

IN718 contains multiple constituent elements that are susceptible to segregation during solidification: Nb, Ti, and C [35, 39, 138]. Segregation occurs in IN718 at the microscale between dendrites when the alloy freezes, because the solidifying phase and the liquid do not have the same compositions. Solute atoms are rejected ahead of the tip of the dendrite and laterally, resulting in a redistribution of alloying components. In the wake of these solidification features, local areas with a high concentration of alloying elements remain. This can result in favorable precipitation of particles that are rich in these elements in areas where segregation occurs.

To analyze segregation in the AB structures of SLM IN718, SEM images and corresponding high-resolution EDS elemental maps of Nb were taken at melt pool boundaries within a focused and defocused sample, as shown in Figure 24. The characteristic columnar dendrites are observed in the defocused condition to span the melt pool boundary, forming a continuous dendrite that spans multiple layers. In the focused condition, the melt pool boundary does not have continuity across it, forming a new grain on either side. Despite morphological differences, segregation still occurs in both conditions within the interdendritic regions. Because there are many fine grains in the focused condition with a random dendritic orientation, segregation results in a more randomized distribution of localized pockets of high Nb concentration. The defocused condition has aligned dendrites that form ordered line arrays rich in Nb. These arrays run parallel to the build direction. Furthermore, the severity of segregation may differ between focal shift conditions; the fast cooling rates of the focused condition will hinder the lateral diffusion of solute atoms and result in less segregation [36].

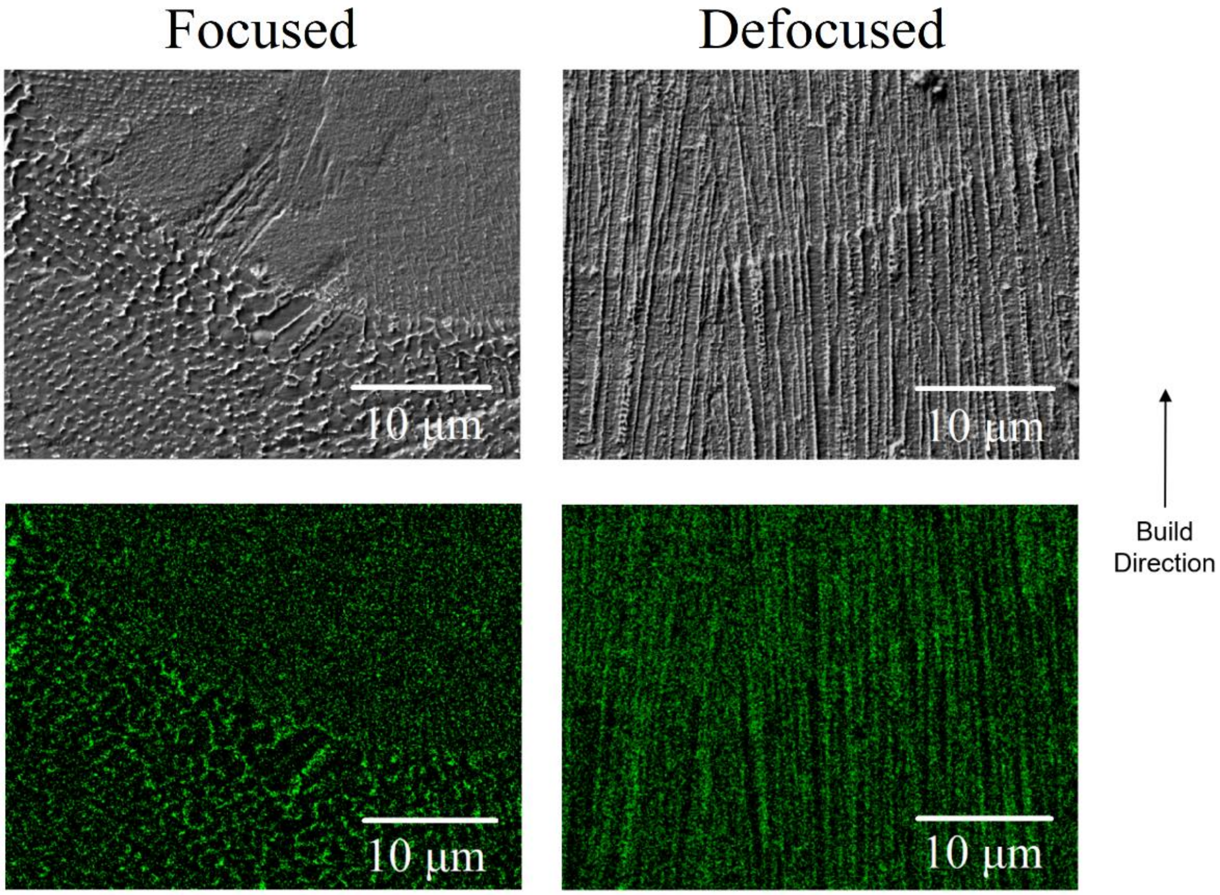

Figure 24: SEM (top) and high-resolution EDS elemental map of Nb (bottom) showing the high Nb concentration areas within focused and defocused samples in the as-built condition. Each sample shows a representative area near a melt pool boundary, highlighting the aligned interdendritic segregation of Nb occurring in the defocused sample and lack of alignment in the focused sample.

To confirm elemental segregation in the interdendritic regions, thin TEM samples were prepared perpendicular to the growth of the dendrites as outlined in Figure 25a. The bright-field TEM image in Figure 25a is normal to the growth direction of the dendrites, presenting a head-on view of them in cross-section. The dendrites have a characteristic hexagonal cross section, which is related to the minimization of boundary energy. At each intersection the dendrite boundaries form a roughly 120° angle with respect to one another, which is an inherently stable configuration [36]. The scale of the segregation in SLM is extremely small when compared to segregation lengths in castings [139] and welds [140, 141] because of the rapid cooling rate. EDS was performed on the TEM sample to produce concentration maps, which can be seen in Figure 25b. The maps show a clear enrichment of Nb and Ti at the dendritic boundaries, and a corresponding dearth of Cr, Fe, and Ni. These regions are more prone to forming undesirable precipitates due to the inhomogeneous local compositions. The Mo and Al concentrations appear uniform throughout the microstructure.

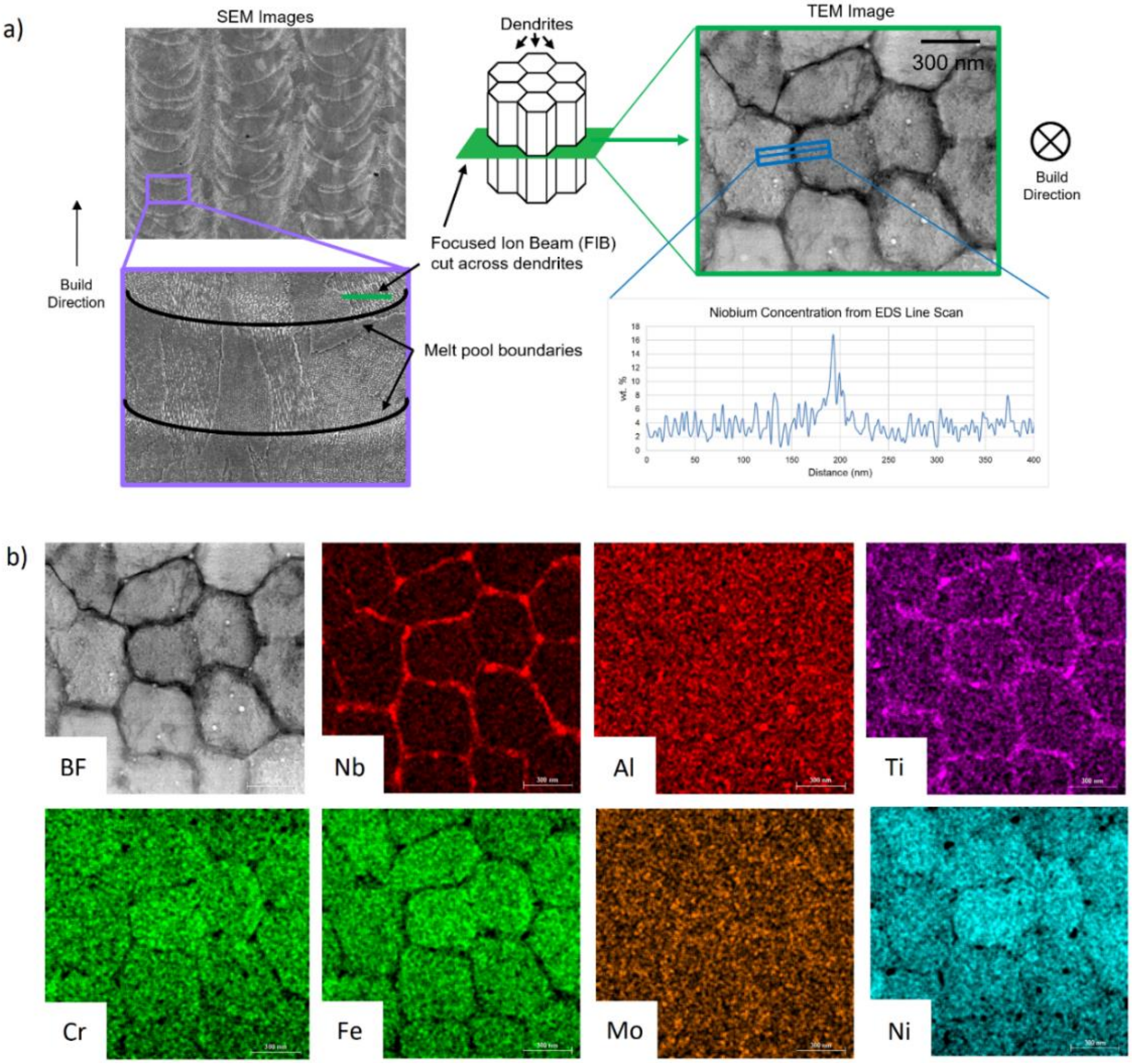

Figure 25: a) SEM images showing where the TEM sample was taken from, highlighting the location and orientation with respect to a melt pool boundary and the dendritic growth direction. The corresponding TEM bright-field image of the cross section is shown on the right-hand side, highlighting the hexagonal structure of each dendrite. b) EDS maps showing enriched and reduced concentrations of various alloying elements.

3.3.1.5 Build Orientation Dependence

For comparison to vertical rods, horizontal rods were printed with the continuous scanning strategy based on the high degree of directionality that was observed. The initial goal was to characterize the mechanical behavior of the anisotropy that forms during SLM, but further analysis of the microstructures led to a study of the effects of build plate proximity as well. Initial microstructures of the AB X-Orientation and Z-Orientation conditions appear similar as shown in Figure 26; the melt pool geometry is dominated by the spot size. All samples made for the comparison of build orientation utilized the continuous scanning strategy and either the focused or defocused condition.

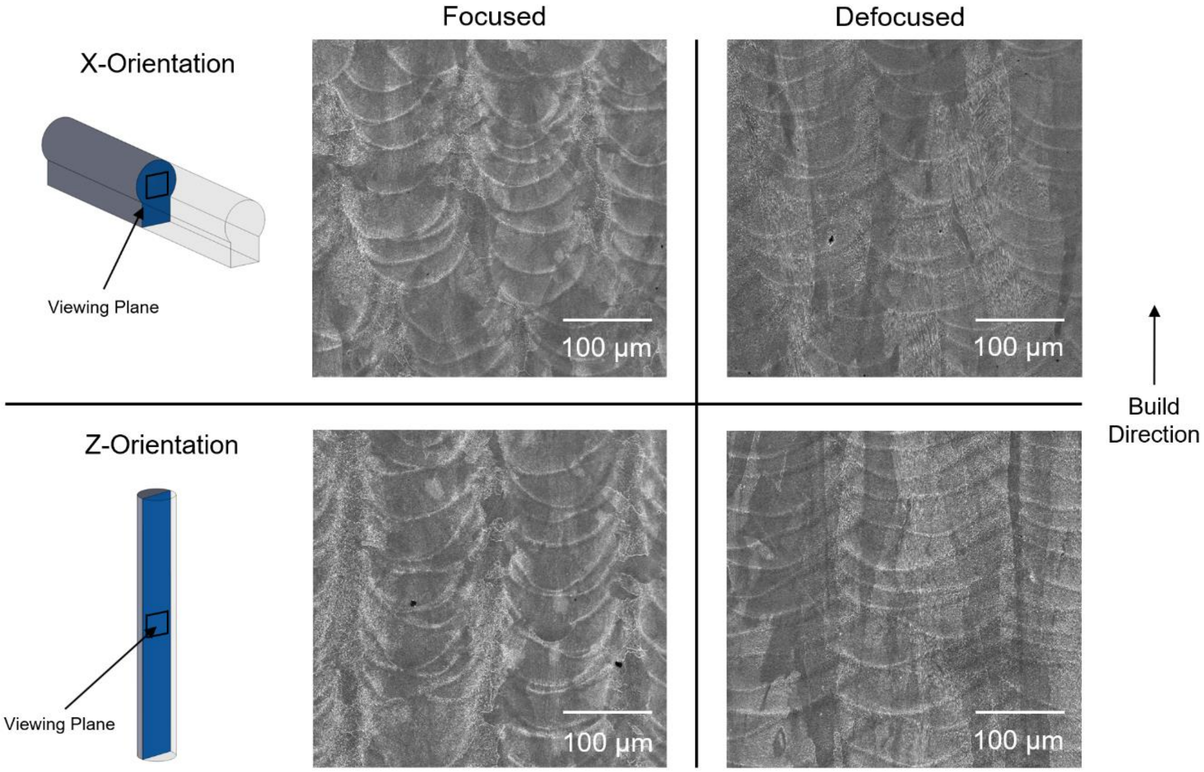

Figure 26: X-orientation and Z-orientation AB structures in both the focused and defocused conditions.

Analysis of the finer features within the microstructure reveals a difference in the primary dendrite arm spacing (PDAS) of the samples, a metric directly related to the cooling rate [38, 142]. Similar to the solidification behavior discussed earlier, PDAS is controlled by G, V, and $\dot{T}$ [36-38, 142, 143]. The PDAS represents the distance between the tips of neighboring γ-cells during solidification and is represented in the current study by the width of these cells. SEM images of the dendrite morphologies and interdendritic regions are shown in Figure 27, and the measured PDAS for each sample are presented in Table 8 as the average of 20 measurements per sample. The current results are in line with simulations by Ghosh et al. and experiments by Amato et al. [83] who observed PDAS in the range of 0.14 – 1.6 μm and 0.5 – 1 μm for SLM IN718, respectively. PDAS of this magnitude correspond to cooling rates between approx. $5 \cdot 10^4$ and $3 \cdot 10^6$ K s^{-1} [38]. Notably, the PDAS of the X-Orientation samples are both smaller than those of the Z-Orientation samples in both focal shift conditions, and a corresponding increase in the microhardness is observed as well. Others have reported that the proximity to the build plate can have an effect on the resulting microstructures due to the change in the thermal history [7, 8]. The built plate acts as an effective heat sink as it remains between 25 °C and 75 °C throughout the building process, constantly drawing heat out of the parts. Wang et al. [7, 8] found that the microstructures nearest to the build plate were finer than those in the middle and top of the parts as a result of this increased cooling efficiency.

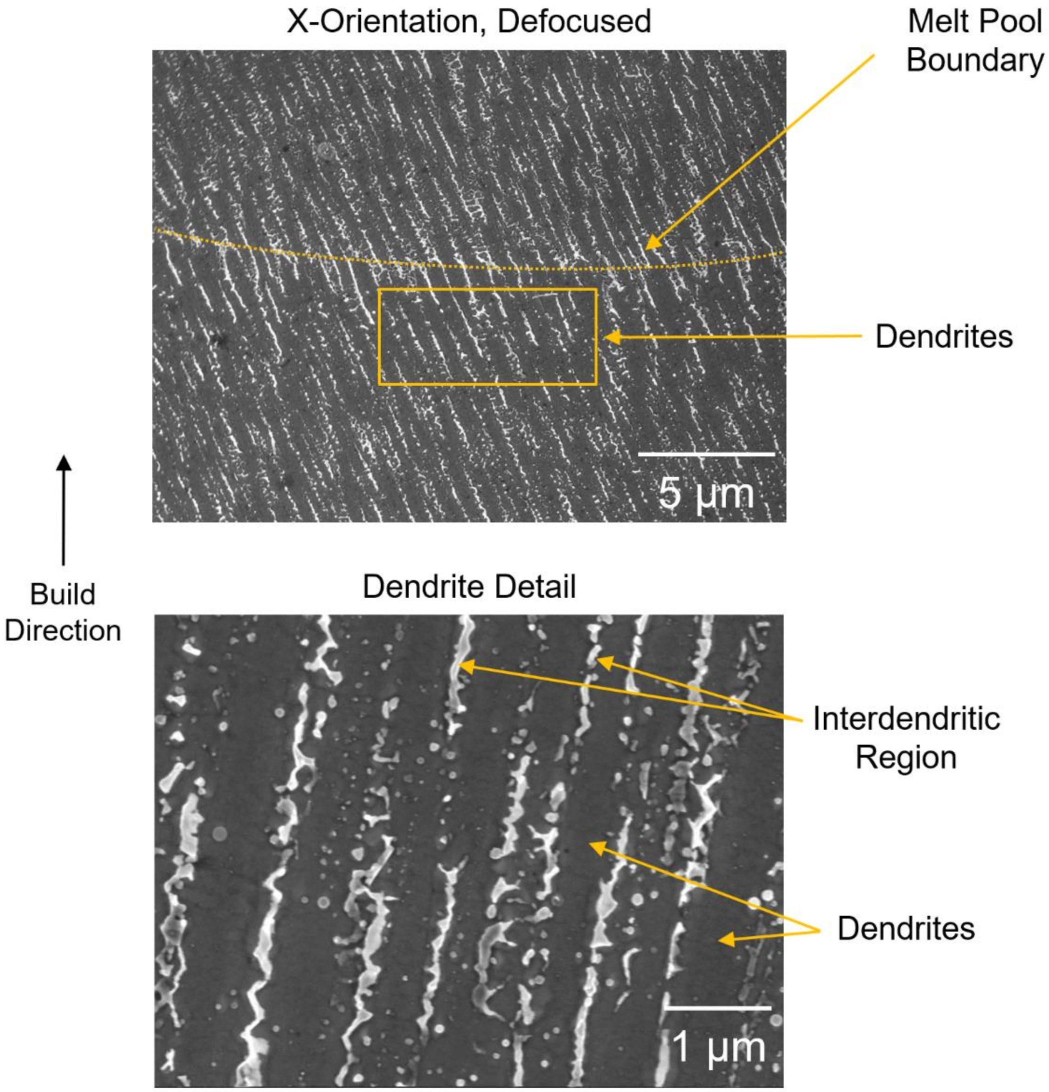

Figure 27: High magnification views of the dendritic structure for the X-Orientation, highlighting the dendrites and interdendritic regions.

Table 8: PDAS and microhardness measurements for build orientation samples in the AB condition.

Sample	**PDAS**	**Microhardness**
	(µm)	**(HV)**
X-Orientation – Focused	0.51 ± 0.07	341.4 ± 8.3
X-Orientation – Defocused	0.57 ± 0.06	340.9 ± 6.1
Z-Orientation – Focused	0.65 ± 0.18	325.6 ± 7.0
Z-Orientation – Defocused	0.78 ± 0.16	323.5 ± 5.8

3.3.2 Post-Processed Microstructures

3.3.2.1 As-HIP Microstructure

To relieve stress in the samples and improve consolidation all samples underwent a standard HIP cycle. After HIPing, most pores present in each of the samples were closed, giving focused and defocused samples respective porosities of 0.05% and 0.06%. The microstructures of samples built in the continuous scanning strategy in both focal shift conditions after a 3-hour 1163° C HIP treatment are shown in Figure 28. Microstructural features, such as melt pool boundaries, primary dendrite arms, and regions of segregation that are characteristic of the AB condition are no longer visible in the as-HIP'ed condition. The high temperature of the HIP process facilitates elemental homogenization and partial recrystallization, eliminating these AB features. However, the as-HIP microstructures still contain interesting features that are reminiscent of the AB condition. From the SEM images in Figure 28, grain size and morphological differences similar to those that existed in the AB condition can be seen.

Morphological textures in the as-HIP condition mimic those of the AB structures, where the focused condition had a finer microstructure with a higher number of equiaxed grains and the defocused structure had an elongation of grains parallel to the building direction. The initial grains have influenced how the retained microstructure has formed. In addition to the grains, obvious blocky precipitates with a high contrast compared to the matrix have formed in the microstructure as a result of the high temperatures used in HIP. At 1163° C, the only stable precipitate in IN718 is NbC, which will preferentially form in regions rich in these elements. The Laves phase is only stable up to the 1140 – 1160 °C range and will dissolve at the current HIP temperatures [144-146]. The focused condition appears to have a random distribution of these precipitates throughout the microstructure, sometimes forming at grain boundaries, but also forming within grain interiors.

The defocused condition contains highly ordered arrays of precipitates that run parallel to the build direction. Both precipitation arrays mimic the previously observed distribution of elemental segregation.

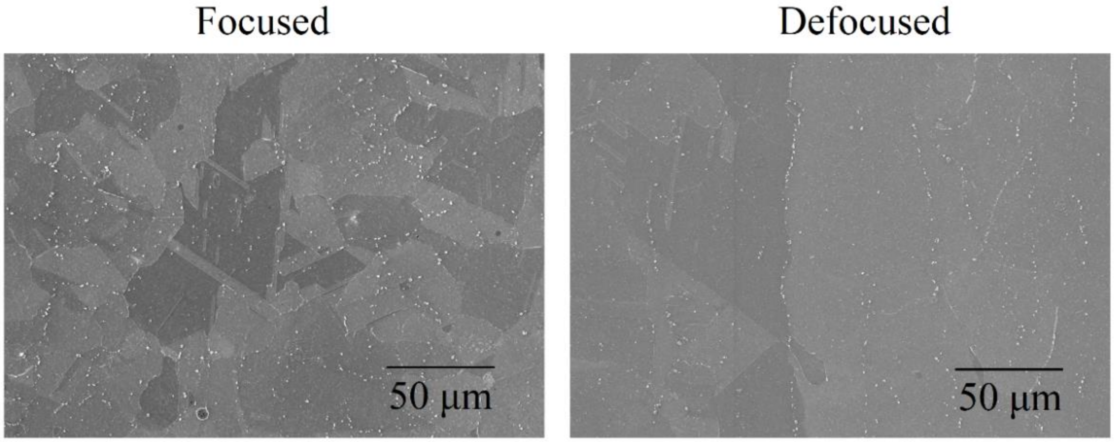

Figure 28: a) As-HIP microstructure of the focused condition, showing relatively fine grains with an overall equiaxed structure, and a more random distribution of precipitates. b) The defocused condition retains the elongated grain morphology of the AB condition, has a much coarser grain size, and has ordered arrays of precipitates that run parallel to the build direction.

Samples built for the study of orientation dependence after HIP processing are shown in Figure 29. The X-orientation samples show that a significant amount of the grain boundary δ phase has nucleated, whereas the Z-orientation samples do not contain obvious δ phase precipitates. This difference may be related to a different rate of cooling from the HIP condition, as well as a difference in the distribution of alloying elements in the AB condition. The build plate will more effectively store heat, and horizontal samples have a large contact area with the plate. Furthermore, compared to the plate with vertical rods, there is much less exposed surface area for convective cooling. Both of these factors may slow down the release of heat from X-orientation samples and can promote the formation of δ phase as it passes through the nose of the TTT curves. From Figure 12, it is seen that GB δ can form in approx. 10-15 minutes as it passes through the nose of the GB δ portion of the TTT curve. Furnace logs indicate that the samples spent at least 1 hour passing through the δ stability region.

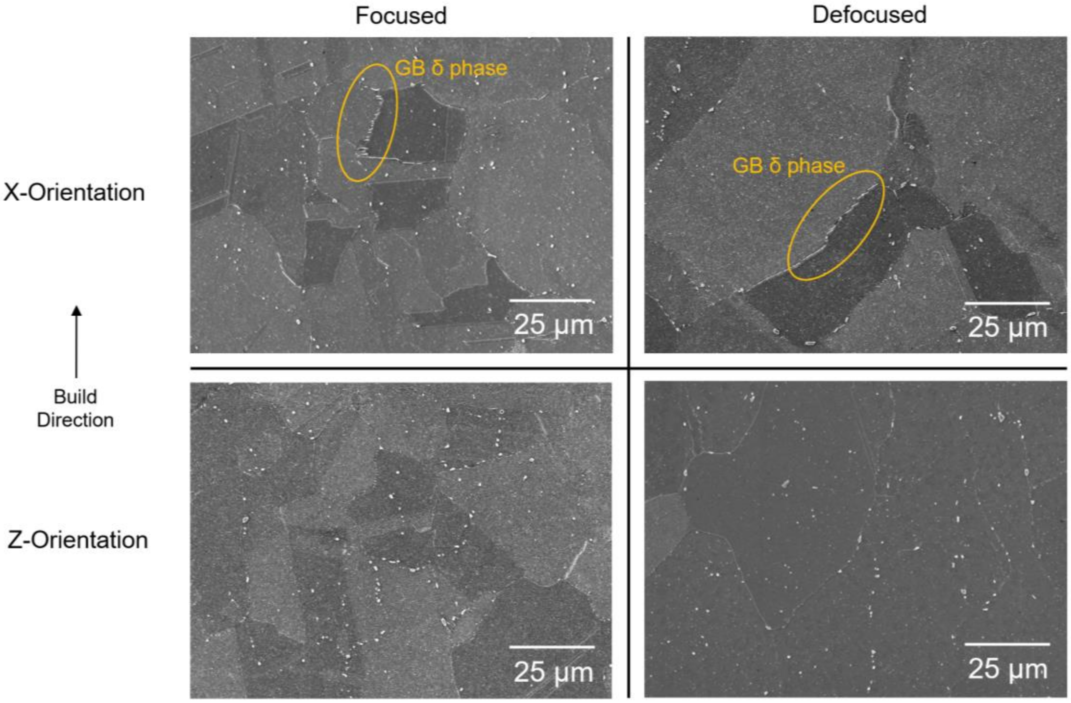

Figure 29: As-HIP build orientation samples, comparing the X- and Z-Orientations. GB δ phase is found in the X-Orientation samples but is absent from the Z-Orientation samples.

3.3.2.2 NbC Identification

All SLM samples contain blocky particles that are ~1 μm in diameter. These are MC-type carbides, (Nb, Ti)C, with a primary enrichment of Nb; other elements, such as Ti or Mo, can substitute for Nb based on EDS measurements taken by Sundararaman et al. [147]. Transmission kikuchi diffraction (TKD) measurements taken on the matrix and one of the particles in Figure 30 shows diffraction pattern index matches of FCC Nickel and NbC. Both images contain an overlaid red pattern representing the simulated phase, with the grey background being the experimentally observed diffraction pattern. Both the location of the diffraction bands and their widths identify match well with their simulated phases. It is unlikely that Figure 30c represents the Laves phase as simulated indexing of the topologically close-packed hexagonal phase did not match the observed diffraction bands. Further confirmation of these particles' chemistry is provided in the form of EDS maps in Figure 31, where a distinct enrichment of Nb and C confirm the presence of carbides. Although NbC has been previously identified in SLM IN718 based on the EDS determined chemistry [6, 27, 39, 148] and TEM diffraction patterns [149], this is the first identification based on structure using TKD. NbC was also found in wrought material, but not in distinct arrays. Wrought carbides were found to be larger than those produced in SLM, roughly ~5-10 μm in diameter, and much more dispersed throughout the matrix.

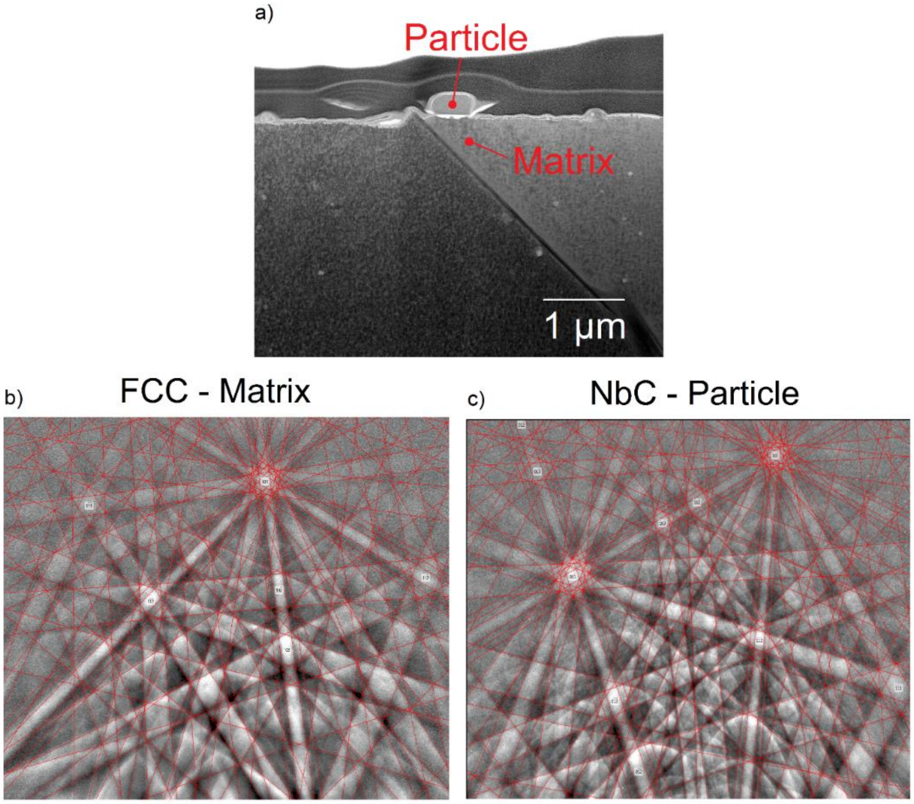

Figure 30: TKD analysis of blocky particles after post-processing. A TEM sample showing both an NbC particle and the γ matrix is shown in (a). Simulated diffraction patterns of FCC Ni (b) and NbC (c) are overlaid on top of the experimental diffraction patterns generated from the particle and matrix locations in (a).

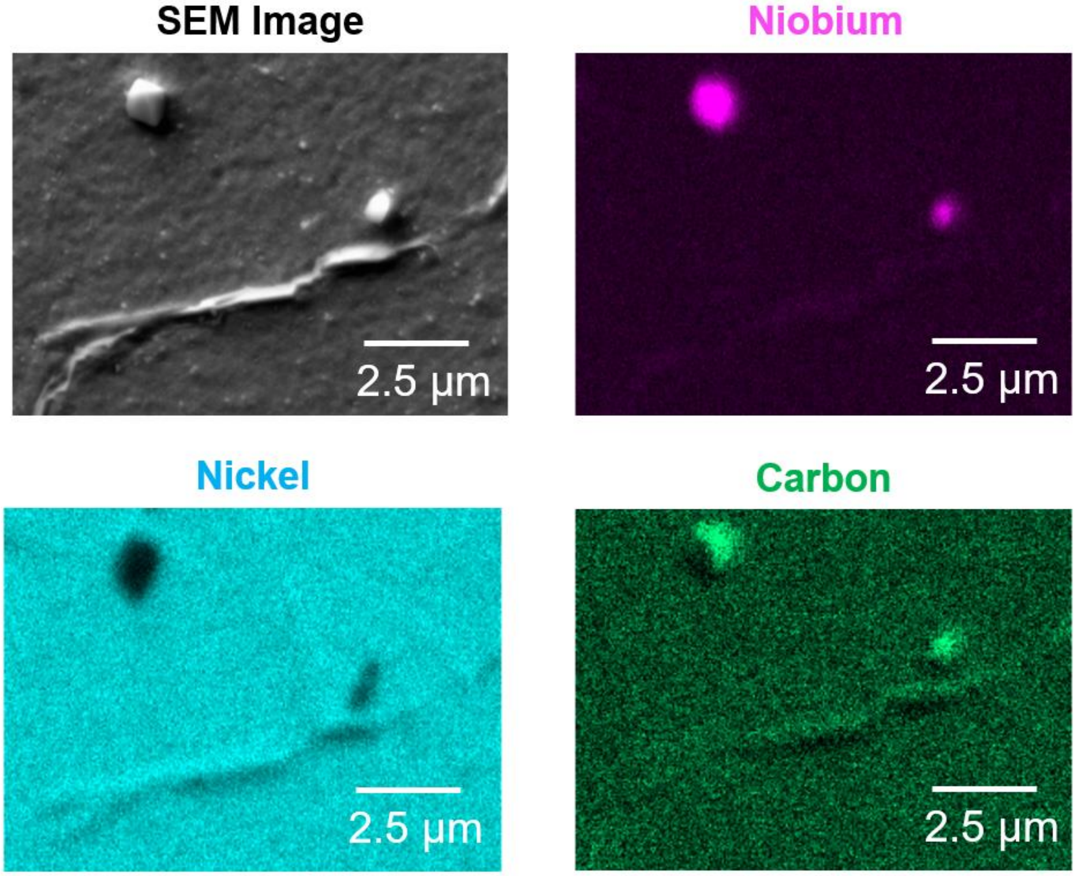

Figure 31: EDS of a NbC particle in proximity to a grain boundary. The enrichment of Nb and C and dearth of Ni provide a positive identification of this particle as NbC.

NbC precipitation occurs in areas where Nb, Mo, Ti, and C are in high concentrations within the melt, a result confirmed by Tian et al. [150] where NbC was found to favorably precipitate in the interdendritic regions of laser additive manufacturing samples. The elongated grains and corresponding dendrites appear much larger and more often for defocused samples than focused ones. In the as-built defocused samples, aligned streaks of Nb-rich areas exist, while for the focused samples these streaks are not aligned to the building direction because of the more equiaxed structure. The nucleation and growth of NbC precipitates during the HIP cycle is similar regardless of laser focus, but the texture that exists in defocused samples due to aligned dendritic growth and subsequent segregation causes their formation to be parallel to the BD.

The alignment of the MC-type carbides is an artifact of the original solidification behavior of each focal shift. Similar to the current TEM work, it has also been observed by Ghosh et al. that high amounts of Nb segregate to the interdendritic areas, which are aligned parallel to the direction of grain formation [38]. The focused condition leads to more rapid solidification, forming fine clusters of horizontally-aligned dendrites at the edges of the melt pools, while the defocused condition has a more uniform thermal gradient and consists of large elongated dendrites. Many of these solute-rich areas coincide with the grain boundaries because the original solidification dendrites determine grain boundary orientation. Therefore, the regions of increased carbide-forming elements lay in an orientation parallel to the BD for the defocused condition, and in a more horizontal orientation in the focused condition. These areas of high local Nb concentration preferentially form Nb-rich precipitates during HIP processing and lead to the formation of aligned stringers of precipitates in the post-HIP microstructures.

3.3.2.3 Fully Heat-Treated Microstructures

The microstructures of the fully heat-treated samples from both focal conditions for the island and continuous scanning strategies are shown in Figures 32 and 33, respectively. For comparison the typical heat-treated wrought microstructure is shown in Figure 34. Grain sizes and aspect ratios of all conditions are given in Table 9 for the heat-treated microstructures. For both scanning strategies, the defocused condition yields a larger grain size and aspect ratio, both of which are directly related to the originally elongated AB microstructures. The columnar growth observed before has had a significant effect on the fully heat-treated microstructures. The wrought structure is shown to have the finest structure with a highly equiaxed microstructure. The precipitate distribution is also quite different in the wrought microstructure, showing a high prevalence of the δ phase along grain boundaries taking on a spheroidal and plate-like morphology. Furthermore, NbC observed in the wrought structure appear as much larger precipitates that are few and far between, rather than the closely spaced small NbC found in SLM microstructures. This may be related to the increased chemical homogeneity in the wrought structure, due to the thermomechanical processing.

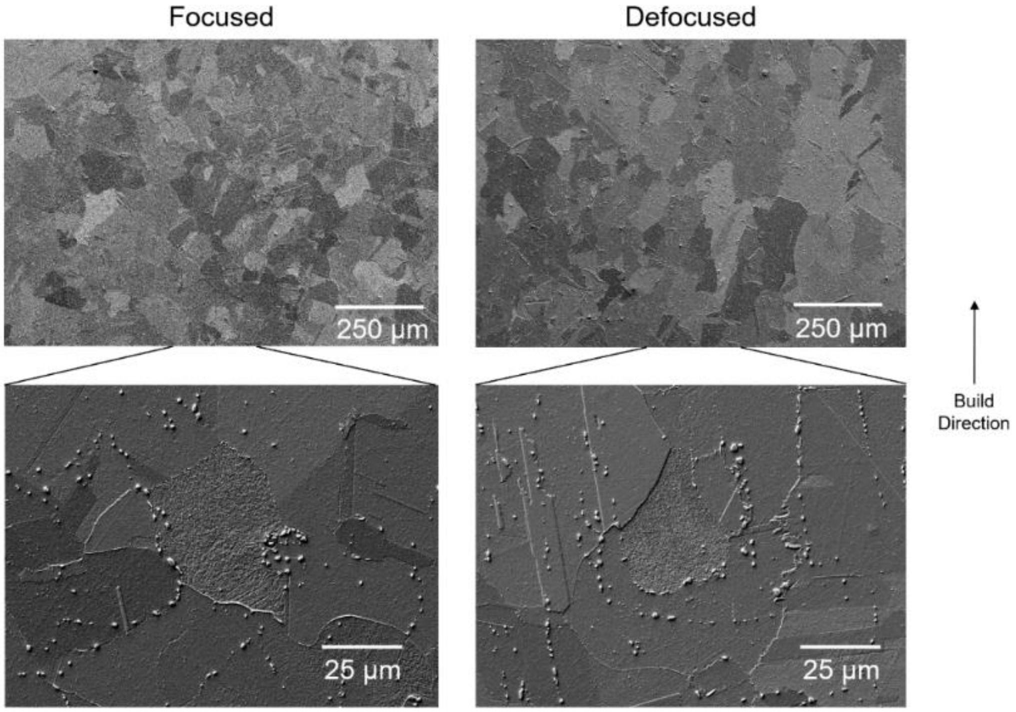

Figure 32: Fully heat-treated SEM images of the focused and defocused conditions produced by the island scanning strategy. Magnifications of 100x and 1000x are shown.

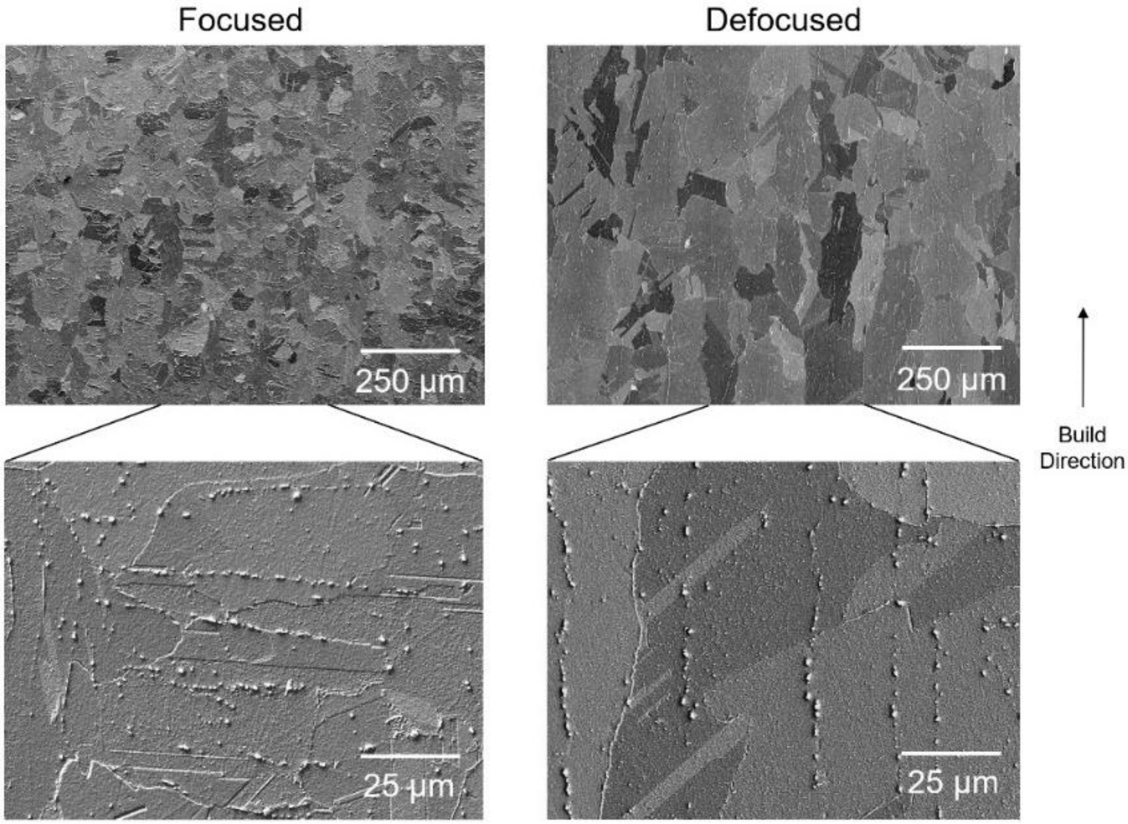

Figure 33: Fully heat-treated SEM images of the focused and defocused conditions produced by the island scanning strategy. Magnifications of 100x and 1000x are shown.

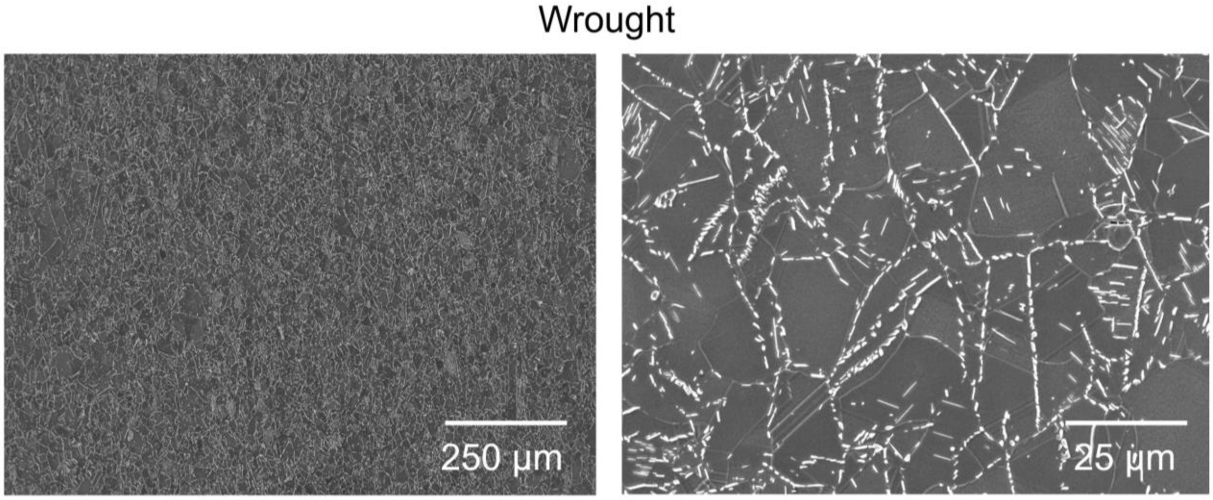

Figure 34: Fully heat-treated SEM images of the wrought material. Magnifications of 100x and 1000x are shown.

Table 9: Measured values of the grain sizes and aspect ratios of samples after heat treatment.

Sample	**Average Grain Size**	**Average Aspect Ratio**	**Max M.U.D. in {100} Pole Figure**
	µm		
Island - Focused	48.6	1.1	1.9
Island - Defocused	64.3	1.2	2.1
Continuous - Focused	43.4	1.1	1.7
Continuous - Defocused	80.4	1.6	3.3
Wrought	21.7	1.1	1.3

Much like the fully HIP-treated microstructures, the heat-treated microstructures have morphologies that are correlated to their AB structures. Popovich et al. [54] demonstrated a similar result where morphological differences observed in the as-built condition were maintained through HIP and heat treatment. In their study, the microstructural differences were induced by large changes in the process parameters, utilizing laser powers ranging from 250 W to 950W and adjusting other parameters—scanning speed, hatch spacing, and layer thickness—to maintain a constant volumetric energy density (VED) of 59.5 J/mm^3. Our results at the focused condition were obtained with a VED of 66.7 J/mm^3 and show a similarly equiaxed microstructure before and after heat treatment. The defocused samples maintained an equivalent VED as (0), but had a much coarser and crystallographically aligned microstructure, a similar contrast exists between the 250W and 950W samples observed by Popovich et al. [54]. As mentioned previously, the solidification mode can be affected by melt pool geometry and thermal history. The defocused samples utilize a larger beam spot size, a variable not accounted for when calculating volumetric energy density. Similarly, the 950W samples used by Popovich et al. [54] have a larger beam diameter and a flat-top distribution, compared to the smaller Gaussian beam used for the 250W samples. These factors can affect the melt pool geometry; both 950W and defocused samples exhibit shallow and wide trough-like melt pools, whereas the 250W and focused samples are narrow and deep. The resulting solidification for the wide melt pools would have a more aligned solidification direction parallel to the direction of maximum heat flow, producing a smaller value of R and a slower cooling rate. The melt pool geometry plays a critical role when determining solidification kinetics and can result in large differences in the scale and alignment of the microstructure.

Not only did the defocused samples exhibit coarser grains in the fully heat-treated condition, but there is a distinct morphological texture as well; elongation along a single axis is present in the fully heat treated condition that mimics the elongation parallel to the BD seen earlier. EBSD grain shape alignment maps are shown in Figure 35 for the focused and defocused samples; a clear NNW/SSE alignment exists for the elongated grains, while the more equiaxed grains of the focused condition show no preferred axis. This microstructural feature can be interpreted as an artifact of the original BD where samples exhibited similar elongation due to the epitaxial growth of columnar grains.

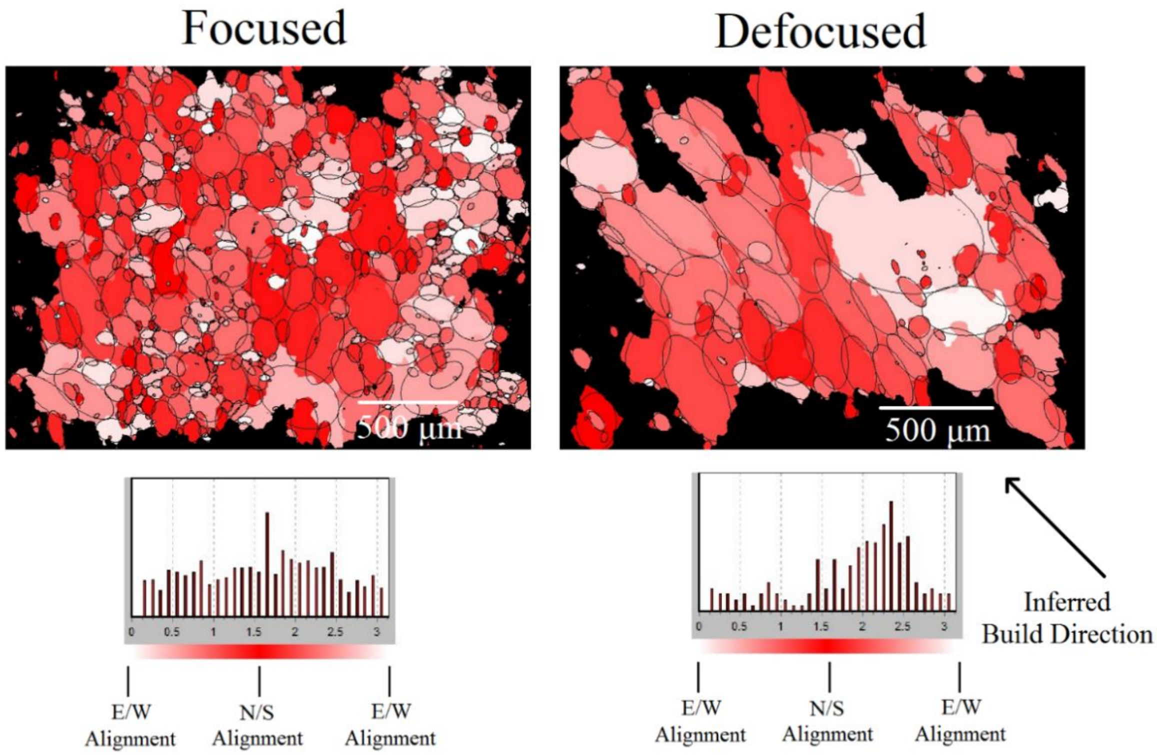

Figure 35: EBSD grain shape alignment maps showing the preferred axis of elongation using the major axes of fitted ellipses. The defocused sample has a strong NNW/SSE alignment, taken to be the build direction, while the focused sample does not show a preferred orientation.

NbC precipitation may play a role in the retention of elongated grains in the fully heat-treated condition that is observed in Figure 36. During the HIP cycle, NbC precipitates at grain boundaries due to the enriched Nb concentration and the ease of nucleation at grain boundaries [109, 151]. After HIP, the samples undergo heat treatment, where there is no grain growth in the samples. The carbide precipitates at grain boundaries pins these grain boundaries and prevent appreciable amounts of grain growth [54]. The result is a fully heat-treated microstructure that retains the morphological texture that formed during solidification; defocused samples exhibit coarser grains that are elongated parallel to the original building direction while focused samples appear finer and more equiaxed. Segregation during solidification thus plays a role in determining the location of carbide formation and the final microstructure.

The fully heat-treated microstructures for the continuous scan strategy and wrought samples are presented in scanning electron micrographs in Figure 36. Three different magnifications are used to highlight different aspects of the microstructure: 250x to show the general morphology of the grains and any preferential elongation, 1,000x to show the nature of the secondary precipitates that form at grain boundaries and within grains, and 50,000x to observe the γ'' and γ' strengthening phases. As shown in Table 9, the grain size of material made in the defocused condition for continuous scanning is roughly 85% larger than the focused condition. The microstructures of the island scanning strategy mimic this behavior to a lesser extent, with grain size increasing by 32% from focused to defocused; the continuous scanning strategy enhances the textural development and growth of elongated grains in the as-built condition, and this morphology is preserved through HIP and heat treatment.

Although the HIP process has eliminated original solidification features such as melt pool boundaries and dendrites, the texture of grain elongation in the build direction has been preserved. In comparison, the wrought material has a significantly smaller grain size, and is equiaxed. NbC particles, identified using EDS and TKD as previously discussed, of approximately 1 μm diameter are highlighted by orange arrows in each of the microstructures, Figure 36d and 36e. In the defocused condition, they appear as vertical stringers parallel to the BD, while in the focused conditions they have a more random distribution. This behavior is identical to that of the island scanning strategy. Many of the NbC particles are located on the grain boundaries, and some appear in grain interiors as well. The wrought microstructure contains much fewer NbC particles compared to the SLM microstructures, and as can be seen in Figure 36f the carbides are significantly larger than in the SLM samples.

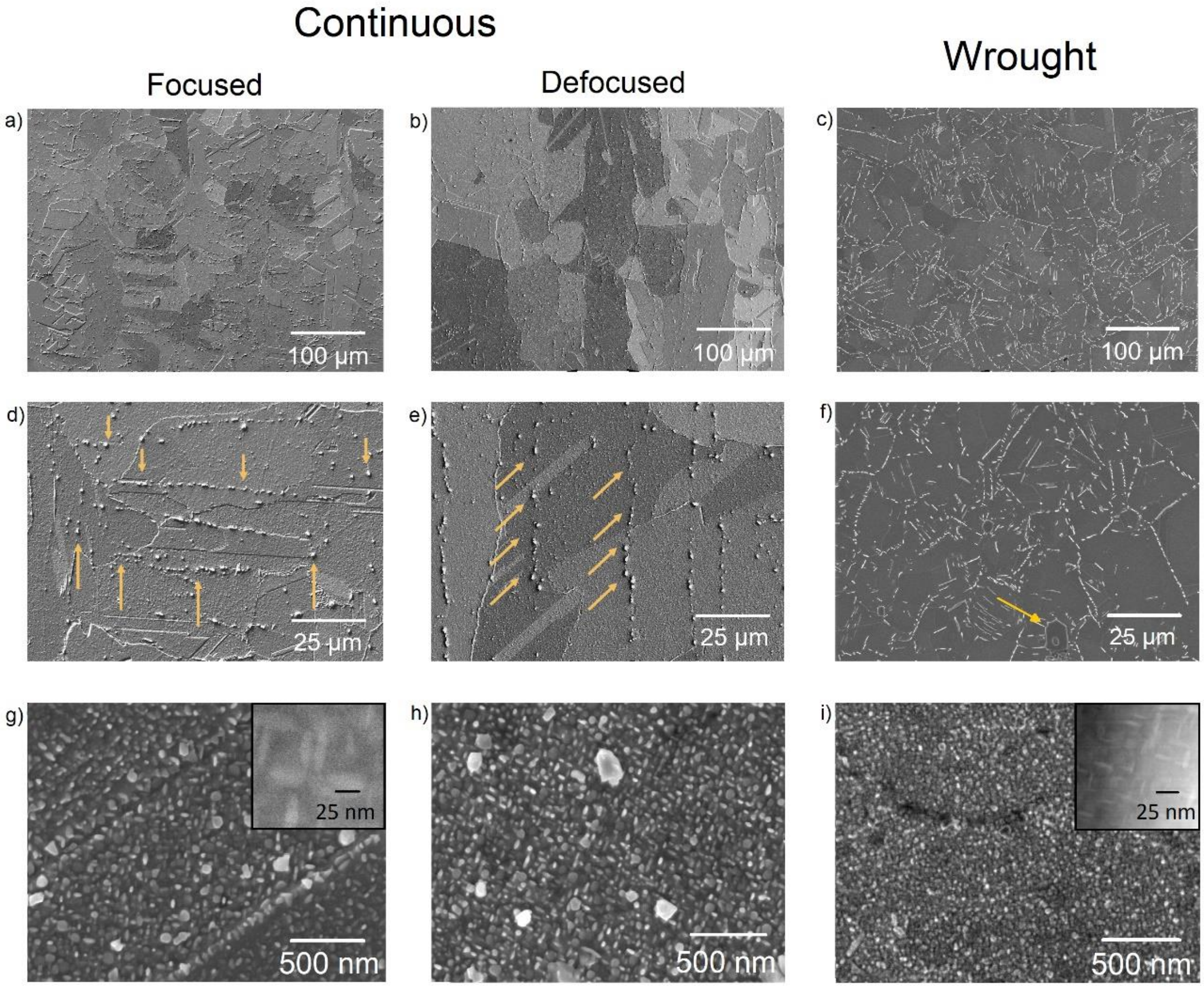

Figure 36: SEM images of samples in the focused continuous (a, d, g), continuous defocused (b, e, h), and wrought (c, f, i) conditions. Three different magnifications of 250x (top row), 1000x (middle row), and 50,000x (bottom row) are used to analyze microstructural scale, secondary particles, and strengthening phases, respectively. Orange arrows point to the secondary particles, NbC, which appear aligned according to the original solidification directions in SLM samples. TEM insets are shown in (g) and (i) to highlight the γ'' size difference.

The strengthening phases of IN718, γ'' and γ', take on ellipsoidal and spherical morphologies, respectively [102, 116]. Despite differences in grain morphology and size, the precipitation of these phases is similar in each SLM microstructure due to their identical post-processing histories. While grain morphologies, microstructural scale, and secondary particle alignment depend on the original as-built condition, the strengthening phases remain relatively unchanged. The wrought microstructure has an equiaxed morphology, with a dispersion of δ phase on the grain boundaries and few NbC particles throughout the matrix. The γ'' is smaller in the wrought samples compared to the SLM samples as seen in Figure 36g-36i, measuring 31 nm on average compared to 63 nm of the SLM sample. This difference is attributed to the thermomechanical processing steps used for wrought samples. The resulting microstructure is more homogeneous, which facilitates the formation of γ'' nucleation, resulting in finer precipitates. A poor distribution of Nb prior to aging can result in the formation of fewer and coarser precipitates. Measurements were made on TEM samples prepared from the focused continuous and wrought samples. One SLM sample was taken as a representative sample because of their identical post-processing thermal histories; the size, morphology, and distribution of the γ'' and γ' precipitates for SLM samples are similar.

For comparative purposes, the precipitates of the island focused condition have been compared to those of the wrought condition. Precipitate populations were quantified based on the previously shown SEM images of both structures. NbC particle measurements of SLM samples were performed on the as-HIP condition to avoid bias from inclusion of the δ phase, and δ phase analysis was performed on the heat-treated condition for both material types, subtracting out the previously calculated NbC content for a final δ phase approximation. The NbC population is stable below the initial HIP temperature and is not altered by the current heat treatment temperatures, so the as-HIP value is representative of the fully HT value [109, 151-153]. The δ phase accounts for roughly 0.9 ± 0.3% of the area in SLM samples and 9.2 ± 0.4% in wrought samples, which is approximately 0.02% and 1.05% volume fraction, respectively. NbC particles are observed to be quite small in the SLM condition relative to the wrought condition, with average diameters of 0.56 ± 0.1 μm and 4.7 ± 2.1 μm, respectively. A large standard deviation is noted for wrought NbC particles due to the wide range of particle sizes found in this material. NbC in SLM samples have a more consistent size range. The interparticle spacing of NbC for SLM is roughly 6.4 ± 0.9 μm, while for wrought samples it is 66.3 ± 6.8 μm; although they are larger they are much fewer and farther between. The overall area % of NbC is 1.4 ± 0.4% in SLM samples and 0.5 ± 0.2% for wrought samples, which correspond to a volume fraction of 0.12% and 0.02%, respectively. There is a much larger amount of Nb taken up in NbC for the SLM samples when compared to wrought, which accounts for the lack of δ phase that nucleates during solution treatment.

EBSD of the fully heat-treated continuous scanning strategy and wrought microstructures are presented in Figure 37. A table showing the max M.U.D. numbers for these samples as well as the island samples for comparison is shown in Table 10. The remaining crystallographic texture in samples built in the focused condition is faint, with a maximum MUD of 1.7; a small peak can be observed in the pole figure parallel to the original SD. In the defocused condition, the original texture can still be observed in the pole figure with a relatively strong peak aligned parallel to the SD, indicating that full recrystallization has not occurred. The wrought sample shows no evidence of crystallographic texture in the heat-treated condition with a M.U.D. of 1.3; a max M.U.D. value of 1.0 would theoretically represent a perfectly uniform distribution of poles in a polycrystal. Recrystallization that occurs during production contributes to the equiaxed morphology and lack of texture.

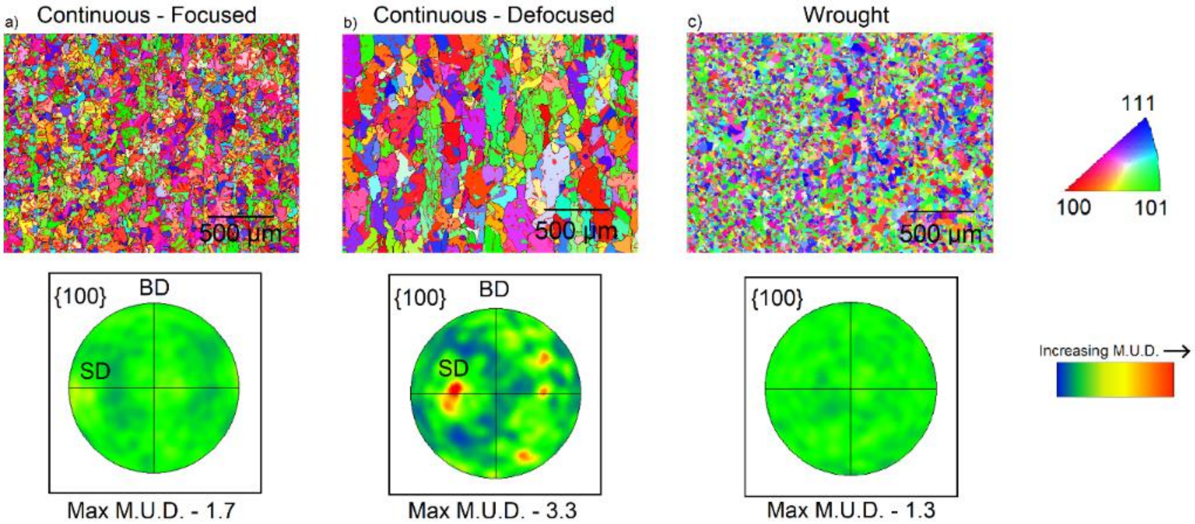

Figure 37: EBSD inverse pole figure maps and corresponding contoured pole figures for the fully heat-treated conditions. The focused condition (a) appears more equiaxed, with only a slight texture observed along the original SD. However, the defocused condition (b) retains a more obvious residual texture, and significant grain elongation. The wrought sample (c) is completely equiaxed, with no evidence of a preferred crystallographic orientation.

Table 10: Measured values of max M.U.D. numbers of samples after heat treatment.

Sample	**Max M.U.D. in Pole Figure**
Island - Focused	1.9
Island - Defocused	2.1
Continuous - Focused	1.7
Continuous - Defocused	3.3
Wrought	1.3

Large grains in the defocused condition contrast with finer grains in the focused condition; grain growth and a lack of complete recrystallization preserve the original morphologies and size disparity found in the as-built condition. Incomplete recrystallization is evident from the EBSD analysis of Figure 37, where crystallographic texture similar to the AB condition is still observed, albeit in a weakened state. Stored energy in the form of strain or residual stress in the as-built condition may not be sufficient to trigger full recrystallization, as suggested by Yan et al. [154], who did not observe full recrystallization after post-processing of SLM 316L. Instead, partial recrystallization coupled with grain growth maintains the elongated morphology, an effect observed by others in the literature [82, 83, 149, 154, 155]. The preservation of the original solidification structures indicates that the current HIP treatment is not sufficient to fully eliminate the as-built microstructure. Other studies that perform HIP treatments have also observed some preservation of the as-built structure under similar thermal conditions [82, 156].

3.3.2.4 Build Direction Dependence of the Microstructure

For comparative purposes to samples built in the Z-orientation, it is of interest to note that the microstructures of samples built in the X-orientation produce subtle changes in the fully heat-treated microstructure due to a difference in the thermal history during production. Microstructures are presented in Figure 38. It has been observed that samples built in the X- and Z-orientations have very similar structures in the AB condition and follow the patterns of scanning strategy and focal shift laid out previously in this chapter. The fully heat-treated condition shows similar grain sizes and grain morphologies in the X- and Z-orientation samples. These factors are still dominated by the laser focal shift. However, in the fully heat-treated conditions differences manifest in the form of the δ phase precipitation on the grain boundaries. Noticeably, the X-orientation samples contain more GB δ phase than their Z-orientation counterparts. Initial nucleation of the δ phase on GBs was noted previously in the as-HIP'ed condition, which was related to a slower cooldown from the HIP process, and a more effective homogenization of alloying elements due to less segregation that occurs during solidification with faster cooling rates.

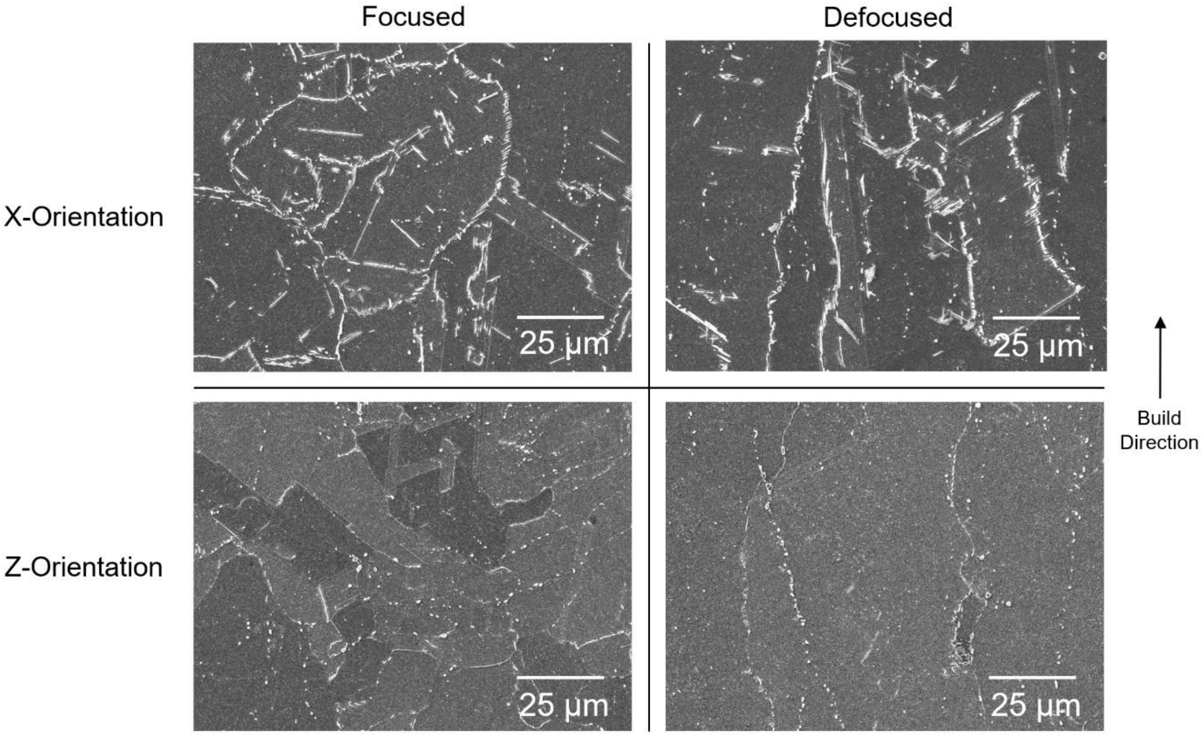

Figure 38: Build orientation dependence of the microstructures in the fully heat-treated condition. X-orientation samples have a higher δ phase population than the Z-orientation samples, but microstructural morphologies remain similar.

3.4 Summary

SLM IN718 was produced utilizing variations in the laser focal shift and scanning strategy. The focused condition resulted in fine microstructures that contained a higher number of equiaxed grains regardless of scanning strategy. The higher energy input at the focal plane resulted in a narrow and deep melt pools, which induced more rapid solidification. Furthermore, the steep sidewalls produced multi-directional solidification, facilitating grain nucleation and producing a microstructure with a weaker overall texture, both morphologically and crystallographically.

In the defocused condition the spot size is larger because the build plane has shifted away from the focal plane of the laser. As it diverges, the spot size grows larger. With a larger spot size, the energy density is decreased, and the shape of the melt pool changes from deep and narrow to shallow and wide. The change in melt pool morphology promotes more uniform solidification, resulting in continuous columnar grains that span multiple layers. These grains contain strong crystallographic and morphological textures aligned parallel to the build direction.

It was shown that a strong {100} texture forms along the scanning direction during solidification, indicating that the scanning strategy has a significant effect on overall microstructural texture. The island scans featured two different scan directions as a result of the alternating and bidirectional pattern. This multi-directional scanning resulted in a {100} peak along each scan direction, and an overall {100} texture parallel to the build direction. This effect was seen in both focal shift conditions, although it was enhanced in the defocused condition because of the increased continuity across layers. The continuous scanning strategy—featuring a single scan direction—exhibited a similar texture to that of the island strategy in the focused condition, but a single dominant {100} texture parallel to the scan direction in the defocused condition. This difference arises from the continuity across layers in the defocused condition. With no offsetting orthogonal scans, the strong {100} texture developed only along the scanning direction rather than the build direction. The end result was a strong {110} texture parallel to the BD.

Elemental segregation, primarily of Nb, was observed in all samples in the interdendritic region. Segregation occurred parallel to the dendritic growth during solidification; in focused samples, areas of Nb enrichment were more random due to the multi-directional solidification while for the defocused conditions stringers of high solute concentration ran parallel to the build direction. These areas promoted the formation of NbC during high-temperature exposure during HIP post-processing. The resulting post-processed structures contained significant amounts of NbC throughout the microstructure in arrays that reflected initial solidification conditions. The focused samples, with more multi-directional heat flow and short unaligned dendrites had a more random pattern of Nb when compared to the defocused condition. The long columnar dendrites of the defocused condition promoted the formation of aligned stringers of NbC parallel to the BD.

After HIP samples received a typical solution and double aging treatment to precipitate the strengthening phases of IN718. These microstructures were observed to still contain some remnant structures from the as-built condition: crystallographic texture, grain elongation, and ordered arrays of precipitates. In both scanning strategies, the defocused condition produced coarser, and more columnar grains aligned to the build direction. The continuous scanning strategy was shown to effectively enhance this texture in the defocused through the alignment of scan vectors, producing the coarsest grains with the highest aspect ratio. Process parameters can be used to enhance specific characteristics of the microstructure based on local heat flow orientations.

A comparison of SLM and wrought microstructures revealed large differences between the two processing techniques. Typical wrought material does not contain crystallographic or morphological textures, as it was found to be equiaxed, fine-grained, and non-textured. Furthermore, the precipitation behavior was different when considering the δ phase, γ'', and NbC distributions. The wrought samples had a significantly larger population of the δ phase that had precipitated on grain boundaries, as well as a low population of NbC that was spread out throughout the microstructure. The primary strengthening phase in wrought material, γ'', was also measured to be about50% smaller than the SLM material, which can have a significant effect on the overall strength. We will observe how these microstructural differences manifest in the mechanical behavior in the following chapter.

The process parameters have been shown to have a significant effect on the microstructural scale, crystallographic texture, and precipitate formation in SLM material. Each of these aspects of the microstructure can play a significant role in the determination of the final mechanical behavior. In order to characterize these differences, and how they compare to wrought material, mechanical properties will be evaluated for all the aforementioned microstructures across various time and temperature scales.

Chapter 4: Mechanical Properties

4.1 Introduction

The SLM process may introduce defects like porosity and inhomogeneous distributions of alloying elements that can have deleterious effects on final mechanical properties [157]. Much of the current literature on the mechanical behavior of SLM IN718 investigated material that retained as-built microstructural features such as solidification dendrites [61, 86, 158], elemental segregation [38, 158], and preferred orientation [61, 83]. IN718 must be heat-treated to obtain optimal properties, and materials retaining the aforementioned features is not likely to prove acceptable for high-reliability and high-temperature applications. The elevated temperatures used in HIP can dissolve undesirable phases, such as the Laves phase, promote the redistribution of alloying elements [144, 145], and eliminate original solidification structures, leading to a more equiaxed and recrystallized γ phase. For example, Kuo et al. [158, 159] tested samples that did not undergo HIP prior to standard heat treatment and observed an accumulation of the δ phase precipitating in interdendritic regions due to Nb segregation during solidification. The alignment of those precipitates led to premature failure and poor elongation in creep. While the literature is quite extensive into studies of the as-built and post-processed microstructures, there is still room for exploration into the detailed mechanical properties of this SLM alloy.

The room temperature tensile (RTT) properties of SLM IN718 are often presented alongside microstructural data. It has been found that the behavior is quite like that of conventionally processed wrought material when both are given identical heat treatments [54, 84]. Testing without heat treatment in the as-built (AB) or as-hot-isostatically-pressed (HIP) condition yields poor strength values due to the absence of the primary strengthening phases, γ’ and γ” [9, 22]. Other studies have shown slight variations in the RTT properties based on build orientation [58, 85]. Despite numerous accounts of SLM RTT properties being similar to traditional wrought material, the elevated temperature response has not been as thoroughly characterized. IN718 was originally designed for a high degree of strength retention at elevated temperatures [95, 115], so characterization of mechanical behavior of the SLM version at potential usage environments requires more attention than it has received to date.

Creep is a common test performed at elevated temperature for alloys that are used in high-temperature applications, but a thorough evaluation of these properties as they relate to the fully heat-treated SLM microstructure has not yet been performed. Shassere et al. [82] demonstrated that in electron beam melted (EBM) IN718 creep properties are directly affected by grain orientation and morphology. Based on fundamental processing differences such as spot size, chamber temperature, and scanning pattern, empirical EBM results cannot be extrapolated for SLM behavior. Studies that analyzed SLM IN718 do not always utilize a homogenization/HIP treatment [86, 148, 158, 160, 161], and much of the work that has been done on thermally post-processed SLM IN718 focuses on compressive creep behavior [160, 162], which may not provide a full view of the limitations of this material produced through AM. At the same time, other evidence has emerged that even after HIP and standard solution treatment and aging, there are differences in notch sensitivity between the SLM and wrought versions of the alloy that are more pronounced at elevated temperature and time-dependent deformation conditions [71]. This suggests that creep of SLM IN718 may also be different than wrought material.

Combination stress rupture testing of SLM IN718 has only been reported once in the literature by Witkin et al. [71], despite being one of the primary mechanical property metrics used in AMS 5663. He noted a severe lack of notch ductility in SLM processed IN718 when tested as combination stress rupture (CSR) test bars at 650 °C. Where wrought samples could pass an acceptance test that required 23 hours of sustained load on the notched section of 690 MPa with a minimum of 4% smooth section elongation, SLM samples always exhibited brittle notch failures with no elongation, often at less than 23 hours. The sensitivity is attributed to the triaxial state of stress and lack of grain boundary compliance due to limited δ phase precipitation. The multi-axial state of stress can induce large stresses on unfavorably oriented grains and result in cavity nucleation [163]. Cavities near the notch root produce a more intense stress concentration which can lead to premature failure.

Current literature on elevated temperature tensile (ETT) properties reports strength and elongation values taken from tests at strain rates on the order of 10^{-3} s^{-1} [54, 164]. Other studies have either not reported the strain rate of testing [70] or focused their results only on metrics of strength in lieu of reporting ductility values [165]. The results of Gao et al. [70] do not offer a comparison of wrought material tested in parallel with their samples, but instead only present the AMS 5663 minimum acceptance criteria as representative wrought properties. Furthermore, samples did not receive a HIP treatment. Caiazzo et al. [165] also does not offer a comparison to wrought material, or a thorough evaluation of their results at elevated temperature.

In this chapter, a comprehensive overview of mechanical properties across a range of test temperatures, strain rates, and sample geometries will be presented. Microstructures will be first correlated to room temperature tensile, creep rupture, and combination stress rupture properties. The effects of variable grain size, grain morphology, and precipitate distribution will be discussed as they relate to the process parameter variation of Chapter 3. Second, the elevated temperature behavior of SLM IN718 will be further analyzed through a series of tests across multiple strain rates and test temperatures. Wrought material will be tested in parallel for all tests to offer comparison points between the two manufacturing methods. Differences between the two manufacturing processes appear in the elevated temperature and slow strain rate regime; identifying these differences and explaining them will follow the discussion of process parameter induced variation. All mechanical properties reported in the current chapter will be on material that has undergone a homogenization + HIP treatment, as well as full heat treatment that includes both solutioning and aging steps. The combination of microstructural manipulation, full heat treatment, and elevated temperature testing has not been presented before, and results show that unique microstructural aspects of the SLM alloy lead to significant differences in behavior in comparison to wrought material. These results provide a more complete view of the process-structure-property relationships that exist when fabricating IN718 using SLM.

4.2 **Experimental**

4.2.1 Materials

The materials studied for mechanical testing were produced under the same conditions and with the same raw material as those of Chapter 3. Many samples were built as vertical cylinders, while others were made as horizontal cylinders for the characterization of build anisotropy as it pertains to microstructural anisotropy.

All samples received the HIP treatment discussed in Chapter 2 prior to heat treatment in order to close porosity and recrystallize the microstructure. Most samples also received the same HT1 in accordance with AMS 5663 [98], but some samples were also given HT2 in accordance with AMS 5664 [121]. This provided a comparison of samples with and without δ phase in the microstructure.

4.2.2 Mechanical Testing

4.2.2.1 Room Temperature Tensile Testing (RTT)

Cylinders were machined after heat treatment to the geometries specified in ASTM E8 [166]; the specified gauge diameter was 6.35 mm, with an accompanying gauge length of 31.75 mm as shown in Figure 39a. For simplicity, all sample geometries can be found in Figure 39 following the description of each test method. RTT properties were tested in accordance with ASTM E8 at a strain rate of 0.015 mm/mm/min ($2.5 \cdot 10^{-4}$ sec^{-1}) on an Instron Model 5989 coupled with Bluehill 3 software [166]. An Epsilon Model 3542-0100-100-LHT extensometer was used to monitor the strain as it developed throughout the test.

4.2.2.2 Creep Rupture Testing (CRT)

CRT was carried out at 650 °C and 690 MPa until rupture, in accordance with ASTM E139 [167]. These parameters were selected based on the typical testing parameters in AMS 5663 [98]. Furthermore, the loading condition corresponds to 80% of the typical σ_{yield} expected for IN718 at 650 °C. The temperature condition is approximately $0.46T_m$. Type-K thermocouples were used to monitor the temperature, and ATS 2320 creep frames paired with Starret 463 extensometers were used for creep testing. Three samples in each SLM condition and two samples in the wrought condition were tested in RTT and CRT.

4.2.2.3 Elevated Temperature Tensile Testing (ETT)

Dogbones were tested at an elevated temperature in accordance with ASTM E21 [168]. Two samples were tested for each condition in this study. Tests were conducted on an Instron Model 5989 universal testing machine within a SF-16-2230 type clamshell furnace. An Epsilon 3448-0100-050 axial furnace extensometer was used to monitor strain during testing. The crosshead displacement rate was set at 1.59, 0.159, or 0.00159 mm/min to achieve strain rates of

$8.33 \cdot 10^{-4}$, $8.33 \cdot 10^{-5}$, or $8.33 \cdot 10^{-7}$ mm/mm/s, respectively. These rates will be referred to as 10^{-3}, 10^{-4} and 10^{-6} s^{-1} for the remainder of the chapter. For these tests the temperature was a constant 650 °C, verified by a Type K thermocouple in direct contact with the specimen. A second set of tests was conducted at a strain rate of 10^{-4} s^{-1} while test temperature was varied between 550 °C, 650 °C, and 750 °C. For all tests, the samples were equilibrated at the test temperature for 30 minutes prior to testing.

4.2.2.4 Combination Stress Rupture Testing (CSR)

Similar to CRT, CSR testing was performed at 650 °C and an initial load of 690 MPa. This testing was conducted in accordance with ASTM E292 [169] and AMS 5663 [98]. As such, after 23 hours of load there was an upload every 8 hours of 34.5 MPa until sample failure. The temperature remained constant throughout the test, monitored with a Type K thermocouple.

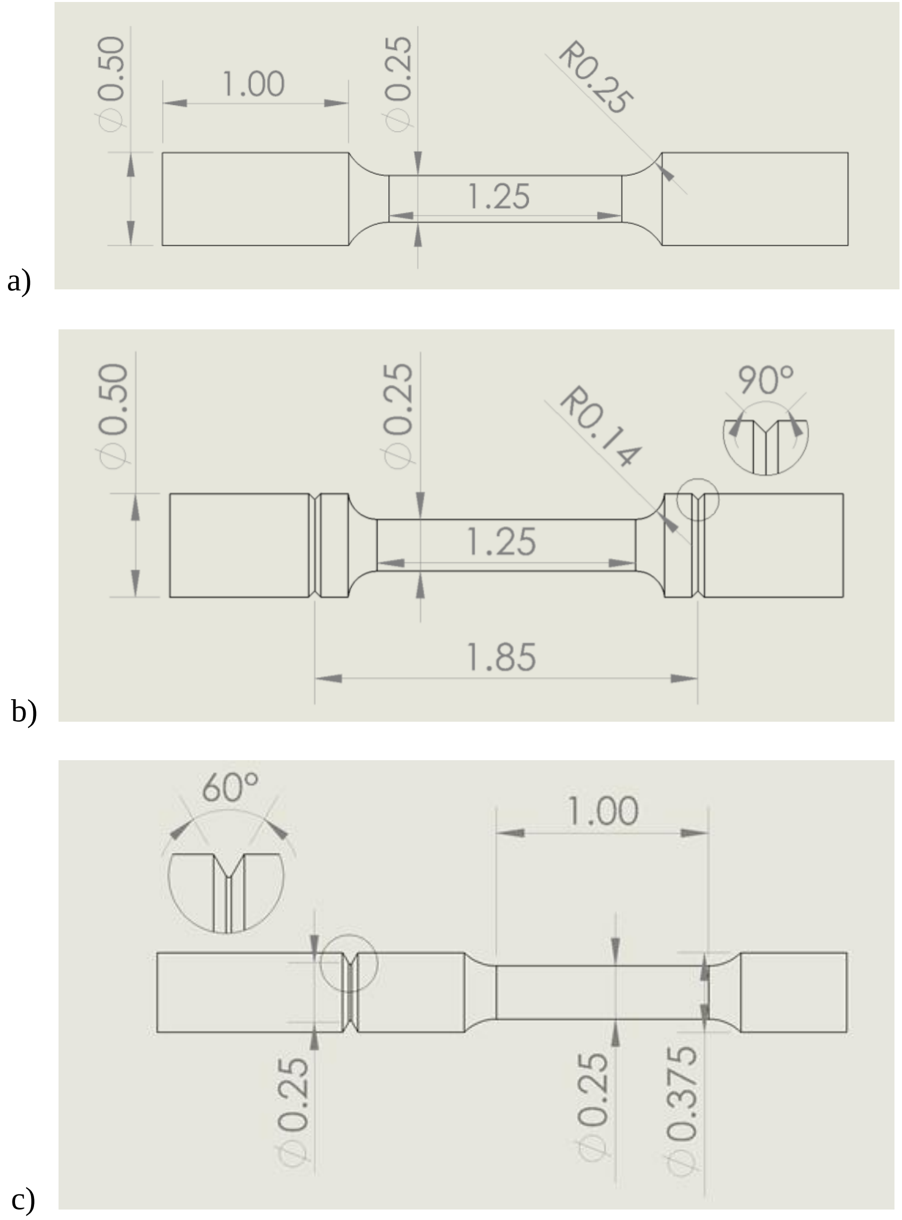

Figure 39: a) Smooth gauge dogbones used for both room and elevated temperature tensile testing. b) Smooth gauge dogbone with notches cut in the grip sections for holding an extensometer during creep rupture testing. c) Combination smooth-and-notched specimen used for combination stress rupture testing.

4.2.3 Characterization

Microstructural characterization was carried out with the same equipment used in Chapter 3; utilization of a variety of techniques—SEM, EBSD, EDS—were found to be essential for the thorough characterization of the microstructures before and after mechanical testing. In addition to electron microscopy, macro-scale images were taken using a Nikon D610 body paired with a AF-S Micro Nikkor 105 mm lens. This allowed for high-resolution color imaging of the entire fracture surface.

4.3 Results and Discussion

4.3.1 Room Temperature Tensile (RTT)

Figure 40 shows the stress-strain curves for both focal conditions and scanning strategies discussed here, and Table 11 presents mean values of the yield strength, ultimate tensile strength, modulus, and elongation as well as the minimum acceptance criteria specified in AMS 5663 [98]. The samples shown exceed the AMS standard minimum values and display comparable properties to those reported in the literature for similarly processed material, such as those of Popovich et al. [54], whose yield strengths and ultimate strengths of SLM 718 were in the range of 1065 – 1145 MPa and 1272 – 1376 MPa, respectively. Other reported values for material that received at least double age heat-treatment similar to the one used in the present study cover a similar range, from 1046 – 1084 MPa yield strength and 1320 – 1371 MPa UTS [35, 39, 70]. Ductility metrics for SLM and wrought material are also quite similar, with no significant variation being observed in either elongation or reduction of area. Although the reduction of area metric is not often reported in the literature, many studies include measured elongations in the range of 10 – 19 % [35, 39, 70].

Overall, the RTT results do not show a high degree of separation between material properties, despite the large differences in the microstructure induced by SLM process parameters. The most significant variation of RTT properties observed is a 13% higher yield strength for wrought material compared to SLM. The ductilities are similar across all material conditions.

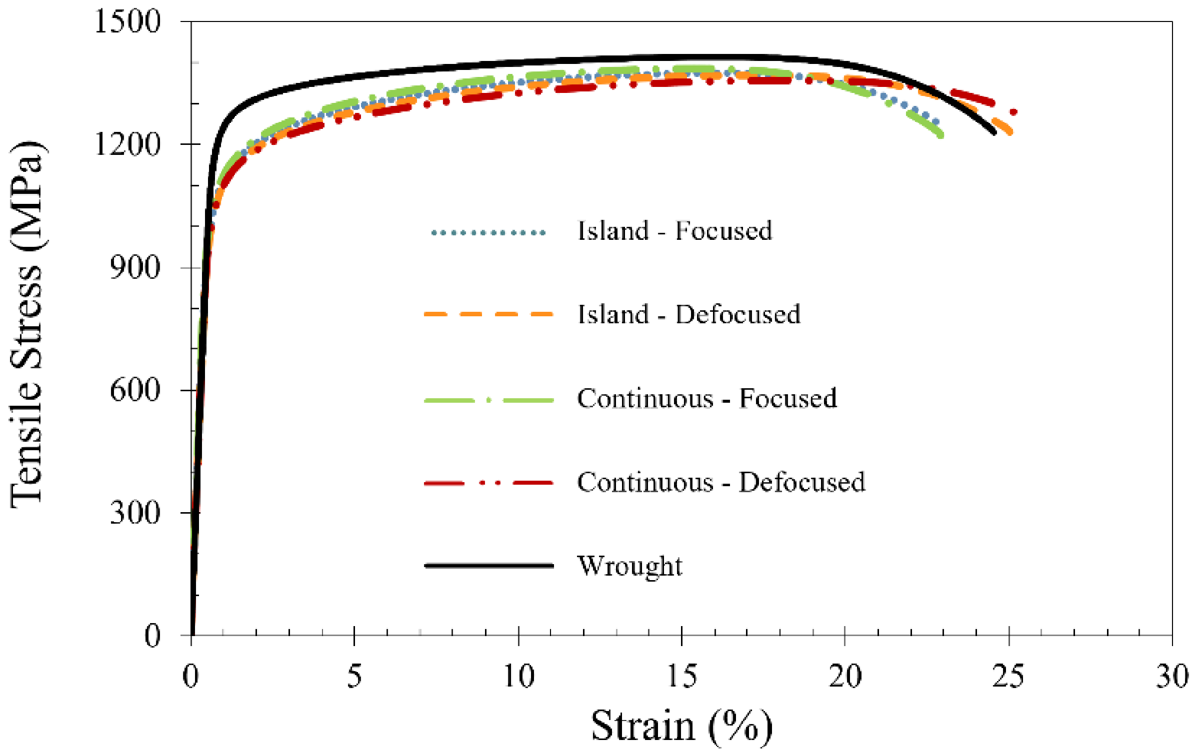

Figure 40: Stress-strain curves for RTT showing the SLM and wrought samples. The SLM samples all exhibit similar RTT behavior, while the wrought material has a distinct increase in yield strength.

Table 11: Room-temperature tensile properties of samples built in the Z-orientation using variable process parameters.

Sample	**Yield Strength**	**Ultimate Tensile Strength**	**Elastic Modulus**	**Elongation**
	MPa	**MPa**	**GPa**	**%**
Island – Focused	1042.7 ± 5.1	1373.8 ± 2.5	207.5 ± 2.1	22.6 ± 1.3
Island – Defocused	1037.4± 1.4	1364.9 ± 11.1	195.1 ± 2.8	23.5 ± 2.2
Continuous – Focused	1056.2 ± 0.4	1385.1 ± 3.3	210.3 ± 9.0	23.2 ± 0.4
Continuous – Defocused	1035.6 ± 0.4	1357.6 ± 3.3	202.7 ± 4.8	25.3 ± 0.6
Wrought	1194.9 ± 10.7	1424.6 ± 15.1	208.9 ± 2.8	25.5 ± 2.0
AMS 5663 Min. Req. [98]	1034	1276	-	12

The difference in yield strength between wrought and SLM samples is attributed to the variation in the γ'' size observed in the microstructure. IN718 derives its strength from the γ'' and γ' phases, which are the main products of the double aging treatment. The dominant deformation mechanism is co-planar slip, which is resisted by the need for dislocations to pass through the strengthening phases [101, 116, 170]. This mechanism depends on the size of these particles, which varies based on the heat treatment temperature and duration [171]. Considering the wrought samples, the higher yield strength is attributed to a smaller γ'' precipitate size. Sundararaman et al. [101] saw a similar drop in yield strength (~12.5%) when comparing IN718 samples of 24 nm and 56 nm. Larger particles facilitate particle bypassing via climb rather than shearing and can lead to lower strengths [172]. Furthermore, the high population of NbC in the SLM samples can starve the matrix of Nb, a critical component of γ''. With reduced Nb available for precipitation, the γ'' population is reduced, further weakening the material.

The Hall-Petch relationship does not appear to have a significant role in these samples, despite the wrought samples finer grain size. Typically, microstructures with finer grains would have a higher yield strength as a result of grain boundaries presenting obstacles for dislocation movement. However, if the Hall-Petch relationship existed for the current samples, it would be expected that both focused conditions would also display an increase in strength over the defocused samples due to the finer microstructure. Because there is not a significant improvement in the yield strength, the effect of grain size is negligible for room temperature tensile testing.

Samples built in the XY-plane were tested to determine how the mechanical properties may be influenced by highly anisotropic SLM microstructures. Stress-strain curves of the horizontal samples compared to vertical samples are shown in Figure 41, with metrics in Table 12. The X-orientation samples have a slight increase in yield strength, at the cost of ductility. The increases in yield strength comparing vertical to horizontal samples are 6.5% and 8.3% for focused and defocused conditions, respectively. Decreases in elongation for the same comparison are 34.1% and 29.6%, respectively. Furthermore, the variation in measured elongation values for horizontal samples is high, indicating a high degree of variability.

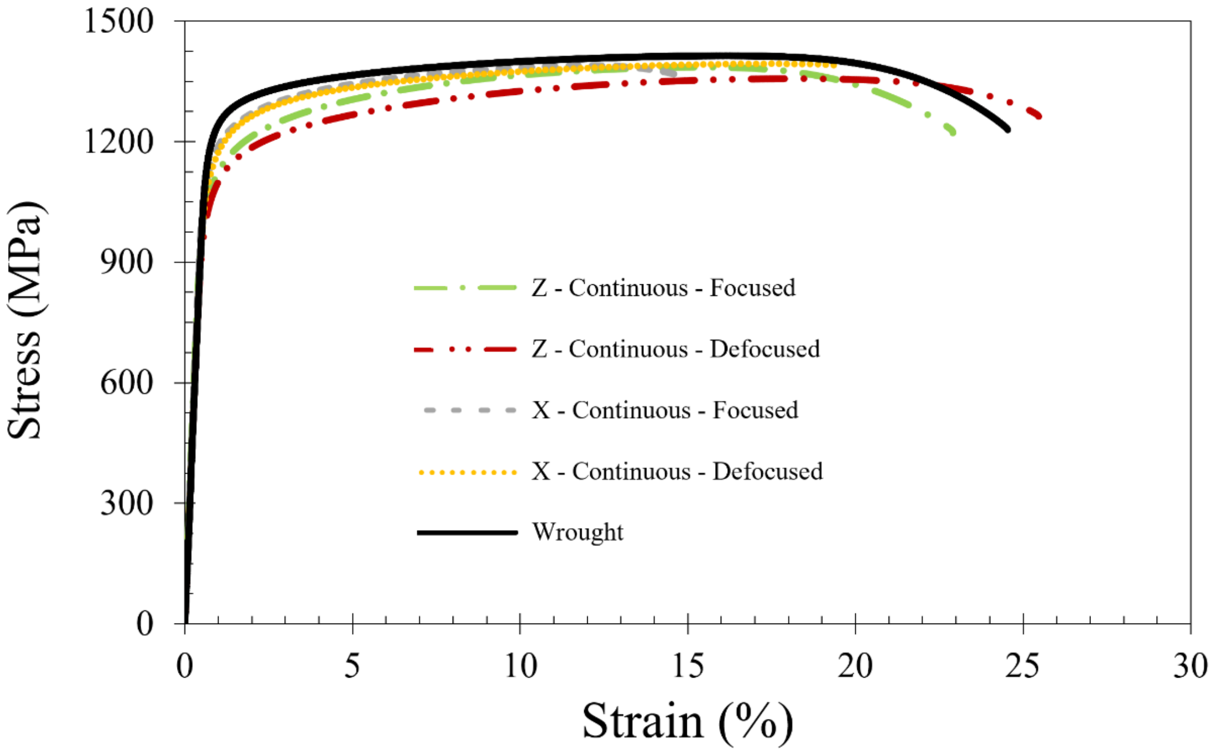

Figure 41: Stress-strain curves for RTT showing the SLM and wrought samples. The SLM samples all exhibit similar RTT behavior, while the wrought material has a distinct increase in yield strength.

Table 12: Room-temperature tensile properties of samples built in the X-orientation using variable laser focus shift.

Sample	Yield Strength	Ultimate Tensile Strength	Elastic Modulus	Elongation
	MPa	MPa	GPa	%
X - Continuous – Focused	1125.3 ± 35.2	1404.5 ± 3.5	210.3 ± 4.8	15.3 ± 3.7
X - Continuous – Defocused	1121.1 ± 4.8	1398.3 ± 0.7	207.5 ± 2.1	17.8 ± 3.5
Z - Continuous – Focused	1056.2 ± 0.4	1385.1 ± 3.3	210.3 ± 9.0	23.2 ± 0.4
Z - Continuous – Defocused	1035.6 ± 0.4	1357.6 ± 3.3	202.7 ± 4.8	25.3 ± 0.6
Wrought	1194.9 ± 10.7	1424.6 ± 15.1	208.9 ± 2.8	25.5 ± 2.0
AMS 5663 Min. Req. [98]	1034	1276	-	12

Small differences in the strength may be linked to improved precipitation of the γ'' phase as a result of a faster heat flow during building. Horizontal samples that are built near the build plate have a shorter overall heat conduction path directly into the large thermal mass of the build plate, meaning that they will have faster overall cooling rates and a better distribution of alloying elements. Gallmeyer et al. [84] found similar results when comparing samples that were printed near the build plate when compared to ones built in the Z-direction. Differences emerge in these samples due to the variation in heat flow experienced during building. Others have also noted a variation in the microstructure as a function of distance from the build plate [7, 8]. Wang et al. [8] noted finer microstructures near the build plate as well as increased hardness closer to the build plate.

4.3.2 Creep Rupture Testing (CRT)

Table 13 gives mean values for the time to rupture, elongation, and minimum creep rate (MCR) while Figure 42 shows the plot of creep strain vs. time for a representative sample from each condition. Figure 42a shows the full-scale creep curves, while Figure 42b highlights the 0 – 5% creep strain range for a better visual of the separation of properties in SLM samples. Minimum creep rate was calculated based on the minimum slope of the curve prior to reaching Stage III creep, which occurred after approximately 20 hours for all conditions. Creep rupture testing (CRT) shows more separation of properties between samples in RTT indicating a higher sensitivity to the microstructural changes induced by process parameter alterations and manufacturing process variation.

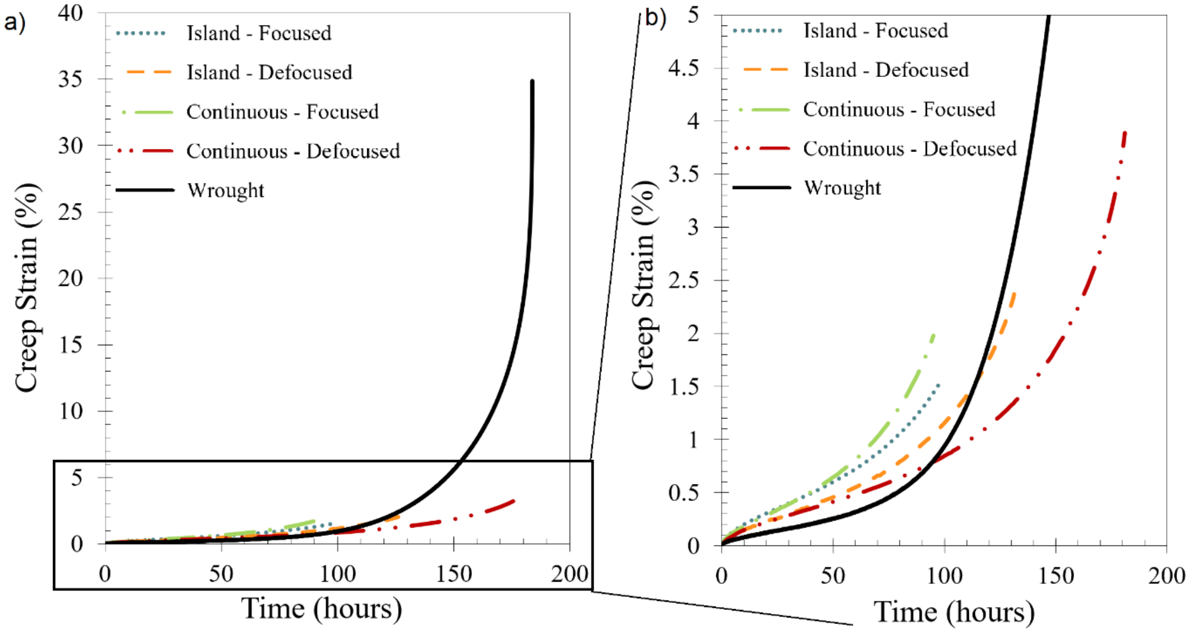

Figure 42: a) Creep curves of all samples together highlight the dramatic difference in the creep behavior of wrought samples when compared to SLM samples. b) Inset up to 5% creep strain demonstrates the separation of properties between SLM samples made with various microstructural morphologies.

Table 13: CRT results at 650 °C and 690 MPa for samples built in the Z-orientation and varying parameters.

Sample	Time to Rupture	Elongation	Minimum Creep Rate
	hours	%	hr^{-1}
Island - Focused	114.2 ± 17.0	5.0 ± 1.7	$3.8\cdot10^{-5} \pm 3.2\cdot10^{-5}$
Island - Defocused	132.3± 7.5	6.7 ± 2.1	$4.9\cdot10^{-5} \pm 3.6\cdot10^{-5}$
Continuous - Focused	109.3 ± 19.9	5.5 ± 1.6	$8.0\cdot10^{-5} \pm 1.8\cdot10^{-5}$
Continuous - Defocused	161.3 ± 17.2	8.3 ± 1.5	$6.3\cdot10^{-5} \pm 1.4\cdot10^{-5}$
Wrought	184.5 ± 0.7	37.2 ± 3.2	$1.0\cdot10^{-5} \pm 1.6\cdot10^{-6}$
AMS 5663 Min. Req. [98]	24	4	-

For both scanning strategies, a transition from the focused to the defocused condition results in better time to rupture, higher elongation, and a slower minimum creep rate. The SLM sample with the longest time to rupture and the highest elongation is that of the continuous defocused condition, which corresponds to the coarsest and most elongated microstructure parallel to the loading axis. Utilizing the continuous scanning strategy in conjunction with the defocused laser exaggerates the elongated texture observed in the island scan strategy, improving creep behavior.

The tertiary regime for the focused samples is much shorter than that of the defocused condition, and both are significantly shorter than the wrought condition. This suggests that although the same mechanisms are active for all SLM processing conditions, a more favorable orientation of grain boundaries provides increased creep resistance in the defocused condition. The wrought condition has a much higher overall damage tolerance than SLM samples, based on the large tertiary creep portion, whereas the SLM samples fail relatively prematurely.

Sample that were built in the horizontal direction were tested and compared to those of the vertical orientation. Variations in the laser focal shift and scanning strategy were employed in order to provide a comparison in the presence of highly anisotropic structures. The creep curves of these conditions, compared to vertical SLM and wrought material, can be seen in Figure 43, with tabulated values in Table 14. The creep properties of the X-orientation built samples are shown to be comparable to Z-orientation in rupture life, but far inferior in ductility.

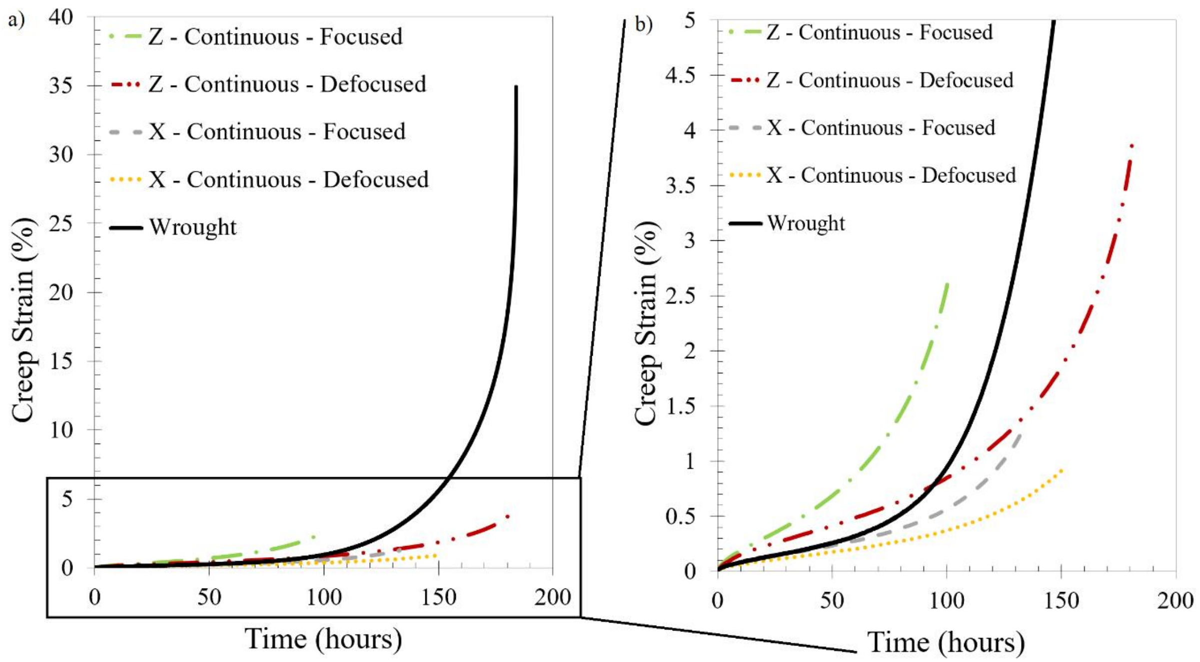

Figure 43: a) Creep curves of all samples together highlight the dramatic difference in the creep behavior of wrought samples when compared to SLM samples. b) Inset up to 5% creep strain demonstrates the separation of properties between SLM samples made with various microstructural morphologies.

Table 14: CRT results at 650 °C and 690 MPa for samples built in the X-orientation and varying laser focus shift.

Sample	**Time to Rupture**	**Elongation**	**Minimum Creep Rate**
	hours	**%**	**hr^{-1}**
X - Continuous – Focused	134.7 ± 3.8	3.0 ± 0.7	$2.4\cdot10^{-5} \pm 4.2\cdot10^{-6}$
X - Continuous – Defocused	150.0 ± 0	2.2 ± 0.3	$1.5\cdot10^{-5} \pm 5.7\cdot10^{-6}$
Z - Continuous – Focused	109.3 ± 19.9	5.5 ± 1.6	$8.0\cdot10^{-5} \pm 1.8\cdot10^{-5}$
Z - Continuous – Defocused	161.3 ± 17.2	8.3 ± 1.5	$6.3\cdot10^{-5} \pm 1.4\cdot10^{-5}$
Wrought	184.5 ± 0.7	37.2 ± 3.2	$1.0\cdot10^{-5} \pm 1.6\cdot10^{-6}$
AMS 5663 Min. Req. [98]	24	4	-

The X-orientation defocused sample has the lowest elongation, at 2.2%, 73% lower than its Z-oriented counterpart. The elongated texture parallel to the building direction creates a highly anisotropic structure, increasing ductility parallel to the grains at the cost of ductility in the transverse orientation. A smaller drop off is observed for the X-orientation focused sample but remains significant at 40%. Looking at the microstructures of the two defocused conditions side-by-side with the build direction and loading direction noted provides an idea of how the reorientation may affect properties. The long vertical stringers of carbides and the columnar grains observed previously exist in both cases, but their orientation relative to the load has changed. The grain boundary orientation transverse to the load provides an easy path for crack propagation. The stress buildup on these unfavorably oriented grains will result in cracking. This result is similar to that of Shassere et al. [82], who found that horizontally built samples were inferior to vertically built samples when paired with a columnar microstructure.

When compared to wrought material, the SLM samples in both orientations are significantly less ductile, have a lower time to failure, and vertical samples exhibit faster minimum creep rates. The wrought sample has a 348% increase in elongation over the defocused continuous sample as well as an order of magnitude decrease in the minimum creep rate. The standard deviation in time to rupture for the wrought samples is also noticeably smaller than those of SLM. These results indicate that there are significant differences in the creep behavior of samples produced by each manufacturing method.

Samples were sectioned after CRT to observe the microstructures after exposure to both elevated temperature and mechanical load (Figure 44). Only the continuous scanning strategy samples are presented here in comparison to the wrought structure. Figure 44a-44f highlight the microstructural morphologies, while Figure 44g-44i are the accompanying pole figures to show crystallographic texture. Evidence of dislocation motion is present in all samples in the form of planar slip bands (PSB) that can be seen in Figures 44d-44f. This is an indicator of an active dislocation creep mechanism for the current samples. An applied load of 690 MPa at 650° C is within the range of parameters outlined by others in the literature who have observed the dislocation creep mechanism in IN718 [82, 173-175]. Dislocation motion is initially resisted by the γ'' particles in all samples, and slower minimum creep rates through the secondary regime of the creep curve in the wrought sample are supported by the smaller size of the γ'' precipitates [172]. Chaturvedi and Han [172, 174] found that IN718 with γ'' particles in the size range of the current wrought samples produce a larger back stress that opposes dislocation motion than those of the SLM size range. A second study by Chaturvedi and Han [176] outlines how an increase in back stress will lead to a lower minimum creep rate in IN718 samples. This phenomenon contributes to the decrease in MCR that is observed in the current creep tests. A correlation can also be drawn to the X-orientation samples, which have a higher yield stress in RTT. This higher stress is related to the γ'' particle size, which must be smaller in the X-orientation samples than those of the Z-orientation. This explains why the MCR of the X-orientation is also lower than that of the Z-orientation; it is a direct result of the higher strengths and smaller γ'' size. Other differences due to microstructural features begin to emerge in the SLM samples with further deformation.

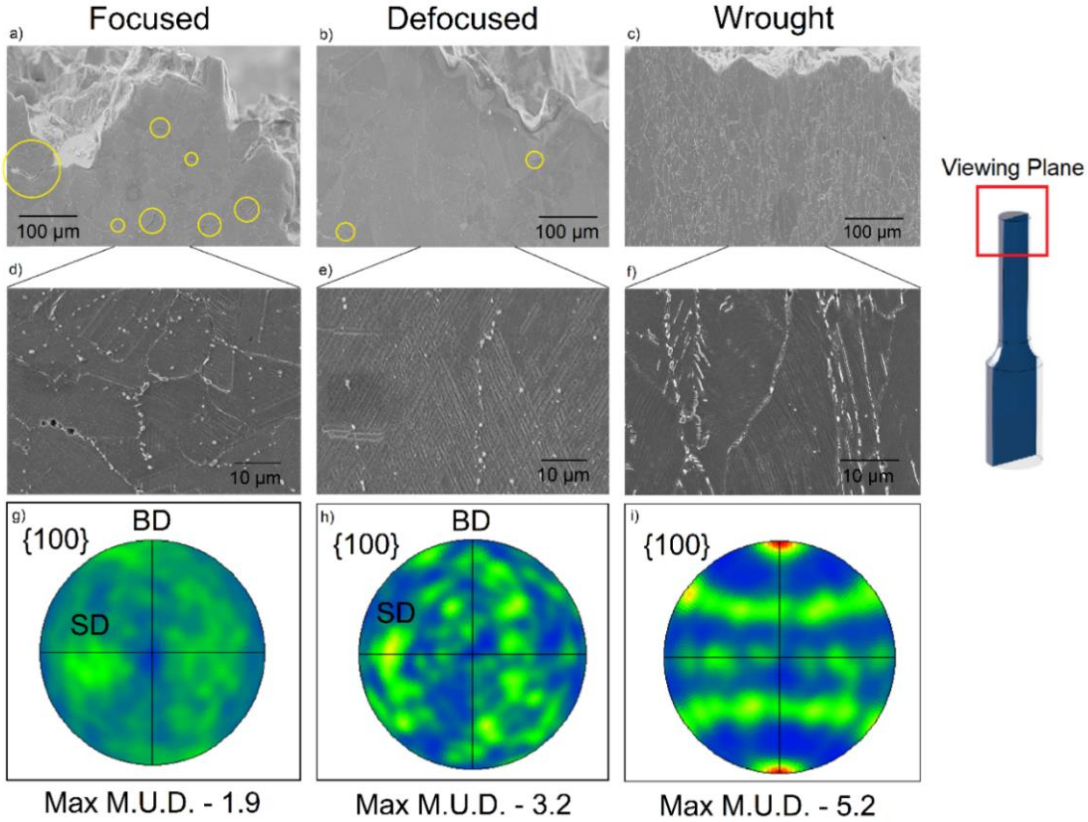

Figure 44: Sectioned creep fracture surfaces, with yellow circles highlighting cracks that have formed. The focused condition (a/d) has many horizontally oriented cracks, which form preferentially on transverse grain boundaries. The defocused condition (b/e) has relatively few cracks due to the limited number of unfavorably oriented grain boundaries. The wrought condition has significant amounts of grain boundary sliding evidenced by the highly elongated microstructure parallel to the load. Evidence of PSBs can be seen in (d), (e), and (f) within the grains due to dislocation movement during creep testing. Pole figures showing textural development during creep testing are seen for each condition in (g), (h), and (i).

Microcracks are observed on the sectioned surface for the SLM samples (highlighted by yellow circles) but are absent from the wrought condition. Most of these cracks form on grain boundaries oriented transverse to the loading direction; a redistribution of stresses that occurs during grain boundary sliding (GBS) can preferentially nucleate cavities on unfavorably oriented boundaries [163]. These voids can coalesce and form microcracks, which are points of weakness within the microstructure. Because SLM samples retain a similar elongated grain morphology as their original as-built condition, the focused condition contains a greater proportion of grain boundaries oriented transverse to the loading direction. The focused condition in both scanning strategies presents the highest number of such boundaries, and these coincide with the lowest creep ductilities. The defocused samples show a slight improvement in creep elongation and time to failure in comparison. The effect of grain boundaries oriented transverse to the load is highlighted by the comparison of X and Z-oriented samples. The continuous defocused condition provides a highly anisotropic structure, and when tested transverse to this elongation there was a ~70% decrease in the elongation. The elongated grain boundaries transverse to the load create large stresses that can easily nucleate cavities and propagate cracks. A similar result was found by Shassere et al. [82] when testing EBM IN718 at a lower stress level. They found that coarser, elongated grains oriented parallel to the loading direction improved time to rupture and elongation compared to finer grained structures.

The wrought samples did not exhibit intergranular voids coalescing into microcracks, but instead contain a high degree of grain rotation and deformation after testing. The aspect ratio in the post-creep condition increases from 0.9 to 1.9, and the M.U.D. from 1.3 to 5.2. The grain rotation observed for the wrought material is a result of the extreme plastic deformation the samples have undergone. It is a result of the FCC slip systems rotating into a more favorable orientation with respect to the tensile axis via dislocation movement.

The M.U.D. numbers and aspect ratios of the SLM samples remain unchanged, indicating a difference in the damage accumulation mechanisms. This behavior is evident through the differences in the tertiary regime of the creep tests as well as the post-test microstructures. Much of the elongation in the samples occurs in the tertiary portion of the curve, which varies widely in size as seen in Figure 42. The wrought samples experience significant amounts of GBS and rotation, but the SLM samples rupture without signs of this behavior. Although the wrought material contains an equiaxed microstructure, it is capable of high degrees of deformation. In comparison, more equiaxed microstructures in the SLM alloy were associated with lower strain to rupture, indicating that microstructural morphology is not the only important consideration in the current creep tests. While the grain boundary orientation may be a significant indicator of creep performance among AM material, other mechanisms may dominate when comparing across manufacturing techniques.

Fracture surfaces of the SLM samples show evidence of different levels of environmental influence compared to the wrought material, which shows a nearly uniform fracture surface. Figure 45 shows a distinctly oxidized area that coincides with an intergranular fracture surface. This oxidation pattern is a result of the slow opening of a crack, and the gradual exposure to the lab air environment forming an oxide layer of varying thickness. The wrought sample in Figure 45 has a more uniform transgranular dimpled pattern, indicative of a ductile failure mode. Environmental attack in the SLM samples is likely related to the dense population of NbC observed throughout the microstructure. A mechanism for increased resistance to intergranular oxygen attack in wrought samples is proposed by Hayes et al. [177] that involves the δ phase precipitated on grain boundaries. These needle-like phases protrude from the grain boundaries into the grain interiors. The mechanism suggests that diffusing oxygen becomes trapped at the incoherent δ-matrix interface which acts as a sink. Although the wrought samples do not contain ordered arrays of NbC, this mechanism may also contribute to the lack of oxidation in the wrought samples, further improving relative creep performance.

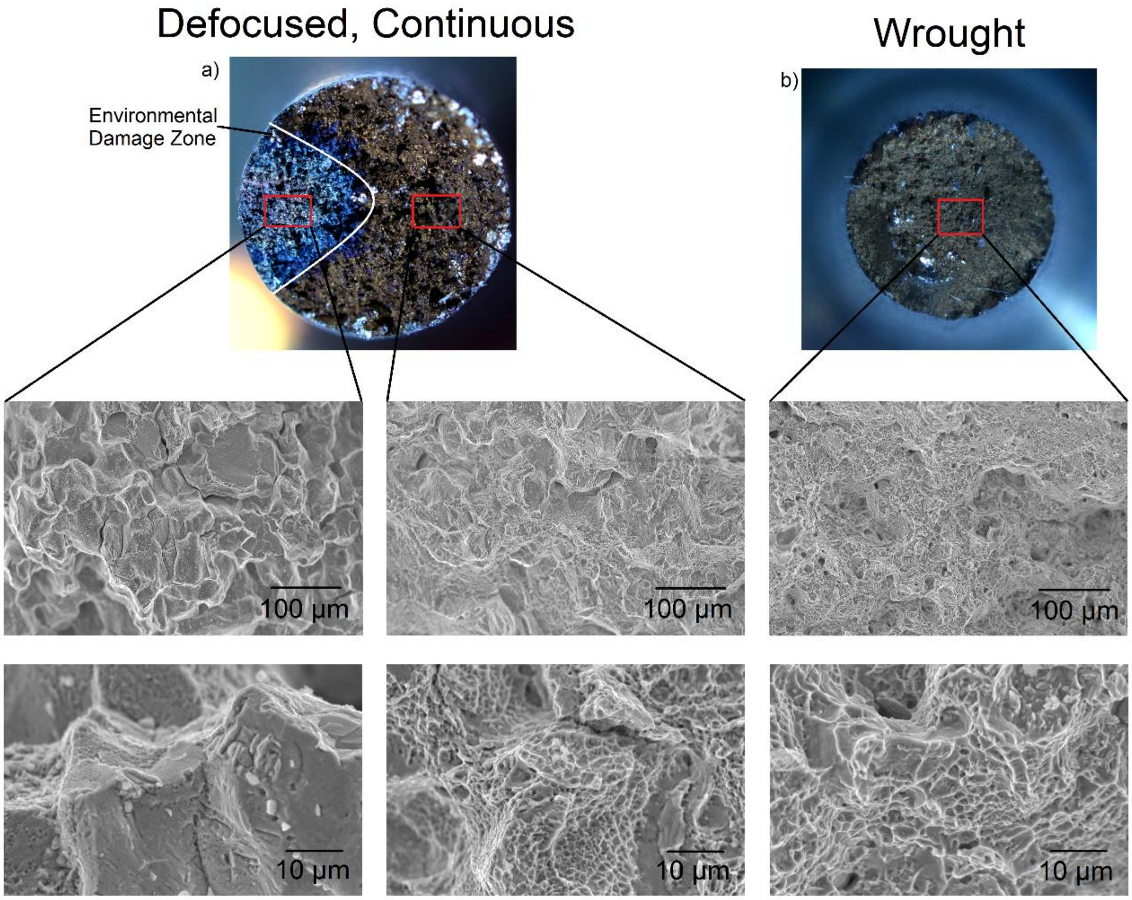

Figure 45: a) The defocused continuous fracture surface shows evidence of environmental attack. A distinct gradient oxide region comprised of intergranular failure, and a more uniformly oxidized region of transgranular failure. b) The wrought fracture surface is uniformly dimpled across the surface, evidence of a more ductile failure that is not sensitive to environmental attack.

The fracture surface in Figure 45 also contains many small white particles in the SLM samples, which have been confirmed via EDS to be rich in Nb and denuded in Ni, Fe, and Cr. These align well with the NbC that was previously identified in SLM materials. Gao et al. [178, 179] have shown that the formation and fracture of a brittle niobium oxide film can enhance crack growth in Inconel 718, and Sundararaman et al. [147] demonstrate that closely spaced NbC particles in wrought IN718 can lead to intergranular fracture similar to what is observed here. The effect of the original solidification conditions once again affects SLM material behavior. The arrays of NbC follow the initial dendritic growth patterns, determined by processing conditions. Samples elongated parallel to the build direction have NbC stringers aligned parallel to the load, and thus present a more tortuous path of crack propagation along these particles. The focused conditions present NbC in a path that is transverse to the load, leading to premature failure and poor creep ductility. A similar effect was observed by Liu et al. [180] where wrought samples containing NbC in parallel and perpendicular orientations to the load were produced. Creep crack growth rates were found to be faster in the samples containing NbC oriented transverse to the load. Zaman et al. [181] found NbC within IN718 to be sites for the nucleation of microvoids, and found them to deteriorate creep strength. Shiozawa and Weertman [182] likened carbides in Astroloy to non-deforming inclusions, which accumulate dislocations and result in decohesion from the matrix and local microcracks. However, this mechanism would also be active during room temperature deformation due to the piling up of dislocations. Since the ductilities of these materials are similar in RTT, the deleterious nature of NbC particles manifests only at elevated temperatures, where oxidation and environmentally assisted cracking occur.

Further evidence of the deleterious effects of NbC are evident when testing horizontally oriented samples. These samples retain a similar microstructural elongation for the defocused condition, but with an orientation of grains and carbide stringers oriented transverse to the load. The defocused X-orientation sample is an extreme example of this due to the intentional elongation of the grains and alignment of NbC stringers transverse to the load. Both features provide an easy path for crack propagation and result in the low elongation values in creep rupture testing.

It is proposed that the onset of oxidation along grain boundaries in SLM IN718 and resulting crack growth does not begin immediately upon loading but depends on the surface connection of a microcrack. Stress assisted grain boundary diffusion has been studied previously for IN718 [183-186], and operates when an embrittling species diffuses along grain boundaries under a high tensile stress, followed by embrittlement at the crack tip. When the embrittling species is oxygen, it can react with NbC that is encountered within the material to further embrittle the material through the formation of a brittle oxide [178, 179, 187, 188]. This mechanism becomes significant upon the surface connection of a microcrack, as this provides a site of stress concentration exposed to the oxidizing environment. Bika and McMahon [187] proposed a kinetic model for this embrittlement driven by the drop in chemical potential as an atom on the material's surface enters the stressed boundary as follows:

$$J = \frac{D\Omega C}{kT}\nabla\sigma \tag{14}$$

Where J is the diffusive flux in the boundary, D is the grain boundary diffusivity of the embrittling element, C is its concentration in the boundary, k is the Boltzmann constant, Ω is the atomic volume, T is the temperature, and ∇σ is the stress gradient resulting from a stress acting on the boundary. The extra driving force from a surface connected microcrack will accelerate the diffusion of oxygen through the grain boundaries and the accumulation of environmental damage which leads to premature failure. The focused samples and the X-oriented samples, with a higher prevalence of transversely oriented grain boundaries and microcracking, are more prone to the onset of stress-assisted embrittlement. Samples will creep similarly until the brittle cracking mechanism takes over, accelerating the damage accumulation to failure. The kinetic basis for this mechanism explains why both SLM and wrought can exhibit a similar deformation mechanism (evidenced by dislocation-mediated planar slip) until a minimum strain rate is achieved, whereupon the two materials diverge. The grain rotation observed previously in wrought material allows for the accommodation of extreme plastic deformation, but is not observed in the SLM material because this deformation cannot be accommodated. Environmental factors begin to dominate the SLM material after a certain amount of plastic deformation, ultimately resulting in low elongation and premature failure.

The increased sensitivity of CRT to microstructural variation when compared to RTT can be attributed to the changes in the temperature and time scales of each test, similar to the results of Witkin et al. [71], who saw large variations in the combination (notched) stress rupture (CSR) behavior when compared to RTT. RTT tests impart rapid deformation at relatively low temperatures, while CRT tests strain slowly with high thermal energy. At an elevated temperature environmental attack was observed in SLM samples because of the large population of NbC; arrays perpendicular to the load were more damaging than those aligned parallel, but both rendered samples vulnerable to environmental attack. The room temperature test is not sensitive to environmental attack due to insufficient thermal energy. Rather, the RTT is mostly dependent upon the γ'' phase and its interactions with dislocations [116]. Interaction with the environment is only observed during slow strain-rate testing at elevated temperature. Additionally, the formation of voids and their coalescence into microcracks occurs when GBS is active, which again is a thermally activated process. While there is a slight increase in the yield strength for wrought material, other metrics such as UTS and ductility remain similar; significant separation of properties are not observed at room temperature.

4.3.3 Combination Stress Rupture (CSR)

CSR tests the notch sensitivity and elevated temperature ductility of an alloy due to the combined testing of notched and smooth sections. CSR testing on SLM Inconel 718 parts and wrought IN718 revealed a stark contrast in behavior; all SLM samples fail to meet the specifications set out by AMS 5663 through failures in the notched portion of the sample. The

CSR results for all microstructural conditions are presented in Table 15. The results are the averages of two samples per test condition, and include data from different focal shifts, scanning strategies, and build orientations. Despite a failure to meet the minimum AMS requirements of all SLM samples, important trends are observed among the groups.

Table 15: CSR results at 650 °C and 690 MPa.

Sample	**Time to Failure**	**Elongation**	**Failure Location**	**Final Load**
	hours	**%**	**-**	**MPa**
Z - Island - Focused	3 ± 1	0	Notch	690
Z - Island - Defocused	10 ± 8	0	Notch	690
Z - Continuous - Focused	13 ± 16	0	Notch	690
Z - Continuous - Defocused	30 ± 2.3	0	Notch	690
X - Continuous - Focused	14.1 ± 12	0	Notch	690
X - Continuous - Defocused	2.3 ± 1	0	Notch	690
Wrought	61 ± 9	27 ± 8	Smooth	896
AMS 5663 Min. Req. [98]	23	4	Smooth	N/A

All groups show a dependence of time to failure on the orientation of grain boundaries and NbC particles with respect to the loading direction. In the case of the Z-orientation samples, there is a favorable change when the samples are produced in the defocused condition; as previously discussed, this results in more columnar grains that run parallel to the build direction. Furthermore, the same favorable alignment of NbC particles that resulted in longer creep lives is present here. Vertical stringers of NbC inhibit crack propagation across the sample. In the case of horizontal samples, the opposite effect is seen when switching focal shifts. This is because the defocused condition will produce the same stringers of NbC, but their orientation is now transverse to the load. The resulting microstructures provide a nearly continuous path along NbC particles that cut across the microstructure, leading to the lowest rupture times in the X-Continuous-Defocused sample. The X-Continuous-Focused sample behaves similarly to the Z-Continuous-Focused sample, as both contain a more equiaxed distribution of grain boundaries and NbC particles.

A representative microstructural image and fracture surface of the focused continuous and wrought samples is shown in Figure 46. The finer grain size, more δ phase extending from the grain boundaries, and a lower population of NbC in the wrought material are all apparent in these images. The failure appears highly intergranular and brittle for the SLM sample, while that of the wrought is highly dimpled and ductile. Samples with an increasing number of grain boundaries oriented transverse to the load will be more sensitive to intergranular failure, as these sites can act as easy crack propagation pathways. Similar to creep rupture, this difference in grain boundary orientation contributes to the differences observed among SLM samples. Furthermore, the NbC particles will act as nondeforming inclusions in the matrix and along grain boundaries, worsening the effects of crack propagation when poorly aligned. The defocused samples of both scan strategies have a more favorable orientation of grain boundaries and NbC and have an improved time to rupture compared to their focused counterparts. The ensuing deformation and failure will occur at the stress concentration in the notched portion of the sample in a notch-sensitive alloy, rather than over the smooth portion where elongation is measured.

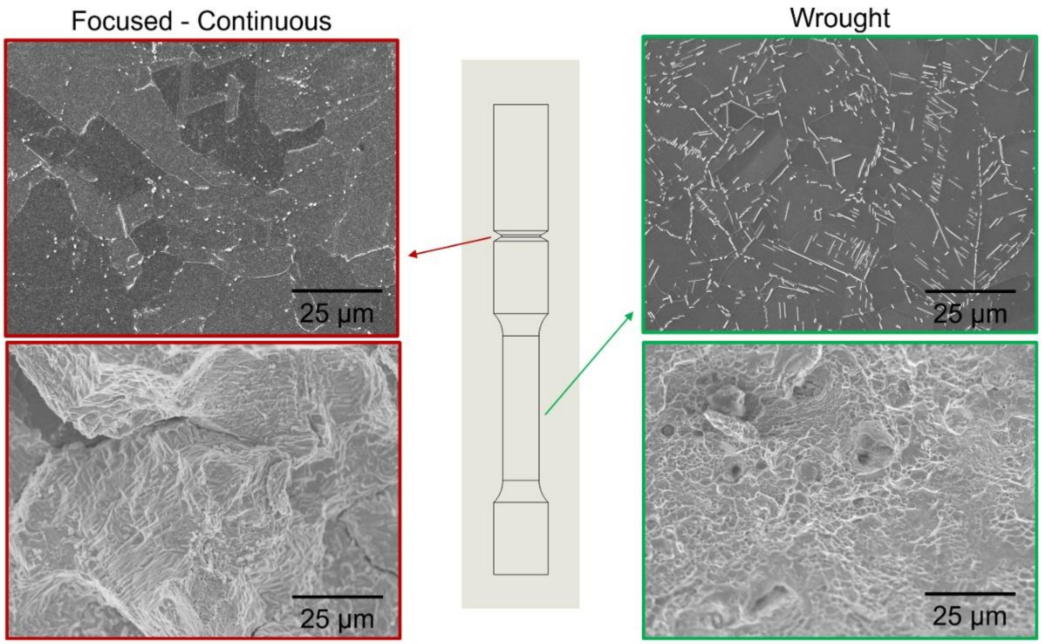

Figure 46: Microstructure and fractography comparison of notch ductile and not sensitive material.

Creep tests performed on SLM material show that the grain size affects metrics like time to rupture and elongation but does not change the underlying failure mechanism. Both coarse/elongated and fine/equiaxed grains in the SLM structures were susceptible to environmental attack, ultimately failing via crack propagation. Although the elongated microstructures along the loading direction did enhance properties, it appears that they only delayed the inevitable environmental failure. These results were echoed by CSR testing, where the more elongated structures held the load for a longer time but could not prevent a notch failure.

Looking at CSR samples tested in the X-orientation shows the significant effect of grain boundary orientation. The defocused continuous samples, which have the longest time to rupture due to the best crack propagation resistance, have the lowest time to rupture when tested with the tensile axis perpendicular to the direction of elongation. Easy crack propagation can occur along the grain boundaries oriented transverse to the load. Furthermore, the unfavorable orientation of NbC exacerbates the deleterious effects in this condition, introducing further stress risers and weakening the microstructure.

Initial fractography results indicate that the SLM samples are failing by environmentally assisted intergranular crack propagation that initiates at the notch, shown in Figure 47. The image of the SLM sample comes from the notched portion of the CSR coupon, while that of the wrought sample is from the smooth section. There is a noticeable difference in the diameter of the fracture surface due to the severe necking of the wrought material. This environmental effect is similar to what was observed for creep samples, where the oxide gradient on the fracture surface indicates the slow movement of the crack. The decreased time to failure in the CSR sample is attributed to the presence of a stress concentration from the onset of the load. The wrought samples display a similar ductile dimpled fracture as before, with no signs of environmental attack.

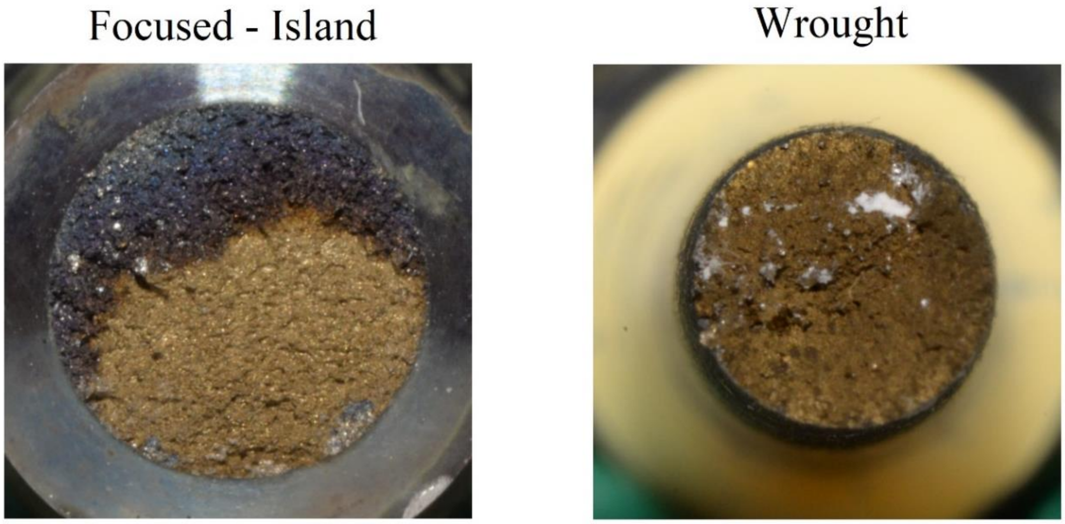
Focused - Island

Wrought

Figure 47: Macro-scale fractography images of the Focused – Island SLM sample and the wrought sample. The SLM sample comes from the notched portion and shows a similar oxidation pattern to the CRT samples, indicating crack growth.

The defocused continuous sample is shown to have the longest time to failure among the SLM samples. A minimal amount of grain boundaries oriented transverse to the load slow down the crack propagation that eventually leads to failure. The more tortuous path presented by grain boundaries elongated parallel to the loading direction improves CSR performance similar to how it improved the CRT behavior. However, both samples still fail, indicating that both microstructures are deficient in at least one microstructural aspect.

The δ phase has been linked to notch sensitivity in the literature before, where increased precipitation of δ phase eliminated notch sensitivity in spray-formed IN718 and even wrought IN718 that was lean of the phase [108, 189]. These studies employed intermediate heat treatments to purposefully precipitate the δ phase on grain boundaries and restore notch ductility. It is proposed that the mechanism involves local plasticity of the grain boundaries near the notch tip. The δ phase competes for Nb with the γ'' phase, as they have the same stoichiometry, Ni_3Nb. With an increased population of δ phase on the GBs, the local matrix is starved of Nb, and cannot form γ''. This creates a precipitate free zone (PFZ) along the grain boundaries, that is free of the primary strengthening phase [190]. An example of this in an SLM sample can be seen in Figure 48, where red arrows point to the PFZ surrounding the acicular δ particles on the grain boundary. The γ'' is observed within the grain interiors but not adjacent to the δ particles. The acicular δ phase shown here does not extend into the grain interior, but rather grows in a direction parallel to the GB itself. The formation of the PFZ in this situation can be deleterious, as there is now an easy direction of crack growth along the GB. This is referred to as a film-like δ phase structure. For wrought samples, where the δ phase extends inwards towards the grain exteriors, a more tortuous path for crack propagation is presented [190].

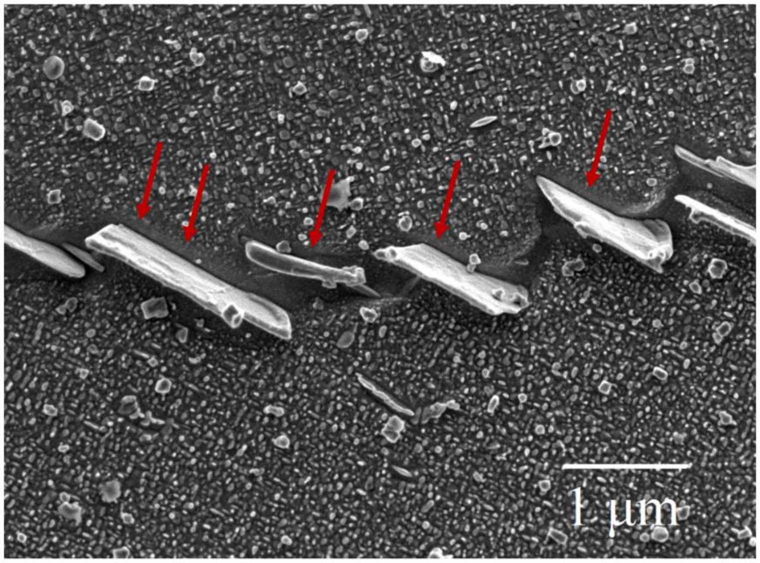

Figure 48: Precipitate free zone (PFZ) around a grain boundary in SLM samples highlighted by red arrows. Large plate-like precipitates are the GB δ phase, and smaller precipitates in the grain interiors are the γ’ and γ’’ phases.

To further evaluate the effects of the δ phase on CSR properties, a super-solvus heat treatment was given to a wrought sample to dissolve the δ phase prior to aging and testing. This heat treatment consisted of a 1065° C solution treatment, followed by a 760° C age for 10 hours, furnace cool to 649° C, and hold for a total aging cycle time of 20 hours. This is the heat treatment outlined by AMS 5664 [121], which is optimized for strength and does not specify a requirement for CSR. The results of CSR testing of this second heat treatment are shown in Table 16, with corresponding microstructures and fracture surfaces shown in Figure 49. Two distinct differences emerge between the microstructures of the sub and super-solvus treatments. First, the obvious dissolution of the δ phase in the former treatment is evident from the clean grain boundaries. The absence of the δ phase promotes grain growth during heat treatment. In typical processing, the δ phase is used to pin GBs in place and control the microstructural scale.

The elimination of the δ phase from GBs has a drastic effect on the CSR properties of wrought IN718, where samples almost immediately fail in the notched portion. Furthermore, the fracture surface reveals a highly intergranular mode of failure at the notch, where grain facets are easily observed. The clean intergranular failure indicates a more brittle failure when compared to the highly dimpled fracture surface of the sub-solvus treatment. The δ phase, or lack thereof, can significantly affect CSR behavior. The limited precipitation of δ phase and short growth into the grain interiors contribute to premature notch failures in SLM IN718.

Table 16: CSR results of super-solvus and sub-solvus heat treatments in wrought material.

Sample	**Time to Rupture**	**Elongation**	**Failure Location**	**Final Load**
	(hours)	**(%)**		**(MPa)**
Wrought - Sub-solvus	61 ± 9	27 ± 8	Smooth	896
Wrought - Super-solvus	0.7 ± 0	0	Notch	690
AMS 5663 Min. Req. [98]	23	4	Smooth	N/A

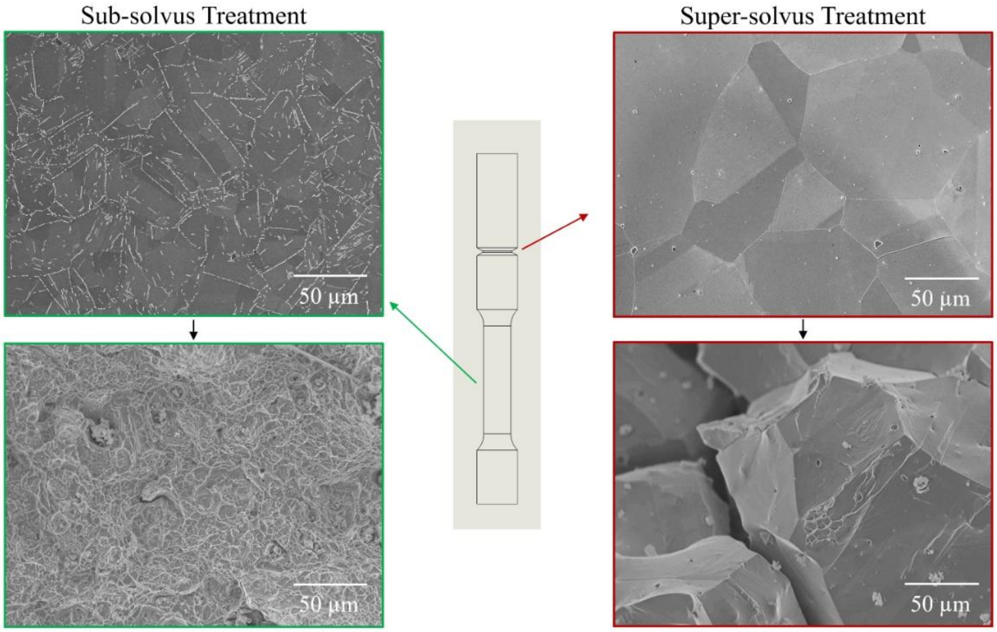

Figure 49: Sub-solvus vs. super-solvus microstructures and fracture locations/surfaces in wrought material.

4.3.4 Elevated Temperature Tensile (ETT)

In the following section, elevated temperature tensile (ETT) testing is used to further our understanding of what factors may be contributing to the lack of elevated temperature ductility observed in CRT and CSR. To reduce the number of variables in the experiment, only samples produced at the focal plane of the laser with the island scanning strategy and wrought material will be tested in the following sections. In place of varying the process parameters the test parameters will be changed. Test temperatures between 550 °C and 750 °C will be used along with strain rates between $8.33 \cdot 10^{-4}$ mm/mm/s (10^{-3} s^{-1}) and $8.33 \cdot 10^{-7}$ (10^{-6} s^{-1}) mm/mm/s. This testing would allow for further investigation of what factors may be affecting the elevated temperature behavior of SLM IN718.

4.3.4.1 Variations in Strain Rate

Stress-strain curves for strain rate variation (SRV) testing at 650 °C are shown in Figure 50 and tabulated values of key tensile properties are presented in Table 17. Values of strength are similar to those reported by Booker and Booker, who studied variations in tensile properties of wrought Inconel 718 at different strain rates and temperatures [191]. Minimum property values for acceptance of commercial wrought material as outlined by AMS 5663 [98] are provided for comparison to the 10^{-4} s^{-1} rate. The UTS falls just short of the requirement, while the yield strength marginally passes. The elongation of SLM samples is 75% lower than the requirement, while reduction of area (RoA) is 60% lower. Despite these shortcomings compared to the standard, comparison to wrought material reveals an even larger separation of properties.

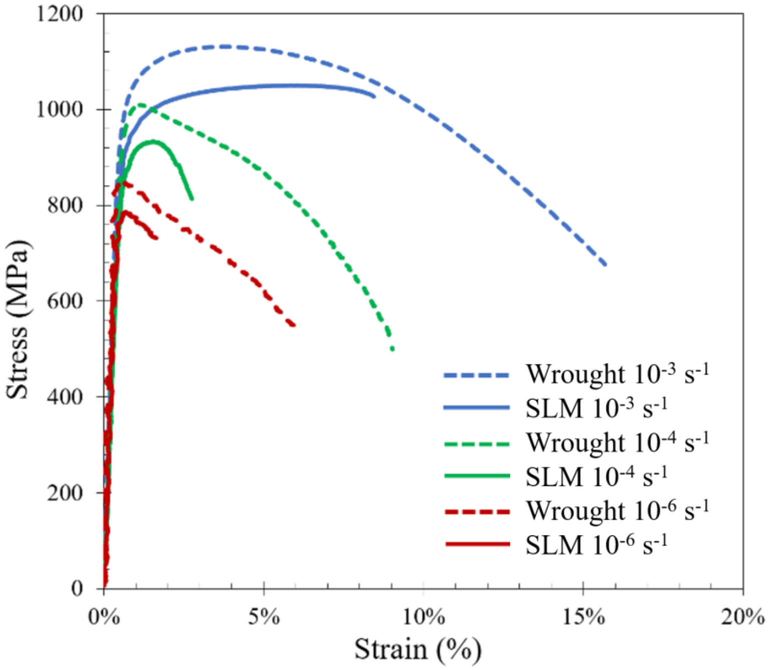

Figure 50: Strain rate variation testing of SLM and wrought material shows a trend of decreasing strength with decreasing strain rate. Ductility is limited in the SLM samples compared to wrought counterparts.

Table 17: Tabulated metrics of strain rate variation tests performed at 650 °C. Results are the average of two tests per condition.

Sample Type	**Strain Rate**	**Yield Strength**	**Ultimate Tensile Strength**	**Elongation**	**Reduction of Area**
	(s^{-1})	**(MPa)**	**(MPa)**	**(%)**	**(%)**
SLM	10^{-3}	907.3 ± 9.0	1048.0 ± 3.4	11.4 ± 1.2	15.2 ± 1.5
	10^{-4}	875.6 ± 17.1	940.4 ± 11.7	2.9 ± 0.4	5.9 ± 0.9
	10^{-6}	779.8 ± 5.5	796.3 ± 13.8	3.6 ± 1.6	6.8 ± 2.7
Wrought	10^{-3}	1023.2 ± 59.4	1112.8 ± 26.5	21.9 ± 0.4	55.8 ± 6.7
	10^{-4}	977.7 ± 15.9	1023.9 ± 19.3	17.8 ± 1.0	52.4 ± 0.9
	10^{-6}	802.5 ± 43.4	815.6 ± 46.2	16.6 ± 0.3	50.7 ± 3.4
AMS 5663 Min. Req. [98]	10^{-5}	862	1000	12	15

For material comparisons, the wrought strengths exceed those of their SLM counterparts at all three strain rates with differences of 7.5%, 10.4%, and 2.5%, respectively. These difference in strength are attributed to the smaller γ'' size in wrought material, similar to what was observed for RTT. Because the primary deformation mechanism in IN718 is massive planar slip, obstructions to dislocation movement introduced by the γ'' precipitates are essential in determining strength [100, 102, 116]. Dislocations cannot cross-slip in IN718 due to the low stacking fault energy, and so they must either cut through particles or loop around them [191, 192]. The smaller particles of the wrought sample promote particle shearing, a more tortuous route for dislocations as they must travel in pairs through the particles [116], whereas the larger particles of the SLM material may facilitate bowing out between or looping around precipitates. Based on creep deformation experiments on IN718 by Han and Chaturvedi [176, 193], the maximum back stress was associated with a γ'' particle size of 23.2 nm, and dropped by ~21% when the particles reached 70.2 nm, which are comparable sizes to the current study. They attribute the dependence of back stress on particle size to a change in the mechanism of deformation. Further support is offered by Devaux et al. [171], who noted a loss of coherency of the γ'' particles around 40 nm. A loss of coherency will reduce the strengthening imparted to the matrix by the γ'' particles and could lead to a change in the deformation process.

As the strain rate decreases the time of testing increases, and it is likely that the particles begin to coarsen during the longest duration tests. The fastest strain rate tests are less prone to this degradation, as tests end within minutes of starting. However, the slow strain rate tests could last for over 30 hours. In these time ranges significant particle coarsening has been observed to occur, as determined by Devaux et al. [171], that is in line with the Lifshitz-Slyozov-Wagner (LSW) theory of volume diffusion-controlled growth that has both a time and temperature dependence. Aging, or testing, for longer times will result in particle coarsening and strength degradation, which may be contributing to the large loss in strength at the slowest strain rates in the current samples.

Compared to the strength values, the ductility metrics offer a more significant separation of properties between SLM and wrought material. In descending strain rate order, the elongations drop by 49%, 84%, and 78%, respectively. These are more significant differences relative to the ~10% differences observed for yield and ultimate strengths. The SLM ductility appears far more sensitive to changes in the strain rate than their wrought counterparts, with a decrease in elongation of 75% going from 10^{-3} s^{-1} to 10^{-4} s^{-1}. In comparison, the wrought material only drops by 20% between these same strain rates. The slight increase in elongation from 10^{-4} s^{-1} to 10^{-6} s^{-1} is likely related to the onset of time-dependent strains occurring during slow strain rate testing, as well as particle coarsening [191].

Differences in the strength of the SLM and wrought material stem from the γ'' particle size, but the significant decrease in ductility cannot be related to this same phenomenon. On the contrary, larger γ'' particles should promote ductility in the samples. To better understand the deformation process, the strain rate sensitivity (SRS), *m*, is evaluated. This parameter relates the flow stress of the material to the strain rate and provides useful information regarding material behavior as a function of strain rate. The flow stress is the stress required to continue plastically deforming the material. SRS can be calculated by the following equation [194]:

$$m = \frac{\log\left(\frac{\sigma_2}{\sigma_1}\right)}{\log\left(\frac{\dot{\epsilon_2}}{\dot{\epsilon_1}}\right)} = \frac{dlog(\sigma)}{dlog(\dot{\epsilon})} \tag{15}$$

Where σ and $\dot{\epsilon}$ are the stress and strain rate for each test, respectively. From the log-log plot of σ and $\dot{\epsilon}$, Figure 51, m_{SLM} and m_W are calculated to be 0.019 and 0.022, respectively. It should be noted that the higher position of the wrought curve in Figure 3 stems from the greater overall strengths. Stress values are taken at approximately 0.6% strain for each material, beyond the yield point where plastic flow has initiated. The strain rate sensitivities are similar enough that it can be assumed the response to a changing strain rate is the same for each material at this level of strain. This indicates that the plastic flow is initially the same for each material and that they are equally sensitive to changes in the strain rate. Another similarity between the two materials is the decreasing amount of strain hardening present with decreasing strain rate. As seen in Figure 50, the stress-strain curves exhibit a decreasing amount of strain hardening after the point of yielding, reaching the UTS almost immediately for the slowest rates. This is a common phenomenon for elevated temperature testing [195, 196]. Based on the initially similar response to a changing strain rate in both sample types, the mechanism that drives the ductility differences must arise after the onset of plastic deformation.

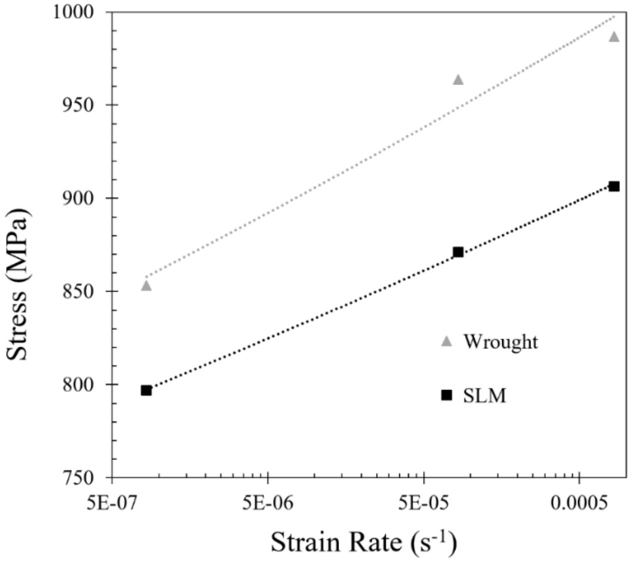

Figure 51: Strain rate sensitivity curves of the SLM and wrought conditions.

The plastic deformation in samples can be observed through EBSD-generated kernel averaged misorientation (KAM) maps. The KAM is a measure of the average misorientation of one pixel relative to its nearest neighbors where higher values indicate increased local deformation. Distortions of the lattice as a result of dislocation accumulation will increase the KAM. KAM maps that highlight differences amongst SLM samples tested at different strain rates and also compare the SLM and wrought material tested at the slowest strain rate are shown in Figure 52. In Figure 52a and 52b, both samples show strain accumulating near the grain boundaries, although there is an increased degree of strain in the 10^{-4} sample. This pattern corresponds well with the elongation and reduction of area values for these two samples; increases of 142% and 87% are observed for these metrics, respectively, when the strain rate is increased from 10^{-6} s^{-1} to 10^{-3} s^{-1}. With increased ductility there is more plastic deformation, which manifests as local misorientation. The accumulation of strain near IN718 GBs has been observed in room temperature studies by Zhu et al. [197].

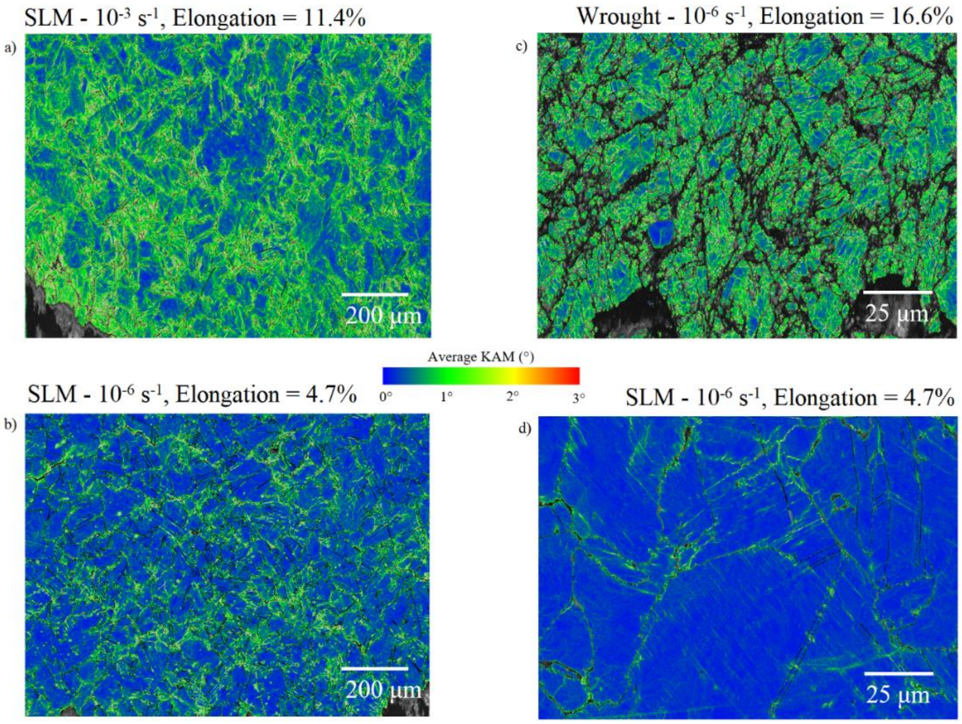

Figure 52: a, b) KAM Map comparison between the fastest (top) and slowest (bottom) strain rates for the SLM samples. Deformation is seen to accumulate near the grain boundaries for these samples. c, d) KAM map comparison at a higher magnification across manufacturing processes for the slowest strain rate in both conditions, showing the large difference in damage accumulation between wrought and SLM.

Comparing the SLM and wrought samples shows the difference between samples with an even larger separation of properties. The KAM maps in Figure 52c and 52d were taken at a higher resolution than Figure 52a and 52b because of the small wrought grain size and to show some of the subgrain structure formation present in each sample. The wrought samples have an immense amount of plastic deformation throughout the sample. Near the grain boundaries no EBSD pattern could be generated due to the distortion of the crystal lattice so these regions appear as black pixels. At this scale, the deformation near grain boundaries in the SLM sample is clear, and evidence of planar slip bands can be seen traversing the grains. Although the mechanism is similar in each sample, the wrought sample shows a more severe progression of deformation.

As shown by the strain rate sensitivity and KAM maps, the means of deformation accommodation in the samples is mostly the same. All samples have evidence of massive planar slip, damage accumulation around the grain boundaries, and sensitivity to the changing γ'' size. The primary difference between SLM and wrought material at elevated temperature is the extent of the deformation. While wrought material is capable of accumulating strains of 20% or more, the SLM material fails prematurely. This is shown in the stress-strain data and the KAM maps. To further analyze what may cause the large differences in overall ductility, the failure mechanism must be understood.

Fractography of the tested samples is highly informative as to the difference in the failure mechanisms between wrought and SLM samples. Optical images of the SLM and wrought fracture surfaces at each strain rate can be seen in Figure 53. The color of the fracture surfaces corresponds to the time that the surface was exposed to the laboratory air environment. While the SLM samples show a variation of color across the fracture surfaces (marked by dotted red lines), the wrought samples from each test appear as a single color. The gradient color change in these marked areas is related to the thickness of the oxide that forms upon exposure to the lab air at elevated temperature. Due to gradual crack progression, different areas of the fracture surface are exposed to air for different amounts of time and the thickness of the oxide—and resulting color—will change as the crack progresses inward. The SLM fracture surface appearance indicates progressive crack growth during testing. The 10^{-6} s^{-1} sample does not have as distinct of a color change due to the sample remaining in the furnace for a prolonged period after testing was complete. With decreasing strain rate, the size of the affected area grows larger. A similar effect was observed by Xu et al. [198] when testing SLM IN738LC bars. They noted a larger area affected by the environment as the strain rate decreased. This oxidized zone is also very similar to that observed in CRT which is attributed to environmental damage.

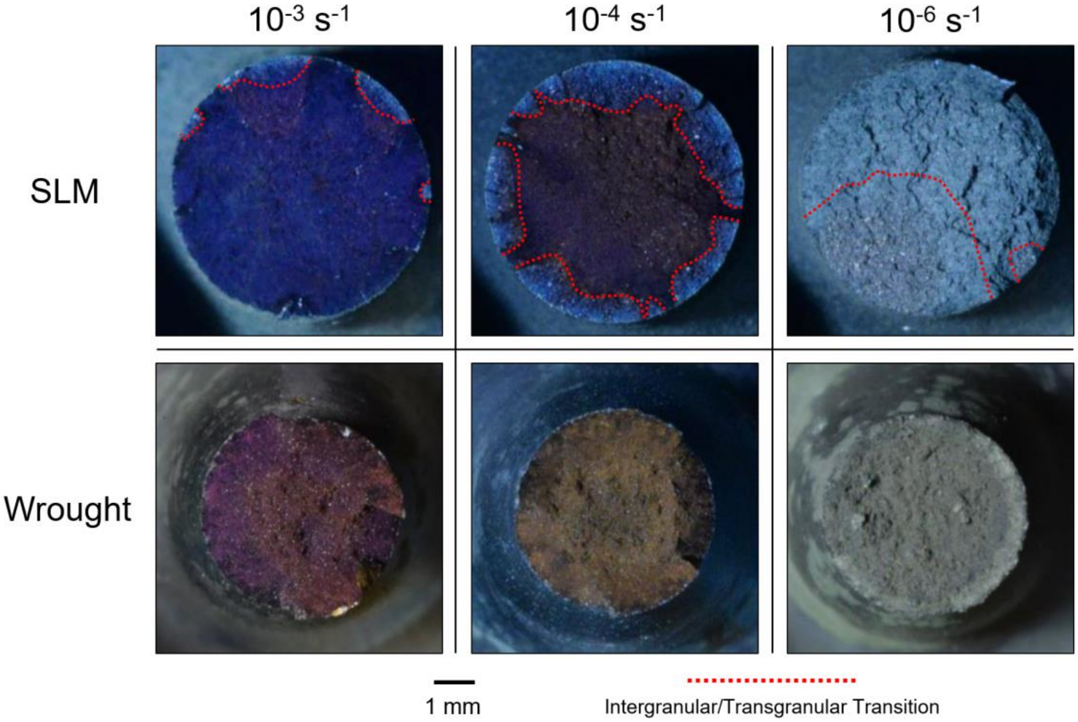

Figure 53: a, b, c) Fractography of the SLM samples in descending strain rate order. The % intergranular area increases with decreasing strain rate. d, e, f) Fractography of the wrought samples in the same order. Large reductions of area can be seen when compared to SLM samples.

Detailed SEM images of the fracture surfaces for the 10^{-4} s^{-1} SLM and wrought samples are shown in Figure 54. The oxidized areas in SLM samples are shown to be comprised primarily of intergranular surfaces while the center is more similar to an overload type of transgranular failure. The wrought sample has a characteristically ductile cup-and-cone type of failure, where large dimples are observed throughout the center of the sample and near the edges a shear lip forms. There is no evidence of intergranular cracking or environmental damage in the wrought samples. In addition to the intergranular fracture surface in SLM materials, oxidized NbC particles are seen on the surface. These particles have a similar feathery appearance as observed in the literature [178, 179, 199]. Miller et al. [200] conducted XPS studies on oxidized NbC particles and found that they readily form Nb_2O_5 and suggest that the oxidation and subsequent decomposition of NbC may promote intergranular failure in IN718. Sjoberg and Ingesten et al. [190] found that upon oxidation, NbC particles will swell considerably and this volume increase will promote intergranular crack growth through local stress risers. They found that IN718 with grain boundary NbC particles caused notch sensitivity. Nb_2O_5 has a considerably larger volume when compared to pure Nb metal and also NbC; the Pilling-Bedworth ratios, a ratio of the volume of the oxide to the base metals, are 2.68 and 2.15 for Nb_2O_5 compared to pure Nb metal and NbC [201, 202]. This significant volume increase will have deleterious effects during oxidation. The NbC distribution was observed as one of the primary differences between the wrought and SLM structures.

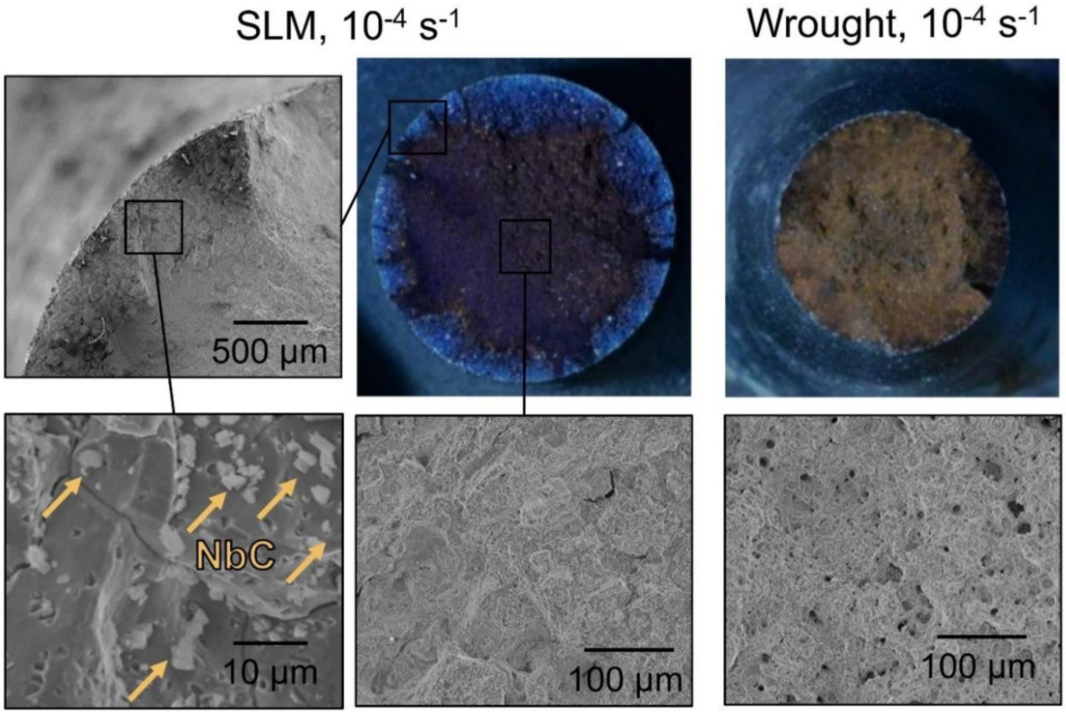

Figure 54: a) Detailed SEM images of the intergranular and transgranular regions of the SLM sample tested at 10^{-4} s^{-1}. Oxidized NbC particles are highlighted with red arrows. b) SEM image showing the ductile dimpled fracture surface in the center of the wrought sample tested at 10^{-4} s^{-1}.

The small interparticle spacing of NbC in SLM samples combined with their placement along the grain boundaries contributes to the enhanced environmental susceptibility of SLM samples compared to the wrought. The SLM samples have an average NbC interparticle spacing of 8 μm and average grain size of 50.9 μm, which means that numerous NbC particles will be found within the same grain or grain boundary. Wrought samples have an interparticle spacing of 66 μm and an average grain size of 21.9 μm, excluding them from adjacent grains or grain boundaries. The close spacing in SLM samples along grain boundaries allows for embrittling oxygen atoms to diffuse to them faster, and the continuity along GBs produces an easy path for crack propagation. Both factors increase SLM material’s susceptibility to environmental attack.

Their appearance along the fracture surface is further evidence of their negative role on elevated temperature properties due to environmental attack.

It was proposed that environmental damage during CRT in SLM IN718 at creep strain rates around 10^{-8} s^{-1} occurs upon the propagation of a microcrack to a free surface in a previous study. This mechanism is driven by the presence of a stress concentration, which promotes the inward diffusion of oxygen as presented in Eqn. 14. Oxygen causes local decohesion of GBs in the material and also reacts with NbC on the GBs or within the matrix to exacerbate the damage. The current results bolster the claim that environmental damage accumulates for this material in the presence of a stress concentration. Intergranular crack propagation is observed in Figure 53 to initiate near the free surfaces of the dogbone and propagate inward. Near these propagating cracks, there will be an increased diffusive flux due to the stress concentration as shown in Eqn. 14. The presence of continuous strings of NbC will enhance the growth of these cracks through selective oxidation and volume expansion of particles near grain boundaries. It has been observed that the onset of plastic deformation reacts similarly to a change in strain rate via the strain rate sensitivity factor, the overall damage accumulation mechanisms within the matrix are similar between SLM and wrought material as demonstrated through KAM mapping, and the SLM samples fail via intergranular crack propagation whereas wrought material fails through microvoid coalescence. The primary difference between wrought and SLM is not in the deformation mechanism as much as it is in the failure mechanism and the amount of strain that can be accommodated prior to onset of failure.

The accumulation of environmental damage on the fracture surface is unique to the SLM materials and supports the DE mechanism. With a decreasing strain rate there is an increase in the time over which environmental damage can occur. DE typically occurs in the presence of a stress concentration, such as a notch or crack, in the material. This may explain why the initial plastic deformation of the samples does not show a sensitivity to the strain rate, but the overall ductility does. A stress concentration does not exist for these samples until a microcrack connects to the surface, and so initially the deformation is similar. Once this occurs local decohesion and oxidation of NbC particles will drive further crack growth, resulting in decreased overall plastic deformation; the crack propagation will begin to dominate overall deformation with limited strain throughout the rest of the gauge length. The δ phase along grain boundaries and spacing of the NbC particles in wrought material mitigate these effects. Local plasticity from the δ phase alleviates the stress concentration that may occur if a crack were to form, and

The large stress gradient facilitates the higher diffusive flux in SLM material. The 10^{-3} s^{-1} condition limits the amount of time available for damage accrual, and therefore deforms plastically like its wrought counterpart. Despite this increased speed there is still susceptibility to the environment as damage can be seen around the edges.

4.3.4.2 Temperature Variation

To further study the limited ductility of SLM material at elevated temperatures, samples of an identical dogbone geometry were tested at 550 °C, 650 °C, and 750 °C at a constant strain rate of 10^{-4} s^{-1}. The stress-strain curves of these tests are presented in Figure 55 with tabulated results in Table 18. The material properties for both SLM and wrought material show a decreasing strength with increasing temperature, and a ductility dip around 650 °C. Strength falling off as a function of temperature is a known phenomenon for IN718, as previously observed in the literature [191, 203]. Higher temperatures result in the overaging of the γ'' precipitates and lowers the overall strength.

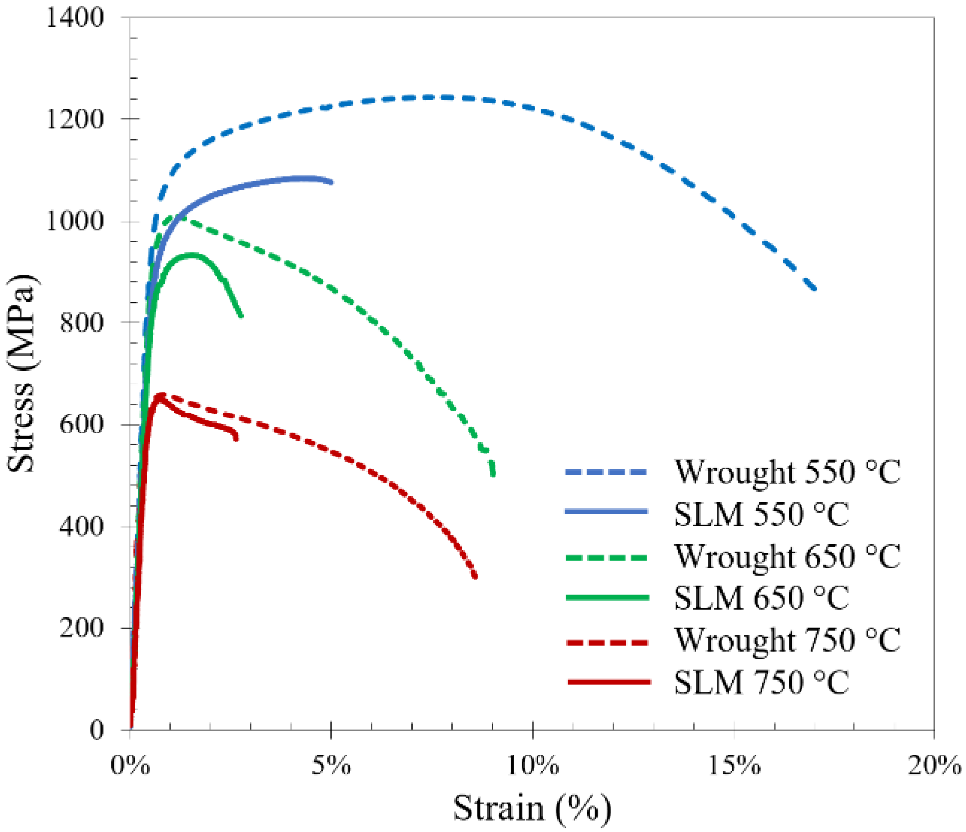

Figure 55: Stress-strain curves of the temperature variation tests pulled at 10^{-4} s^{-1}. Increasing temperature is seen to trend with decreasing strength. Ductility in the SLM samples is again shown to be significantly lower than that of wrought material.

Table 18: Tabulated metrics of test temperature variation tests performed at a strain rate of 10^{-4}.

Sample Type	**Test Temperature**	**Yield Strength**	**Ultimate Tensile Strength**	**Elongation**	**Reduction of Area**
	(°C)	**(MPa)**	**(MPa)**	**(%)**	**(%)**
SLM	550	934.2 ± 12.4	1093.6 ± 12.4	6.1 ± 0.2	10.7 ± 0.5
	650	875.6 ± 17.2	940.5 ± 11.7	2.9 ± 0.4	5.9 ± 0.9
	750	646.7 ± 9.0	653.6 ± 5.5	3.4 ± 0.5	7.6 ± 1.6
Wrought	550	1031.5 ± 10.3	1248.0 ± 6.2	25.6 ± 5.7	44.7 ± 4.4
	650	977.7 ± 15.6	1023.9 ± 19.3	17.8 ± 1.0	52.4 ± 4.9
	750	652.9 ± 10.7	656.4 ± 4.1	28.0 ± 0.6	60.8 ± 5.9
AMS 5663 [98]	650	862	1000	12	15

The ductility of samples is shown to reach a minimum for both processing conditions at 650 °C. On the lower temperature end at 550 °C, the material is not as susceptible to cracking as it is at 650 °C, leading to improved ductility. On the higher end at 750 °C, coarsening and overaging of the γ'' particles occurs, lowering overall strength and facilitating dislocation movement to improve ductility [171, 191]. The SLM and wrought material both display this behavior, but on different scales. The initial drop in ductility from 550 °C to 650 °C is quite pronounced in both SLM and wrought, dropping by 52% and 30%, respectively. However, the recovery of ductility is quite different from 650 °C to 750 °C between SLM and wrought where increases in elongation of 17.2% and 57%, respectively, are seen. The SLM samples, which are prone to oxidation-enhanced crack growth do not recover as much ductility at 750 °C because this temperature also promotes the diffusion of oxygen along grain boundaries. Wrought material, which does not show signs of DE has a large recovery of ductility from 650 °C to 750 °C.

Sensitivity to the testing temperature has been demonstrated for the DE mechanism that is discussed here via the temperature-dependent diffusion constant D in Eqn. 14. Increased temperature promotes the diffusion of oxygen as seen in Eqn. 14 and higher thermal energy results in faster diffusion rates. Oxygen diffusion rates in Ni have been shown to follow an Arrhenius relationship, increasing in diffusivity with temperature [204]. Wei et al. [205] demonstrated a faster crack growth rate in IN718 with increased temperature for this very reason. Their XPS analysis of fracture surfaces confirm the presence of oxides along the boundary that result from the oxidation of Nb-rich carbides.

The fracture surfaces from temperature variation tests revealed similar behavior to those of the strain rate samples, as seen in Figure 56. With increasing temperature, the area of environmental attack and depth of penetration is increased. Both 550 °C and 650 °C conditions show multiple starter sites and corresponding short intergranular crack growth, but the 750 °C shows only a single region of this growth. The wrought samples show significantly reduced fracture surface areas compared to those of SLM, and do not have evidence of intergranular failure or crack propagation. Typical ductile cup-and-cone features are observed for all wrought conditions. The colored fracture surfaces are caused by time left in the furnace after failure. The depths of penetration measured on the fracture surfaces for the 550 °C, 650 °C, and 750 °C samples are 0.4 mm, 1.1 mm, and 4.0 mm, indicating a significant dependence on the test temperature due to a thermally activated rate-controlling step.

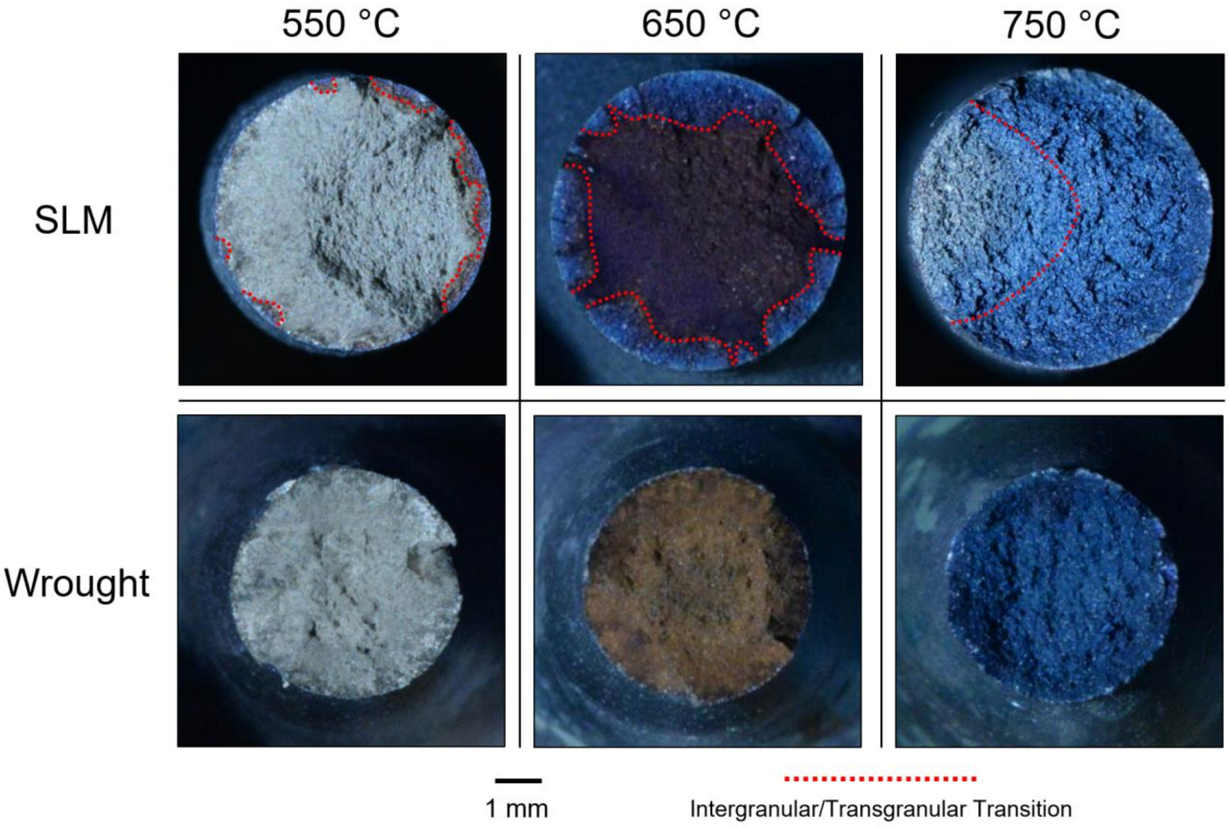

Figure 56: a, b, c) Fractography of the test temperature samples, showing a growing intergranular fracture surface area with increasing temperature in the SLM samples. d, e, f) Wrought samples do not show evidence of intergranular fracture.

This gradient oxide layer has seen in a study by Hayes et. al [199] when studying the temperature dependence of intergranular cracking on ALLVAC 718PLUS, which behaves similarly to IN718. After tensile testing smooth and v-notched bars pulled rapidly to failure after a specified dwell time, he observed a similar intergranular cracking mechanism in his samples that increased in area with increasing temperature. By using the extent of intergranular failure to identify the depth of penetration of the embrittling species, he calculated the activation energy and concluded that the susceptibility to intergranular fracture was related to the moisture content of the testing environment. Taking this approach, the activation energy for grain boundary fracture in the current samples was calculated to be 170.0 kJ/mole, a result very similar to the 177.0 kJ/mole calculated for ALLVAC 718PLUS in laboratory air, as well as the 196.6 kJ/mole reported by Floreen et al. [206]. The present results are compared to those of Hayes et al. [199] in Figure 57, where increasing oxygen content of the environment decreases the activation energy necessary for crack growth. Reactions of intergranular precipitates with grain boundary diffusing oxygen—and hydrogen in high-moisture environments—was the embrittling mechanism in ALLVAC 718PLUS. Based on the calculated activation energy of 170 kJ/mole for IN718, it is likely that a similar mechanism exists.

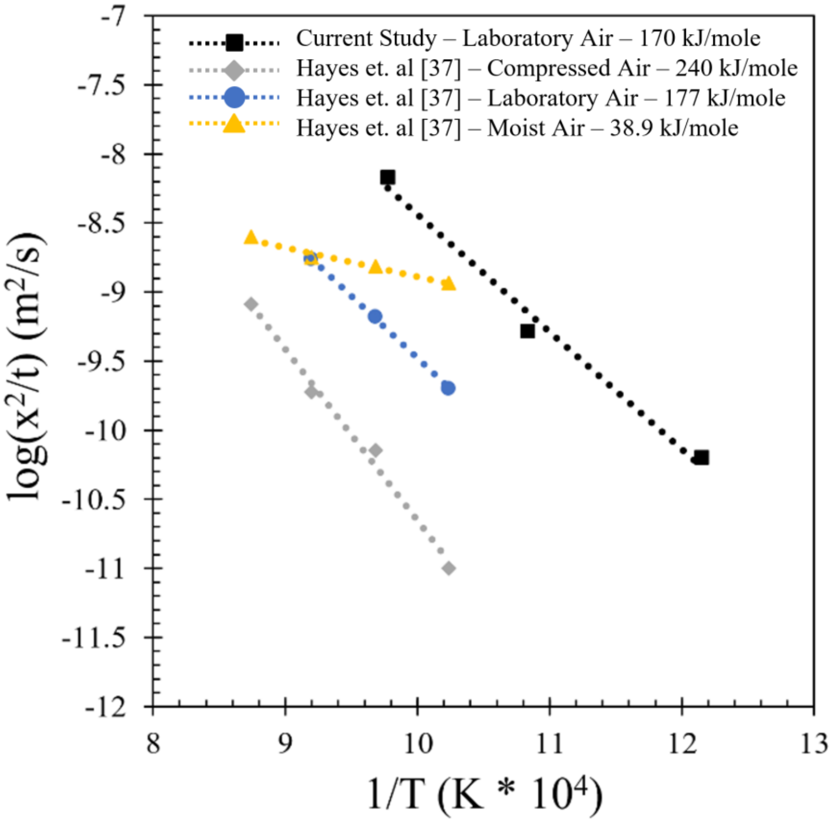

Figure 57: Plot of 1/T vs. log(x2/t) to calculate the activation energy for grain boundary fracture. Results of the current study are plotted against those of Hayes et al. [199] for comparison.

Other literature that has investigated the activation energy of crack growth has found similar values for IN718: 197 kJ/mole in air [206], 287 kJ/mole in oxygen [207], 191 kJ/mole in moist argon [207], and 223 kJ/mole in vacuum [208]. Sadanada and Shahinian [209] further relate the grain boundary diffusion of Monel of 171 kJ/mole to their own experiments on Inconel 718. These results all cite environmental attack via grain boundary diffusion as an embrittling mechanism in IN718, with oxygen being the primary culprit. Valerio et al. [207] elaborates on the potential active mechanisms, saying that the enrichment of Nb at grain boundaries and the decomposition of NbC as it is oxidized are responsible for the environmental susceptibility. They also found oxidized NbC on their fracture surfaces, similar to the current results. In their study, an activation energy of 287 kJ/mole is calculated in pure oxygen, while 191 kJ/mole is the activation energy in moist argon. The decrease in activation energy suggests an additional contribution of hydrogen to the embrittlement of IN718. This result parallels the drop in activation energy found by Hayes et. al [199] when changing from laboratory air to moist air. The moisture concentrations in these studies were not reported but suggest that a varying moisture content in the testing environment may produce a range of results. The current study is well within the range of these activation energies and suggests similar mechanisms are active.

The degree of environmental attack, evidenced by the intergranular fractures and reduced ductility in the SLM samples, has been shown to be both time- and temperature-dependent. Among the SLM samples, decreasing strain rates and increasing temperatures tend to produce lower ductility. At the extreme cases (10^{-6} s^{-1} or 750 °C), however, the general trend in strain-rate or temperature-dependent embrittlement is offset to some extent by overaging of the strengthening particles which improves the ductility. Despite these small improvements, SLM samples have consistently demonstrated a lower ductility than their wrought counterparts across multiple strain rates and temperatures. Areas of brittle intergranular failure, low elongations, and low RoAs are evidence of this behavior, which is linked to a stress-assisted oxygen embrittlement. The behavior demonstrated in the present study agrees well with the dynamic embrittlement mechanism.

4.4 Summary

The mechanical properties of SLM IN718 have been compared to wrought material in room temperature tensile, elevated temperature tensile, creep, and combination stress rupture. The findings not only compare SLM and wrought material, but for certain tests compare the properties from the range of microstructures that can be produced by SLM printing. The results reveal a distinct environmental sensitivity in SLM material that is only apparent at elevated temperature.

The room temperature tensile behavior showed little to no variation among SLM-processed material. Similar heat treatments produced nearly identical distributions of the strengthening phases, and environmental factors did not play a role at this temperature. Wrought-processed samples exhibited a higher yield strength than SLM samples, accounted for by the smaller γ'' particle size. Although RTT can be a strong indicator of a material's response to heat treatment, it does not differentiate between different microstructural scales and textures as well as CRT. The creep behavior of IN718 depends on microstructural scale, grain orientation, and the distribution of precipitates. It was found that with a coarser, more elongated microstructure parallel to the loading direction, the time to rupture and ductility increased; fewer grain boundaries oriented transverse to the loading direction combined with a favorable orientation of NbC precipitates were beneficial to creep behavior. However, despite these improvements through process parameter manipulation, the wrought material exhibited far superior ductility in CRT.

The wrought material was found to be insensitive to environmental effects when compared to SLM material. The fracture surfaces revealed that SLM samples failed by brittle intergranular crack growth and eventual overload. Wrought samples failed via ductile microvoid coalescence with no signs of weakening through environmental effects. This resulted in superior ductility at elevated temperature. The susceptibility to environmental attack is diminished in a microstructure that is lean of oxidation-prone precipitates. The chemical composition with respect to carbide forming elements Nb, Ti, and C are similar for wrought and SLM (Table 4). It is the SLM process that leads to a much larger frequency and closer spacing of carbides that explains the difference in properties, and not a difference in carbon content.

Although the mechanical behavior of SLM material can be altered based on the processing parameters, more significant differences are observed when comparing SLM to wrought material.

Microstructural morphology is seen to play a much smaller role in RTT and CRT when compared to the precipitate distribution; deleterious NbC that is a result of elemental segregation and post-processing forms more easily in SLM material. The differences that exist between SLM and wrought material are most clearly seen at elevated temperatures, where the wrought ductility is significantly higher than that of SLM material.

Elevated temperature tensile testing of SLM IN718 shows that it is susceptible to environmental attack that leads to limited ductility and premature failure. At all strain rates and temperatures tested in the present study, the SLM ductility was lower than that of wrought material. The lack of ductility was ultimately determined to be linked to environmental sensitivity in the form of dynamic embrittlement. The observed deformation behavior indicates that a similar mechanism is active for all samples, but the overall damage tolerance of the wrought material is greater because it is not environmentally sensitive.

At the fastest strain rate (10^{-3} s^{-1}), SLM material showed an improvement in ductility compared to both 10^{-4} s^{-1} and 10^{-6} s^{-1} by 293% and 142%, respectively. With less time for the penetration of oxygen along grain boundaries and subsequent oxidation of NbC, the ductility was improved. Measurements of the strain rate sensitivity, changes in strain hardening behavior, and evidence of plastic deformation along GBs indicate that SLM and wrought material deform similarly during the initial plastic deformation. However, environmental damage that occurs in SLM samples due to the NbC found within the microstructure and lack of δ phase along GBs facilitate crack growth that leads to a brittle failure.

Test temperature variation showed similarities to the strain rate variation when compared to the wrought condition; lower strengths and ductility in SLM material across all test temperatures. Fractography of SLM samples showed an increased prevalence of environmental attack, especially at the higher temperatures of 650 °C and 750 °C, and the wrought samples remained unaffected by the environment. The low temperature of 550 °C improved ductility slightly compared to the higher temperatures, but still had brittle behavior. Temperature dependence of environmental attack was demonstrated with the growing damaged zones and lower elongations at higher temperature where the diffusion of an embrittling species can occur more rapidly.

These tests show the vulnerability of SLM material in elevated temperature environments and their dependence on time and temperature. The root of this behavior stems from the susceptibility of the microstructural components to environmental attack and brittle behavior. To a significant extent, the presence of NbC particles at grain boundaries and lack of delta phase at grain boundaries are attributable to the initial solidification conditions unique to the SLM process. Most published accounts of the mechanical behavior of SLM 718 are based on the use of heat treatments that have been developed for wrought material. Only by testing at elevated temperatures and slow strain rates do differences between SLM and wrought begin to emerge. These differences show that the standard heat treatments intended to precipitate γ” are successful to the extent that static strength of SLM is comparable to wrought 718. It is the other microstructural constituents that lead to significant susceptibility of the SLM version of the alloy to an oxidizing environment. To prevent further elevated temperature sensitivity, heat treatments must be optimized for SLM microstructures to promote local plasticity and reduce the NbC particle density.

Chapter 5: Modified Heat Treatments of SLM Inconel 718

5.1 Introduction

The mechanical test results presented in Chapter 4 have demonstrated that typical heat treatment via AMS 5663 renders SLM material sensitive to environmental attack and notch sensitivity. Through excessive precipitation of NbC and insufficient precipitation of the δ phase, the SLM alloy has inferior strength and ductility when compared to wrought material at elevated temperatures. Dynamic embrittlement has been identified as the embrittling mechanism; the diffusion of oxygen and hydrogen down grain boundaries driven by a stress concentration weakens the grain boundaries and can react with closely spaced NbC particles, leading to premature failure. To optimize the SLM microstructure, modifications to the current thermal processing must be made.

Two processes are employed for thermal post-processing of the current SLM material—hot isostatic pressing (HIP) and heat treating (HT). The former is utilized to homogenize the microstructure, recrystallize the grains, and close porosity, while the latter precipitates the δ, γ'', and γ' phases throughout the microstructure. In developing modified heat treatments, it is necessary to retain all these features while also introducing the ability to reduce the NbC population and change the δ phase distribution. These microstructural features have been identified as the culprits in elevated temperature embrittlement. The closely spaced particles of NbC promote oxidation and create local stress risers, while simultaneously providing a path of easy crack propagation. The lack of δ phase on the grain boundaries prevents local plasticity that could relieve stress concentrations as they form. It has been observed that the wrought alloy is not sensitive to either of these effects and does not display elevated temperature embrittlement.

In the present chapter, various thermal treatments will be proposed and tested to try and alleviate the elevated temperature embrittlement that is affecting the SLM material. Direct comparisons will be made to the tests performed in Chapter 4 to quantify the effects of the novel heat treatments.

5.2 Experimental

5.2.1 Materials and Methods

IN718 samples were printed in the Z-orientation similar to those reported in Chapter 4. To reduce the variability due to process parameters, all cylinders were made using a 0-mm focal shift and the island scanning strategy. Typical laser parameters of 180 W and 600 mm/s were used in a flowing Ar environment. After production, cylinders were given identical HIP treatments and then exposed to various HT steps.

The novel heat treatments for these bars can be found in a visual guide in Figure 58, with a detailed description in Table 19. Steps 1 and 2 correspond to the homogenization treatment, with Step 1 being the HIP treatment and Step 2 being the modified homogenization step. This additional step consisted of a 1200 °C hold for 3 hours followed by a rapid air cool. Steps 3 and 4 are the heat treatment, with step 3 being an additional step designed to precipitate further δ phase, and Step 4 being the typical solution step. The modified δ treatment consists of a hold at 900 °C for 2 hours, prior to raising the temperature to the typical 954 °C solution treatment. Three different sample groups were produced with various combinations of Steps 1-4. HTX consisted of Step 1, 3, and 4; HTY consisted of Steps 1-4;s and HTZ consisted of Steps 1, 2, and 4. Following these heat treatments, all samples were given an identical double age (DA) treatment to what was used in Chapters 3 and 4.

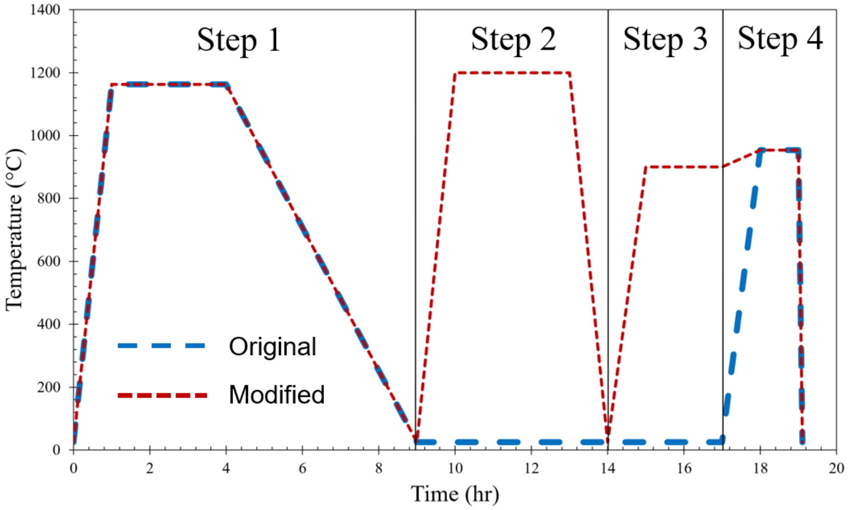

Figure 58: Heat treatment timeline featuring the original steps (Steps 1 and 4), as well as the modified heat treatment steps (Steps 2 and 3). All samples feature identical double aging (DA) treatments after Step 4.

Table 19: Heat Treatment steps for HT1, HTX, HTY, and HTZ.

Heat Treatment	**Procedure**
HT1	1163 °C, 3 hrs, 103 MPa, FC (Step 1) 954 °C, 1hr, WQ (Step 4) 718 °C, 8 hrs, FC, 625 °C, 8.25 hrs (DA)
HTX	1163 °C, 3 hrs, 103 MPa, FC (Step 1) 900°C, 2 hrs, Ramp to 954 °C, 1hr, WQ (Steps 3 & 4) 718 °C, 8 hrs, FC, 625 °C, 8.25 hrs (DA)
HTY	1163 °C, 3 hrs, 103 MPa, FC (Step 1) 1200 °C, 3 hrs, AC (Step 2) 900°C, 2 hrs, Ramp to 954 °C, 1hr, WQ (Steps 3 & 4) 718 °C, 8 hrs, FC, 625 °C, 8.25 hrs (DA)
HTZ	1163 °C, 3 hrs, 103 MPa, FC (Step 1) 1200 °C, 3 hrs, AC (Step 2) 954 °C, 1hr, WQ (Step 4) 718 °C, 8 hrs, FC, 625 °C, 8.25 hrs (DA)

5.2.2 Mechanical Testing

Room temperature tensile, elevated temperature tensile, creep rupture, and combination stress rupture were carried out in a similar manner to the samples described in Chapter 4. In this chapter, additional inert CSR testing was performed by Ar backfilling a vacuum environment. The vacuum level reached is 10.1 kPa.

5.2.3 Material characterization

Characterization of the microstructures and fracture surfaces were carried out with the same methodologies and equipment used in Chapters 3 and 4.

5.3 Results and Discussion

5.3.1 Development of Modified Heat Treatments

The first modified thermal treatment was the introduction of a 1200 °C homogenization treatment for 3 hours followed by a rapid air cool to be performed after the initial 1163 °C HIP treatment. 1200 °C was chosen as the homogenization temperature based on the results of Poole et. al [210], who employed a similar 2-step homogenization treatment on ingots of IN718. Others have found this step practice effective as well [211]. The step practice avoids the potential for incipient melting in areas of high Nb concentration that appear during solidification, which may occur at temperatures around 1170 – 1180 °C, because these phases are dissolved in the initial 1163 °C step [144, 145, 211]. Furthermore, the carbide size and distribution were found to stabilize at the lower temperature and the higher temperature should not result in precipitate coarsening. After dissolution of the Laves phase at 1163 °C and partial homogenization, the second higher temperature step at 1200 °C promotes more diffusion of Nb throughout the matrix [210]. Mitchell [109, 151] found a decrease in the overall carbide size during the first 20 hours when treating at 1200 °C due to a small amount of solutioning of carbide particles. In addition to enhancing the diffusion, carrying out the second homogenization step in a standard furnace allows for rapid air cooling and better retention of alloying elements in solid solution. Typical HIP treatments are cooled slowly, due to the nature of the pressure vessel-type furnaces employed by HIP, which may allow for the early precipitation of δ phase or other precipitates. With a better distribution of alloying elements after the homogenization steps, subsequent heat treatments may be more effective in precipitating important grain boundary and strengthening phases.

The homogenization treatments are well above the solvus temperature of the δ phase—1020 °C—and therefore result in complete dissolution [92, 189, 212]. Changes to the initial solution treatment of HT1 are necessary to achieve larger δ phase populations in the modified heat treatments. The wrought structure features δ phase that has nucleated near the grain boundaries and taken on a spheroidal morphology. Current SLM samples do not have adequate δ phase populations or morphologies, as evidenced by previous microstructural analysis in Chapter 3. The SLM samples have nearly 10x less δ phase by area % when compared to the wrought material, and so do not gain their beneficial stress-rupture properties.

The proposed heat treatment for the current samples therefore involves an intermediate step at 900 °C for 2 hours prior to solutioning at 954 °C for 1 hour to promote the formation of δ phase. A time-temperature-transformation (TTT) diagram that depicts these two heat treatments is shown in Figure 59 [153, 213, 214]. Treatment of the samples ends just prior to the formation of intragranular δ phase and focuses mostly on the GB δ phase. Previous work has shown 900 °C to be an effective temperature for the precipitation of the GB δ phase. Mahadevan et al. [215] showed that plate-like δ phase dominated the microstructure when treating for periods of 20 h and 100 h. Such extreme times are not used in the present study, but the temperature is shown to be effective in forming the δ phase. Azadian et al. [212] found that the δ phase precipitates the fastest at 900 °C in a temperature range from 700 – 1000 °C. Furthermore, they found that a similar heat treatment schedule of 900 °C for 4 hours followed by a 954 °C for 1 hour was sufficient to relieve notch sensitivity in spray-formed IN718. Others, such as Donachie and Muller [108] performed low temperature solution treatments at 917 °C for 10 hours to alleviate notch sensitivity through the enhanced precipitation of the δ phase.

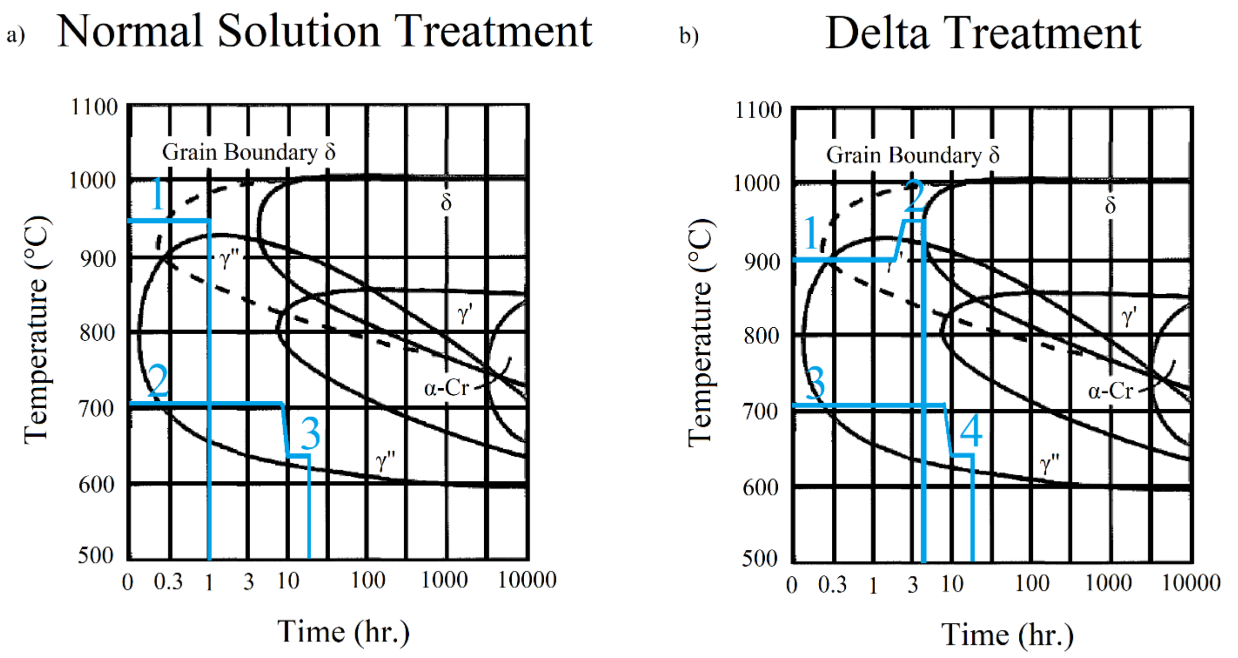

Figure 59: a) Original HT1 heat treatment used in Chapters 3 and 4. b) Modified heat treatment with an extra step at 900 °C for 2 hours [213].

5.3.2 Microstructures

Microstructures after the initial HIP can be found in Chapter 3 in Figure 60a. The resulting microstructure after a post-HIP 1200 °C homogenization treatment is shown below in Figure 60b. Notably, there is no δ phase observed along the grain boundaries like it was in Figure 29 after only HIP treatment. The HIP furnace cool is approx. 6 °C/min, while the air cool is much faster at approx. 500 °C/min through the δ stability region [216]. The δ phase can initiate nucleation rapidly near the nose of the TTT curve, at approximately 900 °C it takes ~15 minutes to nucleate δ phase. Avoiding this nose with a rapid air cool retains more Nb in solid solution for further heat treatment.

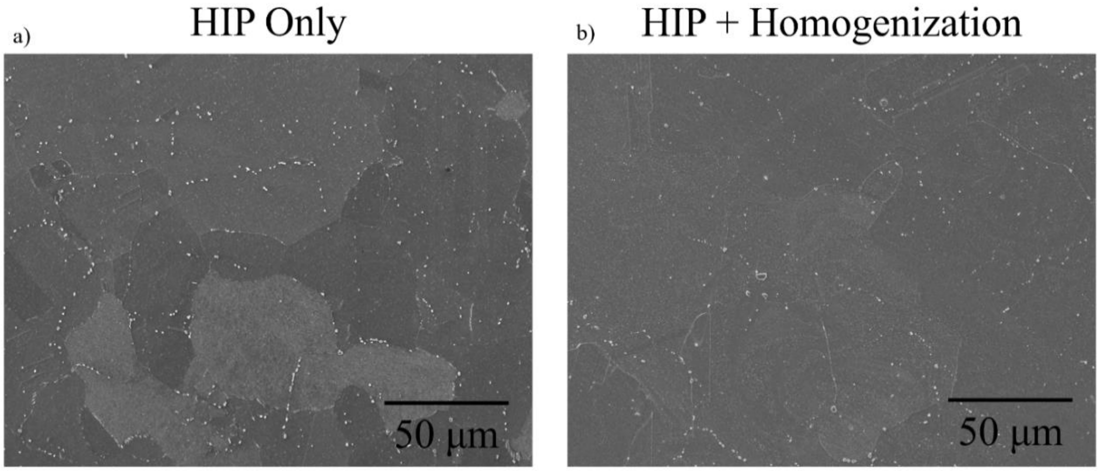

Figure 60: Microstructure of the modified heat treatment samples after HIP + 1200 °C for 3 hrs.

The NbC content of the modified homogenization treatment was determined to be 0.04% volume fraction, with an average NbC particle diameter of 0.58 ± 0.04 µm and interparticle spacing of 9.7 ± 1.3 µm. Compared to the HIP-only samples with an NbC volume fraction of 0.12%, average particle diameter of 0.56 ± 0.1 µm, and interparticle spacing of 6.4 ± 0.9 µm, the modified heat treatments appear to be effective in reducing the number of carbides within the microstructure, although the sizes are similar. Table 20 summarizes the NbC distribution in all current samples. A decreased NbC content in the microstructure will benefit the materials in two ways. With less NbC in the microstructure, there is a higher amount of Nb available for the precipitation of other Nb-rich phases, such as δ and γ''. Furthermore, the increased interparticle spacing should reduce the effects of local stress risers due to volume expansion when NbC reacts with oxygen in the environment. The larger spacing creates a more discontinuous path through the microstructure for crack propagation, similar to the wrought microstructures.

Table 20: Tabulated metrics of NbC characterization: area %, volume %, particle diameter, and interparticle spacing.

Heat Treatment	**Particle Diameter**	**Interparticle Spacing**	**Area %**	**Volume %**
	µm	**µm**	**%**	**%**
SLM - HT1	0.56 ± 0.06	6.4 ± 0.9	1.40	0.12
SLM - HTX	0.56 ± 0.06	6.4 ± 0.9	1.40	0.12
SLM - HTY	0.58 ± 0.04	9.7 ± 1.3	0.64	0.04
SLM - HTZ	0.58 ± 0.04	9.7 ± 1.3	0.64	0.04
Wrought	4.7 ± 2.1	66.3 ± 6.8	0.47	0.02

After homogenization treatment, samples were given a combination of heat treatments to precipitate the δ phase and strengthening phases. All microstructures from HT1, HTX, HTY, and HTZ at both 250x and 1000x can be seen in Figure 61. Table 21 provides a summary of microstructural measurements for all heat treatments. The grain size is seen to be unchanged between HT1 and HTX, as they received identical homogenization treatments. Subsequent precipitation of the δ phase will pin GBs, so grain growth is not expected after HIP. The grain size of HTY and HTZ are shown to be slightly larger than that of HTX and HT1 due to the additional 1200 °C step that results in grain growth. However, this difference is slight because NbC can also pin grain boundaries. The grain morphology appears fairly equiaxed for all modified heat treatment conditions based on the calculated aspect ratios, as expected due to the island and focused process parameters used during production.

Table 21: Tabulated metrics of microstructural characterization: grain size, aspect ratio, δ phase characteristics, and NbC characteristics.

Heat Treatment	**Grain Size**	**Aspect Ratio**
	µm	
SLM - HT1	48.6	1.11
SLM - HTX	48.0	1.05
SLM - HTY	55.1	1.06
SLM - HTZ	61.6	1.05
Wrought	21.7	1.10

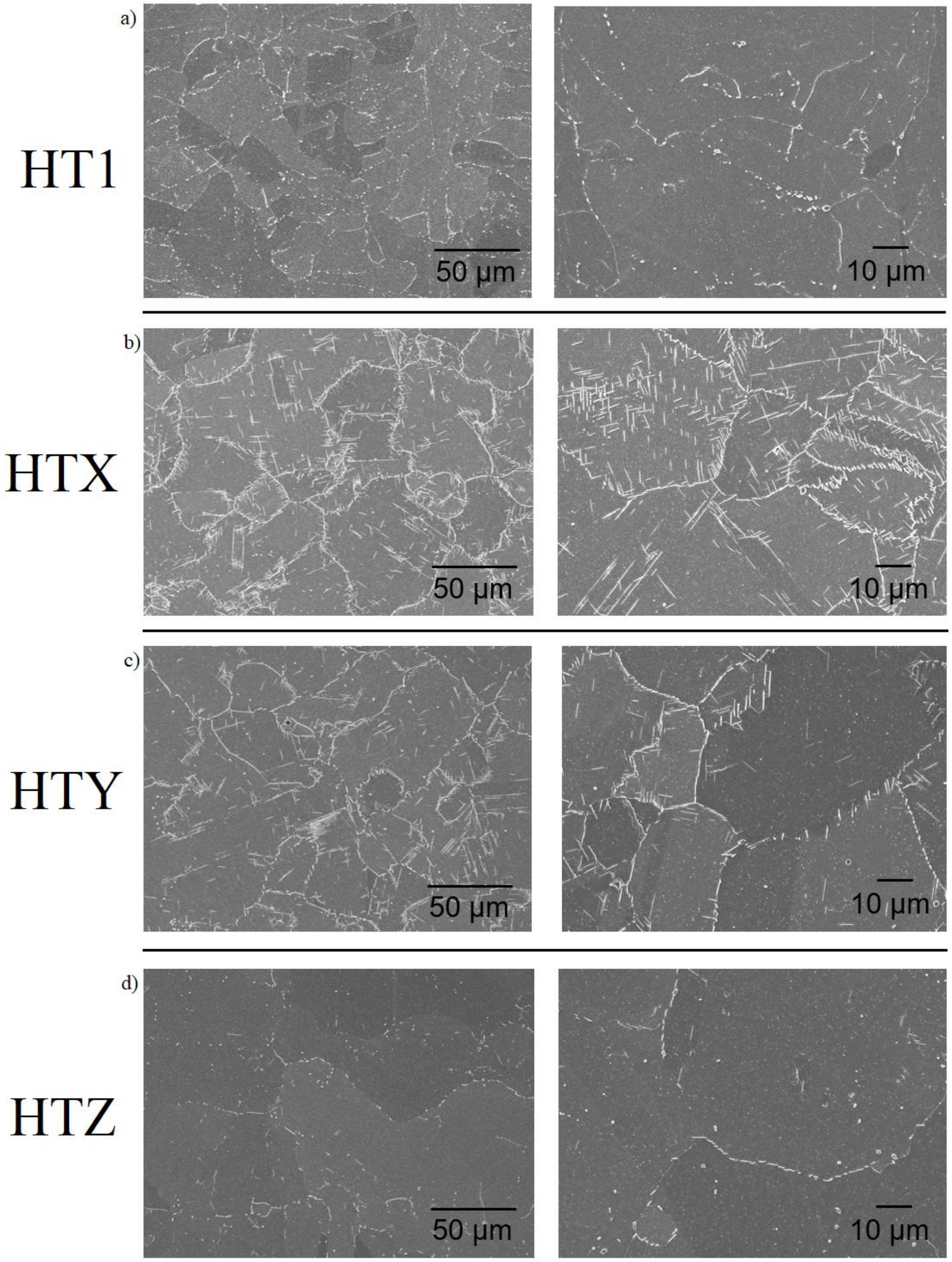

Figure 61: a) HT1 from Chapter 3. b) HTX includes the modified solution treatment step at 900 °C. c) HTY has both the extra homogenization step and also the modified solution treatment. d) HTZ only has the additional homogenization treatment, but the same solution treatment.

The most significant difference in the microstructures appears to be the δ phase population. From Figure 61b and 61c, it is obvious that the delta treatment at 900 °C was effective in precipitating large amounts of the GB δ phase when compared to 61a and 61d. HT1 has a volume fraction of 0.02 % δ phase while HTX, HTY, and HTZ have δ volume fractions of 0.81%, 0.64%, and 0.09%, respectively. These measurements, alongside dimensional measurements of the δ phase are provided in Table 22. HTX provides the highest amount of the δ phase, despite receiving the same solution treatment as HTY. This can be explained by the larger grain size of HTY. Since grain boundaries act as preferential nucleation sites for the δ phase, a decrease in GB area achieved through a larger grain size effectively decreases the number of nucleation sites for the δ phase [108, 217]. This results in a decrease from 0.81% to 0.64% from HTX to HTY. HTZ, with a combination of large grains and no added δ heat treatment, has 0.09% volume fraction, which is an increase over the original HT1. This is justified by the decrease in the NbC population, which allows for more Nb to be involved in δ precipitation. The large volume fraction of NbC present in SLM microstructures negatively affects δ precipitation in all SLM samples.

Table 22: Tabulated metrics of the δ phase morphology.

Heat Treatment	**δ Particle Length**	**δ Particle Width**	**Aspect Ratio**	**δ phase Volume %**
	µm	**µm**	**%**	**%**
SLM - HT1	2.2 ± 2.1	0.3 ± 0.1	7.0 ± 6.0	0.02
SLM - HTX	4.0 ± 1.8	0.3 ± 0.1	15.6 ± 6.8	0.81
SLM - HTY	4.4 ± 1.9	0.4 ± 0.2	13.2 ± 6.3	0.64
SLM - HTZ	2.9 ± 1.4	0.4 ± 0.2	8.1 ± 3.8	0.09
Wrought	2.6 ± 1.3	0.6 ± 0.2	4.9 ± 3.4	1.05

Based on heat treatments by others in the literature in similar temperature and time ranges, the values produced in SLM samples across all heat treatments are lower [212, 218]. For example, after 1 hour of precipitation treatment at 954 °C, approx. 1.5% δ phase volume fraction is achieved

[212], which is more comparable to the volume fraction for the current wrought samples, at 1.05%. The difference in SLM δ precipitation behavior compared to more traditionally manufactured material likely stems from the increased NbC populations. With more Nb occupied in stable NbC precipitates at the solution treatment temperatures, there is less Nb for δ precipitation.

Not only was there a variation in the δ phase volume fraction and content of the modified heat treatments, but also in their morphology relative to one another as well as the wrought samples. These dimensions are also shown in Table 22. First looking at the modified heat treatments, there is a steady decrease in the aspect ratio that correlates well with the decreasing volume % from HTX to HTY to HTZ. The increased aspect ratio in HTX and HTY is attributed to the hold at 900 °C, which promotes the formation of an acicular δ phase [215, 219]. The higher temperature treatment of HTZ, HT1, and wrought samples lead to a smaller aspect ratio, as the δ phase takes on a less acicular and more globular morphology [220, 221].

The wrought samples are noticeably more globular than those of all SLM parts, due in part to its thermomechanical processing. Careful forging operations can be used to bring out the spheroidal form of δ phase in wrought material. Hot working in the upper portion of the δ stability zone (980 °C – 1010 °C) can produce spheroidal δ within the microstructure [94]. A secondary effect of the formation of spheroidal δ is greater retention of Nb within the matrix, which promotes the formation of a greater amount of γ'' in subsequent aging steps. Zhang et al. [220] studied δ-processed IN718, and found that spheroidization occurs in material that has undergone significant working. They found that plate-like δ phase can transform into a globular morphology through dissolution and deformation breakage. Deformation breakage occurs during working, as dislocations build up in the plate-like δ phase particles and are eventually broken up into the globular morphology. These globular particles remain stable during subsequent heat treatment because of the lower phase interface energy around 950 °C for the globular morphology [220]. Mei et al. [222] also found a dependence of the δ phase on deformation prior to heat treatment. They found an increasing amount of spheroidization of needle-like δ phase as the degree of cold-rolling was increased. They attribute this phenomenon to the partial dissolution of needle-like δ phase particles and their subsequent growth of the globular phase [222].

5.3.3 Mechanical properties

The four tests performed in Chapter 4 were repeated for the novel heat treatments shown here: RTT, ETT, CRT, and CSR. This allows for a direct comparison of mechanical behavior, and to quantify the effects that the modified heat treatments have on SLM IN718.

5.3.3.1 Room Temperature Tensile

The room temperature tensile results are shown in a stress-strain plot in Figure 62 with tabulated metrics in Table 23. The results indicate that there is not a significant change in the room temperature properties with the modified heat treatments. Ductility remains the same, along with ultimate tensile strength. However, there is an increase in the yield strength in HTZ by approx. 10.2%. The increase in the yield strength is likely related to the improved precipitation of the γ'' phase in HTZ. A better distribution of alloying elements from the additional homogenization treatment facilitates better precipitation in the alloy. Although HTY receives the same homogenization treatment, it does not exhibit the same increase in the yield strength because of the additional precipitation of the δ phase. As more Nb is taken up in δ phase along the grain boundaries, there is less remaining in the matrix for γ'' precipitation. HT1, HTX, and HTY all have similar properties, and all heat treatments meet typical IN718 requirements. However, significant changes in the RTT properties were not expected to result from modified heat treatment because it is only in the elevated temperature regime where significant deviations from the standard are observed.

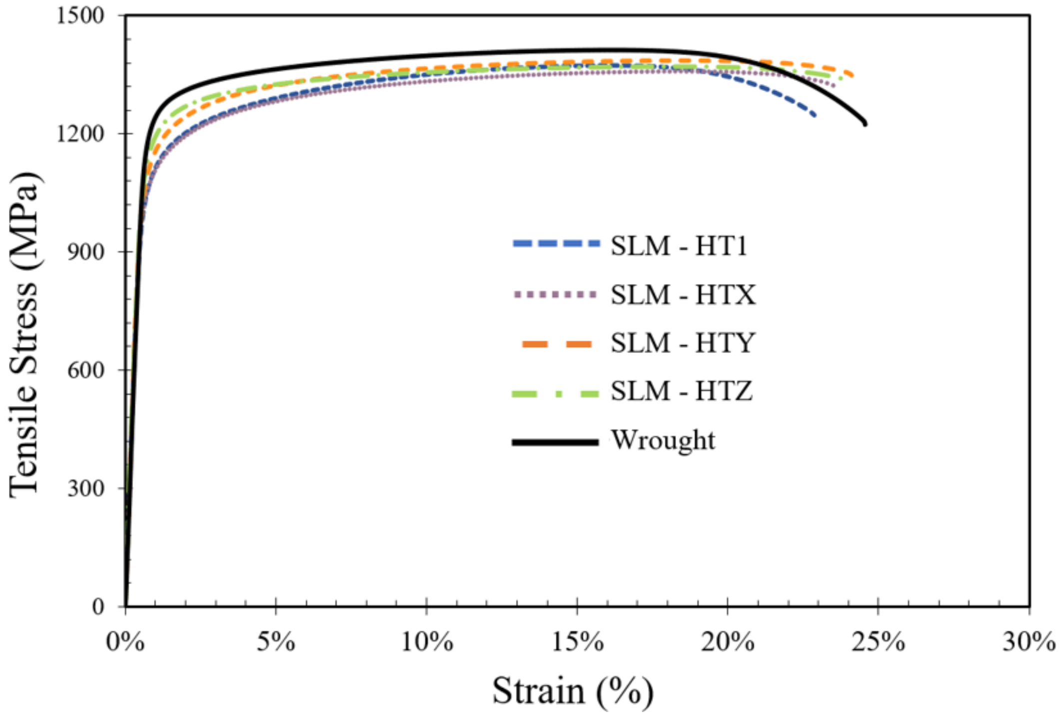

Figure 62: Stress-strain curves for the room temperature tension tests of modified heat treatment samples. No significant differences are observed aside from the increase of yield strength in HTZ.

Table 23: Room-temperature tensile properties of samples with modified heat treatments, compared to previously tested samples.

Sample	**Yield Strength**	**Ultimate Tensile Strength**	**Elastic Modulus**	**Elongation**
	MPa	**MPa**	**GPa**	**%**
SLM – HT1	1042.7 ± 5.1	1373.8 ± 2.5	207.5 ± 2.1	22.6 ± 1.3
SLM - HTX	1050.7 ± 17.3	1359.5 ± 18.3	197.2 ± 18.2	24.6 ± 0.6
SLM - HTY	1077.6 ± 12.0	1374.4 ± 23.7	205.5 ± 23.7	23.4 ± 0.8
SLM - HTZ	1149.5 ± 4.2	1375.1 ± 1.4	192.3 ± 1.4	23.6 ± 1.8
Wrought	1194.9 ± 10.7	1424.6 ± 15.1	208.9 ± 2.8	25.5 ± 2.0
AMS 5663 Min. Req. [98]	1034	1276	-	12

5.3.3.2 Elevated Temperature Tensile

Elevated temperature testing was carried out at 650 °C and a strain rate of $8.33 \cdot 10^{-5}$ s^{-1}, the same as the middle condition used in Chapter 4 for both strain rate and temperature variation testing. This condition was selected as it showed a high degree of environmental embrittlement and would therefore be sensitive to favorable changes induced in the microstructures. The stress-strain curves and tabulated values for ETT properties are seen in Figure 63 and Table 24, respectively. The strength values in ETT mirror those of the RTT tests, where HT1, HTX, and HTY have similar strengths, but HTZ shows an increase in both the yield and ultimate strengths. However, the most significant difference between the modified heat treatments and HT1 are the elongations and reductions of area, key ductility metrics. There is a drastic increase in the elongation for HTX, HTY, and HTZ of 155.1%, 106.9%, and 186.2%, respectively. Similar increases are seen for reduction of area.

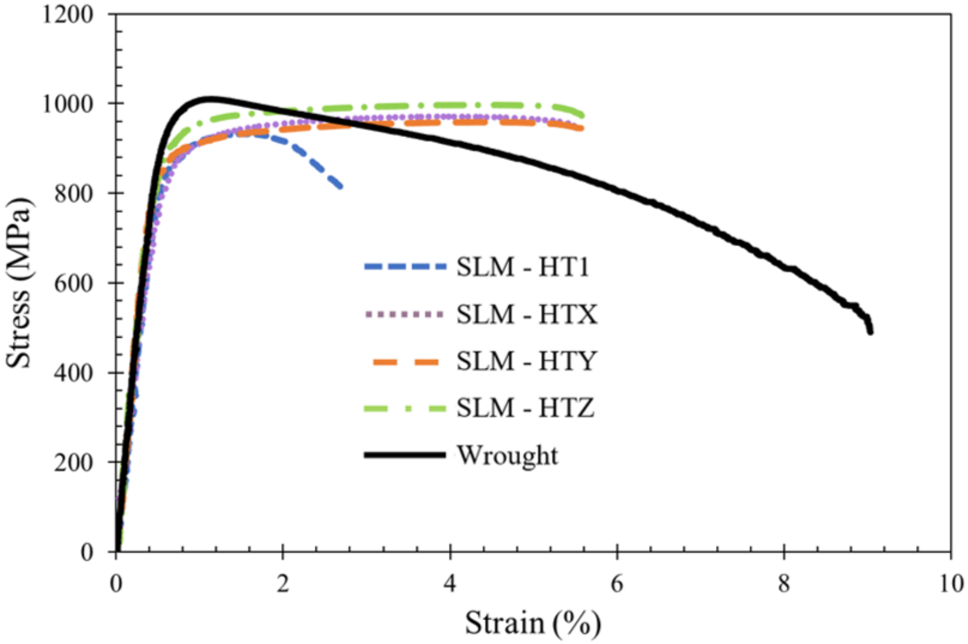

Figure 63: Elevated temperature stress-strain curves of the modified heat treatment samples compared to HT1 and wrought material.

Table 24: Elevated-temperature tensile properties of modified heat treatment samples compared to previous results.

Sample	**Yield Strength**	**Ultimate Tensile Strength**	**Elongation**	**Reduction of Area**
	MPa	**MPa**	**%**	**%**
SLM – HT1	875.6 ± 17.1	940.4 ± 11.7	2.9 ± 0.4	5.9 ± 0.9
SLM - HTX	875.4 ± 4.5	974.2 ± 4.5	7.4 ± 1.1	13.6 ± 1.1
SLM - HTY	868.7 ± 19.8	953.8 ± 27.3	6.0 ± 1.1	13.8 ± 0.7
SLM - HTZ	931.0 ± 5.8	1003.9 ± 5.7	8.3 ± 1.1	11.6 ± 1.3
Wrought	977.7 ± 15.6	1023.9 ± 19.3	17.8 ± 1.0	52.4 ± 4.9
AMS 5663 Min. Req. [98]	862	1000	12	15

Improvements in the elongation can be attributed to the enhanced precipitation of the δ phase in HTX and HTY, and the better distribution of NbC in HTZ. More δ phase allows for increased plasticity near the grain boundaries for samples that underwent a δ dump heat treatment. KAM maps generated for post-mortem sectioned surfaces of HTX and HTZ are shown in Figure 64. While both samples show deformation similar to those of previous ETT in Figure 52, HTX contains a larger amount of deformation near the grain boundaries, resulting in large degrees of non-solution EBSD pixels. This behavior is similar to those of wrought material tested in ETT, which also contained many non-solutions near the GBs due to excessive deformation.

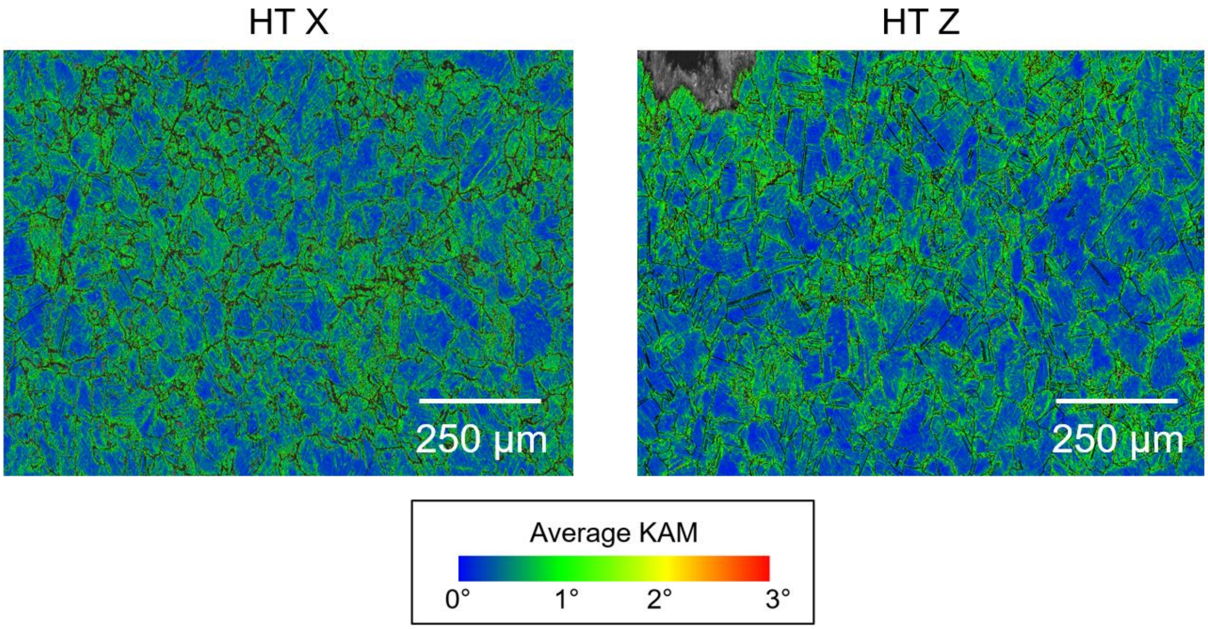

Figure 64: KAM maps of the HTX and HTZ samples, showing similarities in local misorientation, but a higher amount of dislocation accumulation in the δ-rich HTX sample.

Despite improvements in the ductility, it appears that the MHT samples remain environmentally sensitive based on the appearance of the fracture surfaces. Shown in Figure 65, the fracture surfaces for all MHTs show signs of intergranular fracture that is similar in appearance to those observed in Chapter 4. The dashed red line represents the area separating the intergranular and transgranular regions. All samples failed in similar timeframes, and exhibit a similar degree of penetration into the fracture surface.

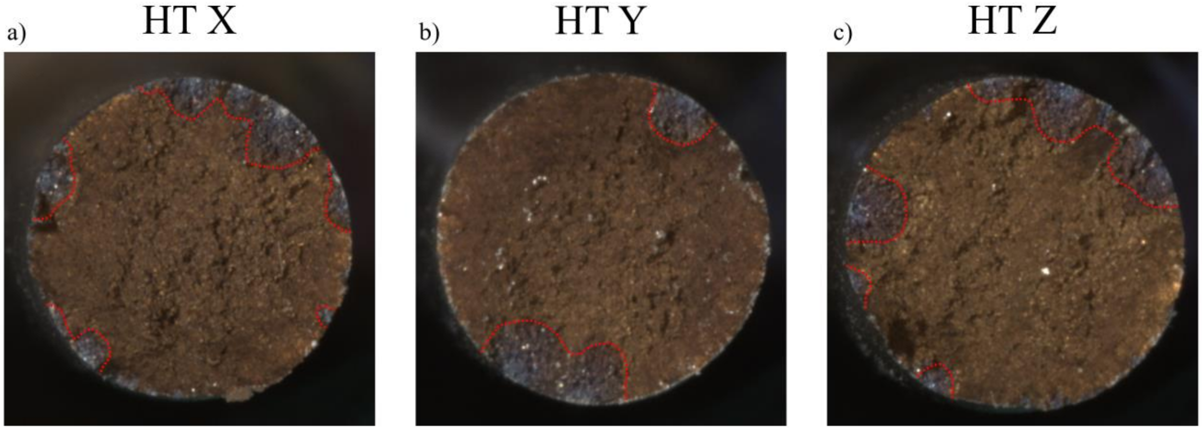

Figure 65: a) HTX ETT fracture surface. b) HTY ETT fracture surface. c) HTZ ETT fracture surface. All sample demonstrate similar oxidation patterns and regions of intergranular failure.

SEM images of the fracture surfaces for HTX and HTZ are shown in Figure 66. These two samples represent the intergranular failures for a sample containing the delta dump HT as well as the additional homogenization step; HTY was omitted as it is similar in appearance to HTX. The intergranular fractures reveal a rough intergranular failure in the HTX condition, and a smoother failure in the HTZ grains. This difference is attributed to the population of grain boundary δ phase that extends inwards towards the grain centers. A crack propagating along the grain boundary δ phase will have a more tortuous path through the material, as it will be affected by local deformation near the grain boundaries in the PFZ. The HTZ sample, with limited δ precipitation similar to HT1, does not show evidence of deformation near the grain boundary on the fracture surface. Smooth intergranular failure can be seen throughout the structure. However, the increased distribution of the NbC particles within the Z structure due to improved homogenization is attributed for the increase in elongation in these materials.

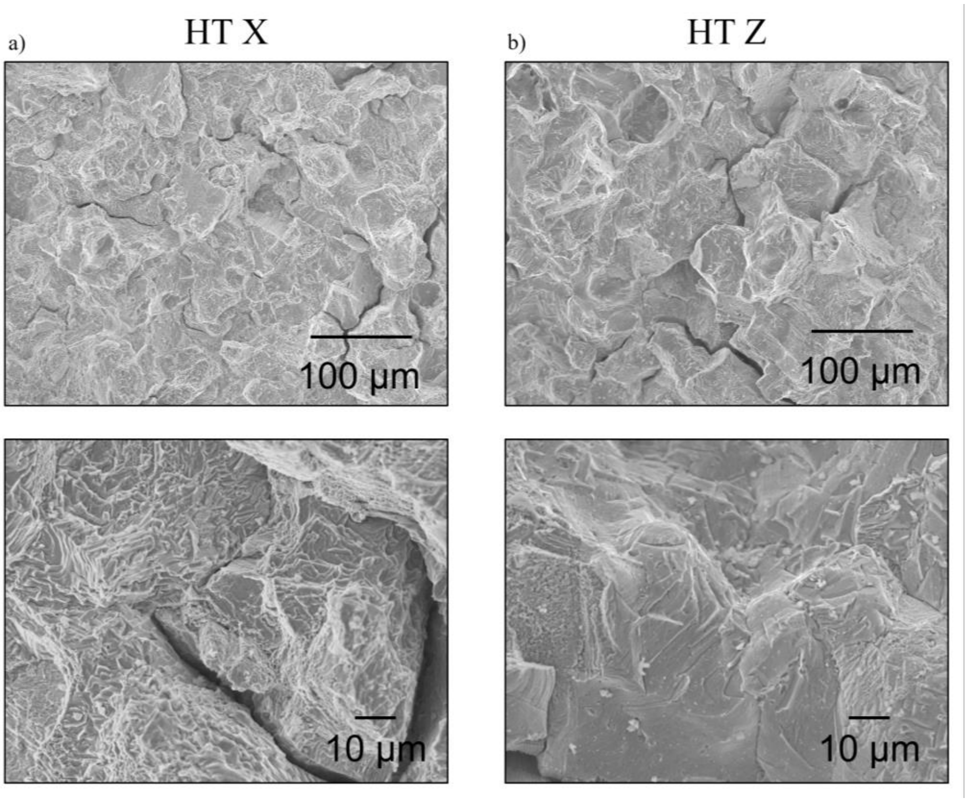

Figure 66: Detailed SEM images of the a) HTX and b) HTZ fracture surfaces showing the regions of intergranular fracture at 250x and 1000x magnifications.

5.3.3.4 Combination Stress Rupture

Combination stress rupture testing was performed to determine if the modified heat treatments could alleviate notch sensitivity in SLM material. Tests were conducted in both laboratory air and an argon backfilled vacuum environment, the results of which can be seen in Table 25. The tests in air yielded notch failures for all heat treatments with 0% elongation; all samples were deemed notch sensitive in air. Some improvement was observed in the time to rupture in all MHT as compared to HT1, with the biggest increase coming in HTX, as the rupture time increased from 3 hrs. to 21 hrs. This change is attributed to the large δ population from HTX, as well as the small grain size. Looking again to the results of Li et al. [211], who compared a δ-rich IN718 sample to a δ-lean one, they observed a much larger time to crack initiation in compact tension samples in the δ-rich samples. A similarity is shown here, since both tests are initiated in the presence of a stress concentration. The δ population on the GBs provides much needed localized plasticity, which can relax the effects of a stress concentration. Despite this improvement, there is still environmental sensitivity in these samples, likely due to the carbide population and inability for the material to disperse the oxygen diffusing down grain boundaries.

Table 25: CSR results at 650 °C and 690 MPa for modified heat treatments.

Sample	**Time to Failure**	**Elongation**	**Failure Location**	**Final Load**
	hr.	**%**	**-**	**MPa**
SLM – HT1, Air	3 ± 1	0	Notch	690
SLM – HTX, Air	21 ± 5	0	Notch	690
SLM – HTY, Air	8.6 ± 10	0	Notch	690
SLM – HTZ, Air	13.3 ± 1	0	Notch	690
SLM – HTY, Vacuum/Argon	29.8 ± 5	0	Notch	741
SLM – HTZ, Vacuum/Argon	14.5 ± 8	5.9	Notch/Smooth	690
Wrought	61 ± 9	27 ± 8	Smooth	896
AMS 5663 Min. Req. [98]	23	4	Smooth	N/A

Further testing was conducted in an Ar-backfilled vacuum environment to isolate the variable of the environment when comparing to previous tests. This testing demonstrated an improvement in the time to rupture of the SLM samples. Both specimens tested for HTY exceeded the 23-hour requirement, and one sample from HTZ failed in the smooth section, meeting the elongation requirement but not the time to failure. The dramatic increase in performance in an inert environment is an indication that the notch sensitivity and reduced elevated temperature ductility is due to a reaction with the environment. However, observations of the fracture surfaces in these samples reveal that the environment was not devoid of oxygen, as shown in Figure 67.

The vacuum level prior to backfilling only reached 76 torr, and so was not completely evacuated prior to the Ar backfill. The residual oxygen in the testing environment may have reacted with the samples. The same oxidation fracture pattern is observed for these samples, indicating the presence of oxygen during testing and its reaction with the samples. However, this process of inertization will result in a decreased oxygen concentration, which was shown to improve the CSR performance. A decrease in the depth of penetration of the oxidized area is observed in both samples tested in an inert environment. A similar effect is seen in the testing by Valerio et al. [207] when analyzing creep crack growth rates in air and Ar. They found a significantly faster crack growth rate in air when compared to Ar, attributing increased sensitivity to the reaction of NbC and segregated Nb at the grain boundaries with oxygen.

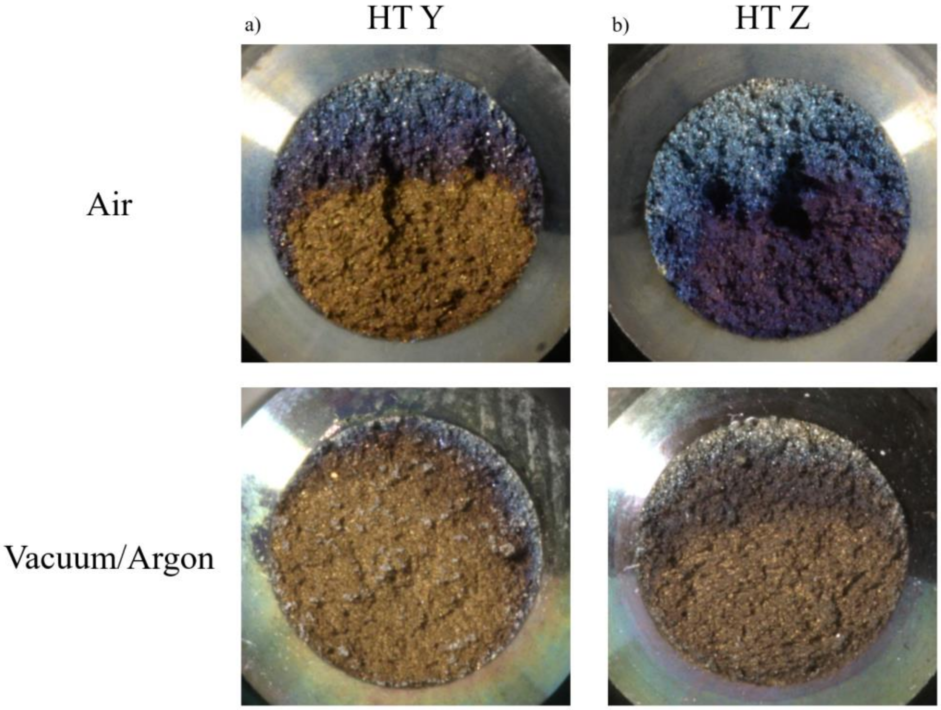

Figure 67: CSR fracture surfaces showing a) HTY in air and inert environments, and b) HTZ in ir and inert environments. Intergranular cracking transitioning to transgranular failure is observed regardless of the testing environment.

5.3.3.5 Creep Rupture

The creep rupture testing of modified heat treatment samples was carried out in the same way as prior samples, at 650 °C and a constant load of 690 MPa. Creep curves are shown in Figure 68. HTX and HTY show a decrease in the time to rupture compared to HT1. HTY has a very similar elongation value as HT1, while HTX is lowered. On the other hand, HTZ is shown to have a similar time to rupture, as well as elongation, showing no obvious differences from HT1. From the creep curves, the onset of the tertiary creep regime in HTX and HTY samples is much faster than that of HT1 or HTZ, likely contributing to the decreased time to rupture.

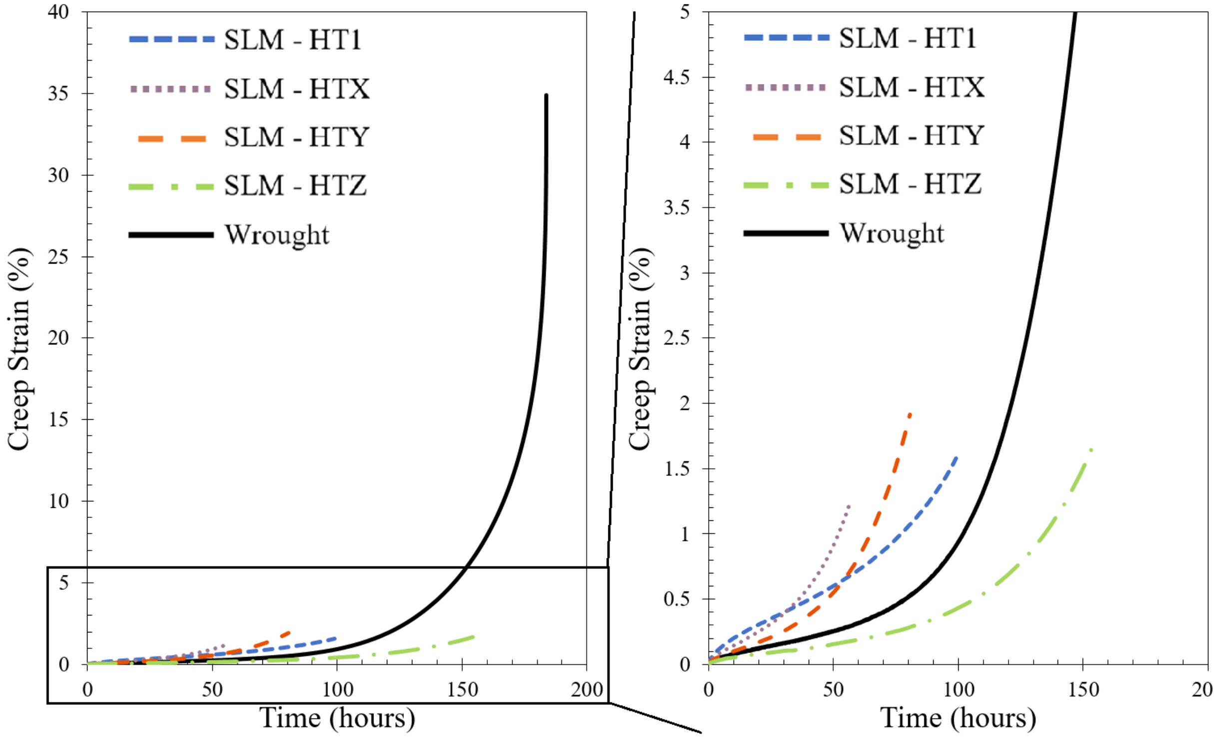

Figure 68: Creep rupture curves for the modified heat treatment samples, showing the rapid onset of the tertiary regime in HTX and HTY, which leads to a shortened time to rupture.

Table 26: CRT results at 650 °C and 690 MPa for samples with the modified heat treatments.

Sample	**Time to Rupture**	**Elongation**	**Minimum Creep Rate**
	hours	**%**	**hr^{-1}**
SLM – HT1	114 ± 17	5 ± 2	$3.8\cdot10^{-5} \pm 3.2\cdot10^{-5}$
SLM - HTX	66.1 ± 11.9	3.1 ± 0.4	$8.9\cdot10^{-5} \pm 1.8\cdot10^{-6}$
SLM - HTY	82.8 ± 0.9	5.0 ± 0.2	$7.3\cdot10^{-5} \pm 1.1\cdot10^{-5}$
SLM - HTZ	139.5 ± 21.9	4.6 ± 0.9	$1.2\cdot10^{-5} \pm 1.3\cdot10^{-6}$
Wrought	184.5 ± 0.7	37.2 ± 3.2	$1.0\cdot10^{-5} \pm 1.6\cdot10^{-6}$
AMS 5663 Min. Req. [98]	24	4	-

The poor performance of HTX and HTY samples may be related to the distribution and morphology of the δ phase. Although these heat treatments were successful in precipitating large amounts of the δ phase with respect to the original HT1 samples, the morphology was highly acicular when compared to the wrought δ phase. The literature suggests that the acicular phase can be detrimental to creep rupture lifetimes and ductility, whereas the globular phase is more beneficial in elevated temperature environments. Desvalles et al. [107] found that the acicular δ phase acts as a preferential site for cavity growth during creep testing and is harmful to the microstructure in comparison to the more spheroidal/globular morphology. This different may explain why samples with large amounts of the acicular phase—HTX and HTY—display shorter times to rupture and poor elongation when compared to HT1 and HTZ. Furthermore, the beneficial spheroidal form of the δ phase, as observed in the wrought material in Figure 69 may be a contributing factor in its increased elevated temperature ductility. Li et al. [211] specifically cite the globular δ phase as the beneficial phase in a study on rack propagation in Inconel 718. They argue that the localized ductility imparted by these precipitates at grain boundaries effectively blunts crack tips and prevents further propagation. They also noticed that δ phase precipitated in excess will result in a degraded strength that cannot meet specifications; a careful balance is necessary.

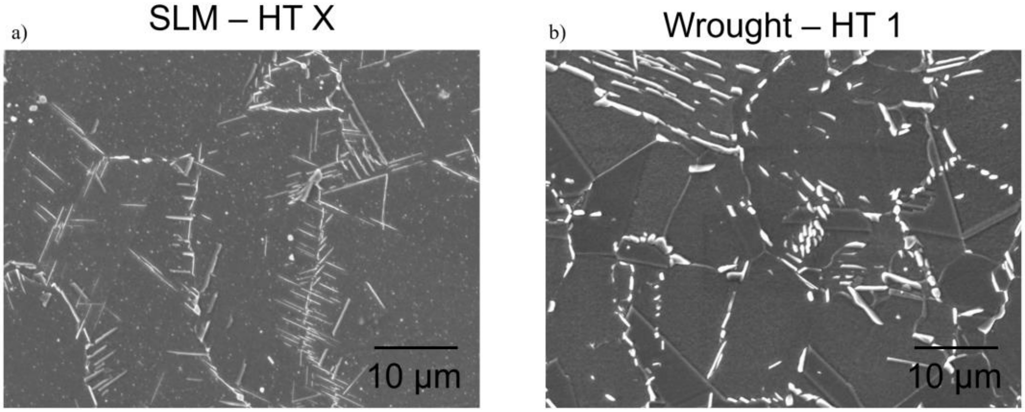

Figure 69: The difference in δ phase precipitation between a) SLM HTX and b) W – HT1. The wrought sample has a thicker and more globular δ phase morphology when compared to the thin plate-like δ phase precipitates of HTX.

The deleterious effects of the acicular δ phase are not observed in ETT or CSR; the primary differences are in elongation and times to rupture of HTX and HTY in CRT. This is because the increased propensity for cavity nucleation is only brought out by the slow strain rates and low stresses of the creep test. In ETT there is not a large degree of cavity formation, the high stresses cause dislocation movement and faster failure. Localized plasticity in the case of ETT is beneficial to the properties and results in enhanced ductility. In the presence of a stress concentration like in the CSR test, the increased plasticity will also enhance crack propagation resistance, providing an increased time to failure in HTX and HTY samples. The effects of dynamic embrittlement and eventual intergranular failure are present from the onset of the CSR test; the deformation of the microstructure is therefore isolated to the local vicinity of the growing crack tip. The formation and coalescence of cavities does play a role in determining CSR properties for notch-sensitive materials. Furthermore, in CRT there are other mechanisms in play such as grain boundary sliding, which can enhance the formation of cavities [223].

Fracture surfaces for the modified heat treatment CRT samples can be seen in Figure 70. Both SEM and macro-scale optical images are included and show that the MHT fracture surfaces are characterized by a dual intergranular and transgranular fracture surface similar to all previous SLM samples. There is evidence of the same intergranular propagation that is attributed to dynamic embrittlement; the slow opening at the crack tip produces a gradient of oxide thickness as it progresses towards the sample center. The HTZ sample's intergranular surface area spans more colors than the HTX and HTY samples, indicative of the slower crack propagation in this sample which corresponds well with the longer rupture life.

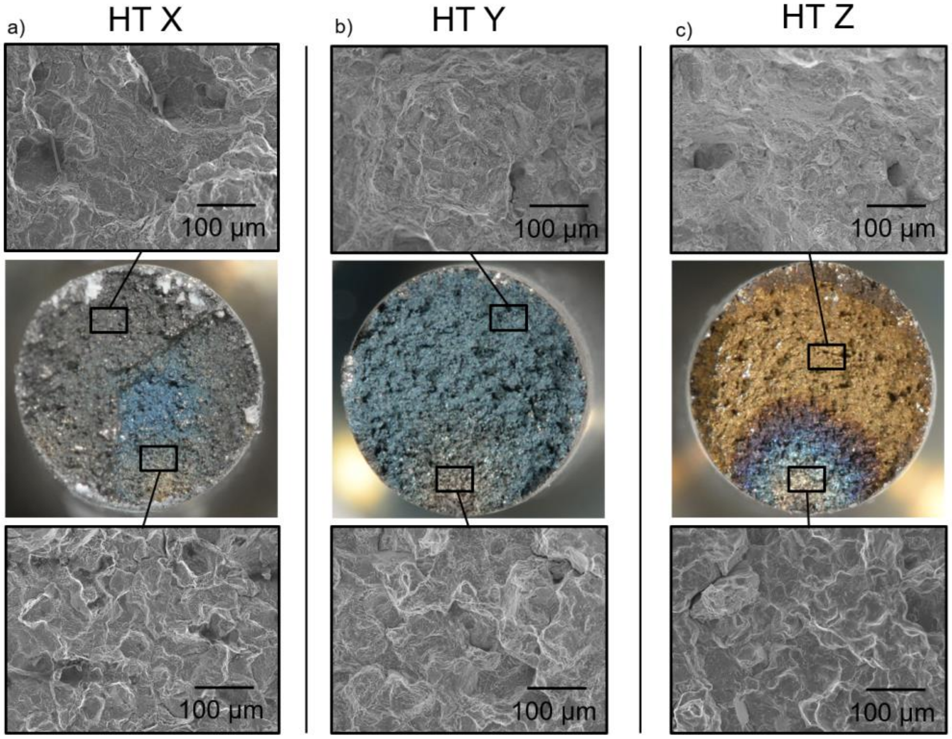

Figure 70: Fractography of a) HTX, b) HTY, and c) HTZ. All samples feature the gradient oxide pattern that is characteristic of intergranular failure as a result of environmental attack that was seen previously.

5.4 Summary

Modified heat treatments of IN718 were utilized in order to address the microstructural features that render SLM IN718 excessively brittle in elevated temperature testing. Previously it was observed that the low δ phase volume fraction may inhibit the redistribution of stresses in the vicinity of a crack tip, which can lead to notch sensitivity and enhanced crack propagation behavior. Furthermore, an excessive amount of NbC was found in the microstructure which may enhance crack propagation through a reaction with the environment and depletes Nb that could be used to precipitate strengthening phases. The modified heat treatments were found effective in precipitating volume fractions of δ phase more similar to that of wrought material, as well as decreasing the NbC population.

The modified heat treatments were found to have a minimal effect on the room temperature properties, but a beneficial effect in ETT and CSR. CRT properties were worsened in samples featuring the δ dump heat treatment, evidenced by the shorter times to rupture and lower elongation values when compared to the original SLM heat treatment. Despite the improvements in properties, the fractography of elevated temperature samples revealed the persistence of the same environmentally sensitive embrittling mechanism observed in Chapter 4.

Room temperature tensile testing demonstrated an improved yield strength in HTZ samples, but no other significant deviations resulted from typical HT1 properties. The additional homogenization followed by air cool resulted in a better distribution of alloying elements and led to an improved γ’’ precipitation. However, samples were still not up to the level of wrought strength.

In ETT testing, the improved ductility is attributed to both the increased precipitation of the δ phase in HTX and HTY and the more dispersed NbC population in HTZ. The δ phase allows for increased ductility, as well as the reduction of stress concentration in the presence of a surface connected microcrack. The improved NbC distribution will inhibit reactions with the environment and slow the crack propagation in these samples, without eliminating it. Fractography revealed crack propagation and intergranular failure for all samples, with similar depths of penetration into the sample. The effects of dynamic embrittlement are still active in MHT samples.

CSR testing showed an improved rupture life for similar reasons, where δ phase could help to relax the stress concentration, and limited NbC particles decreased the rate of crack propagation. All modified heat treatments still resulted in notch failures though, as the environmental embrittlement mechanism persisted. Testing in a semi-inert environment showed a further improvement in the CSR performance; with less oxygen present in the testing environment, samples showed an improvement in the time to rupture and one sample demonstrated notch ductility. The fracture surfaces in the inert environment had evidence of intergranular crack propagation but was shown to be less severe than typical testing in laboratory air.

CRT testing did not demonstrate improved ductility, but actually showed a decrease in the rupture lives and elongations of HTX and HTY samples. HTZ samples behaved similarly to HT1. The decrease in rupture life is attributed to the non-ideal morphology of δ phase precipitates, which may facilitate microcracking in the matrix during initial deformation. This cracking, when coupled with environmental attack led to premature failure, but only appeared in the slow strain rates and long duration of the creep test. The current heat treatments promote the formation of a more acicular δ phase, whereas the ideal morphology is more spheroidal. Further optimization of δ phase heat treatments is necessary to produce the correct morphologies, which may further enhance the elevated temperature performance of SLM IN718.

Despite the observed improvements in ductility, environmental cracking dominated the elevated temperature behavior of MHT samples. While further improvements can be achieved in the δ phase morphology and distribution, the elimination of NbC from the matrix may require a different approach. Research into the use of a raw material with a reduced carbon content is necessary, as heat treatments are not able to fully remove the NbC from the matrix. This research, in combination with an optimized δ phase heat treatment may be beneficial in restoring elevated temperature ductility to SLM IN718.

Chapter 6: Conclusion

The current work has investigated the effects of SLM process parameters on microstructures in the AB condition and related them to the final material properties in terms of both microstructures and mechanical behavior. It was found that the solidification mechanisms and resulting AB microstructures were heavily dependent on the local heat flow conditions. The laser focal shift and scanning strategy were both found to alter the solidification pathways within SLM material.

The focal shift could be used to alter the spot size and the resulting laser-powder interaction volume during the melting process. Using the smallest spot size at the focal plane resulted in narrow and deep melt pools that facilitated the nucleation of many grains through multi-directional heat flow, dendrite fragmentation, and large thermal gradients. Larger spot sizes achieved through shifts away from the focal plane resulted in shallow and wide melt pools with a less severe and more uniformly oriented thermal gradient. The result was a more columnar microstructure, with grains growing epitaxially from one layer to the next. Larger grains with a more apparent crystallographic texture were observed in this condition because of the aligned solidification pathways induced by the change in melt pool geometry.

While the focal shift served to align heat flow within individual melt pools at a local scale, the scanning strategy aligned the heat flow between melt pools on a larger scale. The continuous strategy made adjacent laser scan vectors parallel to one another, eliminating offsetting effects induced by multi-directional island scanning. Shifting the laser scan vectors to better align with one another resulted in further alignment of the microstructures; longer, more heavily textured grains could be achieved through a combination of laser defocusing and continuous parallel scans.

Modifications to the AB SLM structure impacted the fully heat-treated microstructures. The high temperature HIP and solution treatments did not eliminate the AB structures; the final grain size, grain morphology, crystallographic texture, and precipitate distribution were all significantly affected by the changes in the process parameters. Samples that were produced with more uniform solidification pathways produced columnar grains elongated parallel to the building direction, while those with multi-directional heat flow produced finer and more equiaxed microstructures. Furthermore, the distribution of NbC in the SLM microstructures was related to the original orientation of dendritic growth. The interdendritic regions that form during solidification are enriched in Nb due to elemental segregation, and their orientation within the microstructure determines the resulting NbC distribution. The short, randomly oriented dendrites of samples with multi-directional heat flow produce more randomly oriented NbC throughout the microstructure while long, highly columnar dendrites produce BD-parallel stringers of NbC. The effects of these altered microstructures were analyzed for their effect on mechanical performance in comparison to one another as well as standard wrought IN718.

The room temperature tensile behavior showed little to no variation among SLM-processed material despite the variations in microstructure. Similar heat treatments produced nearly identical distributions of the strengthening phases. Wrought-processed samples exhibited a higher yield strength than SLM samples, accounted for by the smaller γ’’ particle size. Although RTT can be a strong indicator of a material’s response to heat treatment, it does not differentiate between different microstructural scales and textures for IN718.

Moving into the elevated temperature regime, significant differences became apparent between the mechanical properties of samples produced through process parameter variation. These differences trended positively with microstructural scale and morphological alignment.

Furthermore, large disparities emerged when comparing SLM to typical wrought standards and wrought material tested in parallel.

CRT revealed the first separation of properties observed for SLM material. It was found that increased times to rupture and elongations could be achieved in microstructures that were more heavily aligned to the building direction. With a decreased amount of GB area oriented transverse to the loading direction, profuse nucleation of microcracks could be avoided. Furthermore, the vertically aligned distribution of NbC in the microstructure created a more tortuous path of crack propagation when compared to the more random alignment in fine-grained samples. However, despite these improvements in the creep properties, the SLM material is far less ductile in creep than wrought counterparts. An investigation into the deformation mechanisms and failure mode revealed profuse intergranular cracking in all SLM materials that was related to a gas-phase embrittlement known as dynamic embrittlement. Wrought samples did not exhibit this same behavior. The GB diffusion of O can cause local decohesions as well as reactions with NbC, which can enhance crack growth through local stress risers. Environmental attack led to premature failure and elevated temperature embrittlement in SLM material.

CSR testing revealed another discrepancy between wrought and SLM material in the form of notch sensitivity. All SLM samples were found to fail in the notched portion of the CSR sample, indicating an inability to relieve a stress concentration. Furthermore, the fracture surfaces revealed a similar intergranular failure to what was observed in CRT. A primary difference between the wrought and SLM microstructures was the δ phase population. The effects of the δ phase on notch sensitivity was studied for IN718 in wrought material, and it was found that the absence of the δ phase leads to rapid intergranular failure and notch sensitivity in CSR. The δ phase imparts localized plasticity near grain boundaries through the formation of a precipitate free zone. Without this effect a stress concentration cannot be relieved and will eventually lead to crack propagation. The SLM samples, which lack δ phase, suffer from both a vulnerability to stress concentrations and environmental embrittlement. This combination leads to the notch sensitivity observed in CSR testing and degrades the elevated temperature integrity of this material.

ETT testing allowed for the analysis of the kinetic and thermal aspects of environmental sensitivity in SLM samples; testing was performed at multiple strain rates and temperatures. It was found that at all strain rates and test temperatures the wrought material had a higher ductility and strength than SLM samples. However, at the fastest strain rates and lowest test temperatures, the elongation of SLM material significantly improved. Faster strain rates will reduce the time available for diffusion to occur, and therefore reduce the degree of embrittlement that can be achieved. It was found that the deformation mechanisms across the strain rate levels were the same between SLM and wrought material, reflected by equal values of the strain rate sensitivity. While the fracture surfaces of these samples revealed the presence of intergranular crack propagation in all samples, the depth of penetration was much lower in the fast strain rate samples. Lower test temperatures decrease the thermal energy available for diffusion and resulted in an improvement in the elevated temperature ductility as well. Based on the analysis of the fracture surfaces, an activation energy was calculated for the embrittling process that was in line with that of a mixture of oxygen and hydrogen diffusion along grain boundaries, confirming the mechanism of environmental attack in these samples.

The elevated temperature environmental embrittlement observed in SLM material is related to both an inability to blunt crack tips through a lack of δ phase and an increased susceptibility to crack propagation because of the large and continuous NbC networks. To address these microstructural shortcomings, modified heat treatments were developed specifically for

SLM material, featuring three combinations of two novel processes—a higher temperature homogenization to drive dissolution of NbC and a longer hold within the δ stability range.

The resulting microstructures from modified heat treatment were successful in reducing the NbC population and increasing the δ phase along grain boundaries. The resulting mechanical properties reflected these changes in ETT and CSR. The ETT ductility was found to increase in all three modified heat treatments, and improvements in time to rupture were also noted in CSR. However, both tests failed via environmental attack and intergranular crack propagation. CRT testing showed a decrease in the mechanical performance of samples that were given the δ phase treatment. Analysis of these phases uncovered a difference in the morphology of these precipitates when compared to wrought material. The more acicular morphology promotes microcracking in CRT and led to premature failure that was coupled with the environmental embrittlement mechanism observed earlier.

The shortcomings of the current modified heat treatments point us in a new direction for addressing elevated temperature embrittlement in SLM IN718. Although high temperature homogenization treatment was effective in reducing the NbC population, it was not able to fully eliminate it or bring it to the level of wrought material. Therefore, the production of a new alloy formulation is of great interest; a reduction in the initial carbon content of the powder could prevent the formation of NbC in the first place, eliminating the need for higher temperature homogenization treatments. Further optimization of the δ phase morphology is also necessary in addressing elevated temperature behavior. The spheroidization of this phase would serve to improve stress rupture behavior and improve notch ductility. Further research into both areas is necessary.

The current work has demonstrated the immense potential for microstructural control and manipulation in SLM-manufactured parts. Although the current material is IN718, the understanding of microstructural formation and solidification kinetics presented here can be applied across many different alloys systems. The comparisons between these microstructures and the fully heat-treated condition has definitively shown the influence the AB structure can have on final material performance. Furthermore, the link to mechanical properties provides current users with a relevant point of comparison to wrought material.

The finding of environmental sensitivity in SLM material as it relates to microstructural constituents formed by typical post-processing is a critical finding of the current work. A thorough understanding of elevated temperature behavior for this alloy has not yet been presented in the literature, and the current findings will hopefully bring these issues into the light. Further research into this topic will expand the capabilities of SLM IN718 by building confidence in its structural integrity and demonstrating its appropriateness as a drop-in replacement for wrought material used in the aerospace industry today.

References

1. Sun, J., Y. Yang, and D. Wang, *Parametric optimization of selective laser melting for forming Ti6Al4V samples by Taguchi method.* Optics & Laser Technology, 2013. **49**: p. 118–124.

2. Dilip, J.j.s., et al., *Influence of processing parameters on the evolution of melt pool, porosity, and microstructures in Ti-6Al-4V alloy parts fabricated by selective laser melting*. Vol. 2. 2017.

3. Thijs, L., et al., *Fine-structured aluminium products with controllable texture by selective laser melting of pre-alloyed AlSi10Mg powder.* Acta Materialia, 2013. **61**(5): p. 1809-1819.

4. Sateesh, N.H., et al., *Microstructure and Mechanical Characterization of Laser Sintered Inconel-625 Superalloy.* Procedia Materials Science, 2014. **5**: p. 772-779.

5. Murr, L.E., et al., *Fabrication of Metal and Alloy Components by Additive Manufacturing: Examples of 3D Materials Science.* Journal of Materials Research and Technology, 2012. **1**(1): p. 42-54.

6. Seede, R., et al., *Microstructural and microhardness evolution from homogenization and hot isostatic pressing on selective laser melted Inconel 718: structure, texture, and phases.* Journal of Manufacturing and Materials Processing, 2018. **2**(2): p. 30.

7. Wang, X. and K. Chou, *Effects of thermal cycles on the microstructure evolution of Inconel 718 during selective laser melting process.* Additive Manufacturing, 2017. **18**: p. 1-14.

8. Wang, X., T. Keya, and K. Chou, *Build height effect on the Inconel 718 parts fabricated by selective laser melting.* Procedia Manufacturing, 2016. **5**: p. 1006-1017.

9. Wang, Z., et al., *The microstructure and mechanical properties of deposited-IN718 by selective laser melting.* Journal of Alloys and Compounds, 2012. **513**: p. 518-523.

10. Kanagarajah, P., et al., *Inconel 939 processed by selective laser melting: Effect of microstructure and temperature on the mechanical properties under static and cyclic loading.* Materials Science and Engineering: A, 2013. **588**: p. 188-195.

11. Martin, J.H., et al., *3D printing of high-strength aluminium alloys.* Nature, 2017. **549**(7672): p. 365-369.

12. Mumtaz, K., E. Poonjolai, and N. Hopkinson, *High density selective laser melting of Waspaloy (R).* Journal of Materials Processing Technology, 2008. **195**: p. 77-87.

13. Dietrich, S., et al., *A New Approach for a Flexible Powder Production for Additive Manufacturing.* Procedia Manufacturing, 2016. **6**: p. 88-95.

14. Abu-Lebdeh, T.M., et al., *Gas atomization of molten metal: part II. Applications.* American Journal of Engineering and Applied Sciences, 2016. **9**(2).

15. Sames, W.J., et al., *The metallurgy and processing science of metal additive manufacturing.* International Materials Reviews, 2016. **61**(5): p. 315-360.

16. Uhlmann, E., et al., *Additive Manufacturing of Titanium Alloy for Aircraft Components.* Procedia CIRP, 2015. **35**: p. 55-60.

17. Abu-Lebdeh, T., et al., *Powder Packing Density and Its Impact on SLM-Based Additive Manufacturing*. 2019. p. 355-367.

18. Gürtler, F.-J., et al., *Influence of powder distribution on process stability in laser beam melting: Analysis of melt pool dynamics by numerical simulations*. Vol. 25. 2014.

19. Spierings, A.B., et al., *Powder flowability characterisation methodology for powder-bed-based metal additive manufacturing.* Progress in Additive Manufacturing, 2016. **1**(1): p. 9-20.

20. Cordova, L., M. Campos, and T. Tinga, *Revealing the Effects of Powder Reuse for Selective Laser Melting by Powder Characterization.* JOM, 2019. **71**(3): p. 1062-1072.

21. Ardila, L.C., et al., *Effect of IN718 Recycled Powder Reuse on Properties of Parts Manufactured by Means of Selective Laser Melting.* Physics Procedia, 2014. **56**: p. 99-107.

22. Popovich, V.A., et al., *Functionally graded Inconel 718 processed by additive manufacturing: Crystallographic texture, anisotropy of microstructure and mechanical properties.* Materials & Design, 2017. **114**: p. 441-449.

23. David, S.A. and J.M. Vitek, *Correlation between solidification parameters and weld microstructures.* International Materials Reviews, 1989. **34**(1): p. 213-245.

24. Yadroitsev, I., et al., *Energy input effect on morphology and microstructure of selective laser melting single track from metallic powder.* Journal of Materials Processing Technology, 2013. **213**(4): p. 606-613.

25. King, W.E., et al., *Observation of keyhole-mode laser melting in laser powder-bed fusion additive manufacturing.* Journal of Materials Processing Technology, 2014. **214**(12): p. 2915-2925.

26. Rai, r.r., et al., *Heat transfer and fluid flow during keyhole mode laser welding of tantalum, Ti–6Al–4V, 304L stainless steel and vanadium.* Journal of Physics D: Applied Physics, 2007. **40**: p. 5753.

27. Calandri, M., et al., *Texture and Microstructural Features at Different Length Scales in Inconel 718 Produced by Selective Laser Melting.* Materials, 2019. **12**(8): p. 1293.

28. Moussaoui, K., et al., *Effects of Selective Laser Melting additive manufacturing parameters of Inconel 718 on porosity, microstructure and mechanical properties.* Materials Science and Engineering: A, 2018. **735**: p. 182-190.

29. Sun, S.-H., K. Hagihara, and T. Nakano, *Effect of scanning strategy on texture formation in Ni-25 at.% Mo alloys fabricated by selective laser melting.* Materials & Design, 2018. **140**: p. 307-316.

30. Cao, J., et al., *Effect of overlap rate on recrystallization behaviors of Laser Solid Formed Inconel 718 superalloy*. Vol. 45. 2013. 228-235.

31. Helmer, H.E., C. Körner, and R.F. Singer, *Additive manufacturing of nickel-based superalloy Inconel 718 by selective electron beam melting: Processing window and microstructure.* Journal of Materials Research, 2014. **29**(17): p. 1987-1996.

32. Dehoff, R.R., et al., *Crystallographic texture engineering through novel melt strategies via electron beam melting: Inconel 718.* Materials Science and Technology, 2015. **31**(8): p. 939-944.

33. Dehoff, R.R., et al., *Site specific control of crystallographic grain orientation through electron beam additive manufacturing.* Materials Science and Technology, 2015. **31**(8): p. 931-938.

34. Chauvet, E., et al., *Producing Ni-base superalloys single crystal by selective electron beam melting.* Scripta Materialia, 2018. **152**: p. 15-19.

35. Zhang, D., et al., *Effect of standard heat treatment on the microstructure and mechanical properties of selective laser melting manufactured Inconel 718 superalloy.* Materials Science and Engineering: A, 2015. **644**: p. 32-40.

36. Porter, D.A., K.E. Easterling, and M. Sherif, *Phase Transformations in Metals and Alloys (Revised Reprint)*. 2009: CRC Press.

37. Glicksman, M.E., *Principles of Solidification: An Introduction to Modern Casting and Crystal Growth Concepts*. SpringerLink : Bücher. 2010: Springer New York.

38. Ghosh, S., et al., *On the primary spacing and microsegregation of cellular dendrites in laser deposited Ni–Nb alloys.* Modelling and Simulation in Materials Science and Engineering, 2017. **25**(6): p. 065002.

39. Chlebus, E., et al., *Effect of heat treatment on the microstructure and mechanical properties of Inconel 718 processed by selective laser melting.* Materials Science and Engineering: A, 2015. **639**: p. 647-655.

40. Dantzig, J.A. and M. Rappaz, *Solidification: 2nd Edition - Revised & Expanded*. 2016: EPFL Press.

41. Xiao, R. and X. Zhang, *Problems and issues in laser beam welding of aluminum–lithium alloys.* Journal of Manufacturing Processes, 2014. **16**(2): p. 166-175.

42. Aboulkhair, N.T., et al., *Reducing porosity in AlSi10Mg parts processed by selective laser melting.* Additive Manufacturing, 2014. **1-4**: p. 77-86.

43. Kasperovich, G., et al., *Correlation between porosity and processing parameters in TiAl6V4 produced by selective laser melting.* Materials & Design, 2016. **105**: p. 160-170.

44. Gu, D. and Y. Shen, *Balling phenomena in direct laser sintering of stainless steel powder: Metallurgical mechanisms and control methods.* Materials & Design, 2009. **30**(8): p. 2903-2910.

45. Gu, D.D., et al., *Effects of processing parameters on direct laser sintering of multicomponent Cu based metal powder.* Materials Science and Technology, 2006. **22**(12): p. 1449-1455.

46. Zhong, M., et al., *Boundary liquation and interface cracking characterization in laser deposition of Inconel 738 on directionally solidified Ni-based superalloy.* Scripta Materialia, 2005. **53**(2): p. 159-164.

47. Hu, Y.L., et al., *Effect of Ti addition on cracking and microhardness of Inconel 625 during the laser solid forming processing.* Journal of Alloys and Compounds, 2017. **711**: p. 267-277.

48. Gasser, A., et al., *Laser Additive Manufacturing.* Laser Technik Journal, 2010. **7**(2): p. 58-63.

49. Kou, S., *Solidification and liquation cracking issues in welding.* JOM, 2003. **55**(6): p. 37-42.

50. Qiu, C., et al., *On the solidification behaviour and cracking origin of a nickel-based superalloy during selective laser melting.* Materials Characterization, 2019. **148**: p. 330-344.

51. Mercelis, P. and J.-P. Kruth, *Residual stresses in selective laser sintering and selective laser melting.* Rapid prototyping journal, 2006. **12**(5): p. 254-265.

52. Shi, X., et al., *Parameter optimization for Ti-47Al-2Cr-2Nb in selective laser melting based on geometric characteristics of single scan tracks.* Optics & Laser Technology, 2017. **90**: p. 71-79.

53. Sadowski, M., et al., *Optimizing quality of additively manufactured Inconel 718 using powder bed laser melting process.* Additive Manufacturing, 2016. **11**: p. 60-70.

54. Popovich, V.A., et al., *Impact of heat treatment on mechanical behaviour of Inconel 718 processed with tailored microstructure by selective laser melting.* Materials & Design, 2017. **131**: p. 12-22.

55. Gong, X. and K. Chou. *Microstructures of Inconel 718 by Selective Laser Melting*. in *TMS 2015 144th Annual Meeting & Exhibition*. 2016. Cham: Springer International Publishing.

56. Robinson, J., et al., *Determination of the effect of scan strategy on residual stress in laser powder bed fusion additive manufacturing.* Additive Manufacturing, 2018. **23**: p. 13-24.

57. Carter, L.N., et al., *The influence of the laser scan strategy on grain structure and cracking behaviour in SLM powder-bed fabricated nickel superalloy.* Journal of Alloys and Compounds, 2014. **615**: p. 338-347.

58. Bean, G.E., et al., *Build Orientation Effects on Texture and Mechanical Properties of Selective Laser Melting Inconel 718.* Journal of Materials Engineering and Performance, 2019.

59. Bean, G.E., et al., *Effect of laser focus shift on surface quality and density of Inconel 718 parts produced via selective laser melting.* Additive Manufacturing, 2018. **22**: p. 207-215.

60. McLouth, T.D., et al., *The effect of laser focus shift on microstructural variation of Inconel 718 produced by selective laser melting.* Materials & Design, 2018. **149**: p. 205-213.

61. Wan, H.Y., et al., *Effect of scanning strategy on mechanical properties of selective laser melted Inconel 718.* Materials Science and Engineering: A, 2019. **753**: p. 42-48.

62. McLouth, T.D., et al., *Variations in ambient and elevated temperature mechanical behavior of IN718 manufactured by selective laser melting via process parameter control.* Materials Science and Engineering: A, 2020. **780**: p. 139184.

63. Kirka, M.M., et al., *Mechanical behavior of post-processed Inconel 718 manufactured through the electron beam melting process.* Materials Science and Engineering: A, 2017. **680**: p. 338-346.

64. Anam, M.A., et al., *Effect of Scan Pattern on the Microstructural Evolution of Inconel 625 during Selective Laser Melting*. 2014.

65. Nadammal, N., et al., *Effect of hatch length on the development of microstructure, texture and residual stresses in selective laser melted superalloy Inconel 718.* Materials & Design, 2017. **134**: p. 139-150.

66. Sufiiarov, V.S., et al., *The effect of layer thickness at selective laser melting.* Procedia engineering, 2017. **174**: p. 126-134.

67. Ma, M., et al., *Layer thickness dependence of performance in high-power selective laser melting of 1Cr18Ni9Ti stainless steel.* Journal of Materials Processing Technology, 2015. **215**: p. 142-150.

68. Ladewig, A., et al., *Influence of the shielding gas flow on the removal of process by-products in the selective laser melting process.* Additive Manufacturing, 2016. **10**: p. 1-9.

69. Bean, G.E., et al., *Process gas influence on microstructure and mechanical behavior of Inconel 718 fabricated via selective laser melting.* Progress in Additive Manufacturing, 2020.

70. Gao, Y., et al., *Effect of δ phase on high temperature mechanical performances of Inconel 718 fabricated with SLM process.* Materials Science and Engineering A, 2019. **767**: p. 138327.

71. Witkin, D.B., et al., *Anomalous Notch Rupture Behavior of Nickel-Based Superalloy Inconel 718 Due to Fabrication by Additive Manufacturing.* Metallurgical and Materials Transactions A, 2019. **50**(8): p. 3458-3465.

72. Giacobbe, F., *Heat Transfer Behavior of Gaseous Mixtures Containing Helium and Argon or Nitrogen.* Journal of Thermophysics and Heat Transfer - J THERMOPHYS HEAT TRANSFER, 2003. **17**: p. 112-119.

73. Faubert, F.M. and G.S. Springer, *Measurement of the Thermal Conductivity of Argon, Krypton, and Nitrogen in the Range 800–2000°K.* The Journal of Chemical Physics, 1972. **57**(6): p. 2333-2340.

74. Grünberger, T. and R. Domröse, *Direct Metal Laser Sintering: Identification of process phenomena by optical in-process monitoring.* Laser technik journal, 2015. **12**(1): p. 45-48.

75. Ferrar, B., et al., *Gas flow effects on selective laser melting (SLM) manufacturing performance.* Journal of Materials Processing Technology, 2012. **212**(2): p. 355-364.

76. Metelkova, J., et al., *On the influence of laser defocusing in Selective Laser Melting of 316L.* Additive Manufacturing, 2018. **23**: p. 161-169.

77. Shi, W., et al., *Beam Diameter Dependence of Performance in Thick-Layer and High-Power Selective Laser Melting of Ti-6Al-4V.* Materials, 2018. **11**(7).

78. Ramsay, J.F. *Rayleigh Distance as a Normalizing Range for Beam Power Transmission*. in *G-MTT Symposium Digest*. 1965.

79. Bertoli, U.S., et al., *On the limitations of volumetric energy density as a design parameter for selective laser melting.* Materials & Design, 2017. **113**: p. 331-340.

80. NASA, *MSFS-SPEC-3717 - Specification for Control and Qualification of laser Powder Bed Fusion Metallurgical Processes.* 2017.

81. Tillmann, W., et al., *Hot isostatic pressing of IN718 components manufactured by selective laser melting.* Additive Manufacturing, 2017. **13**: p. 93-102.

82. Shassere, B., et al., *Correlation of microstructure to creep response of hot isostatically pressed and aged electron beam melted Inconel 718.* Metallurgical and Materials Transactions A, 2018. **49**(10): p. 5107-5117.

83. Amato, K.N., et al., *Microstructures and mechanical behavior of Inconel 718 fabricated by selective laser melting.* Acta Materialia, 2012. **60**(5): p. 2229-2239.

84. Gallmeyer, T.G., et al., *Knowledge of process-structure-property relationships to engineer better heat treatments for laser powder bed fusion additive manufactured Inconel 718.* Additive Manufacturing, 2020. **31**: p. 100977.

85. Deng, D., et al., *Microstructure and mechanical properties of Inconel 718 produced by selective laser melting: Sample orientation dependence and effects of post heat treatments.* Materials Science and Engineering: A, 2018. **713**: p. 294-306.

86. Kuo, Y.-L., S. Horikawa, and K. Kakehi, *Effects of build direction and heat treatment on creep properties of Ni-base superalloy built up by additive manufacturing.* Scripta Materialia, 2017. **129**: p. 74-78.

87. Ni, M., et al., *Anisotropic tensile behavior of in situ precipitation strengthened Inconel 718 fabricated by additive manufacturing.* Materials Science and Engineering: A, 2017. **701**: p. 344-351.

88. Mills, W.J., *Fracture Toughness Variations for Alloy 718 Base Metal and Welds.* Superalloy 718-Metallurgy and Applications, The Minerals, Metals & Materials Society, 1989: p. 517-532.

89. Shankar, V., K. bhanu sankara rao, and S.L. Mannan, *Microstructure and mechanical properties of Inconel 625 superalloy*. Vol. 288. 2001. 222-232.

90. Hassan, B. and J. Corney, *Grain boundary precipitation in Inconel 718 and ATI 718Plus.* Materials Science and Technology, 2017. **33**(16): p. 1879-1889.

91. Sundararaman, M. and P. Mukhopadhyay, *Carbide Precipitation in Inconel 718*, in *High Temperature Materials and Processes*. 1993. p. 351.

92. Sundararaman, M., P. Mukhopadhyay, and S. Banerjee, *Precipitation of the δ-Ni3Nb phase in two nickel base superalloys.* Metallurgical Transactions A, 1988. **19**(3): p. 453-465.

93. Raghavan, N., et al., *Numerical modeling of heat-transfer and the influence of process parameters on tailoring the grain morphology of IN718 in electron beam additive manufacturing*. Vol. 112. 2016. 303-314.

94. Donachie, M.J. and S.J. Donachie, *Superalloys: A Technical Guide, 2nd Edition*. Ingenieria de minas. 2002: ASM International.

95. Wagner, H.J. and A.M. Hall, *Physical Metallurgy of Alloy 718*. 1965: Defense Metals Information Center, Battelle Memorial Institute.

96. Eiselstein, H.L., *US3046108 - Age-hardenable nickel alloy*. 1959.

97. Keiser, D.D. and H.L. Brown, *Review of the physical metallurgy of Alloy 718*. 1976, Idaho National Engineering Lab., Idaho Falls (USA).

98. *Nickel Alloy, Corrosion and Heat Resistant, Bars, Forgings, and Rings 52.5Ni 19Cr 3.0Mo 5.1Cb 0.90Ti 0.50Al 19Fe, Consumable Electrode or Vacuum Induction Melted 1775°F (968°C) Solution and Precipitation Heat Treated*. 1965, SAE International.

99. *Nickel Alloy, Corrosion and Heat-Resistant, Bars, Forgings, and Rings 52.5Ni - 19Cr - 3.0Mo - 5.1Cb (Nb) - 0.90Ti - 0.50AI - 18Fe Consumable Electrode or Vacuum Induction Melted 1775 °F (968 °C) Solution Heat Treated, Precipitation-Hardenable*. 2016, SAE International.

100. Paulonis, D.F., J.M. Oblak, and D.S. Duvall, *PRECIPITATION IN NICKEL-BASE ALLOY 718.* 1969.

101. Sundararaman, M., P. Mukhopadhyay, and S. Banerjee, *Deformation behaviour of γ" strengthened inconel 718.* Acta Metallurgica, 1988. **36**(4): p. 847-864.

102. Oblak, J.M., D.F. Paulonis, and D.S. Duvall, *Coherency strengthening in Ni base alloys hardened by DO22 γ' precipitates.* Metallurgical Transactions, 1974. **5**(1): p. 143.

103. Reed, R.C., *The Superalloys: Fundamentals and Applications*. 2006, Cambridge: Cambridge University Press.

104. Lingenfelter, A., *Welding of Inconel alloy 718: A historical overview.* Superalloy, 1989. **718**: p. 673-683.

105. Gordine, J., *Some problems in welding Inconel 718.* WELD J, 1971. **50**(11): p. 480.

106. Ram, G.D.J., et al., *Microstructure and tensile properties of Inconel 718 pulsed Nd-YAG laser welds.* Journal of Materials Processing Technology, 2005. **167**(1): p. 73-82.

107. Y. Desvallees, M.B., F. Bois, N. Beaude, *Delta Phase in Inconel 718: Mechanical Properties and Forging Process Requirements.* Superalloys 718, 625, 706 and Various Derivatives, 1994: p. 281-291.

108. Muller, J.F. and M.J. Donachie, *The effects of solution and intermediate heat treatments on the notch-rupture behavior of Inconel 718.* Metallurgical and Materials Transactions A, 1975. **6**(12): p. 2221.

109. Mitchell, A., et al., *The precipitation of primary carbides in alloy 718.* superalloys, 1994. **718**(625,706): p. 65-78.

110. Antonsson, T. and H. Fredriksson, *The effect of cooling rate on the solidification of INCONEL 718.* Metallurgical and Materials Transactions B, 2005. **36**(1): p. 85-96.

111. Slama, C., C. Servant, and G. Cizeron, *Aging of the Inconel 718 alloy between 500 and 750 °C.* Journal of Materials Research, 1997. **12**(9): p. 2298-2316.

112. Silva, C., et al., *Characterization of alloy 718 subjected to different thermomechanical treatments.* Materials Science and Engineering: A, 2017. **691**: p. 195-202.

113. Knorovsky, G.A., et al., *INCONEL 718: A solidification diagram.* Metallurgical Transactions A, 1989. **20**(10): p. 2149-2158.

114. Cieslak, M.J., et al., *A comparison of the solidification behavior of INCOLOY 909 and INCONEL 718.* Metallurgical Transactions A, 1990. **21**(1): p. 479-488.

115. Eiselstein, H.L., *Metallurgy of a Columbium-Hardened Nickel-Chromium-Iron Alloy*

Advances in the Technology of Stainless Steels and Related Alloys. 1965, West Conshohocken, PA: ASTM International. 62-79.

116. Chaturvedi, M.C. and Y.-f. Han, *Strengthening mechanisms in Inconel 718 superalloy.* Metal Science, 1983. **17**(3): p. 145-149.

117. Hertzberg, R.W., R.P. Vinci, and J.L. Hertzberg, *Deformation and Fracture Mechanics of Engineering Materials, 5th Edition*. 2012: Wiley.

118. *Copyright*, in *Introduction to Dislocations (Fifth Edition)*, D. Hull and D.J. Bacon, Editors. 2011, Butterworth-Heinemann: Oxford. p. iv.

119. Groover, M.P., *Fundamentals of Modern Manufacturing: Materials, Processes, and Systems*. 2010: John Wiley & Sons.

120. *Heat Treatment Wrought Nickel Alloy and Cobalt Alloy Parts*. 2001, SAE International.

121. *Nickel Alloy, Corrosion and Heat Resistant, Bars, Forgings, and Rings, 52.5Ni - 19Cr - 3.0Mo - 5.1Cb - 0.90Ti - 0.50Al - 18Fe, Consumable Electrode or Vacuum Induction Melted, 1950 °F (1066 °C) Solution Heat Treated, Precipitation Hardenable*. 1965, SAE International.

122. Mostafa, A., et al., *Structure, texture and phases in 3D printed IN718 alloy subjected to homogenization and HIP treatments.* Metals, 2017. **7**(6): p. 196.

123. *Inconel 718 Technical Data.* 2015.

124. *Inconel 625 Technical Data.* 2015.

125. *Haynes Waspaloy alloy*. 2017.

126. Kumar, S., K. Chattopadhyay, and V. Singh, *Tensile Behavior of Ti-6Al-4V alloy at Elevated Temperatures.*

127. *Composition/Properties.*

128. Committee, A.S.M.H., *Properties and Selection: Nonferrous Alloys and Special-Purpose Materials*. 1990, ASM International.

129. Pereira, J.M. and B.A. Lerch, *Effects of heat treatment on the ballistic impact properties of Inconel 718 for jet engine fan containment applications.* International Journal of Impact Engineering, 2001. **25**(8): p. 715-733.

130. Hinojos, A., et al., *Joining of Inconel 718 and 316 Stainless Steel using electron beam melting additive manufacturing technology.* Materials & Design, 2016. **94**: p. 17-27.

131. E. Leshock, C., J.-N. Kim, and Y. Shin, *Plasma enhanced machining of Inconel 718: Modeling of workpiece temperature with plasma heating and experimental results*. Vol. 41. 2001. 877-897.

132. Fernandez, D., et al., *Comparison of machining inconel 718 with conventional and sustainable coolant*. Vol. 2014. 2014. 506-510.

133. *ASTM E407 - Standard Practice for Microetching Metals and Alloys*. 2015.

134. Tan, X.P., et al., *Carbide precipitation characteristics in additive manufacturing of Co-Cr-Mo alloy via selective electron beam melting.* Scripta Materialia, 2018. **143**: p. 117-121.

135. Jia, Q. and D. Gu, *Selective laser melting additive manufacturing of Inconel 718 superalloy parts: Densification, microstructure and properties.* Journal of Alloys and Compounds, 2014. **585**: p. 713-721.

136. Wei, H.L., J. Mazumder, and T. DebRoy, *Evolution of solidification texture during additive manufacturing.* Scientific reports, 2015. **5**: p. 16446.

137. Liu, F., et al., *The effect of laser scanning path on microstructures and mechanical properties of laser solid formed nickel-base superalloy Inconel 718.* Journal of Alloys and Compounds, 2011. **509**(13): p. 4505-4509.

138. Zhang, F., et al., *Effect of heat treatment on the microstructural evolution of a nickel-based superalloy additive-manufactured by laser powder bed fusion.* Acta Materialia, 2018. **152**: p. 200-214.

139. Shi, X., et al., *Solidification and Segregation Behaviors of Superalloy IN718 at a Slow Cooling Rate.* Materials (Basel, Switzerland), 2018. **11**(12): p. 2398.

140. Manikandan, S.G.K., et al., *Effect of weld cooling rate on Laves phase formation in Inconel 718 fusion zone.* Journal of Materials Processing Technology, 2014. **214**(2): p. 358-364.

141. Radhakrishna, C.H. and K. Prasad Rao, *The formation and control of Laves phase in superalloy 718 welds.* Journal of Materials Science, 1997. **32**(8): p. 1977-1984.

142. Whitesell, H.S., L. Li, and R.A. Overfelt, *Influence of solidification variables on the dendrite arm spacings of Ni-based superalloys.* Metallurgical and Materials Transactions B, 2000. **31**(3): p. 546-551.

143. Keller, T., et al., *Application of finite element, phase-field, and CALPHAD-based methods to additive manufacturing of Ni-based superalloys.* Acta materialia, 2017. **139**: p. 244-253.

144. Sohrabi, M.J., H. Mirzadeh, and M. Rafiei, *Solidification behavior and Laves phase dissolution during homogenization heat treatment of Inconel 718 superalloy.* Vacuum, 2018. **154**: p. 235-243.

145. Miao, Z.-j., et al., *Quantitative analysis of homogenization treatment of INCONEL718 superalloy.* Transactions of Nonferrous Metals Society of China, 2011. **21**(5): p. 1009-1017.

146. Liang, X., et al. *An investigation of the homogenization and deformation of alloy 718 ingots*.

147. Sundararaman, M., P. Mukhopadhyay, and S. Banerjee, *Carbide precipitation in nickel base superalloys 718 and 625 and their effect on mechanical properties.* Superalloys, 1997. **718**: p. 625-706.

148. Xu, Z., et al., *Effect of post processing on the creep performance of laser powder bed fused Inconel 718.* Additive Manufacturing, 2018. **24**: p. 486-497.

149. Tucho, W.M., et al., *Microstructure and hardness studies of Inconel 718 manufactured by selective laser melting before and after solution heat treatment.* Materials Science and Engineering: A, 2017. **689**: p. 220-232.

150. Tian, Y., et al., *Rationalization of microstructure heterogeneity in Inconel 718 builds made by the direct laser additive manufacturing process.* Metallurgical and Materials Transactions A, 2014. **45**(10): p. 4470-4483.

151. Mitchell, A. *Primary carbides in Alloy 718*.

152. Oradei-Basile, A. and J.F. Radavich, *A current TTT diagram for wrought alloy 718.* Superalloys, 1991. **718**(625): p. 325-335.

153. Brooks, J.W. and P.J. Bridges, *Metallurgical Stability of Inconel Alloy 718*. 1988. 33-42.

154. Yan, F., W. Xiong, and J.E. Faierson, *Grain Structure Control of Additively Manufactured Metallic Materials.* Materials, 2017. **10**(11).

155. Kuo, Y.-L., T. Nagahari, and K. Kakehi, *The Effect of Post-Processes on the Microstructure and Creep Properties of Alloy718 Built Up by Selective Laser Melting.* Materials (Basel, Switzerland), 2018. **11**(6): p. 996.

156. Jiang, R., et al., *Varied heat treatments and properties of laser powder bed printed Inconel 718.* Materials Science and Engineering: A, 2019. **755**: p. 170-180.

157. Strondl, A., et al., *Microstructure and mechanical properties of nickel based superalloy IN718 produced by rapid prototyping with electron beam melting (EBM).* Materials Science and Technology, 2011. **27**(5): p. 876-883.

158. Kuo, Y.-L., S. Horikawa, and K. Kakehi, *The effect of interdendritic δ phase on the mechanical properties of Alloy 718 built up by additive manufacturing.* Materials & Design, 2017. **116**: p. 411-418.

159. Kuo, Y.-L. and K. Kakehi, *Influence of Powder Surface Contamination in the Ni-Based Superalloy Alloy718 Fabricated by Selective Laser Melting and Hot Isostatic Pressing.* Metals, 2017. **7**(9).

160. Pröbstle, M., et al., *Superior creep strength of a nickel-based superalloy produced by selective laser melting.* Materials Science and Engineering: A, 2016. **674**: p. 299-307.

161. Xu, Z., et al., *Creep Behaviour of Inconel 718 Processed by laser powder bed fusion.* Journal of Materials Processing Technology, 2018. **256**(High Temperature Materials and Processes 35 2015): p. 13-24.

162. Hautfenne, C., S. Nardone, and E. De Bruycker, *Influence of heat treatments and build orientation on the creep strength of additive manufactured IN718*. 2017.

163. Nix, W.D., et al., *The principal facet stress as a parameter for predicting creep rupture under multiaxial stresses.* Acta Metallurgica, 1989. **37**(4): p. 1067-1077.

164. Trosch, T., et al., *Microstructure and mechanical properties of selective laser melted Inconel 718 compared to forging and casting.* Materials Letters, 2016. **164**: p. 428-431.

165. Caiazzo, F., et al., *Laser powder-bed fusion of Inconel 718 to manufacture turbine blades.* The International Journal of Advanced Manufacturing Technology, 2017. **93**(9): p. 4023-4031.

166. *ASTM E8 - Standard Test Methods for Tension Testing of Metallic Materials*.

167. *ASTM E139 - Standard Test Methods for Conducting Creep, Creep-Rupture, and Stress-Rupture Tests of Metallic Materials*. 2018.

168. *ASTM E21 Standard Test Methods for Elevated Temperature Tension Tests of Metallic Materials*.

169. *ASTM E292 - Standard Test Methods for Conducting Time-for-Rupture Notch Tension Tests of Materials*.

170. Kalluri, S., et al., *Deformation and Damage Mechanisms in Inconel 718 Superalloy.* 1994.

171. Devaux, A., et al., *Gamma double prime precipitation kinetic in Alloy 718.* Materials Science and Engineering: A, 2008. **486**(1): p. 117-122.

172. Chaturvedi, M.C. and Y. Han, *Effect of particle size on the creep rate of superalloy Inconel 718.* Materials Science and Engineering, 1987. **89**: p. L7-L10.

173. Caliari, F.R., et al., *Effect of Double Aging Heat Treatment on the Short-Term Creep Behavior of the Inconel 718.* Journal of Materials Engineering and Performance, 2016. **25**(6): p. 2307-2317.

174. Chaturvedi, M.C., *Creep Deformation of Alloy 718.* Superalloy 718-Metallurgy and Applications, The Minerals, Metals & Materials Society, 1989: p. 489-498.

175. Hayes, R.W., *Creep Deformation of Inconel Alloy 718.* Superalloys 718, 625 and Various Derivatives, 1991: p. 549-562.

176. Han, Y. and M.C. Chaturvedi, *A study of back stress during creep deformation of a superalloy inconel 718.* Materials Science and Engineering, 1987. **85**: p. 59-65.

177. Hayes, R.W., et al., *Effect of environment on the rupture behavior of alloys 909 and 718.* Materials Science and Engineering: A, 1994. **177**(1): p. 43-53.

178. Gao, M., D.J. Dwyer, and R.P. Wei, *Niobium enrichment and environmental enhancement of creep crack growth in nickel-base superalloys.* Scripta metallurgica et materialia, 1995. **32**(8): p. 1169-1174.

179. Gao, M., D.J. Dwyer, and R.P. Wei, *Chemical and microstructural aspects of creep crack growth in Inconel 718 alloy.* Superalloys 718, 625, 706 and various derivatives, 1994: p. 581-592.

180. Liu, C.D., et al., *Creep crack growth behaviour of Alloy 718.* Superalloys, 1991. **178**(625): p. 537-548.

181. Zaman, T., et al., *Investigation of low stress rupture properties in Inconel-718 super alloy.* IOP Conference Series: Materials Science and Engineering, 2016. **146**: p. 012051.

182. Shiozawa, K. and J.R. Weertman, *Studies of nucleation mechanisms and the role of residual stresses in the grain boundary cavitation of a superalloy.* Acta Metallurgica, 1983. **31**(7): p. 993-1004.

183. Christ, H.-J., K. Wackerman, and U. Krupp, *On the mechanism of dynamic embrittlement and its effect on fatigue crack propagation in IN718 at 650°C.* Procedia Structural Integrity, 2016. **2**: p. 557-564.

184. Pfaendtner, J.A. and C.J. McMahon Jr, *Oxygen-induced intergranular cracking of a Ni-base alloy at elevated temperatures—an example of dynamic embrittlement.* Acta Materialia, 2001. **49**(16): p. 3369-3377.

185. Krupp, U., et al., *Brittle intergranular fracture of a Ni-base superalloy at high temperatures by dynamic embrittlement.* Materials Science and Engineering: A, 2004. **387-389**: p. 409-413.

186. Carpenter, W., B.S.J. Kang, and K.M. Chang, *SAGBO Mechanism on high temperature cracking behavior of Ni-base superalloys.* Superalloys 718, 625, 706 and Various Derivatives, 1997: p. 679-688.

187. Bika, D. and C.J. McCmahon Jr, *A kinetic model for dynamic embrittlement.* physica status solidi (a), 1992. **131**(2): p. 639-649.

188. Pang, X.J., et al., *Surface enrichment and grain boundary segregation of niobium in inconel 718 single-and poly-crystals.* Scripta Metallurgica et Materialia;(United States), 1994. **31**(3).

189. Azadian, S., *Aspect of Precipitation in Alloy Inconel 718.* 2004.

190. Ingesten, G.S.a.N.G., *Grain Boundary δ-phase Morphologies, Carbides and Notch Rupture Sensitivity of Cast Alloy 718.* Superalloys 718, 625 and Various Derivatives, 1991: p. 603-620.

191. Booker, M.K. and B.L.P. Booker, *Elevated-temperature tensile properties of three heats of commercially heat-treated Alloy 718*. 1980, Oak Ridge National Lab., TN (United States).

192. P.J. Kanetas, L.A.R.O., M. P. Guerrero Mata, M. De La Garza, V. Paramo Lopez, *Influence of the Delta Phase in the Microstructure of the Inconel 718 subjected to "Delta-Processing" Heat Treatment and Hot Deformed.* Procedia Materials Science, 2015. **8**: p. 1160-1165.

193. Han, Y. and M.C. Chaturvedi, *Steady state creep deformation of superalloy inconel 718.* Materials Science and Engineering, 1987. **89**: p. 25-33.

194. Dieter, G.E. and D. Bacon, *Mechanical metallurgy*. Vol. 3. 1986: McGraw-hill New York.

195. Manjoine, M.J., *Influence of rate of strain and temperature on yield stresses of mild steel*. 1944, [Place of publication not identified]: [publisher not identified].

196. Manjoine, M.J., *Ductility Indices at Elevated Temperature.* Journal of Engineering Materials and Technology, 1975. **97**(2): p. 156-161.

197. Zhu, Q., et al., *Tensile Deformation and Fracture Behaviors of a Nickel-Based Superalloy via In Situ Digital Image Correlation and Synchrotron Radiation X-ray Tomography.* Materials, 2019. **12**(15): p. 2461.

198. Xu, J., et al., *Short-term creep behavior of an additive manufactured non-weldable Nickel-base superalloy evaluated by slow strain rate testing.* Acta Materialia, 2019. **179**: p. 142-157.

199. Hayes, R.W., *Oxygen Embrittlement and Time-Dependent Grain-Boundary Cracking of ALLVAC 718PLUS.* Metallurgical and Materials Transactions A, 2008. **39**(11): p. 2596-2606.

200. Miller, C.F., G.W. Simmons, and R.P. Wei, *High temperature oxidation of Nb, NbC and Ni 3 Nb and oxygen enhanced crack growth.* Scripta Materialia, 2000. **42**(3): p. 227-232.

201. Xu, C. and W. Gao, *Pilling-Bedworth ratio for oxidation of alloys.* Materials Research Innovations, 2000. **3**(4): p. 231-235.

202. Douglass, D.L., *The thermal expansion of niobium pentoxide and its effect on the spalling of niobium oxidation films.* Journal of the Less Common Metals, 1963. **5**(2): p. 151-157.

203. Brinkman, C. and G. Korth, *Strain Fatigue and Tensile Behavior of Inconel® 718 from Room Temperature to 650°C.* Journal of Testing and Evaluation, 1974. **2**(4): p. 249-259.

204. Garruchet, S., et al., *Diffusion of oxygen in nickel: A variable charge molecular dynamics study.* Solid State Communications, 2010. **150**(9): p. 439-442.

205. Wei, R.P., et al., *Oxygen enhanced crack growth in nickel-based superalloys and materials damage prognosis.* Engineering Fracture Mechanics, 2009. **76**(5): p. 715-727.

206. Floreen, S., *The creep fracture of wrought nickel-base alloys by a fracture mechanics approach.* Metallurgical Transactions A, 1975. **6**(9): p. 1741.

207. Valerio, P., M. Gao, and R.P. Wei, *Environmental enhancement of creep crack growth in Inconel 718 by oxygen and water vapor.* Scripta Metallurgica et Materialia;(United States), 1994. **30**(10).

208. Varela, A.d.V., et al., *Oxidation assisted intergranular cracking in 718 Nickel Superalloy: on the mechanism of dynamic embrittlement.* Journal of Materials Research and Technology, 2018. **7**(3): p. 319-325.

209. Sadananda, K. and P. Shahinian, *Creep crack growth in alloy 718.* Metallurgical Transactions A, 1977. **8**(3): p. 439-449.

210. Poole, J.M., K.R. Stultz, and J.M. Manning. *The □Effect of Ingot Homogenization Practice on The Properties of Wrought Alloy 718*.

211. Li, S., et al., *The effect of phase on crack propagation under creep and fatigue conditions in alloy 718.* Superalloys, 1994. **718**: p. 625-706.

212. Azadian, S., L.-Y. Wei, and R. Warren, *Delta phase precipitation in Inconel 718.* Materials Characterization, 2004. **53**(1): p. 7-16.

213. Totten, G.E., *ASM Handbook Volume 4E - Heat Treating of Nonferrous Alloys*. ASM International.

214. Michal, J., et al., *Phase Transformations in Nickel base Superalloy Inconel 718 during Cyclic Loading at High Temperature.* Production Engineering Archives, 2017. **15(**15): p. 15-18.

215. S. Mahadevan, S.N., J. B. Singh, A. Verma, B. Paul, K. Ramaswamy, *Evolution of δ Phase Microstructure in Alloy 718.* 7th International Symposium on Superalloy 718 and Derivatives, 2010: p. 737-750.

216. Ding, H.-h., et al., *Effect of cooling rate on microstructure and tensile properties of powder metallurgy Ni-based superalloy.* Transactions of Nonferrous Metals Society of China, 2018. **28**(3): p. 451-460.

217. Wei, X.-p., et al., *Strain-induced Precipitation Behavior of δ Phase in Inconel 718 Alloy.* Journal of Iron and Steel Research, International, 2014. **21**: p. 375–381.

218. Beaubois, V., et al., *Short term precipitation kinetics of delta phase in strain free Inconel* 718 alloy.* Materials Science and Technology, 2004. **20**(8): p. 1019-1026.

219. Cone, F.P., *Observations on the Development of Delta Phase in IN718 Alloy*. Vol. 1. 2001. 323-332.

220. Zhang, H.Y., et al., *Deformation characteristics of δ phase in the delta-*processed Inconel *718 alloy.* Materials Characterization, 2010. **61**(1): p. 49-53.

221. Anderson, M., et al., *δ Phase precipitation in Inconel 718 and associated mechanical properties.* Materials Science and Engineering: A, 2016. **679**.

222. Mei, Y., et al., *Effects of cold rolling on the precipitation kinetics and the morphology evolution of intermediate phases in Inconel 718 alloy*. Journal of Alloys and Compounds, 2015. **649**: p. 949-960.

223. Zhang, J.-S., *High temperature deformation and fracture of materials*. 2010: Elsevier.